Politechnika Wrocławska

FIELD OF SCIENCE: NATURAL SCIENCES
DISCIPLINE OF SCIENCE: CHEMICAL SCIENCES

DOCTORAL DISSERTATION

Amyloids: correlating autofluorescence in one- and two-photon regimes with morphology and secondary structure

Manuela Grelich-Mucha, MSc. Eng.

Supervisors:
Prof. Joanna Olesiak-Bańska (Politechnika Wrocławska, Poland)
Prof. Vladimir Torbeev (Université de Strasbourg, France)

Keywords: amyloid structures, autofluorescence, secondary structure, β-sheet structure, peptides and proteins

WROCŁAW 2025

„Jeden ojciec znaczy więcej niż stu nauczycieli”

“One father is more than a hundred schoolmasters”

George Herbert

In memory of my Dad,
who was for me a big inspiration.

Acknowledgements

First of all, I would like to thank my supervisors, **Prof. Joanna Olesiak-Bańska** and **Prof. Vladimir Torbeev**. I am very thankful for your mentoring and guidance throughout my doctoral studies. **Prof. Joanna Olesiak-Bańska** – I am especially grateful for the time you devoted to the discussions, your enthusiasm, and support. **Prof. Vladimir Torbeev** - I am very thankful for your constant openness to my stays at your research group, for your explanations of scientific problems, and inspiring ideas. I am glad to you both that my research was well organized, especially considering the pandemic restrictions.

I am grateful to **Prof. Katarzyna Matczyszyn** for selecting me from the group of students and proposing a scientific journey. If not you, I would not be at this stage today.

I express my gratitude to all persons from Prof. Torbeev's research group. I am especially thankful to **Elise** and **Valentin**, who taught me how to perform solid-phase peptide synthesis, and to my collaborators, **Ana**, **Thomas**, and **Alexis**, for their help and support.

I am also very grateful to **Asia** for the help with accommodation in Strasbourg, discussions, and pieces of advice.

I appreciate the whole team of Prof. Olesiak-Bańska – **Agata**, **Aleksandra**, **Ania**, **Karolina**, **Maciek**, and **Patryk** for the common collaboration, for the time spent in the laboratory and outside.

I am very thankful to my scientific collaborators, **Prof. Łukasz Berlicki**, **Dr. Katarzyna Ożga**, **Prof. Marek Samoć**, **Dr. Mirosława Różycka**, **Prof. Borys Ośmiałowski**, **Dr. Patryk Rybczyński**, **Prof. Robert Zaleśny**, **Prof. Magdalena Rowińska-Żyrek**, and **Dr. Joanna Wątły**.

Dominika, **Ania**, **Agata** - thank you for the time we spent together while organizing the PANIC conference. I appreciated our talks and fruitful cooperation.

Last but not least, I would like to thank my family: my parents, sisters, brother, and parents-in-law. I am thankful for your support, your faith in me in moments of my doubts, and your patience while I was talking about my research.

Foremost, I am thankful to you, **Sebastian**, for your constant support, forbearance, and presence by my side. **Sebastian** and **Janek**, I am thankful to you for everything. This dissertation is dedicated to you.

Table of Contents

List of abbreviations

1P - one-photon
1PA - one-photon absorption
1PEF - one-photon excited fluorescence
1PExc - one-photon excitation
2P - two-photon
2PA - two-photon absorption
2PEF - two-photon excited fluorescence
2PIF - two-photon-induced fluorescence
2PM - two-photon microscopy
3PA - three-photon absorption
AAs- amino acids
Ac- - *N*-acetyl-α-amino group
AD - Alzheimer's disease
AFM - atomic force microscopy
ATR-FTIR - attenuated total reflectance Fourier-transform infrared
Aβ - amyloid-β peptide
BBB - blood-brain barrier
Boc/Bzl - tert-butyloxycarbonyl/benzyl
CD - circular dichroism
CR - Congo Red
DiMe- - *N*,*N*-dimethyl-α-amino group
DiTyr - dityrosine
DMF - *N,N*-dimethylformamide
DMSO - dimethyl sulfoxide
DUVRR – deep ultraviolet resonance Raman
EM - electron microscopy
ESI – electrospray ionization
F_{cor} – corrected fluorescence
Fmoc/tBu – fluorenylmethoxycarbonyl/ /tert-butyl
FQY – fluorescence quantum yield
HEWL - hen egg-white lysozyme
hIAPP – human islet amyloid polypeptide
HPLC - high-performance liquid chromatography
IAPP - islet amyloid polypeptide
IR - infrared
K_d – dissociation constant

LC-MS - liquid chromatography–mass spectrometry
LO - linear optical
MD - molecular dynamics
MPEF – multiphoton excited fluorescence
MW – molecular weight
MW_{theor} – theoretical molecular weight
NIR - near-infrared
NLO - non-linear optical
NMR - nuclear magnetic resonance
PBS - phosphate-buffered saline
PD - Parkinson's disease
PLM - polarized light microscopy
ProCharTS - protein charge-transfer spectra
r.t. – room temperature
SEM – scanning electron microscopy
SHB - short hydrogen bonds
SHG - second harmonic generation
SPPS - solid-phase peptide synthesis
SV AUC - Sedimentation Velocity Analytical Ultracentrifugation
TCSPC - time-correlated single-photon counting
TEM - transmission electron microscopy
TFA - trifluoroacetic acid
ThT - thioflavin T
TTR – transthyretin
UV - ultraviolet
Vis – visible
XRD - X-ray diffraction
αs - α-synuclein
β-LG - β-lactoglobulin

Summary of the Doctoral Thesis

Amyloids are peptide or protein aggregates, characterized by the presence of the secondary β-sheet structure, stabilized by a dense hydrogen-bond network. They occur mainly in the form of elongated fibrils, and their deposition is related to some pathological conditions, including Alzheimer's disease. An interesting fact about amyloids is their peculiar property – autofluorescence. Upon excitation at 340-380 nm, they demonstrate the autofluorescence in the visible range of the electromagnetic spectrum (440-530 nm). Despite several hypotheses were put forward, the exact mechanism still remains elusive. Additionally, their autofluorescence properties upon a multiphoton excitation have been scarcely investigated. The improved knowledge of these non-linear optical properties could enhance the potential for *in vivo* detection of amyloid deposits.

This Doctoral Thesis covers interdisciplinary research of amyloid structures on the border of chemistry and materials science. The research involves (i) solid-phase peptide synthesis of amyloidogenic sequences and elaboration of the optimal incubation conditions, (ii) characterization of linear and non-linear optical properties, morphology, secondary structure of samples of interest, and (iii) molecular dynamics (MD) simulations.

Within the framework of this Doctoral Dissertation, the autofluorescence properties of amyloid fibrils formed from transthyretin 105-115 fragments, TTR(105-115), were investigated. The research covers enantiopure *L*- and *D*-samples along with their racemic mixture. The TTR(105-115) sequences were functionalized at the N- and C-termini with α-amino and amide groups, respectively. The morphology analysis indicated significant differences between the enantiopure and racemic fibrils. Interestingly, the racemic mixture exhibited a blue-shifted autofluorescence signal compared to both enantiopure analogues. In addition, the respective fibrils possessed different arrangements of the secondary β-sheet structure. The combined data provided evidence that variations in morphology and the organization of β-sheets can affect the autofluorescence properties of amyloid fibrils.

To better understand the correlations between the morphology and the secondary structure, the research was extended to other terminal functionalities of TTR(105-115). Indeed, the enantiopure and quasi-racemic samples significantly differed in terms of their morphology. The respective fibrils had different organization of the secondary β-sheet structure. The MD simulations evidenced that a sufficient number of hydrogen bonds is required for amyloid fibrils to be formed. These outcomes demonstrate that modifications of peptides' terminal groups dictate the morphology and secondary structure of the resulting peptide aggregates.

The main research concerns also one- (1P) and two-photon (2P) excited autofluorescence of amyloids derived from hen egg-white lysozyme (HEWL), and correlations between the optical properties, morphology, and the secondary structure. Incubation of HEWL samples at varying ionic strengths led to the formation of amyloid fibrils differing in their morphology and the content of the β-sheet structure. Although the 2P excitation involved nearly twice the lower energy of the corresponding 1P process, the 1P and 2P excited emission signals had different relaxation pathways. The red-shifted 2P autofluorescence signal (compared to the 1P signal) was further confirmed by different fluorescence lifetimes for the 1P and 2P processes. These outcomes evidence that autofluorescence can be excited in a 2P process, which opens the possibility of detecting amyloids *in vivo*.

Overall, the results demonstrate that the interpretation of the morphology and secondary structure of amyloids helps to better understand the autofluorescence phenomenon and that amyloids can be investigated from different points of view, which encourages further research in the field.

Streszczenie Pracy Doktorskiej

Amyloidy należą do agregatów peptydowych lub białkowych, charakteryzujących się obecnością struktury drugorzędowej typu β-kartki, stabilizowanej przez gęstą sieć wiązań wodorowych. Amyloidy występują głównie w formie podłużnych fibryli, a ich odkładanie się związane jest z patologicznym stanem, jakim jest np. choroba Alzheimera. Amyloidy posiadają bardzo ciekawe właściwości optyczne. W wyniku wzbudzenia w zakresie 340-380 nm, emitują sygnał autofluorescencji w zakresie światła widzialnego (440-530 nm). Pomimo wysuniętych kilku hipotez na temat mechanizmu odpowiedzialnego za autofluorescencję amyloidów, właściwe źródło nie zostało jeszcze poznane. Zjawisko autofluorescencji, do którego dochodzi w wyniku wzbudzenia wielofotonowego, zostało zbadane dotychczas w nieznacznym stopniu. Lepsze zrozumienie nieliniowych właściwości optycznych amyloidów daje potencjalną możliwość do ich wykrywania *in vivo*.

Niniejsza Praca Doktorska ma charakter interdyscyplinarny i obejmuje zagadnienia z pogranicza chemii oraz inżynierii materiałowej w badaniu struktur amyloidowych. Przeprowadzone badania obejmują (i) syntezę amyloidogennych peptydów metodą syntezy peptydów na podłożu stałym oraz optymalizację protokołów inkubacji, (ii) charakteryzację liniowych i nieliniowych właściwości optycznych, morfologii, struktury drugorzędowej oraz (iii) symulacje dynamiki molekularnej (MD).

W ramach Pracy Doktorskiej została zbadana autofluorescencja fibryli amyloidowych otrzymanych z fragmentu 105-115 transtyretyny, TTR(105-115). Zostały rozpatrzone *L*- i *D*-enancjomery oraz ich mieszanina racemiczna. Peptydy TTR(105-115) zostały sfunkcjonalizowane grupą α-aminową oraz amidową odpowiednio na N- i C-końcach. Obrazowanie morfologii wskazało na znaczne różnice między fibrylami enancjomerów oraz racematu. Co ciekawe, próbka racemiczna miała przesunięty ku krótszym długościom fal sygnał autofluorescencji względem obu enancjomerów. Ponadto, enancjomeryczne i racemiczne fibryle różniły się ułożeniem struktury typu β-kartki. Otrzymane wyniki pokazują, że różnice w morfologii oraz organizacji struktury β-kartkowej mogą wpływać na autofluorescencję fibryli.

W celu lepszego zrozumienia zależności między morfologią i strukturą drugorzędową, badania zostały poszerzone o różne grupy funkcyjne na N- i C-końcach fragmentów TTR(105-115). Otrzymane enancjomeryczne oraz quasi-racemiczne próbki różniły się pod względem morfologii. Ponadto, badane fibryle charakteryzowały się różnym ułożeniem struktury typu β-kartki. Symulacje MD wskazały, że do powstania fibryli niezbędna jest odpowiednia liczba wiązań wodorowych. Otrzymane wyniki pokazują, że modyfikacje grup końcowych peptydów wpływają na strukturę drugorzędową powstających agregatów.

Przeprowadzone badania obejmują także jedno- (1P) i dwu-fotonowo (2P) wzbudzaną autofluorescencję amyloidów lizozymu białka jaja kurzego (HEWL) i szukania zależności między właściwościami optycznymi, morfologią, a ich strukturą drugorzędową. W wyniku inkubacji HEWL w funkcji siły jonowej powstały fibryle różniące się morfologią i zawartością struktury typu β-kartki. Pomimo tego, że proces wzbudzenia 2P charakteryzuje się niemal dwukrotnie niższą energią niż proces 1P, sygnały 1P i 2P wzbudzanej autofluorescencji charakteryzowały się innymi drogami relaksacji. Przesunięty ku dłuższym długościom fal sygnał 2P autofluorescencji (względem sygnału 1P) został dodatkowo potwierdzony przez różne czasy życia fluorescencji wzbudzanej w procesie 1P i 2P. Otrzymane wyniki udowodniły, że autofluorescencja może zostać wzbudzona w procesie 2P, co otwiera możliwość do wykrywania amyloidów *in vivo.*

Przedstawione wyniki badań pokazują, że interpretacja morfologii i struktury drugorzędowej amyloidów może pomóc w lepszym zrozumieniu zjawiska autofluorescencji oraz wskazują, że struktury te mogą być badane pod wieloma względami. Tym samym, zachęcają do kontynuacji badań w obszarze amyloidów.

Preface

The deposition of amyloid structures is associated with some disorders, including age-related Alzheimer's or Parkinson's diseases, currently being incurable. Their prevalence is forecasted to rise in the coming years due to population aging. Thus, it is of high importance to develop tools aimed at the detection of amyloid deposits. One such possibility offers the peculiar optical property of amyloids - autofluorescence. Its origin has not been deciphered yet, but several hypotheses have been put forward to better understand this phenomenon. Amyloids, when excited at 340-380 nm, emit autofluorescence signal in the blue-green regime (440-530 nm) of the electromagnetic spectrum. Interestingly, the autofluorescence could be investigated in a nonlinear optical regime, opening the possibility of *in vivo* investigations of amyloid deposits. However, the literature provides scarce information in this regard.

Remarkably, some amyloids possess functional properties and play beneficial roles in biological processes. They occur in various morphological forms which corresponds to a phenomenon known as polymorphism. Moreover, they are characterized by beneficial mechanical properties making them suitable candidates for developing novel biomaterials.

The above-mentioned aspects motivated me to undertake the research presented in this Doctoral Dissertation entitled "*Amyloids: correlating autofluorescence in one- and two-photon regimes with morphology and secondary structure"*.

To gain more knowledge and fill some gaps in the field of amyloids, I stated the following hypotheses:

- **Hypothesis 1:** The morphology and the secondary structure affect the autofluorescence properties of amyloid fibrils.
- **Hypothesis 2:** The morphology and secondary structure of supramolecular aggregates can be controlled by the terminal groups of the constituting peptide units.
- **Hypothesis 3:** The autofluorescence of amyloids can appear upon a multi-photon excitation process.
- **Hypothesis 4:** The mechanism behind the one- and multi-photon excited fluorescence emission is different for these two processes.

Throughout my doctoral studies, my research was devoted to setting the accomplished objectives and verifying the posed hypotheses. The theory behind this topic is explained in part **I. INTRODUCTION**, which is divided into three chapters. **Chapter 1** provides theoretical principles on one- and multi-photon optical processes. In **Chapter 2**,

the fundamentals behind peptides and proteins are explained. Then, **Chapter 3** constitutes the current state of knowledge about amyloid structures.

The second part of the Doctoral Dissertation, **II. MAIN RESEARCH CONDUCTED**, is composed of five chapters. **Chapter 4** describes the materials, methods, and general procedures for conducting the experiments and simulations. In Chapters 5-7, the major research results are presented and discussed. Namely, in **Chapter 5** the outcomes regarding autofluorescence of enantiopure *L*- and *D*-samples, and their racemic mixture are presented. The chosen peptide was transthyretin 105-115 (TTR(105-115)) fragment, functionalized at the N- and C-termini with α-amino and amide groups, respectively. The main conclusion is that the spectral shift between the autofluorescence of enantiopure and racemic mixture is dictated by differences in the morphology and the alignment of the secondary β-sheet structure in the studied entities. The discussed research was then extended to other functionalities at both termini of the TTR(105-115) fragment, and it constitutes **Chapter 6**. The N-terminus was functionalized with α-amino, *N*-acetyl-α-amino, or *N,N*-dimethyl-α-amino groups, and the C-terminus with amide or carboxyl groups. Within the frames of the experiments, enantiopure samples and quasi-racemic mixtures were studied. The outcomes demonstrated that the terminal group plays an important role in determining the morphology and the secondary structure of the resulting assemblies. **Chapter 7** provides research regarding one- and two-photon excited autofluorescence of hen egg-white lysozyme (HEWL). Indeed, it has been presented that HEWL can be excited through a two-photon process. Interestingly, the relaxation pathways for the one- and two-photon excited emission processes are different. Nevertheless, the possibility of exciting amyloids in a nonlinear optical regime gives hope for their non-invasive *in vivo* detection. In **Chapter 8**, a summary of the conducted research, the ensuing perspectives, and challenges are included. Afterwards, the author's scientific achievements and activities are presented. Finally, all references and publishing statements are provided.

I. INTRODUCTION

1 Chapter 1. One- and multi-photon optical processes

In this chapter, I discuss the fundamental principles regarding the one- and multi-photon optical processes. To do so, firstly I explain the basics of light-matter interactions, then I describe the Jablonski diagram and the accompanying electronic transitions. I explain two essential fluorescence parameters: fluorescence lifetime and fluorescence quantum yield. I also elucidate two-photon absorption and fluorescence processes and describe how two-photon absorption cross-section can be determined.

1.1 Fundamentals of light-matter interactions

As an electromagnetic wave, light is composed of electric and magnetic fields. The electric field vector $\vec{E}$ and the magnetic field vector $\vec{B}$ are perpendicular to each other and the propagation direction of the wave. To simplify the further description, particular attention will be paid only to $\vec{E}$. When the light travels through a material, its $\vec{E}$ leads to displacement of the charges, resulting in the formation of dipoles expressed by the polarization vector $\vec{P}$. $\vec{P}$ is proportional to the amplitude of $\vec{E}$ and this relationship is described by the following equation:

$$\vec{P} = \overrightarrow{P_0} + \underbrace{\varepsilon_0 \chi^{(1)} \vec{E}}_{\text{LO}} + \underbrace{\varepsilon_0 \chi^{(2)} \vec{E}^2 + \varepsilon_0 \chi^{(3)} \vec{E}^3 + (\dots)}_{\text{NLO}} \quad [1]$$

where $\vec{P}$ is the induced polarization vector; $\overrightarrow{P_0}$ is the permanent polarization vector; $\vec{E}$ is the applied electric field vector; ε_0 is the vacuum permittivity of the material; $\chi^{(1)}, \chi^{(2)}, \chi^{(3)}$ are electric susceptibilities of the medium of given orders (tensors).

At the molecular level, the local electric field $\vec{F}$ can induce a dipole moment, and the optical response of a molecule can be described as follows:

$$\vec{\mu} = \overrightarrow{\mu_0} + \underbrace{\alpha \vec{F}}_{\text{LO}} + \underbrace{\beta \vec{F}^2 + \gamma \vec{F}^3 + (\dots)}_{\text{NLO}} \quad [2]$$

where $\vec{\mu}$ is the induced dipole moment vector; $\overrightarrow{\mu_0}$ is the permanent dipole moment of a molecule; $\vec{F}$ is the local electric field vector; α is the polarizability (tensor); β is the quadratic hyperpolarizability or second order polarizability (tensor); γ is the cubic hyperpolarizability or third order polarizability (tensor).

In both equations ([1] and [2]), the optical effects of materials depend linearly and non-linearly on the external electric field. These two regimes can be denoted as **LO** and **NLO**; they stand for linear optical and non-linear optical responses, respectively.[1-3]

1.2 Jablonski diagram and electronic transitions

When considering the wave-like behaviour, the light can be characterized by its frequency (or wavelength). It can also be described as a group of elementary particles (*i.e.* photons). Thus, when a molecule **absorbs** a photon of appropriate energy, the energy of a single photon can be expressed by the following relationship:

$$E_{photon} = h \cdot \nu = \frac{h \cdot c}{\lambda} = \hbar \cdot \omega \qquad [3]$$

where: E_{photon} is the energy of a photon (J), E_{photon} can also be represented in (eV), where 1 (eV) = $1.602 \cdot 10^{-19}$ (J); h is the Planck constant ($6.626 \cdot 10^{-34}$ ($\frac{J}{Hz}$); ν is the frequency, typically in (Hz); c represents the speed of light; λ denotes the wavelength; $\hbar$ denotes the reduced Planck constant ($1.054 \cdot 10^{-34}$ ($\frac{J}{Hz}$)); ω is the angular frequency (Hz).

A schematic representation of the possible electronic transitions illustrates the Jablonski diagram (**Figure 1**). The **absorption** process is on the order of 10^{-15} s and it typically refers to a transition from the singlet ground state (S_0) to a vibrational level of one of the excited singlet states (*e.g.* S_1 or S_2) when E_{photon} matches the energy bandgap between these two electronic states. Upon promotion to a higher-energy state, the energy is typically relaxed to the lowest vibrational level of the S_1. This process is known as **internal conversion** (**IC**). It is a non-radiative transition since no photons are emitted during this event. To return to the S_0, the excess energy can be released *via* the **non-radiative relaxation** or the radiative transitions (*i.e.* emitting a photon of a specific energy). Particular attention will be paid to the two most fundamental processes in the molecular systems. **Fluorescence** (S_1-S_0 transition) is defined as a de-excitation process during which an electron occupying an orbital in the singlet excited state has an opposite spin direction to an unpaired electron occupying an orbital in the singlet ground state. Thus, this transition is spin-allowed. It is in the order of 10^{-10}-10^{-7} s. When an electron undergoes de-excitation from the excited triplet state (T_n) to the singlet ground state, the underlying relaxation is recognized as **phosphorescence** (T_1-S_0 transition). This transition is spin-forbidden (kinetically unfavoured) and therefore a timescale for this process spans from milliseconds to seconds. The phosphorescence is preceded by the radiationless transition from S_1 to T_1 (with a different spin multiplicity), known as **intersystem crossing** (**ISC**). Both fluorescence and phosphorescence are radiative transitions during which the energy is released by emitting a photon of a specific energy.[4-5]

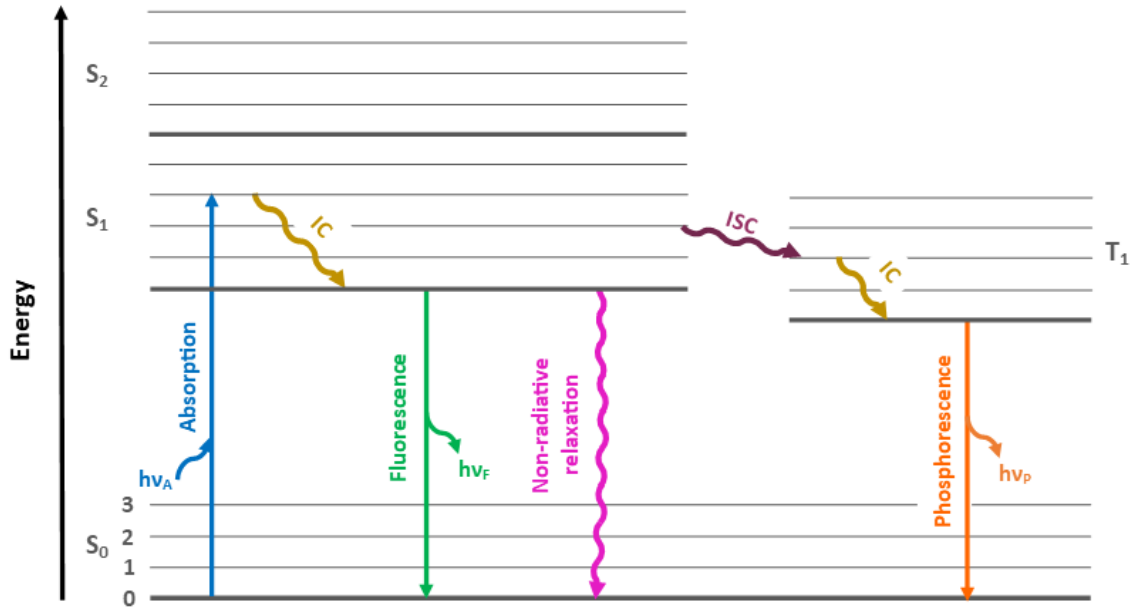

Figure 1. The schematic representation of the Jablonski diagram. Radiative transitions: absorption, fluorescence, and phosphorescence are denoted as straight lines. Non-radiative transitions, IC – internal conversion, ISC – intersystem crossing, and non-radiative relaxation are demonstrated as curvy lines. S_0 – singlet ground state, S_1 – first excited singlet state, S_2 – second excited singlet state, T_1 – first excited triplet state. Horizontal lines numbered (0-3) in S_0 refer to vibrational states. To simplify the scheme, the vibrational states in S_1 and S_2 were not numbered. The designations $h\nu_A$, $h\nu_F$, and $h\nu_P$ correspond to photon energies involved in absorption, fluorescence, and phosphorescence processes, respectively.

1.3 Fluorescence parameters: lifetime and quantum yield

As one of the main objectives of this dissertation concerns the (auto)fluorescence properties of amyloidogenic structures, here I introduce the fundamental parameters quantitatively describing the fluorescence. In general, the de-excitation from the S_1 state (**Figure 1**) can be expressed by the equation [4]:

$$-\frac{d[S^*]}{dt} = (k_r + k_{nr}) \cdot [S^*] \qquad [4]$$

where $[S^*]$ is a concentration of fluorescent species in the S_1 state;

$k_r = k_f$ is a rate constant for radiative pathway being here equal to the rate constant of fluorescence (k_f);

$k_{nr} = k_{IC} + k_{ISC} + k_{nr\_relaxation}$ is a rate constant for all non-radiative deactivation pathways being equal to the sum of the rate constant for internal conversion (k_{IC}), the rate constant for intersystem crossing (k_{ISC}), and the rate constant for relaxations to the ground state ($k_{nr\_relaxation}$).

The k_r and k_{nr} parameters can be then combined to define the **fluorescence lifetime**, as follows:

$$\tau = \frac{1}{k_r + k_{nr}} \quad [5]$$

The τ is the fluorescence lifetime and represents the average time a fluorophore remains excited before returning to the ground state.

Nevertheless, the most essential parameter characterizing the efficiency of fluorescence is **fluorescence quantum yield** (FQY, φ). In principle, the FQY is the ratio of a number of photons emitted through fluorescence to the number of photons absorbed, and is described by equation [6]:

$$FQY = \frac{k_r}{k_r + k_{nr}} = k_r \cdot \tau \quad [6]$$

FQY values range between 0 and 1, or they can be represented as percentages (and the values range between 0% and 100%).[4-5]

1.4 Two-photon processes: absorption and fluorescence

The processes described in subchapter 1.2 Jablonski diagram and electronic transitions are induced by **low-intensity irradiation** (*i.e.* low photon-flux), typically in the ultraviolet (UV) or visible (Vis) range of the electromagnetic spectrum. They belong to **linear optical** processes. In this regard, the explained in subchapter 1.2 Jablonski diagram and electronic transitions absorption phenomenon relates to **one-photon absorption** (1PA), as one photon allows a transition of an electron to a higher-energy state (**Figure 1, 2a**). Following this nomenclature, the 1PA transition may result in **one-photon excited fluorescence** (1PEF) (**Figure 1, 2a**).

However, when **high-intensity radiation** interacts with matter, its optical response may be **non-linear**, *i.e.* the induced polarization vector does not linearly depend on the electric field strength (see equation [1]).

At high photon-flux (*i.e.* the high number of photons per unit area and unit time), a simultaneous **multiphoton** (*e.g.* two- and three-photon) absorption is possible. For instance, the **two-photon absorption** (2PA) process occurs when 2 photons are simultaneously absorbed and the sum of their energy matches the energy bandgap between the ground and excited electronic states (**Figure 2b**). Consequently, the 2PA process can lead to **two-photon excited fluorescence** (2PEF) (**Figure 2b**). One of the requirements for the 2PA transition is spatial and temporal coincidence of photons which can be achieved by irradiation with laser pulses having a pulse width of picoseconds to femtoseconds.[6-8] The first predictions on NLO processes were presented by Maria Goeppert-Mayer. In her doctoral dissertation (1931) she hypothesized a possible two-

photon absorption phenomenon. Her theoretical assumptions were first experimentally verified in the 1960s, after the invention of the first pulsed laser.[2, 9]

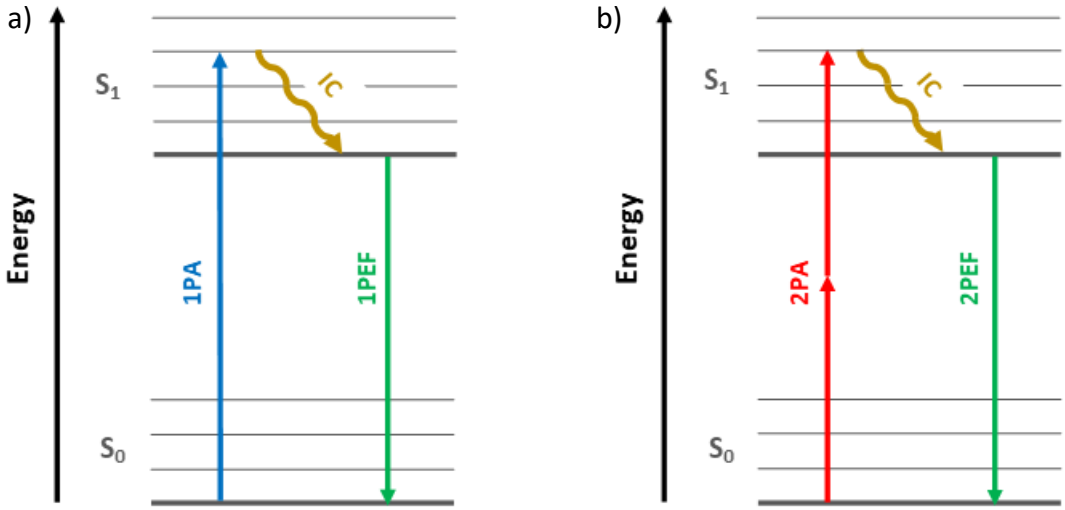

Figure 2. Simplified Jablonski diagrams comparing one-photon absorption (1PA) transition and one-photon excited fluorescence (1PEF) (a); two-photon absorption (2PA) process and two-photon excited fluorescence (2PEF) (b). IC indicates internal conversion and belongs to a non-radiative transition; S_0 – singlet ground state, S_1 – first excited singlet state.

A quantitative description of the 2PA process at the microscopic level provides the **two-photon absorption cross-section** (σ_2), usually quoted in Goeppert-Mayer (GM) units, where:[10]

$$1\ GM \equiv\ 10^{-50}\ (\frac{cm^4 \cdot s}{photon})$$

The σ_2 parameter relates to the probability of a simultaneous absorption of two photons to occur; σ_2 can be defined by using the propagation equation:[10-11]

$$\frac{d\Phi}{dz} = -\sigma_2 \cdot N \cdot \Phi^2 \qquad [7]$$

where Φ denotes the photon flux (in $\frac{photon}{cm^2 \cdot s}$), z corresponds to the propagation direction of the incident light beam (cm), σ_2 is the 2PA cross-section ($\frac{cm^4 \cdot s}{molecule \cdot photon}$), N relates to the number of molecules per unit volume ($\frac{molecule}{cm^3}$).

When the absorbing species exhibit both 1PA and 2PA transitions at the monochromatic incident light, the attenuation of the light beam passing through the optical medium is given by the following formula:

$$\frac{d\Phi}{dz} = -\sigma_1 \cdot N \cdot \Phi\ - \sigma_2 \cdot N \cdot \Phi^2 \qquad [8]$$

where σ_1 is the 1PA cross-section ($\frac{cm^2}{molecule}$).

The photon flux is expressed by:

$$\Phi = \frac{I}{E_{photon}} \quad [9]$$

where I corresponds to the intensity of the incident beam, E_{photon} is the energy of a photon (see equation [3]).

Therefore, the propagation equation in terms of the irradiation intensity can be written as follows:

$$\frac{dI}{dz} = -\sigma_1 \cdot N \cdot I - \frac{\sigma_2}{E_{photon}} N \cdot I^2 \quad [10]$$

Macroscopic equivalents of molecular parameters σ_1 and σ_2 constitute one-photon absorption coefficient (α) and two-photon absorption coefficient (β), respectively. In this regard, the equation [10] can be expressed as follows:

$$\frac{dI}{dz} = -\alpha \cdot I - \beta \cdot I^2 \quad [11]$$

As a result, formulas for σ_1 and σ_2 can be given as:

$$\sigma_1 = \frac{\alpha}{N} \quad [12]$$

$$\sigma_2 = \frac{\beta \cdot E_{photon}}{N} = \frac{\beta \cdot h \cdot c}{N \cdot \lambda} \quad [13]$$

For fluorescent examples, as the 2PEF relates strongly to the corresponding 2PA process, it can be successfully applied to identify and quantify the 2PA (see the next subchapter 1.5 Determination of two-photon absorption cross-section). Hence, at the high-intensity laser irradiation (high photon-flux) with no linear absorption (*i.e.* 1PA) at the incident wavelength, equations [7-8] and [10-11] emphasize that the **2PEF intensity is proportional to the square of the incident light intensity**. Therefore, the power dependence of fluorescence intensity can be measured to confirm the 2P nature of the measured fluorescence signal excited under the laser beam. Namely, the power exponent (*n*) value is determined according to the following equation:

$$n = \frac{\Delta \log (I)}{\Delta \log (P)} \quad [14]$$

where P is the incident laser average power.

1.5 Determination of two-photon absorption cross-section

Experimental methods commonly used to determine σ_2 can be divided into (i) direct and (ii) indirect. The **direct methods** rely on measurements of the attenuation of the incident light during transmission through the studied sample, for instance, using the Z-scan technique. They provide several advantages, such as utility for fluorescent and nonfluorescent specimens; for liquid and solid samples. However, high concentrations of

the studied samples are often required. This may induce heterogeneity within the sample and consequently, interfere with the results. Thus, the direct methods are not selective for the 2PA process only. In the **indirect methods**, radiative or nonradiative processes induced by 2PA transition are monitored, *e.g.* 2PEF or thermal lensing. The advantages of **fluorescence-based methods** lay in the requirement of relatively low concentrations of studied samples. However, these methods can be applied only to fluorescent samples.[11-15] One of the fluorescence-based methods requires measurements using a reference sample.[16] In this approach, to determine the σ_2 of a given material, the fluorescence measurements of a reference sample are performed in parallel with the measurements of the sample of interest; these spectroscopic experiments are carried out for the same parameters of the laser beam (*i.e.* the wavelength range). The database of the σ_2 values of the commonly used reference samples (fluorescent dyes), at selected wavelengths, are given *inter alia* in the article of Makarov *et. al.*[16] The **two-photon absorption cross-section** value of the investigated sample is calculated *via* the following equation:[16-17]

$$\sigma_{2,s} = \frac{F_s(\lambda)\cdot C_r\cdot \varphi_r\cdot n_r^2}{F_r(\lambda)\cdot C_s\cdot \varphi_s\cdot n_s^2}\cdot \sigma_{2,r} \qquad [15]$$

where F corresponds to the integral over the whole two-photon excited emission band, *C* is the molar concentration, φ denotes the fluorescence quantum yield (FQY), *n* is the refractive index. The indices *s* and *r* correspond to the sample and reference, respectively.

Further, the **effective two-photon absorption cross-section** (two-photon excitation action cross-section, also known as two-photon brightness)[18-19] is given by:[20]

$$\sigma_{2,eff} = \sigma_{2,s}\cdot \varphi_s = \frac{F_s(\lambda)\cdot C_r\cdot \varphi_r\cdot n_r^2}{F_r(\lambda)\cdot C_s\cdot n_s^2}\cdot \sigma_{2,r} \qquad [16]$$

To note is the fact that the fluorescence-based method is truly selective for detecting 2PA if the measured **fluorescence signal** is **proportional to the square** of the incident laser **irradiation**.

2 Chapter 2. Peptides and proteins

Proteins and peptides are very interesting biomolecules, playing important roles in numerous life processes. Herein, I summarize the general information about peptides and proteins. I explain solution-phase and solid-phase peptide synthesis, and I describe the hierarchical structure of proteins. Finally, I discuss protein folding and misfolding processes.

2.1 Peptides and proteins - introduction

Peptides and proteins are prominent in diverse biochemical processes and physiological functions. Peptides include biologically active hormones, neurotransmitters, signalling molecules, or growth factors. In the pharmaceutical market, peptide-based drugs are used to treat obesity, cancer, or osteoporosis.[21] Proteins perform various biological functions such as catalysis of metabolic reactions, energy transfer, gene expression, or transport of solutes across membranes.[22] A common feature of peptides and proteins are their building blocks which constitute amino acids (AAs); generally, they are α-amino acids. Typically, a molecule of less than 50 amino acids is defined as a peptide, and of more than 50 – as a protein.[23-24] In all AAs except for glycine, the α-carbon (C_α) is stereogenic. It indicates that, besides glycine, all AAs can form mirror images of each other and appear as *L*- or *D*-enantiomers. Among them, *L*-amino acids occur more predominantly than their *D*-counterparts. Although more than 300 AAs can be found in nature, only 20 are encoded by the genetic code.[25-26] The 20 canonical *L*-α-amino acids give rise to many possible combinations of proteins' and peptides' sequences. In a protein or peptide chain, the consecutive AAs are covalently linked by **amide bonds**, also known as **peptide bonds** (-CO-NH-) (**Figure 3**). Peptide bonds owe their stability to the possible electron delocalization (resonance) in the amide group. Resonance causes the amide bond to have a partial double-bond character. Hence, peptide bonds exhibit a non-zero dipole moment. The partial double-bond character hinders rotation around peptide bonds. Thus, the non-hydrogen atoms forming peptide bonds are coplanar.[26] Nevertheless, in the polypeptide chain also single bonds are present which allow a free rotation around them. These bonds are on either side of C_α, namely N-C_α and C-C_α bonds, and the rotation degree depends on steric interference, *e.g.* side chains.[26-27]

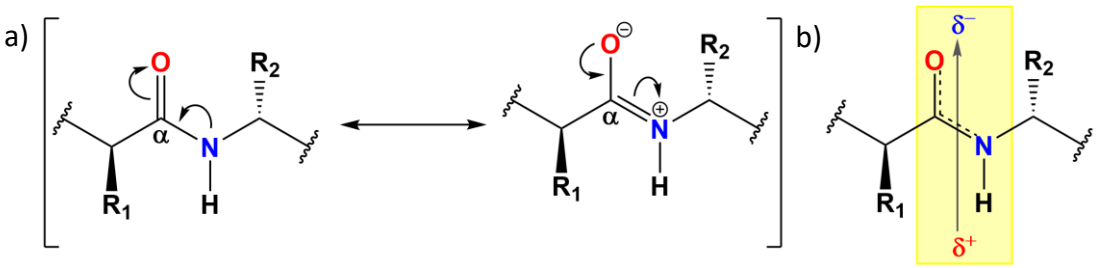

Figure 3. Peptide-bond resonance structures (a) contribute to their double-bond character; the α-carbon (C_α) is indicated by the α letter. The double-bonded resonance form leads to a partial negative charge (δ^-) located at the oxygen atom, and a partial positive charge (δ^+) at the nitrogen atom, which in result gives a dipole moment represented by an arrow in (b).

2.2 Chemical synthesis of peptides

Amide bond formation between a carboxylic acid and an amine is a condensation reaction. To occur, the carboxylic acid has to be first activated, which typically occurs by converting the -OH group into a good leaving group. To activate carboxylic acid, one can use coupling reagents. To date, many have been developed, and they can generate *e.g.* acid chlorides, carbonic anhydrides, or active esters. One such example are carbodiimides, including diisopropylcarbodiimide (DIC) or dicyclohexylcarbodiimide (DCC). For example, the reaction between DCC and a carboxylic acid (**Figure 4**) results in the formation of a reactive intermediate, *O*-acylisourea. To minimize epimerization caused by *O*-acylisourea intermediates, additives are used, such as 1-hydroxy-1H-benzotriazole (HOBt). The resulting OBt active ester is more reactive toward a nucleophilic attack than the initial *O*-acylisourea, allowing the formation of an amide bond upon the amino group ($-NH_2$) attack (**Figure 4**).[28]

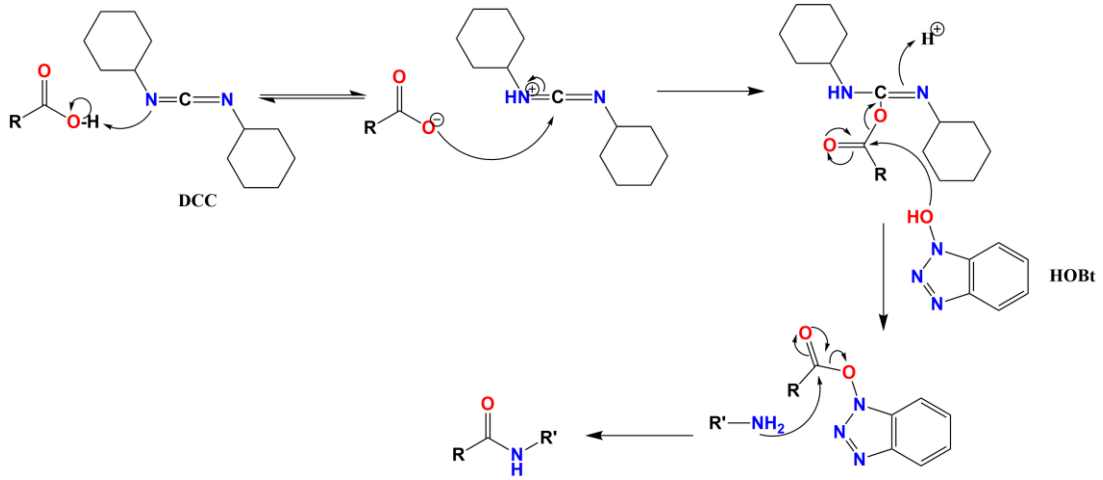

Figure 4. A representative example of amide bond formation through DCC and HOBt activation of carboxylic acid.

In living organisms, such activation occurs thanks to molecular machinery, ribosomes, which are responsible for protein biosynthesis. The protein is **biosynthesized** from its **N- to C-terminal direction**.[29]

To successfully form an amide bond in the peptide sequence in a chemical laboratory, the reaction must be performed under controlled conditions using activating reagents. As mentioned above (**Figure 4**), amide bond formation is possible thanks to a nucleophilic attack of the amino group on the activated carbonyl group. To minimize undesirable reactions, the AAs' reactive functionalities are blocked by appropriate protecting groups. The protecting groups are selectively removed, without interfering with other protecting groups of given entities. Based on these principles, two synthesis techniques have been developed – solution-phase and solid-phase peptide synthesis, typically carried out in the **C- to N-terminal direction**.

The history of peptide synthesis began over 100 years ago. In 1901, Emil Fischer published the synthesis of a dipeptide, glycylglycine. He was the originator of the term *peptide*.[30-31] In the first decade of the 20th century, E. Fischer and his collaborators synthesized ~100 peptides; the longest one contained 18 AA residues. Besides peptides, he was also working on sugar and purine syntheses, for which he was awarded the Nobel Prize in Chemistry in 1902.[32-34] In 1953, Vincent du Vigneaud and co-workers reported on synthesizing the hormone oxytocin.[35] In 1955, du Vigneaud became the Nobel Prize laureate in Chemistry *"for his work on biochemically important sulphur compounds, especially for the first synthesis of a polypeptide hormone"*.[36] Over the years, a significant progress has been made in **solution-phase peptide synthesis**. The solution-phase peptide synthesis relies on a convergent strategy. To obtain the desired sequence, given building blocks and fragments are selected, isolated, and coupled in solution (**Figure 5**). This strategy has some drawbacks, as every intermediate needs to be isolated and purified before the next reaction step, the total synthesis time is long and the total reaction yield is low. Therefore, this method is mostly dedicated for short peptide sequences.[21, 37-38]

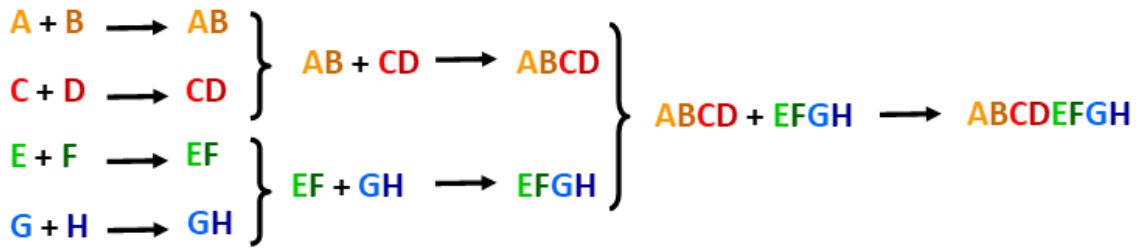

Figure 5. Convergent strategy of solution-phase peptide synthesis.

Solid-phase peptide synthesis (SPPS) (**Figure 6**) was pioneered by R. Bruce Merrifield who for his breakthrough invention was honoured with the Nobel Prize in

Chemistry in 1984.[39-40] The SPPS offers several advantages over solution-phase peptide synthesis, as it is a less time-consuming procedure, excess reagents are easily removed by filtration and washing, and it can be utilized for larger and more complex peptides. In the SPPS (**Figure 6**), the growing peptide chain is anchored by its C-terminus to a cross-linked polymeric support, a resin. The resin is functionalized by a linker which determines the C-terminal functional group of the desired peptide sequence. In the first step, the N^{α}-protected AA is loaded to the solid support which proceeds through activation of the AA carboxyl group. Then, the N-terminal protecting group is removed using an appropriate deprotecting agent. Subsequently, a coupling reaction occurs during which the carboxyl group of the next amino acid is activated which allows the formation of an amide bond. The deprotection and coupling steps are repeated until the desired sequence is completed. In the meantime, the resin with the attached growing peptide chain is washed and filtered several times. In the final step, *i.e.* cleavage, side-chain protecting groups are removed by appropriate scavengers and the target peptide sequence is detached from the solid support, yielding a crude peptide.[21, 37-38, 40]

In the SPPS methodology, two protecting-group strategies are commonly employed: (i) *tert*-butyloxycarbonyl (Boc)/benzyl (Bzl) and (ii) 9-fluorenylmethoxycarbonyl (Fmoc)/*tert*-butyl (tBu). While the N^{α}-protecting Boc group can be removed by trifluoroacetic acid (TFA), for cleavage and side-chain deprotection liquid anhydrous HF is used, which is a hazardous chemical. In an alternative strategy, the N^{α}-protecting Fmoc group is removed at basic reaction conditions (20% piperidine in *N,N*-dimethylformamide (DMF)). To remove side-chain protecting groups and to liberate the target peptide from the solid support, a high content of TFA (~95%) is needed.[21, 40-41]

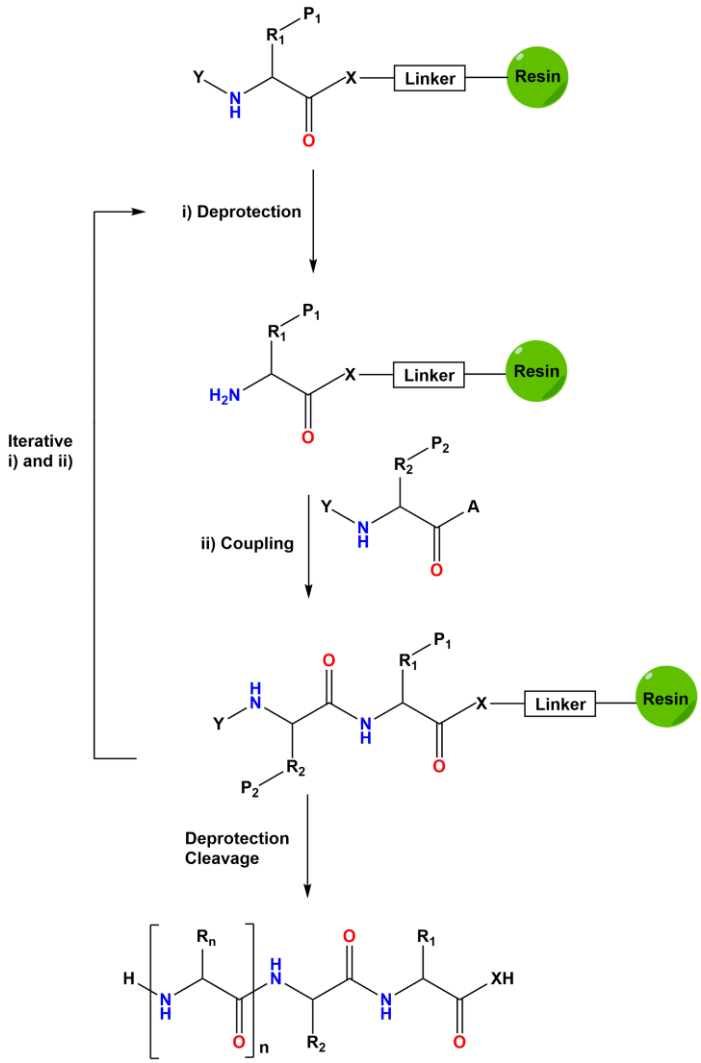

Figure 6. The principles of solid-phase peptide synthesis (SPPS). The SPPS relies on a stepwise addition of protected amino acids. Deprotection and coupling reactions are performed as long as the desired peptide sequence is assembled. After the final N^{α}-deprotection and cleavage, a crude peptide is obtained. Depending on the linkage, X relates to NH or O; R_1, R_2, and R_n are amino acid side chains; P_1, P_2, and P_n denote side-chain protecting groups, and Y is the N^{α}-protecting group (Fmoc or Boc).

Although the SPPS has provided significant improvements in peptide synthesis, there are still some challenges. Currently, microwave-assisted automated SPPS is available. This technique offers several advantages over manual SPPS. For example, it reduces inter- and intramolecular aggregation originating from hydrogen bonding and hydrophobic side chains in AAs; it also provides increased reaction rates, higher crude peptide purity, and higher overall reaction yield.[42-43]

2.3 The hierarchical structure of proteins

Proteins are complex structures organized into four hierarchical levels which include: (i) the primary, (ii) the secondary, (iii) the tertiary, and (iv) the quaternary structure. The

primary structure of a protein is determined by a linear order of amino acid residues composing its chain, where individual amino acids are covalently linked by amide bonds.[44] The **secondary structure** is dictated by the local conformation of the polypeptide chain and by interactions between backbone constituents. The secondary structure is stabilized through multiple hydrogen bonds.[44-45] The most common types of secondary structure include (i) α-helix and (ii) β-sheets.

The **α-helical structure** is one of the major types of proteins' secondary structure (**Figure 7a, b**). It is formed due to hydrogen bonds between C=O and N-H groups, located at *n* and *n+4* amino acid residues in the sequence (**Figure 7b**), respectively. All C=O and N-H groups are involved in the hydrogen bonding, except for the terminal groups (*i.e.* N- and C-termini). The α-helix adopts a cylindrical structure; each turn includes 3.6 residues corresponding to 1.5 Å per residue.[26-27]

The second commonly known form of the secondary structure is the **β-sheet structure**. The β-sheets contain β-strands which are typically 5 to 10 AA residues long. The β-strands are aligned laterally and hydrogen-bonded between C=O of one strand and N-H of the adjacent one, and *vice versa*. The resultant structure has a pleated sheet topography. It means that all C_α point alternatively a little above and below the β-sheet, with the side chains also following this pattern. There are two common types of the β-sheet structure, accordingly:

(i) the **parallel β-sheet** in which N-termini of β-strands run in the same direction (**Figure 7c**);

(ii) the **antiparallel β-sheet** in which N-termini of adjacent β-strands run in the opposite direction (**Figure 7d**).[27, 46]

The **tertiary structure** refers to a spatial arrangement of the entire polypeptide chain and is determined by interactions of side chains of proper AAs. The tertiary structure can be stabilized *via* disulfide bridges, hydrophobic forces, hydrogen bonds, and van der Waals interactions.[44, 47] The tertiary structure can be assembled around more than one subunit, *i.e.* a domain. The domains can then interact with each other *via* hydrogen bonds and van der Waals forces between nonpolar side chains and adopt different folds. This is the highest classification level of proteins and is assigned to their **quaternary structure**.[44, 48]

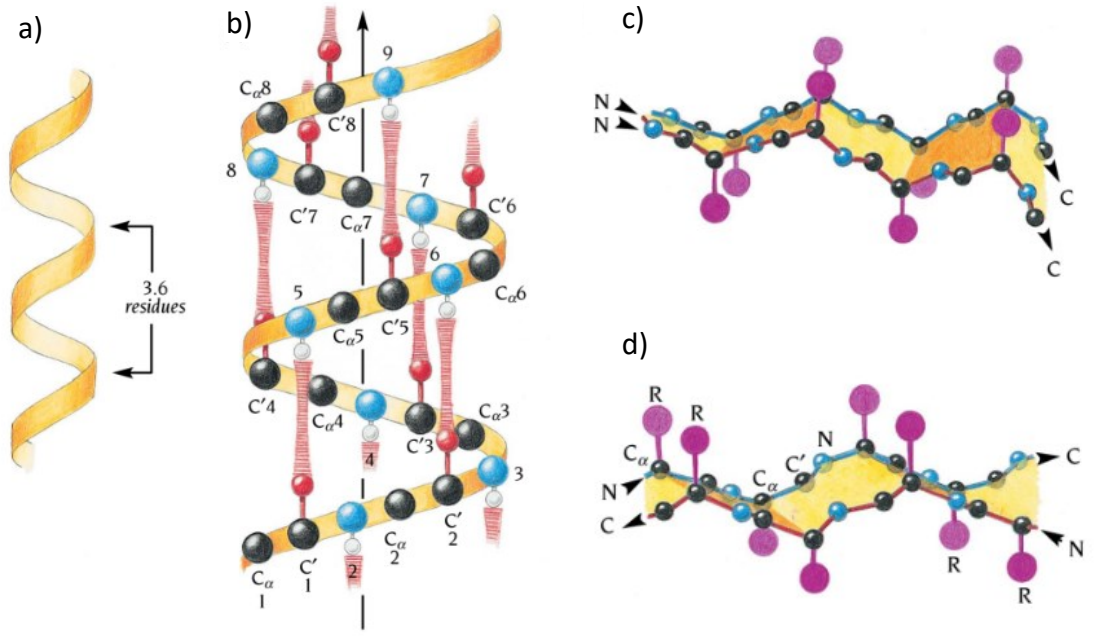

Figure 7. The common types of protein secondary structure. A ribbon depiction of α-helix (a); approximate positions of main chain atoms and hydrogen bonds in α-helix (b), the arrow indicates the direction towards C-terminus, hydrogen bonds between C=O and N-H are represented as red and striated lines; parallel (c) and antiparallel β-sheets (d); the pleat is highlighted in yellow.[27] The pictures were adapted with permission.

2.4 Protein folding and misfolding

To accomplish their diverse biological functions, proteins need to acquire a well-defined native conformation. The folding process into the native state is schematically demonstrated by an energy landscape (**Figure 8**).[49] The dominant forces governing protein folding include intramolecular hydrogen bonds, van der Waals and electrostatic interactions, and the hydrophobic effect. The latter relies on the tendency of hydrophobic regions of proteins to collapse in the interior of the folded protein to minimize their exposure to water molecules.[50-51]

During the folding process, a polypeptide chain (at the top of the funnel) undergoes multiple conformational rearrangements characterized by local minima until it reaches the native structure (**Figure 8**). Therefore, the energy landscape is characterized by ruggedness correlating to kinetic traps/energy barriers on the way to the thermodynamically favorable native state. As the protein folds, the entropy (corresponding to the number of possible conformations) of the polypeptide and the energy decrease.[52] When the polypeptide chain fails to fold correctly, the aggregation process is triggered, and misfolded conformations are formed (**Figure 8**). In the misfolding process, intermolecular non-specific interactions dominate between aggregated misfolded proteins. This can further lead to the formation of amorphous aggregates without a defined shape. On the other hand, highly ordered

structures can be also formed like **amyloid fibrils**[50] which will be discussed in the upcoming Chapter 3. State-of-the-art: amyloids.

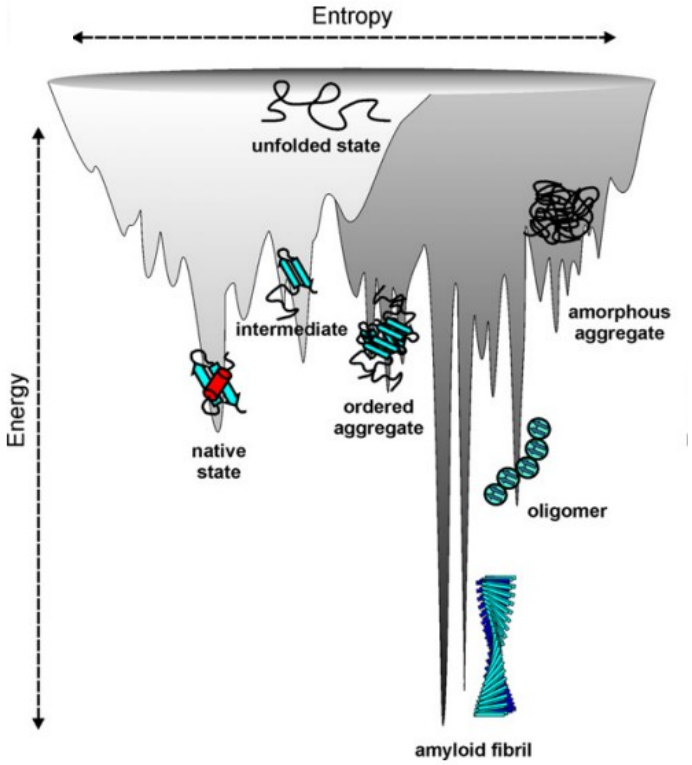

Figure 8. A schematic energy landscape for protein folding (light grey) and aggregation (grey).[53] Given polypeptide chain in its unfolded state (top of the funnel) before reaching the thermodynamically favoured native state, encompasses several intermediate states. The picture was adapted with permission.

3 Chapter 3. State-of-the-art: amyloids

Amyloids belong to self-assembled peptide or protein aggregates. Despite their implication in some human pathologies, they possess many interesting features including the peculiar autofluorescence whose origin remains elusive. In this chapter, I i) introduce the timeline of amyloid discovery and relate to the most common amyloid structures, i.e. fibrils and spherulites, ii) describe the functions of amyloids, and iii) expound the phenomenon of the amyloid fibrils' polymorphism. Then, I describe the main techniques to characterize the secondary structure and morphology of amyloid structures. I explain the autofluorescence property of amyloids and enumerate the existing hypotheses claiming the possible mechanism responsible for their autofluorescence. Finally, I present the techniques for imaging the amyloids that are available thanks to the commonly used fluorophores and describe the possibility of in vivo amyloid detection using near-infrared fluorescent probes or by using the label-free method based on amyloid autofluorescence.

3.1 Historical aspects

Under certain pathological conditions, some **peptides and proteins** can **misfold** and undergo self-assembly into **amyloid aggregate structures**. The history behind the current knowledge about amyloids is quite extensive. Therefore, in this subchapter, I included only the key discoveries (**Figure 9**). The term *amyloid* first time was coined in the medical literature in 1854 by Rudolph Virchow who noticed that cerebral corpora amylacea exhibited a positive iodine staining reaction, similar to starch (*amylum* in Latin, *amylon* in Greek) (**Figure 9**). However, the first description of a lardaceous liver and a spongy spleen containing "*white stones*" has been reported already in 1639.[54-55] In 1859 Carl Friedreich and August Kekule demonstrated that in fact the deposits do not possess carbohydrates and have a proteinaceous origin.[55-56] Over the years, knowledge about amyloids significantly evolved and much progress has been made. It was found that the histopathologic dye Congo Red (CR) binds to amyloids, and observations under polarized light microscopy (PLM) revealed that CR-stained amyloids exhibit apple-green birefringence (1927). This finding suggested that amyloids are not structurally amorphous, contrary to the previous assumptions.[55, 57] In 1959, Alan S. Coven and Evan Calkins performed observations with the help of Electron Microscopy (EM), which evidenced that

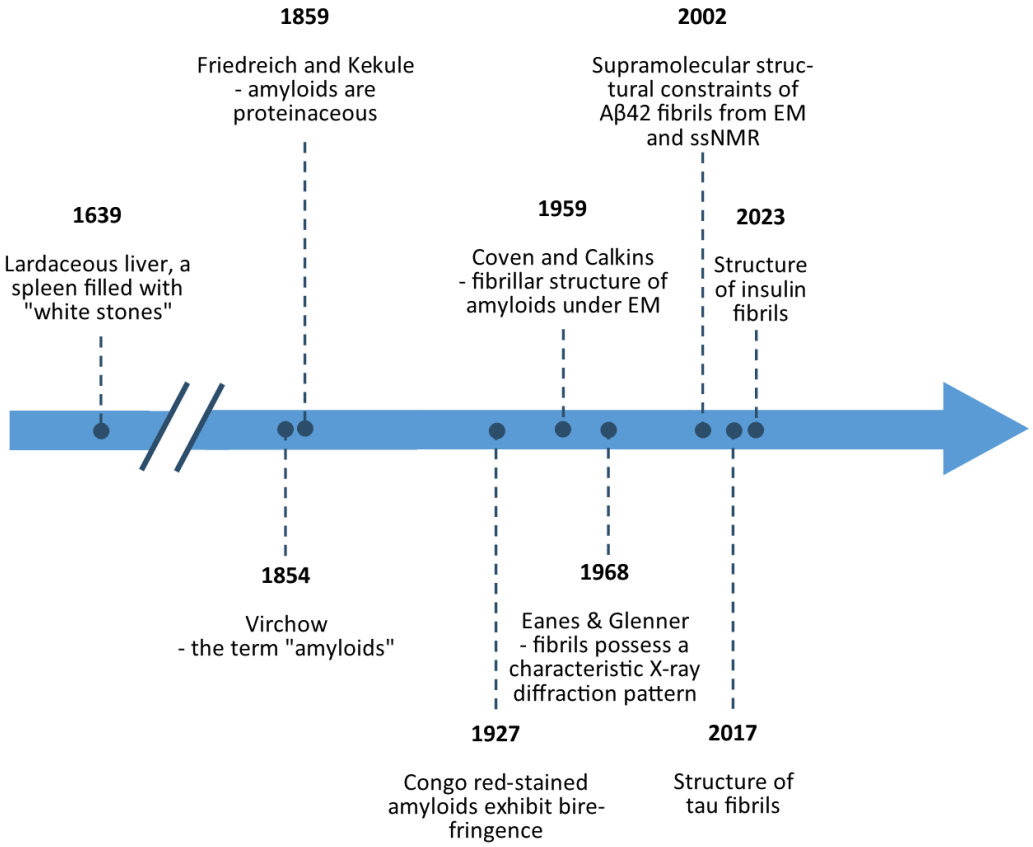

Figure 9. A timeline of the key discoveries in the field of amyloids. The description of a lardaceous liver and a spleen with *"white stones"* was reported in 1639; in 1854 R. Virchow introduced the term "*amyloids*", five years later, C. Friedreich and A. Kekule demonstrated a proteinaceous nature of amyloid deposits; in 1927 it was presented that Congo red-stained amyloids exhibit birefringence when observed under polarized microscopy; in 1959 A. S. Coven and E. Calkins observed a fibrous structure of amyloids under an electron microscope (EM); in 1968 E. D. Eanes and G. G. Glenner discovered that the fibrils possess a characteristic X-ray diffraction pattern, the cross-β pattern. In 2002, supramolecular structure of Aβ42 fibrils was obtained thanks to the development of EM and solid-state nuclear magnetic resonance (ssNMR). With the evolvement of cryogenic-EM, the structure of tau fibrils (2017) or insulin fibrils (2023) could be resolved.

amyloid fibrils possess a fibrillar structure.[57] With the use of X-ray diffraction (XRD) Eanes & Glenner[58] (1968) and Bonar *et al*.[59] (1969) discovered that amyloids possess a distinctive pattern with a conserved meridional reflection at 4.6-4.8 Å and a more variable equatorial one at 6-11 Å.[58-60] The presence of two reflections perpendicular to each other suggested that amyloids share similar structural properties at atomistic length scale.[61-62] In recent years, many exciting breakthroughs have been made which helped to gain more information about the structure of amyloids. For example, solid-state nuclear magnetic resonance (ssNMR) methods can provide detailed structural information and therefore help to develop full molecular models of amyloid fibrils.[63] For example, in 2002 O. N. Antzutkin and colleagues[64] thanks to EM and ssNMR, could obtain a number of distance constraints for the supramolecular structure of fibrils forming from the full-length form of Aβ peptide, Aβ42, and of its 10-35 fragment, Aβ(10-35). Another technique, cryogenic-EM (cryo-EM), is now revolutionizing the field of structural biology as it can

provide a three-dimensional atomic resolution structure of amyloid fibrils.[65] For example, the cryo-EM studies enabled to characterize tau filaments (**Figure 10**) from patient-derived material (2017),[66] Aβ(1-42) fibrils (2017),[67] or full-length insulin fibrils (2023).[68]

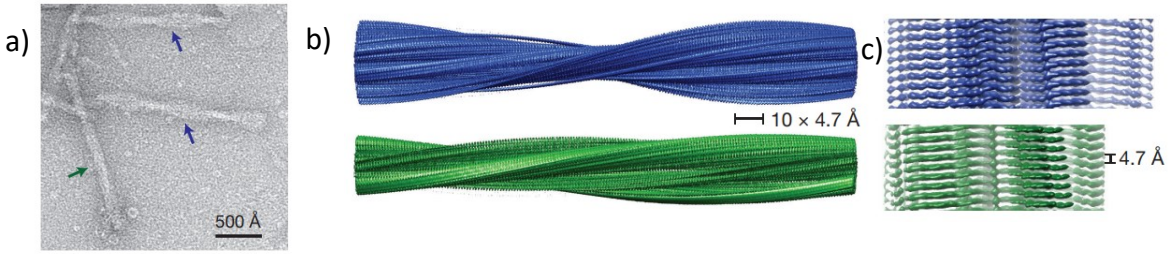

Figure 10. Electron micrograph of tau filaments (a) with a scale bar set to 500 Å. Paired helical filaments and straight filaments are indicated with blue and green arrows, respectively (b). Cryo-EM reconstructions of the paired helical filaments and the straight filaments (c).[66] The pictures were adapted with permission.

3.2 Amyloid fibrils

Amyloid fibrils are defined as **filamentous aggregates** which can reach up to microns in length, and 5-20 nm in width.[69-71] XRD studies revealed that they possess a common underlying structure, namely cross-β-conformation.[72-73] The meridional reflection (~4.7 Å) corresponds to β-strand spacing, whereas the equatorial reflection (~6-11 Å) to the distance between stacked β-sheets (**Figure 11**).[61, 74-75] As is demonstrated in **Figure 11**, β-sheets run parallel to the main fibril axis, whereas β-strands are perpendicular to this axis.[75] Amyloid fibrils are usually composed of 2-6 constituent protofilaments.[69-70] Each protofilament is ~2-7 nm in diameter. They can be twisted around each other or associated laterally.[76-77] The possible diverse three-dimensional arrangements of protofilaments lead to different mesoscopic structures of amyloid fibrils and this phenomenon is known as **polymorphism**.[50, 71, 78]

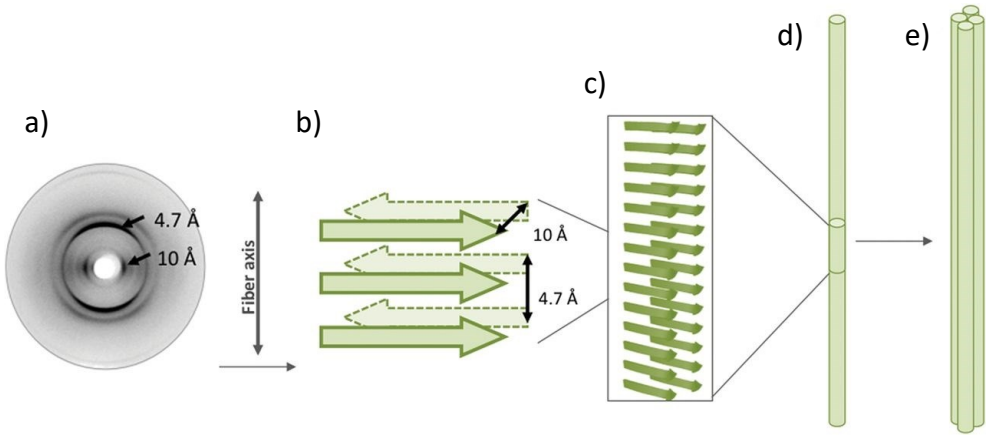

Figure 11. X-ray diffraction pattern of amyloid fibrils with characteristic meridional and equatorial reflections of ~4.7 Å and 6-11 Å, respectively (a), cross-β-sheets running through the entire length of amyloid fibrils composed of β-strands which are presented as green arrows (b, c), typically 2-6 protofilaments (d) compose mature amyloid fibrils (e).[75] The pictures were adapted with permission.

The most widely accepted model to describe the formation of amyloid fibrils assumes nucleation-dependent polymerization. The kinetic profile has a characteristic sigmoidal-shaped curve which consists of a lag phase, followed by a rapid exponential growth phase, and finally is completed with a saturation phase (*plateau*) (**Figure 12**). In the initial lag phase, the peptide chains assemble into nuclei which then grow into oligomers. During the growth phase, these species assemble into protofibrils. Finally, the protofibrils assemble into mature amyloid fibrils and this process refers to a saturation phase. To monitor fibril formation, typically ThT assay is used based on monitoring changes in ThT fluorescence intensity over time.[50, 79]

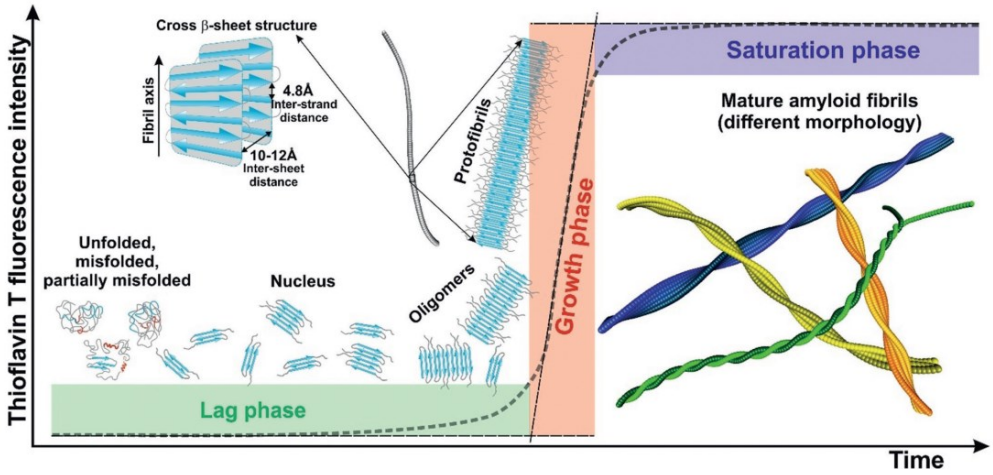

Figure 12. Polymerization-dependent formation of amyloid fibrils displaying a characteristic sigmoidal curve. The process begins with peptide chains assembling into nuclei and oligomers which governs a lag phase. Then, the growth phase occurs during which protofibrils are forming. Finally, the protofibrils assemble into mature amyloid fibrils. This process corresponds to the saturation phase.[50] The picture was reprinted with permission.

3.3 Spherulites

Although fibrils belong to the most commonly studied amyloid aggregates, there are also **spherical structures** composed of amyloids, **spherulites** (**Figure 13a**). Their diameter ranges from 10 µm to 150 µm, but typically reaches a value of ~50 µm.[80] Spherulites can be readily identified under polarized light microscopy (PLM), as they exhibit a distinctive **Maltese cross pattern** (**Figure 13b**).[80-81] The dark centres in spherulites (**Figure 13b**) indicate that the core is nonbirefringent, *i.e.* contains irregularly oriented polypeptide chains and non-specific protein aggregates. The core of spherulites is surrounded by fibrils oriented radially.[81-82]

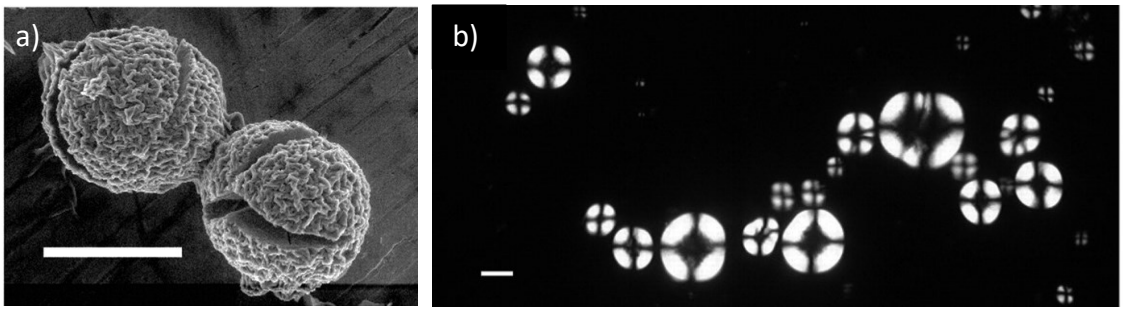

Figure 13. Bovine insulin spherulites under an environmental scanning electron microscope with a scale bar set to 50 µm (a).[80] Bovine insulin spherulites under a polarized light microscopy (PLM) (b); the scale bar is 50 µm.[80] The PLM image presents characteristic Maltese cross patterns. The pictures were adapted with permission.

3.4 Functions of amyloids

One of the most known functions of amyloids is their **pathological role**. To date, approximately 40 proteins have been identified to form amyloidogenic deposits in human diseases, mostly in the form of amyloid fibrils. The amyloidogenic proteins share no common features in sequence, structure, or function. Some proteins deposit in the central nervous system and are responsible for neurodegenerative disorders including Alzheimer's (AD) and Parkinson's diseases (PD). Some proteins form deposits in tissues, *e.g.* heart, kidney, or pancreas, and give rise to non-neuropathic diseases such as type II diabetes or atrial amyloidosis. Many amyloidogenic proteins and peptides are involved in several pathological conditions (**Table 1**).[76, 83-84] Unfortunately, many of these diseases are still incurable.[85]

Table 1. Peptides and proteins involved in some amyloidogenic human disorders.[76, 83-84]

Name of peptide or protein	Number of residues	Associated diseases
Amyloid-β peptide (Aβ)	40 or 42	1) Alzheimer disease 2) Hereditary cerebral hemorrhage with amyloidosis
α-Synuclein (αs)	140	1) Parkinson disease 2) Parkinson disease with dementia 3) Dementia with Lewy bodies
Islet amyloid polypeptide (IAPP)	37	1) Type II diabetes 2) Insulinoma
Microtubule-associated protein tau	352-441[a]	1) Tangle predominant dementia 2) Guam Parkinson dementia complex
Transthyretin (TTR)	127	1) Senile systemic amyloidosis 2) Familial amyloidotic polyneuropathy 3) Familial amyloid cardiomyopathy

[a] For *ex vivo* fibrils, fragments of various lengths have been reported.

Amyloid fibrils, besides their pathological role described above, also possess **functional properties**, as they perform biological activity in different organisms such as bacteria, fungi, plants, insects, mice, and humans.[84, 86] For example, curli fibrils expressed by *Escherichia coli* (*E. coli)* colonize inert surfaces, mediate binding to different host proteins, and they are involved in biofilm formation which protects from physical and chemical stresses (**Figure 14a**).[87-89] Another bacteria, *Streptomyces coelicolor*, secretes amyloidogenic proteins – chaplins which play an important role in the formation of aerial hyphae.[86, 90] Formation of functional amyloids has been identified in mammalian systems. For example, melanosomes are organelles specialized in the synthesis of melanin in melanocytes. It has been found that the melanocytes produce a protein Pmel17 which can form a fibrillar matrix over which melanin is deposited during melanosome maturation (**Figure 14b**).[91-92]

Interestingly, amyloids possess remarkable **mechanical properties**. For example, their Young's moduli (E) is on the order of several GPa which is comparable to the E values of the most rigid proteinaceous materials including silk or collagen (**Figure 14c**).[93] They exhibit remarkable stability and resistance to high hydrostatic pressures and temperatures.[94-95]

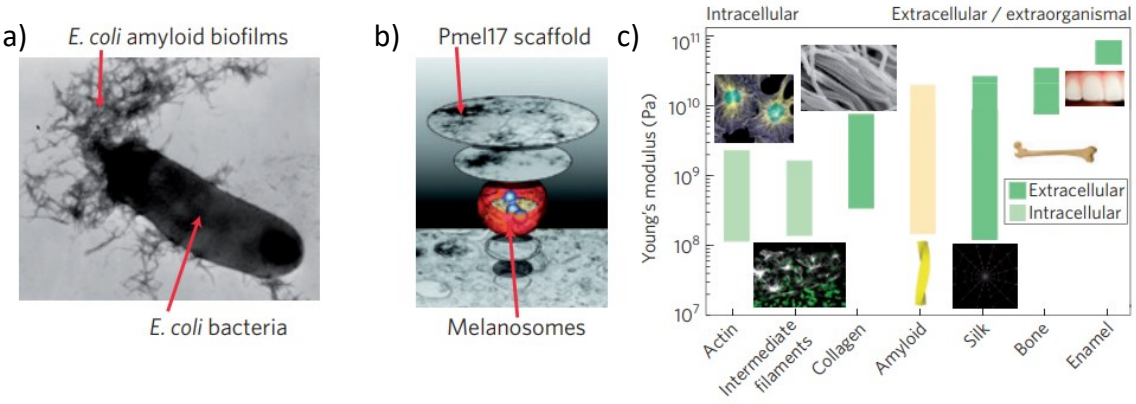

Figure 14. Curli fibrils growing on the surface of *Escherichia coli* play many important roles including biofilm formation which protects the bacteria from chemical and physical stresses (a). A fibrillar scaffold formed by the protein Pmel17 allows melanin biosynthesis (b). Young's modulus of amyloid fibrils as compared to some other intra- and extracellular biological materials (c).[93] The pictures were adapted with permission.

3.5 Polymorphism of amyloid fibrils

Although at atomistic length scale amyloid fibrils share a common cross-β structure, at the molecular level they present a **high degree of polymorphism**.[96-97] Polymorphism defines variations in fibril structures formed by a given polypeptide chain. Amyloid polymorphs can be directly examined using *e.g.* atomic force microscopy (AFM) or EM

which enable measuring some parameters including persistence length, fibril bending, cross-over distance (*i.e.* distance along the fibril length which takes to complete 180^{o} turn (**Figure 15a**)),[98-99] or width. Analysis of these parameters reveals that different morphology of fibrils can be identified in one sample. Fibril polymorphism is observed among samples formed *in vivo* and *in vitro* and can arise from differences in:

(i) protofilament number,

(ii) protofilament arrangement,

(iii) protofilament substructure.

The differences in fibrils' morphology arise from environmental factors, including pH, temperature, agitation, salt content, and other co-solutes. However, even within one test tube amyloid fibrils' polymorphism is noticeable. It suggests that under given physicochemical parameters a specific ensemble of fibril structures is favoured.[99-100]

The structural diversity of fibrils results in a variety of morphological forms; the **main mesoscopic polymorphs** (**Figure 15b**) include:

(i) **twisted ribbons** – they undergo a pure torsion around the fibril axis, periodicity increases linearly with the number of protofilaments, possess specific handedness, and cross-over distance; probably the most frequent polymorph;[50, 101]

(ii) **helical ribbons** – they undergo winding around a hypothetical cylinder of a finite radius, possess specific handedness and a defined mean curvature,[50, 102-103]

(iii) **crystals** – they are tape-like aggregates, possess flat morphology and unidentifiable macroscopic chirality;[50, 104]

(iv) **nanotubes** – they possess a defined mean curvature.[103]

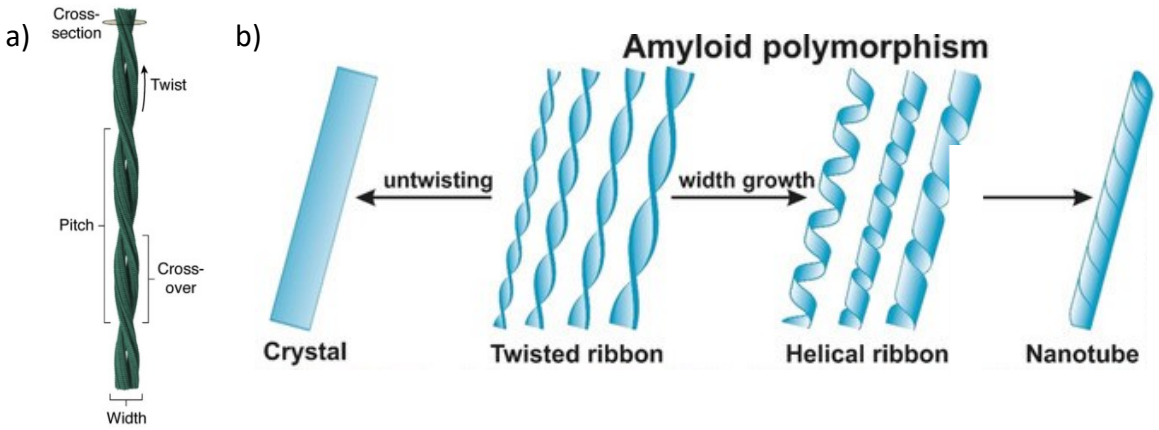

Figure 15. Amyloid fibrils possess characteristic parameters such as width, pitch, and cross-over distance. The cross-section is usually shown to demonstrate molecular arrangement (a).[105] Main amyloid fibril polymorphs and their possible transitions (b). Twisted ribbon polymorph can evolve into crystal or helical ribbon. The latter can transfer into a nanotube.[50] The pictures were adapted with permission.

As demonstrated in **Figure 15**, the twisted ribbon polymorph, through untwisting and lateral aggregation, can evolve into crystals. The other scenario is a transformation from a twisted ribbon into a helical ribbon which is accompanied by an increase in lateral width. The helical ribbon can further evolve by closing into nanotubes.[50] The polymorphic transitions of amyloid fibrils may occur as a function of time and have been observed among some peptides and proteins including *e.g.* β-lactoglobulin (β-LG),[106] human islet amyloid polypeptide (20-29) fragment ($hIAPP_{20-29}$),[107] Aβ(16-22),[108] and αs(37-44).[109]

3.6 Characterization techniques

3.6.1 Secondary structure determination

The secondary structure of amyloids can be determined *via* various spectroscopic techniques. One of them is the **attenuated total reflectance Fourier-transform infrared** (ATR-FTIR) spectroscopy approach in which the samples of interest are examined as thin films, which reduces the contribution of water absorptive properties.[110-111] In total, there are 9 spectral regions that allow the characterization of the secondary structure of peptides/proteins. These include the following IR absorption bands: amide A, B, and I-VII. Among them, the **amide I** band is very sensitive to the protein/peptide backbone structure, primarily due to transition dipole coupling. The amide I band is located between 1700-1600 cm^{-1} and arises mainly from the carbonyl stretching vibrations (~80% content).[112-115] The amide I band of amyloids is dominated by a narrow, intense absorption falling within 1615-1630 cm^{-1}, indicating the presence of the secondary β-sheet structure. Thus, this technique allows an easy identification of β-sheet-rich amyloid structures. Moreover, it can be used to distinguish parallel from antiparallel β-sheet configuration, as the latter is characterized by an additional weaker peak centred at ~1695 cm^{-1} (**Figure 16a**).[110, 116] In the Amide I band, other secondary structure components can be identified, including α-helix, random coil, or β-turns.[112, 114]

Another way to examine the secondary structure components of proteins/peptides is **circular dichroism** (CD) spectroscopy which measures the difference in absorbance of left- and right-handed circularly polarized light as a function of the wavelength. Particularly, the **far-UV CD**, spanning from ~190 nm to ~250 nm, gives information about amide transitions of the polypeptide backbone and allows recognition of α-helical structure, β-sheet structure, random coil, or β-turns.[117] The CD spectra of α-helical proteins/peptides possess two prominent negative bands at ~222 nm and ~208 nm, and a positive band at ~193 nm (**Figure 16b**). However, quantitative analysis of β-sheet-rich structures is difficult to interpret due to their spectral and structural diversity (**Figure 16c**). The structural diversity arises among others from the possible parallel/antiparallel orientation of the

neighbouring β-strands and the degree of twist or distortion of the β-sheets. These factors account for the diversity of CD spectra and a difficult analysis of β-sheet-rich structures. To overcome this limitation, several algorithms have been developed over the years to extract information about the secondary structure components.[118-121]

The secondary structure of amyloids can be characterized by other techniques, *e.g.* deep ultraviolet resonance Raman (DUVRR) spectroscopy.[122-123] In **Table 2**, I included a summary of the described above ATR-FTIR and CD spectroscopy approaches, as well as of DUVRR spectroscopy.

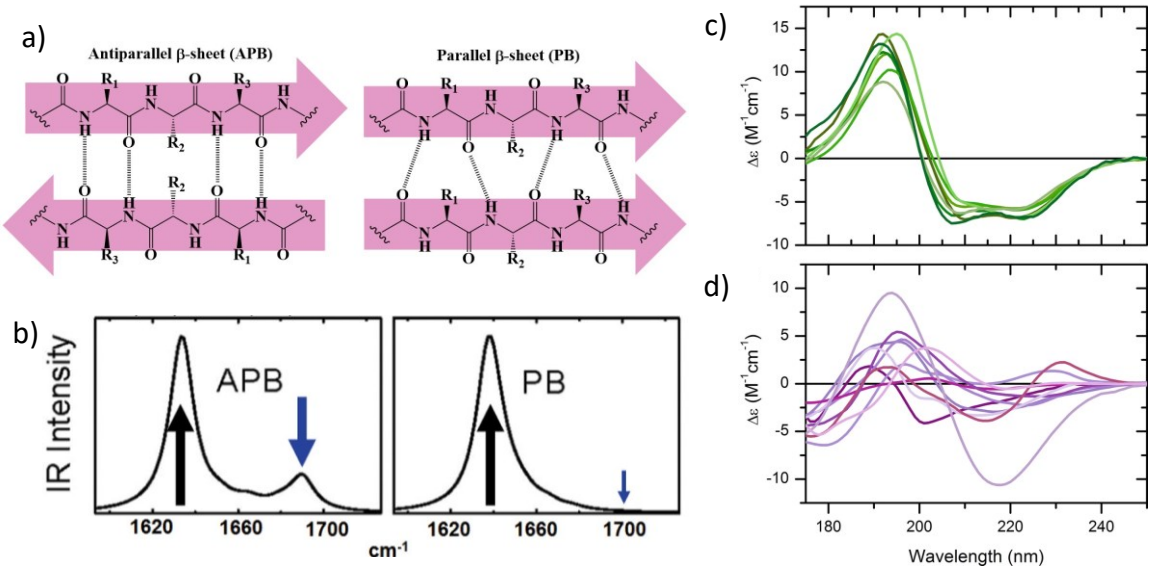

Figure 16. Schematic representation of antiparallel and parallel β-sheets, APBs and PBs, respectively (a). In APB, the constituent β-strands (depicted as lilac arrows) point in alternate directions, whereas in PB are aligned in the same direction. The differences in the arrangement of the β-strands result in different hydrogen-bonding arrays. In the ATR-FTIR technique, APBs are characterized by an absorption band centred at 1615-1630 cm^{-1} and a weaker absorption band with a maximum at ~1695 cm^{-1}, whereas in the PB alignment, the latter, high-frequency absorption band is absent (b).[124] In the CD spectroscopy, α-helical peptides/proteins possess a uniform spectral shape with a positive band at ~193 nm and two negative bands at ~208 nm and ~222 nm (c); the spectra in (c) are presented for proteins containing ~50% α-helix. However, proteins possessing ~50% β-sheet structure content and a negligible α-helical content show spectral diversity in the amplitude, number, and spectral component positions (d).[125] The pictures (b, c and d) were adapted with permission.

Table 2. A summary of practical aspects of methods commonly used to identify and characterize the secondary structure and the morphology of amyloid structures.

Characterization principle	Technique	Abbreviation	Advantages	Limitations	Refs.
Secondary structure	Attenuated total reflectance Fourier-transform infrared spectroscopy	ATR-FTIR spectroscopy	Facile identification of the β-sheet structure in Amide I band; Rapid collection of data;	A high concentration of sample is needed;	112, 114
	Circular dichroism spectroscopy	CD spectroscopy	A relatively small amount of sample is needed; Rapid collection of data;	Difficult interpretation of the β-sheet structure due to structural and spectral diversity of the β-sheets;	118-119, 126
	Deep ultraviolet resonance Raman spectroscopy	DUVRR spectroscopy	Fluorescence background elimination; Selective enhancement of peptide backbone modes;	Multivariate data analysis requirement;	122-123, 127
Morphology	Atomic force microscopy	AFM	Nanometer-scale resolution; Gives information in 3-spatial dimensions;	Time-consuming scanning;	128-129
	Transmission electron microscopy	TEM	High resolution, *e.g.*: a) conventional TEM: typically better than 0.2 nm; b) cryo-EM: atomic-scale	Laborious sample preparation procedure; conventional TEM gives information in 2-spatial dimensions;	65, 130-132
	Scanning electron microscopy	SEM	Nanometer-scale resolution; Detailed 3-dimensional and topographical imaging;	The preparation of samples can result in some artifacts.	131

3.6.2 Morphology determination

Techniques commonly used to observe the morphology of amyloid fibrils include scanning probe microscopy and EM (**Figure 17a, b**). A commonly used type of scanning probe microscopy constitutes **AFM** (**Figure 17a**). The AFM imaging allows investigations of surface morphology, mechanical properties, and the visualization of a **three-dimensional structure** of a sample of interest with **high vertical and lateral nanometer-scale resolution** (**Figure 17c**). In the AFM technique, a sharp tip mounted at a free end of a flexible cantilever is used to scan the surface of the target specimen. It operates by measuring the attractive and retractive forces between the tip and the sample by the cantilever deflection, under the control of a feedback mechanism. While scanning the surface, the laser beam is reflected from the cantilever into a position-sensitive photodiode. Then, the recorded voltage signal is used to develop the samples' surface topography. There are 2 basic modes of the AFM operation: (i) **static** (contact) mode and (ii) **dynamic** mode which is further subdivided into tapping (intermittent contact) and non-contact mode.[128-129]

A powerful technique to study morphology is **transmission electron microscopy** (TEM) (**Figure 17b**) – one of the EM assays. The high resolution of TEM is provided by the short wavelengths of electrons (~pm) and the possibility of the electron beam to strongly and specifically interact with the matter by scattering. In TEM, accelerated electrons pass through a thin sample and interact with its atoms. The TEM setup is composed of important elements: an electron gun, condenser/objective/projector lenses, specimen holder, and a camera. To limit the electron beam to interact only with the specimen, a high vacuum is required. Different TEM methods can be distinguished. The most accessible and convenient is **conventional TEM** which typically provides a **resolution better than 0.2 nm** and a **two-dimensional structure** (**Figure 17d**) of the target specimen. This method requires dry samples which are priorly deposited onto a grid. To obtain a sufficient image contrast, the samples should have adequate scattering power compared to the background or substrate. Therefore, organic specimens have to be stained with appropriate markers based on heavy metal salts, *e.g.* uranyl acetate.[130-132] Interestingly, **cryo-EM** allows the structural insights on **atomic level**. Indeed, **three-dimensional atomic resolution** structures of some amyloid fibrils derived from the human brain or assembled *in vitro* forms have been resolved; they include, *e.g.:* tau, α-syn, Aβ, and recently insulin fibrils.[65, 67-68]

Besides AFM and TEM, the morphology of amyloid structures can be examined using, *e.g.* scanning electron microscopy (SEM) (**Table 2**).

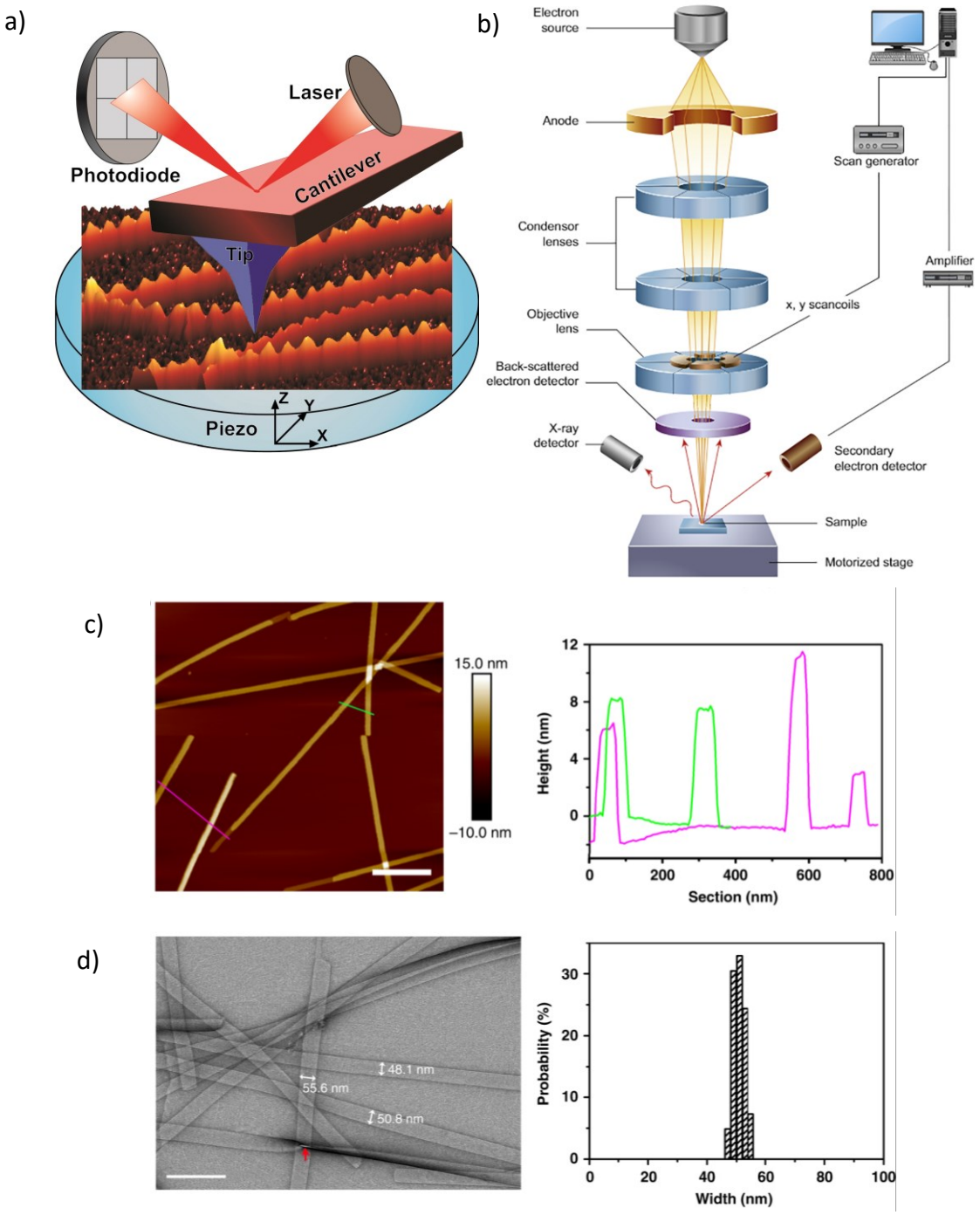

Figure 17. Schematic representation of atomic force microscope (AFM) (a)[128] and transmission electron microscope (TEM) (b).[130] Morphology of amyloid fibrils investigated using AFM (c) and TEM imaging (d).[133] AFM imaging allows to determine the width, length, and height of fibrils (c), whereas conventional TEM imaging provides detailed information regarding the width and length of amyloid fibrils and thereby calculations of width distribution (d). The pictures were adapted (a, c, d) or reprinted (b) with permission.

3.7 Optical properties - autofluorescence

Proteins and peptides absorb primarily in the ultraviolet (UV) range of the electromagnetic spectrum, between 185-320 nm. These absorptive properties arise in tryptophan, tyrosine, and phenylalanine which possess aromatic chromophores in their side chains (**Figure 18a**) absorbing in the case of (i) tryptophan (W) at ~280 nm (molar extinction coefficient/molar absorptivity (ε) ~5600 M^{-1} cm^{-1}), (ii) tyrosine (Y) at ~275 nm (ε ~1420 M^{-1} cm^{-1}), and (iii) phenylalanine (F) at ~257 nm (ε ~197 M^{-1} cm^{-1}) (**Figure 18b**). Other characteristic absorptive regimes of amino acids include among others weak absorption from 250 nm (ε ~360 M^{-1} cm^{-1}) to 320 nm (ε ~6 M^{-1} cm^{-1}) resulting from disulphide bonds. Additionally, the amide groups in peptide bonds strongly absorb at ~190 nm (ε ~7000 M^{-1} cm^{-1}) and weakly between 210-220 nm (ε ~100 M^{-1} cm^{-1}).[134-135] Fluorescence of proteins, originating mostly from aromatic residues, can be used for instance to study thermodynamic and kinetic information of proteins.[136]

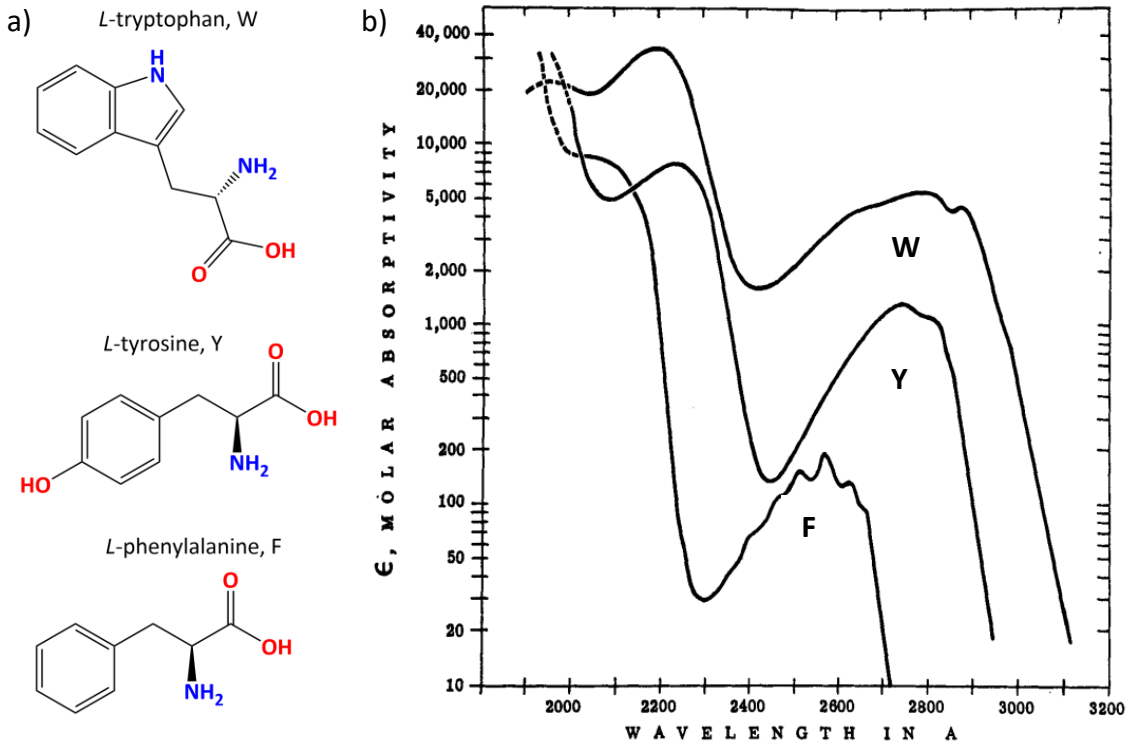

Figure 18. Chemical structures of aromatic amino acids and their symbols: *L*-tryptophan (W; upper panel), *L*-tyrosine (Y; middle panel), and *L*-phenylalanine (F; lower panel) (a). Absorption spectra of these amino acids at pH 6: tryptophan indicated as W, tyrosine indicated as Y, and phenylalanine marked as F (b).[135] The X-axis in (b) is given in Å units; 1 (Å) = 0.1 (nm), molar absorptivity on the Y-axis is presented in a logarithmic scale. The picture (b) was adapted with permission.

Amyloids, besides the optical properties described above, absorb in the range 340-380 nm and exhibit **autofluorescence** in the 440-530 nm region.[137-138] As I mentioned previously, the presence of amyloids in living organisms is linked with some diseases,

including AD or PD. As these disorders are incurable, there is a particular need to develop tools to detect the amyloids' deposits. Such possibility offers their autofluorescence in the visible (Vis) range of the electromagnetic spectrum. Interestingly, this intrinsic fluorescence also emerges in amyloids void of aromatic residues in their sequence.[137-139] Although the exact mechanism still remains elusive, there have been postulated some hypotheses regarding the origin of amyloids' autofluorescence properties:

(i) Pinotsi *et al.*[138] proposed that the intrinsic fluorescence arises from **intermolecular proton transfer** along hydrogen bonds formed **between N- and C-termini** (**Figure 19**).

(ii) Jong *et al.*[140], by combining experimental and theoretical approaches, suggested that the intrinsic fluorescence of amyloids originates from **charge-transfer excitations** around **peptides' termini**.

(iii) Grisanti *et al.*[141] proposed that the **large number of nπ* states** in the secondary β-sheet structure increases the excitation probability. They have reported on decrease of excitation energy of n→π* transitions upon deplanarization of the corresponding amide group and elongation of the carbonyl (CO) bond.

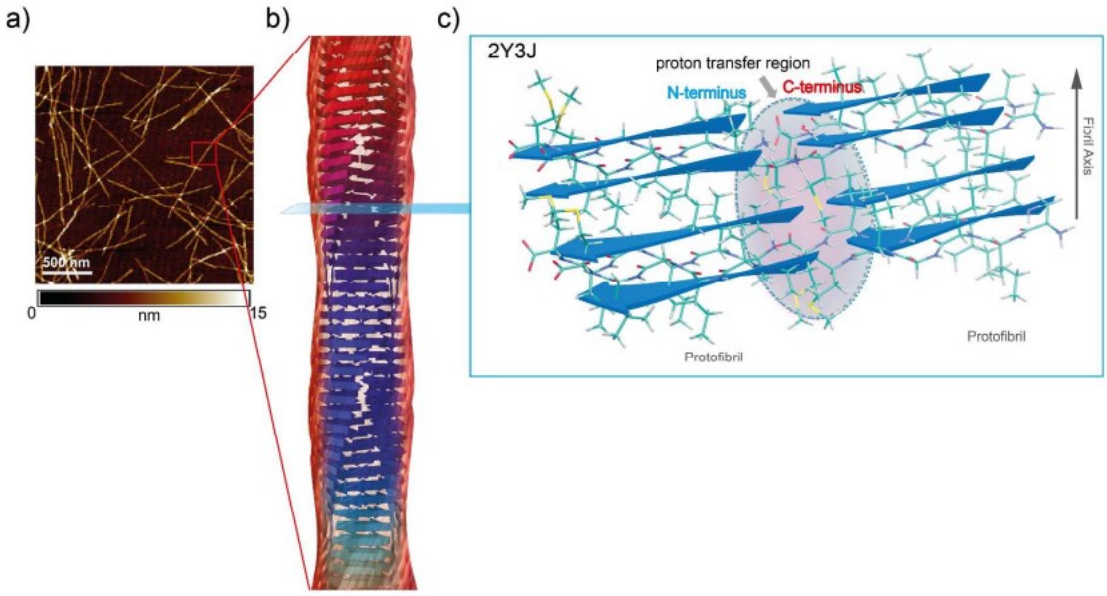

Figure 19. Demonstration of proton transfer between N- and C-termini. AFM image of amyloid fibrils; scale bar set to 500 nm (a), three-dimensional peptide arrangement in amyloid fibrils (b), magnified depiction of cross-section indicated in b) (c).[138] The pictures were adapted with permission.

The above-mentioned hypotheses refer to the key role played by a dense hydrogen-bonding network, which stabilizes the secondary β-sheet structure. Indeed, early findings claimed that the intrinsic fluorescence in the Vis range is characteristic for protein and

peptide aggregates, *i.e.* amyloids. However, it has also been revealed that synthetic peptide nanostructures, *i.e.* amyloid-like structures formed from di- or tripeptide sequences, and even single amino acids display autofluorescence signals.[142-144] Hence, this phenomenon encouraged other researchers to seek the mechanistic explanations behind the intrinsic fluorescence. Therefore, some additional hypotheses have been formulated:

(iv) Not only **intermolecular**, but also **intramolecular proton transfer** along hydrogen bonds may be responsible for the emission origin.[145]

(v) Specific hydrogen bond networks, especially **short hydrogen bonds** (SHB), ubiquitous in biological matter,[146] can affect autofluorescence properties.[147]

(vi) **Charge transfer** either between peptide backbone and side chains of charged amino acids, or between the side chains of charged amino acids, **followed by charge recombination** account for the observed fluorescence.[148]

(vii) **CO-lock mechanism**[149] in which authors used a theoretical approach to explain that non-aromatic fluorescence occurs when the CO bond stretching is prevented which results in the S_1 lifetime elongation. When the CO bond is free (**Figure 20a**) or weakly bound (**Figure 20b**), its stretching decreases the band gap between S_1 and S_0 states, possibly leading to a situation where S_1 and S_0 are isoenergetic (conical intersection, CoIn in **Figure 20**) and thereby contributing to non-radiative decay. However, the CO stretching can be hindered by strong local interactions which stiffen the CO group, impeding its elongation and therefore, leading to a larger S_1-S_0 band gap. Such strong local interactions can provide (i) short hydrogen bonds (**Figure 20c**) or (ii) hydrogen bonds between the CO and the NH groups of the opposite β-strands in amyloid structures (**Figure 20d**). The latter two cases may be responsible for non-aromatic autofluorescence.

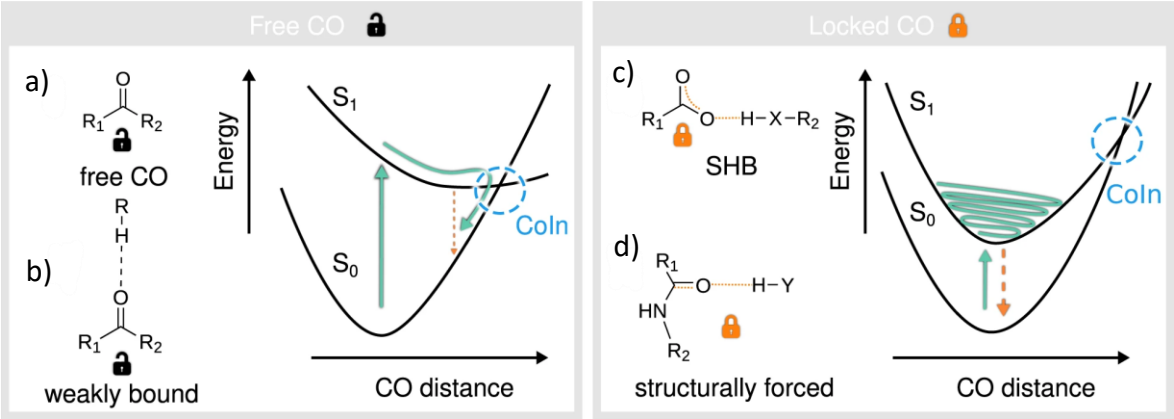

Figure 20. Schematic representation of the CO-lock mechanism of non-aromatic fluorescence. When the CO bond is free (a) or weakly bound (b) its elongation is possible which results in decreasing S_1-S_0 energy band gap. CO stretching can be prevented by SHB (c) or structurally forced (d) by establishing hydrogen bonds with the CO group.[149] The pictures were adapted with permission.

3.8 Imaging of amyloids for *in vivo* applications

The AD and the PD, associated with the amyloids' deposition, constitute a growing societal challenge. Accordingly, the AD and the PD affect ~50 million and ~10 million patients worldwide, respectively. It is forecasted that by the year 2050 AD and PD will afflict ~150 million and ~12 million patients, respectively. Unfortunately, the current treatments only mitigate the symptoms.[100, 150] This data implies that early detection of amyloidosis is essential in preventing amyloid fibril deposition in the human body.

3.8.1 Standard fluorophores

To date, **thioflavin T (ThT)** has been commonly used to detect amyloid fibrils in laboratory conditions. ThT, when bound to amyloid fibrils and excited at ~450 nm, emits an enhanced fluorescence signal with a maximum located at ~480 nm. The increase of fluorescence intensity upon binding to amyloid fibrils occurs because ThT is a molecular rotor. Namely, the ThT molecule possesses a single C-C bond linking benzothiazole and aniline rings (**Figure 21a**). In an aqueous solution, ThT can freely rotate around the C-C bond. In contrast, when bound to amyloid fibrils, this rotation is hindered; consequently, the probability of the radiative relaxation to the ground state increases (*i.e.* the FQY is enhanced).[151-152] It is suggested that ThT binds with its long axis parallel to the long axis of amyloid fibrils (**Figure 21b**). The vicinity of amino acid side chains and the ThT may lead, *e.g.* to hydrophobic or π-π interactions between them, which favors the adoption of a flat conformation of ThT.[153-155]

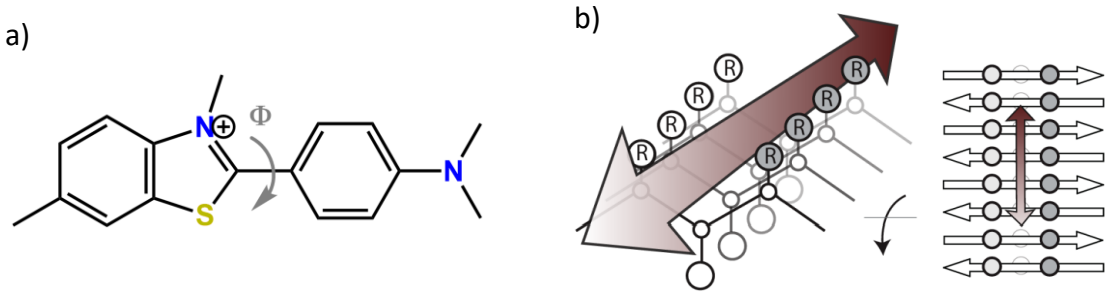

Figure 21. Thioflavin T (ThT) cationic structure with depicted torsion angle (ϕ) demonstrating rotation around C-C bond between benzothiazole and aniline rings (a), a channel model representing ThT binding to amyloid fibrils (b).[155] The picture (b) was adapted with permission.

Another common amyloid-specific dye is Congo red (CR) (**Figure 22**). As I mentioned in subchapter 3.1 Historical aspects, when the CR is bound to amyloids, one can observe apple-green birefringence in the presence of polarized light. In an aqueous solution, CR has a maximum absorption at ~490 nm. However, when bound to amyloid fibrils, the absorption peak is red-shifted and centers at ~540 nm.[156] There are 2 contradictory models describing the CR binding mode to amyloid fibrils. Namely, it has been suggested that the CR molecule binds with its long axis parallel to the long axis of amyloid fibrils (**Figure 22a**).[157] In this model, the CR molecules are proposed to be stabilized by electrostatic interactions between negatively charged sulfonic acid groups of CR and positively charged amino acid residues in the polypeptide chain.[157] Another model postulates that CR molecules align perpendicularly to the main axis of fibrils, *i.e.* parallel to the peptide chains (**Figure 22b**).[158-159]

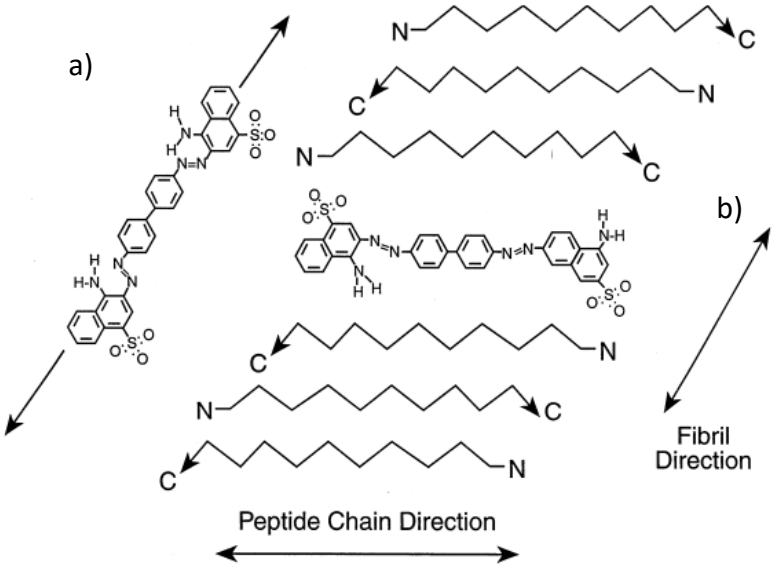

Figure 22. A simplified scheme demonstrating two competing models of the CR binding, namely parallel (a) and antiparallel (b) to the main fibril axis.[158] The picture was adapted with permission.

3.8.2 Near-infrared fluorescent probes

Due to the pathological role of amyloids, developing tools to detect them *in vivo* is paramount. One such technique constitutes fluorescence imaging in the red and the near-infrared (NIR) range of the electromagnetic spectrum. The irradiation with these wavelengths range penetrates tissues deeper than UV and Vis light and causes less photodamage to biological systems (**Figure 23**). Taking into account the reduced light absorption and scattering in biological matter, so-called **biological (therapeutic) windows** have been established, where the light absorption and scattering are the lowest: **the first biological window** (NIR-I) falling within **650-950 nm**, **the second** one (NIR-II) ranging from **1000 nm to 1350 nm**, and **the third** one (NIR-III) covering the region from **1550 nm to 1870 nm** (**Figure 23a**).[160-161]

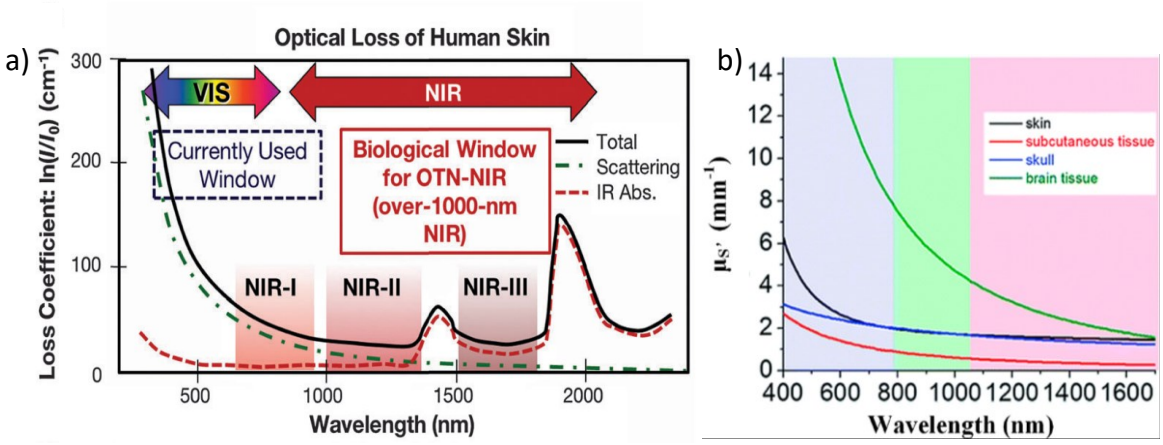

Figure 23. The extinction spectrum of human skin (expressed as loss coefficient) over the visible (Vis) and near-infrared (NIR) regions with the first (NIR-I), the second (NIR-II), and the third (NIR-III) biological window ranges indicated (a).[160] Reduced scattering coefficients ($\mu_{s'}$) plotted as a function of wavelength spanning, from 400 nm to 1700 nm, for various biological tissues including skin (black), subcutaneous tissue (red), skull (blue), and brain tissue (green) (b).[162] The degree of scattering is inversely proportional to the wavelength. The pictures were adapted with permission.

NIR fluorescent probes give an opportunity for *in vivo* detection of amyloids. However, several other requirements should be met, including:[163-167]

(i) high Stokes shift (*i.e.* the difference between absorption and emission maxima) to minimize the risk of re-absorption,

(ii) low molecular weight (<500 Da) and high lipophilicity (logP 1-4) to assure high blood-brain barrier (BBB) permeability,

(iii) high (selective) affinity binding with amyloids, and in parallel, low affinity binding with other proteins,

(iv) significant change in the fluorescence properties upon binding to amyloids (involving *inter alia* the fluorescence intensity and wavelength shift, the FQY, and the fluorescence lifetime),
(v) straightforward synthesis,
(vi) photostability,
(vii) low toxicity.

Although ThT and CR are commonly used to stain amyloids, these dyes are charged which excludes them to cross the BBB.[164] Over the years, various red and NIR probes have been designed and studied for the *in vivo* detection of amyloid aggregates.[166, 168-170] M. Hintersteiner and co-workers described a series of oxazine dyes.[167] In particular, the fluorescent probe **AOI987** (**Figure 24a**) demonstrated favourable properties. Its excitation and emission occurred in the red spectral range (λ_{exc} = 650 nm, λ_{em} = 670 nm), the dye can penetrate the BBB, exhibits high FQY in mouse serum (41%), and facilitates the real-time monitoring of Aβ deposits in mice models *in vivo*. However, the AOI987 exhibited a narrow Stokes shift (20 nm), fluorescence intensity decrease upon binding to Aβ deposits, and a dissociation constant (K_d) reaching a value of ~200 nM indicating a moderate affinity for Aβ aggregates.[166-167] Another NIR probe for Aβ deposits' identification constitutes a curcumin derivative, **CRANAD-2** (**Figure 24b**). This dye demonstrates a large Stokes shift (λ_{exc} = 640 nm, λ_{em} = 805 nm), and a low FQY (0.6%) in phosphate-buffered saline (PBS). Interestingly, when bound to Aβ aggregates, the CRANAD-2 exhibits a 70-fold fluorescence intensity increase, FQY increase to 40%, and a significant blue-shift (by 90 nm) in the maximum emission position to 715 nm. Additionally, the dye demonstrates a reasonable log P value equal to 3, can cross the BBB, shows high binding affinity toward Aβ aggregates (K_d=38.69 nM), and can specifically label Aβ plaques *in vivo*.[165-166] We reported on **difluoroborate (BF_2)-functionalized benzothiazole dyes** which could serve as amyloid markers.[20] The fluorescence probes were functionalized at one or both of the termini with a methoxy group (-OMe). Taking into account the presence of the electron-accepting (A) BF_2 moiety and electron-donating (D) -OMe group within their molecular architecture, we referred to the studied dyes as DA-, DAD, and -AD (**Figure 24c**). We performed systematic investigations of their LO and NLO properties to evidence that they could be used for *in vivo* studies. All three dyes showed a significant increase in the fluorescence intensity and the FQY upon binding with amyloids, with the FQY rising up to 94% when bound to amyloids (for -AD). We confirmed the 2P nature of absorption processes and determined σ_2 values of these dyes in various chemical environments (**Figure 24d**). The highest σ_2 value in water/dimethysulfoxide (H_2O/DMSO) solution was found for the DAD (28 GM at 780 nm) (**Figure 24d**).

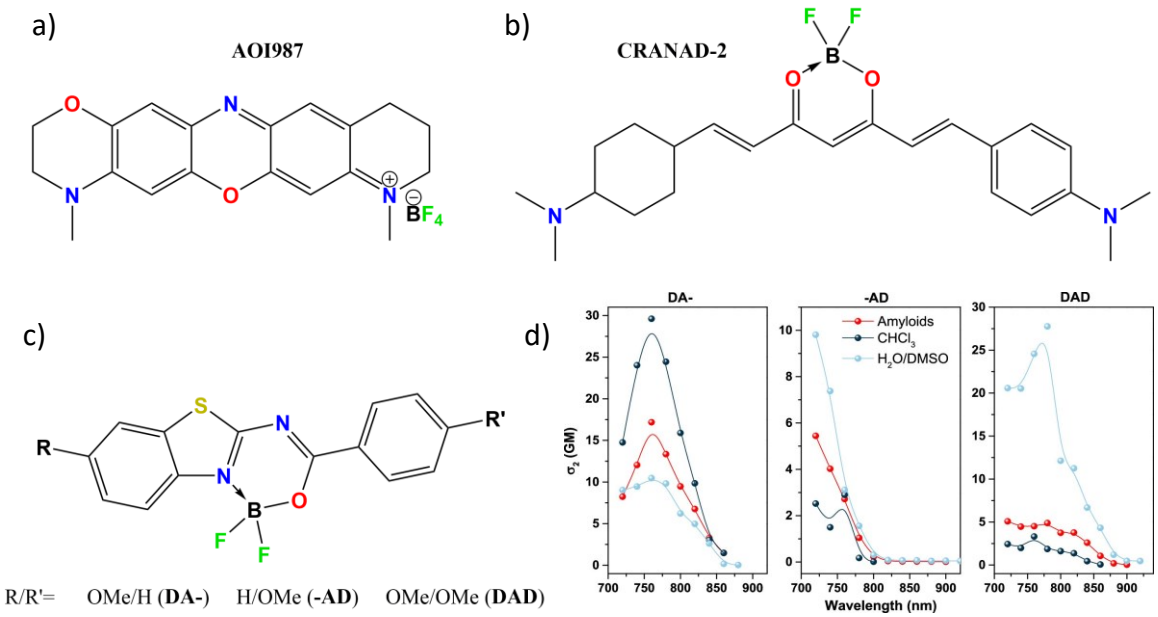

Figure 24. Molecular structures of AOI987 (a), CRANAD-2 (b), BF_2-functionalized benzothiazole molecules, substituted at both termini with proper R/R', namely OMe/H, H/OMe, OMe/OMe which refers to DA-, -AD, and DAD, respectively (c). Two-photon absorption cross-section (σ_2) of DA-, -AD, and DAD in various media: amyloid solution (red), chloroform ($CHCl_3$) (dark blue), water/dimethylsulfoxide (H_2O/DMSO) mixtures (light blue) (d).[20] Picture (d) was adapted with permission.

3.8.3 Label-free imaging

As I mentioned in the previous subchapter 3.7 Optical properties – autofluorescence, there are several hypotheses claiming the origin of amyloid autofluorescence. However, these hypotheses refer to linear optical processes including emission in the Vis range of the electromagnetic spectrum. To investigate amyloids *in vivo*, they should be studied in the NLO regime. Unfortunately, the literature provides little information on the NLO properties of amyloid aggregates. A. C. Kwan *et al.*[171] performed *ex vivo* experiments on brain slices from AD transgenic mouse models where they applied multiphoton and second harmonic generation (SHG) microscopies. The authors demonstrated that these techniques are suitable for identifying the autofluorescence signal. In the case of multiphoton microscopy, upon excitation at 774 nm and 830 nm, the resulting emission bands were centred at ~525 nm. In another study, P. Johansson and P. Koelsch[172] used among others scanning confocal fluorescence microscopy, multiphoton and SHG microscopy assays to study the LO and NLO properties of bovine insulin and β-LG spherulites (**Figure 25a-e**). Indeed, the power dependences demonstrated a quadratic relationship for the SHG (1.95 and 2.05 for bovine insulin and β-LG, respectively), and for multiphoton excited fluorescence signal (1.78 and 1.86 for bovine insulin and β-LG, respectively) (**Figure 25e**). P. Hanczyc *et al.*[173] used the Z-scan technique to examine

multiphoton absorption of insulin, lysozyme, and α-synuclein in their fibrillar state, comparing them to their native state.[173] The authors revealed that amyloids display the 2PA (in the range of 525-600 nm) and even three-photon absorption (3PA) (in the range of 700-750 nm). They demonstrated that the formation of fibrils leads to enhanced multiphoton absorption - amyloid fibrils possess stronger NLO absorption than the corresponding peptides in the native state.[173] We investigated bovine insulin spherulites using a polarization-sensitive two-photon excited fluorescence microscope.[174] We showed that the 2P excited autofluorescence was polarization-dependent, suggesting that it can be correlated with the orientation of amyloid fibrils within the spherulites. We noticed the highest 2P excited autofluorescence signal when the polarization of the excitation and emission beams were parallel to each other, indicating a parallel orientation of both absorption and emission transition dipoles with respect to the long axis of amyloid fibrils (**Figure 25f**). Finally, we evidenced that the 2P excited autofluorescence is distributed within ~30^{o} around the long axis of fibrils.[174] Although J. Pansieri *et al.*[175] did not describe the NLO properties of amyloid fibrils, their methodology could also be used for some *in vivo* applications because the measured signal appeared in the first biological window. Namely, they reported on near-infrared (NIR) luminescence of amyloid fibrils recorded for excitation wavelengths in the range of 600-670 nm. The observed NIR emission signal was continuously redshifted with a linear dependency between the excitation and the maximum emission wavelength, providing a constant Stokes shifts of ~55-60 nm and rather narrow emission bands (**Figure 25g**). The luminescence lifetimes could not be precisely determined, as they were shorter than 0.1 ns. The origin of this optical signature should be further explored and understood. Nevertheless, the NIR luminescence may be beneficial in the potential detection of amyloid deposits in living organisms.

As I indicated above, the NIR imaging allows the investigation of amyloids *in vivo*. There are 2 approaches, either using NIR fluorescent markers or utilizing label-free imaging of amyloids. Both of these methods have pros and cons. When using NIR fluorophores, several criteria have to be fulfilled, and the fluorescent probes may interfere with the aggregation process or structural properties of amyloid aggregates. On the other hand, the labels provide a high signal-to-noise ratio and thereby ensure an easy identification of amyloids. Label-free imaging of amyloids in NIR suffers from limited detection sensitivity, but it does not affect either the aggregation pathway or the structure of amyloids.

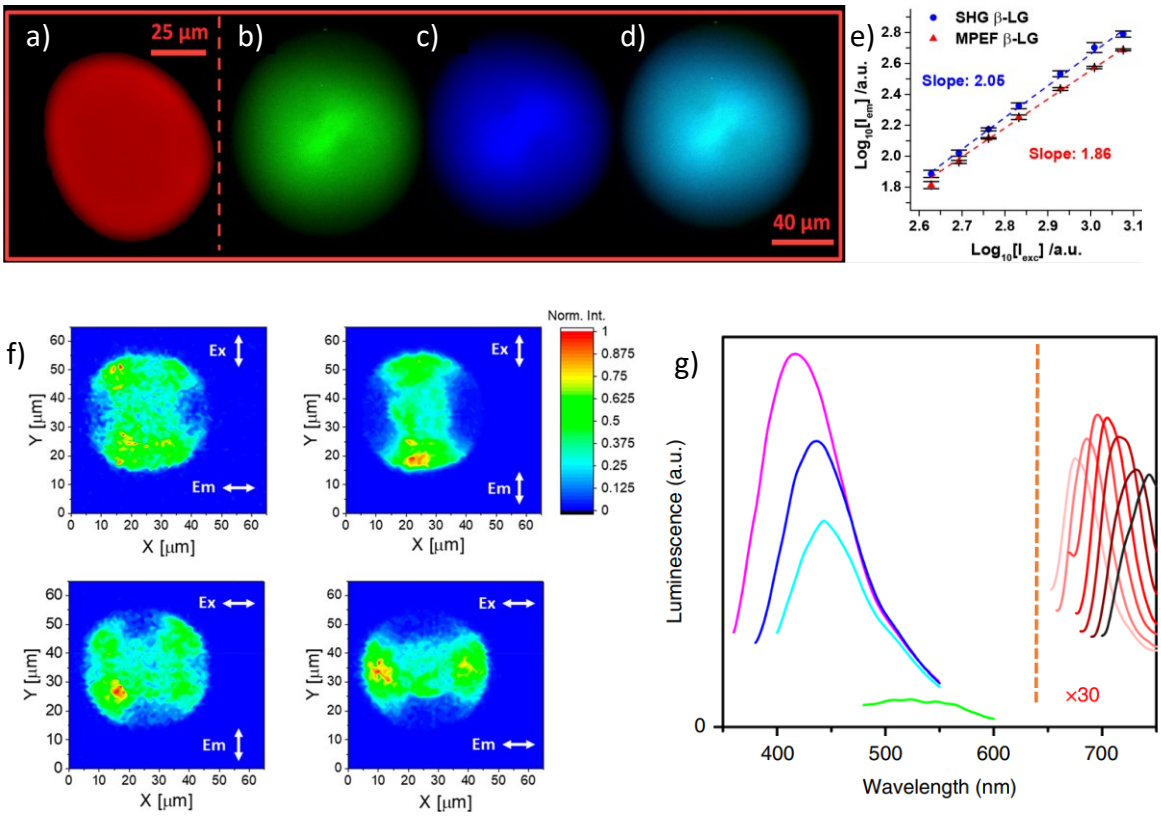

Figure 25. Amyloid spherulites obtained from β-lactoglobulin (β-LG) from bovine milk observed under scanning confocal fluorescence microscopy (a), multiphoton excited fluorescence (MPEF) microscopy (b), second harmonic generation (SHG) microscopy (c), and overlay of MPEF and SHG microscopies (d). The scale bar is 40 µm. For the MPEF and SHG, the power dependence plots evidenced a quadratic relationship with the slope equal to 1.86 and 2.05, respectively (e).[172] Raster scans of two-photon excited autofluorescence of bovine insulin spherulites (f).[174] The white arrows indicate the polarization of the excitation (Ex) and emission beam (Em). The luminescence properties of amyloid fibrils by the example of amyloid-β (1-42) under excitation at 340 nm (pink), 360 nm (blue), 380 nm (cyan), 440 nm (green), and excitation spanning from 600 to 670 nm (red color gamut) (g). A multiplying factor (x30) has been applied for the latter.[175] The pictures (a-g) were adapted with permission.

II. MAIN RESEARCH CONDUCTED

4 Chapter 4. Materials, methods, and general procedures

In this chapter, I described the materials, methods and general procedures applied to conduct target experiments. The more specified procedures are described in the subsequent chapters wherein I discuss the selected experiments.

Reagents. All solvents, chemicals, and reagents were purchased from commercial sources and used without further purification. Fmoc-*L*-amino acids, Fmoc-*D*-amino acids, resins for SPPS, coupling reagents *N*,*N*'-diisopropylcarbodiimide (DIC) and ethyl cyano(hydroxyimino)acetate (Oxyma pure), diisopropylethylamine, piperidine, triisopropylsilane (TIPS), 1,4-dithiothreitol (DTT), and *N*,*N*-dimethylformamide (DMF) were purchased from Iris Biotech (Marktredwitz, Germany) or Sigma Aldrich (St. Louis, Missouri, USA). Trifluoroacetic acid (Biograde) (TFA) was purchased from Halocarbon (Peachtree Corners, Georgia, USA). Acetonitrile hypergrade for LC-MS was purchased from LiChrosolv®, hydrochloric acid (35%-38%) was purchased from Stanlab sp. z o.o., throughout the experiments Milli-Q water was used.

Automated synthesis of peptides. SPPS was performed using the standard Fmoc/tBu-protecting group strategy, in the LibertyBlue (CEM Corporation, USA) automated microwave peptide synthesizer, on a 0.1 or 0.25 mmol scale. Target resins were swollen for ~20 minutes in DMF before usage in the synthesis. Amino acids were dissolved in DMF (0.2 M). For coupling reactions DIC (0.5 M) and Oxyma Pure (1 M) activation reagents in DMF were used; for deprotection reaction 20% (*v/v*) piperidine in DMF was used.

Cleavage and further steps. Before cleavage, target resins were washed several times with DMF, then DCM, and dried under vacuum for ~30 min. Then, the peptides were cleaved and globally deprotected (1 mL of mixture for 100 mg of resin). The cleaved reaction mixture was transferred to 50 mL centrifuge tubes and cold diethyl ether (-20 °C) was added for precipitation. After centrifugation, the precipitates were dissolved in H_2O/CH_3CN (1/1, *v/v*) containing 0.1% TFA, and finally lyophilized.

Analytical High-Performance Liquid Chromatography (HPLC). Analytical reversed-phase HPLC was performed on either (i) a NexeraXR (Shimadzu) HPLC instrument equipped with a CBM-20 A communication module, a SPD-M20 A photodiode array detector, a column heater set to 40 ^oC, LC-20AD pumps and a SIL-20AC autosampler or (ii) an Agilent 1100 HPLC instrument equipped with a G1365B UV detector, a column heater set to 40 °C, G1212 A pumps and a G1367 A autosampler. Either (i) a Reprosil-XR C18 (50×2 mm^2, 3 µm, 120 Å) or (ii) a Kinetex XB C18 (dimensions 50x2.1 mm^2, 2.6 µm, 100 Å) columns were used

at a flow rate of 1 mL/min with a gradient of water with TFA (0.1 %, *v/v*) and acetonitrile with TFA (0.08 %, *v/v*).

Preparative HPLC. Purifications of peptides were performed using a semi-preparative Shimadzu HPLC instruments equipped with two LC-20AP pumps and an SPD-20 A Prominence UV/Vis detector connected to an FRC-10 A fraction collector. Phenomenex Kinetex XB-C18 columns (250×21.2 mm, 100 Å, 5 µm) were used at 10 mL/min with a gradient of water with TFA (0.1%, *v/v*) and acetonitrile with TFA (0.08%, *v/v*).

Liquid chromatography–mass spectrometry (LC-MS). LC-MS spectra of peptides were recorded with a Thermo Ultimate 3000 system integrated with a Thermo Scientific LCQ ion trap mass spectrometer using an X-select peptide CSH C18 column (50×2.1 mm^2, 2.5 µm, 130 Å). Electrospray ionization (ESI) was utilized as the ionization source. The raw data were deconvoluted in MagTran 1.03 software (Amgen, Thousand Oaks, USA).

Atomic force microscopy (AFM) imaging. The morphology of samples was analyzed using a Dimension V Veeco AFM instrument in the tapping mode with NANOSENSORS™ SSS-NCHR tip mounted. The samples were diluted to a proper concentration (enabling analysis of the morphology). Aliquots (30-40 µL) were deposited on mica. After the adsorption process, they were rinsed (or not, depending on the sample of interest) with Milli-Q water and dried afterwards. Dimensions of the investigated samples were estimated based on 50 individual profiles. The AFM images were visualized using the Gwyddion software.[176] The mean height of the assemblies was calculated based on the highest value of the measured profile, the mean width using the full width at half-maximum (FWHM) method.

Absorption and fluorescence spectroscopies. Absorption spectra were acquired with a Jasco V-670 spectrophotometer. Fluorescence excitation and emission spectra were recorded using a FluoroMax-4 spectrofluorimeter (Horiba Jobin Yvon). For absorbance and fluorescence measurements, quartz cuvettes were used.

ATR-FTIR spectroscopy. ATR-FTIR spectra were acquired using Bruker Vertex series spectrometer. In the case of the synthesized peptides, the residual TFA was removed by treatment with 10 mM HCl and lyophilization (3 cycles). For the ATR-FTIR spectra measurements, a droplet of a sample of interest was deposited on the diamond surface. After a background measurement, the ATR signals from samples were collected 64 times and averaged. The spectra were recorded in 4000–400 cm^{-1} spectral range with a resolution equal to 4 cm^{-1}.

Molecular Dynamics (MD) simulations. The initial models of parallel two-layered β-sheet were prepared based on the ssNMR structure of 105-115 transthyretin (TTR) fragment (PDB id: 2m5n). The structure was extended by 8 additional strands, resulting in 24-mer bilayered structure of enantiomerically pure peptides (*L*-enantiomers). For the racemic or quasi-racemic mixtures (of the *L*-enantiomers and the *D*-enantiomer), an antiparallel two-layered β-sheet model was prepared by applying on every second strand transformation matrix for 180° rotation and reflection. The peptide models were minimized using the Discovery Studio Smart Minimizer protocol with distance-dependent dielectric as an implicit water model. Then, target capping groups on the N- and C-termini were added to the models. The optimized models were obtained by energy minimization in explicit water (spc216) using the steepest descent algorithm (GROMACS software, Amber03 forcefield). To examine the stability of the models, 50 ns- or 100 ns-long simulations were performed using GROMACS software and Amber03 force field, including parameters of different terminal capping and in explicit water (spc216). The minimization of the system was conducted using the steepest descent algorithm with 5000 maximum number of steps and PME electrostatic method and converged in 700 steps. Equilibration of the system comprised two phases: (i) 100 ps (50 000 steps) under the canonical ensemble (NVT), and (ii) 100 ps (50 000 steps) under the NPT ensemble for temperature and pressure stabilization followed by 50 000 ps (2 500 000 steps) production run. All the dynamics were conducted under periodic boundary conditions using the leapfrog scheme and PME electrostatics with a 1 nm cut-off at a constant temperature T=300 K and a pressure p=1 bar.

5 Chapter 5. Autofluorescence of amyloids determined by enantiomeric composition of peptides

In this chapter, I compare the structural and optical properties of amyloid fibrils formed from L- and D-enantiomers of the 105-115 fragments of transthyretin (TTR) and the racemic mixture. The results demonstrate that the autofluorescence position is blue-shifted for racemic fibrils compared to the enantiopure ones. These observations were explained thanks to a detailed analysis of the structure and morphology of the fibrils. Namely, the enantiopure and racemic fibrils differ in terms of the secondary β-sheet structure organization and thus the arrangement of the hydrogen bonding network. The samples exhibit another fluorescence signal at ~400 nm which also depends on the organization of hydrogen bonds, but is not amyloid-specific and originates from noncovalent interactions between tyrosine residues. Overall, the outcomes show the influence of supramolecular structure controlled by the chirality of amino acids on the optical properties of the resulting amyloid fibrils.

5.1 Motivation

Amyloid-related diseases constitute a growing societal problem. As I mentioned in subchapter 3.7 Optical properties - autofluorescence, amyloid structures possess a peculiar property, autofluorescence. Despite several hypotheses put forward, the origin of this phenomenon remains elusive.[137-138, 140-141, 145, 147-149] A common attribute of amyloids is the presence of the secondary β-sheet structure, stabilized by multiple hydrogen bonds. However, they demonstrate considerable differences in their morphology, known as polymorphism.[96-97]

Pauling and Corey were the first who provided detailed information on parallel and antiparallel β-sheet structure, constructed entirely of *L*- or *D*-amino acid residues which they called pleated sheets. They also introduced the concept of rippled sheets (both parallel and antiparallel configuration) composed of alternating *L*/*D* pattern wherein every second peptide strand has an opposed chirality.[177-178] The key structural differences between pleated and rippled sheets are hydrogen bonding and relative side-chain distributions on the surface of β-sheets.[179] Many articles have been published reporting on differences between enantiopure peptides and their racemic mixtures over the years. For example, S. Dutta *et al.*[180] reported that mixing two enantiomers (*L*- and *D*-) of Aβ42 leads to fibrils of similar morphology, but in the case of a racemic mixture, the process of fibril formation is significantly accelerated. Some other groups confirmed the prediction stated

by Pauling and Corey that enantiomeric β-sheet peptides co-assemble into rippled β-sheets with alternating *L*- and *D*-peptides.[181-183]

Taking into account the above-mentioned issues, I decided to verify the autofluorescence of racemic fibrils and their enantiopure counterparts. I hypothesized that autofluorescence is correlated with the secondary structure and morphology of amyloid fibrils. Transthyretin (TTR) is a 55-kDa protein that in physiological conditions is responsible for the transport of a thyroid hormone and retinol (vitamin A). Wild-type TTR can misfold into amyloid fibrils which leads to a disorder, senile systemic amyloidosis.[184-185] It has been reported that full-length TTR, some TTR variants, as well as synthetic 10-20 and 105-115 fragments are prone to form amyloid fibrils *in vitro*.[185] Thus, I have chosen the 105-115 fragment of TTR to investigate.

5.2 Additional information and contributions

Data discussed within this chapter is published in **Grelich-Mucha, M.**; Garcia, A. M.; Torbeev, V.; Ożga, K.; Berlicki, Ł.; Olesiak-Bańska, J., *Autofluorescence of Amyloids Determined by Enantiomeric Composition of Peptides*. The Journal of Physical Chemistry B 2021, 125 (21), 5502-5510.

I synthesized the TTR(105-115) sequences, both *L*- and *D*-enantiomers, during my internship at Prof. V. Torbeev's group (Université de Strasbourg, France) within the frames of Erasmus+ 2014-2020 program. MD simulations were performed by Dr. K. Ożga and Prof. Ł. Berlicki (using GROMACS software available at the Wrocław Centre for Networking and Supercomputing (WCSS, Wrocław, Poland), TEM imaging was performed by Dr. A. M. Garcia (at Imaging Center of Institut de génétique et de biologie moléculaire et cellulaire (IGBMC, Illkirch-Graffenstaden, France), and theoretical simulations of isotopically resolved mass spectra were carried out by Prof. V. Torbeev.

5.3 Materials and methods

Synthesis of peptides. The peptides were synthesized using a Liberty Blue automated microwave peptide synthesizer. To obtain peptide-$^{\alpha}$amides, Fmoc-Rink Amide AM resin (100−200 mesh, 0.74 mmol/g, 1% DVB) was used. The peptides contained α-amino group (H-) at the N-terminus. The *L*- and *D*- enantiomers of TTR(105-115) (YTIAALLSPYS) were named H-TTR-NH_2 and *D* hereafter.

Preparation of the samples. The enantiopure samples were dissolved at a concentration of 1 mM in acetonitrile/water (1/9, *v/v*); the final pH of the samples was adjusted to 2.0 using HCl. The racemic mixture was prepared by mixing in 1/1 molar ratio

the prepared *L*- and *D*-enantiopure samples. All three samples were incubated during the first 2 days at 37 °C in an Eppendorf Thermomixer C. Then, they were kept at room temperature (r.t.) for the next 14 days.[185]

Morphology analysis. Morphology of the samples was investigated before and after the incubation period using AFM, which is referred to as t_0 and t_1, respectively; the H-TTR-NH_2 and *D* samples were not diluted; the racemic mixture at t_0 was not diluted, but at t_1 the sample was 60-times diluted. Aliquots of the samples were deposited on the mica surface and after 5 minutes of adsorption, they were rinsed with Milli-Q water. The morphology of fibrils was also investigated using TEM imaging, by a Philips CM12 electron microscope operating at 80 keV. Firstly, TEM grids (carbon-coated 300 mesh copper TEM grids) were exposed to the UV−ozone cleaner for 5 min. Then, the grids were placed coated-side-down for 60 s onto sample drops (20 µL). Afterward, the grids were retrieved, washed with deionized water, and stained with 2% (*w/v*) uranyl acetate for 20 s. Grids were air-dried overnight and then kept under vacuum before analysis. The dimensions of the species were calculated using Nanoscope 7.30 or ImageJ software.

Spectroscopic studies. The enantiomeric samples were diluted for fluorescence and extinction spectra measurements to a concentration of 166 µM, whereas the racemic mixture - of 83 µM (due to a strong light scattering). The extinction spectra were measured from 240 nm to 650 nm. Fluorescence excitation spectra were measured at emission wavelength (λ_{em}) set to 440 nm, and emission spectra at excitation wavelength (λ_{exc}) set to 360 nm. Fluorescence excitation−emission intensity maps were acquired in the spectral range of λ_{exc} = 270−400 nm and of λ_{em} = 330−550 nm, respectively. The excitation and emission slits were set to 5 nm. For ATR-FTIR spectra measurements, the peptides were dissolved at a concentration of 1 mM acetonitrile/D_2O (1/9, *v/v*); the pH of the solution was adjusted to 2.0 with HCl.

Molecular Dynamics Simulations. The stability of the models was examined for 50 ns-long simulations, using GROMACS software and Amber03 force field.

Mass spectra. The LC-MS (**Figure 34**) were performed using a Waters LC Premier XE mass spectrometer, for enantiopure H-TTR-NH_2, *D*, and their racemic mixture; before and after the incubation period, utilizing ESI method. Then, theoretical simulations (**Figure 34**) of isotopically resolved mass spectra were implemented using IsoPro (v.3) software.

5.4 Results and discussion

First, I confirmed the composition and high purity of the *L*- (H-TTR-NH_2) and *D*-enantiomers (*D*), using ESI-MS (**Figure 26a, b**) and analytical RP-HPLC (**Figure 26c**), respectively. In the ESI-MS spectra, except the peaks of the highest signal intensity corresponding to hydrogen ion adducts ($M+H^+$), peaks assigned to ion clusters were also present (*i.e.* $3M+2H^+$ species).

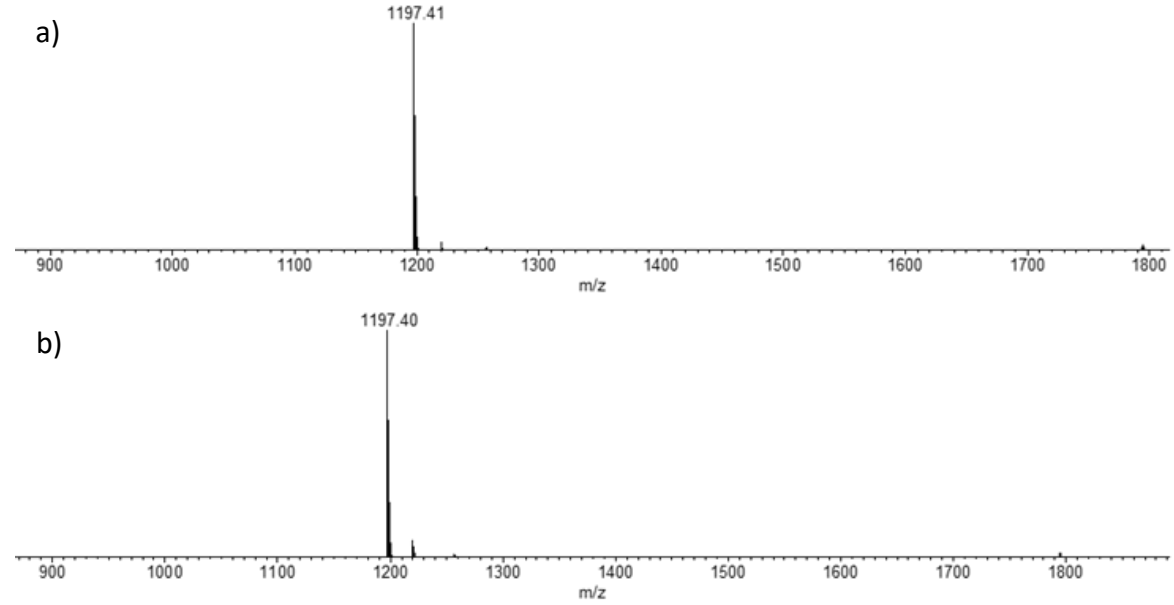

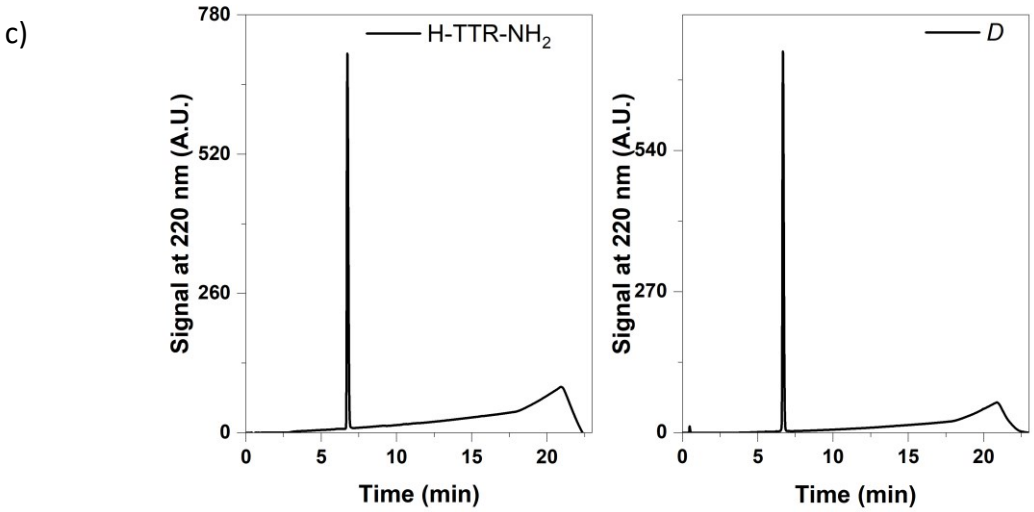

Figure 26. ESI-MS spectra of H-TTR-NH_2 (a) and *D* (b); analytical RP-HPLC traces of H-TTR-NH_2 (left) and *D* (right) (c) peptides.

After the incubation, *i.e.* at t_1, I investigated the morphology of both enantiopure samples and their equimolar mixture (*D* + H-TTR-NH_2) using AFM. I noticed significant

differences among the samples. Namely, in both enantiopure samples helical fibrils were present (**Figure 27b, d**), whereas in the racemate – straight, tape-like fibrils (**Figure 27f**). Interestingly, the helical fibrils formed from H-TTR-NH_2 were right-handed, and from *D* – left-handed. Besides the differences in their handedness, fibrils obtained from the *L*- and

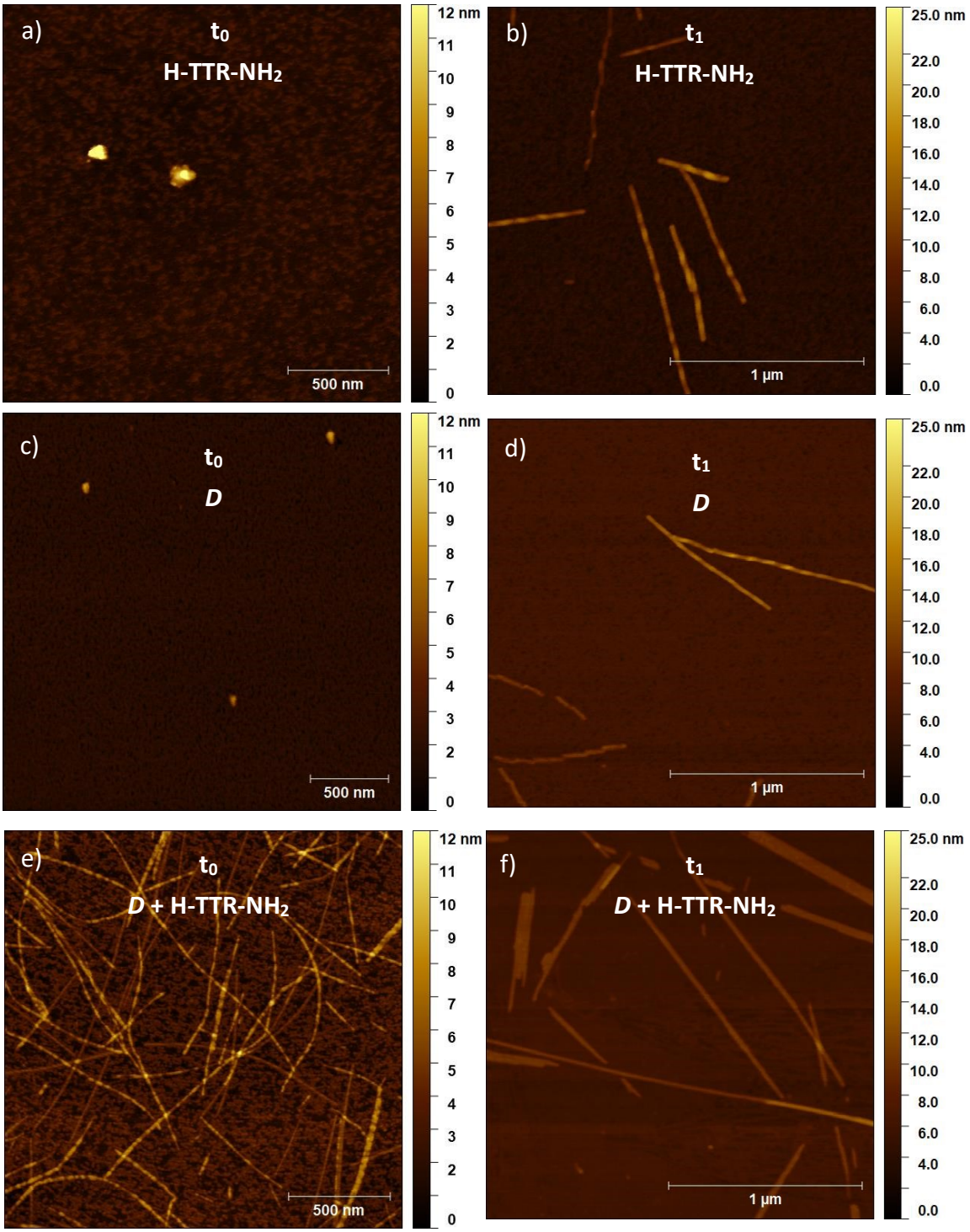

Figure 27. AFM images of enantiopure H-TTR-NH_2, *D*, and racemic mixture *D* + H-TTR-NH_2 before the incubation (t_0) (a, c, e) and after (t_1) (b, d, f), respectively.[187] In (a, c ,e) the scale bar is set to 500 µm, and the height contrast to 12 nm; in (b, d, f) the scale bar is set to 1 µm, and the height contrast to 25 nm. The images (b, d, f) were reproduced with permission.

D-enantiomers shared similarities in their dimensions. Namely, the cross-over distance for the *L*- and *D*-fibrils was estimated to be equal to 101 ± 8 nm and 102 ± 8 nm, respectively (**Table 3**). The exemplary cross-over distances of H-TTR-NH_2 fibrils are demonstrated in **Figure 28**. The average height for the *L*- and *D*-fibrils equalled 7.5 ± 1.7 nm and 7.4 ± 1.6 nm, respectively (**Table 3**). To avoid tip-sample convolution artifacts, the width was estimated based on images obtained under TEM (**Figure 29**). The width for the *L*- and *D*-enantiomers was equal to 17 ± 3.0 nm and 18 ± 3.4 nm for the *L*- and *D*-fibrils, respectively (**Table 3**). The dimensions are in agreement with the ones Fitzpatrick *et al*. [186] published and suggest these are quadruplet fibrils. In the case of the racemic mixture, I noticed a dense network of fibrils formed. For AFM imaging, the sample was 60-times diluted. For comparison, the enantiopure samples were not diluted. Besides the differences in the number of fibrils, the racemic fibrils were lower and wider as than the enantiopure ones. Their height and width were estimated to be 4.0 ± 0.9 nm and 23 ± 5.1 nm, respectively (**Table 3**).

Table 3. Average width (nm), height (nm), and cross-over distance (nm) of the investigated fibrils formed from H-TTR-NH_2, *D*, and *D* + H-TTR-NH_2.[187]

Sample	Width (nm)	Height (nm)	Cross-over distance (nm)
H-TTR-NH_2	17 ± 3.0	7.5 ± 1.7	101 ± 8
D	18 ± 3.4	7.4 ± 1.6	102 ± 8
***D* + H-TTR-NH_2**	23 ± 5.1	4.0 ± 0.9	-

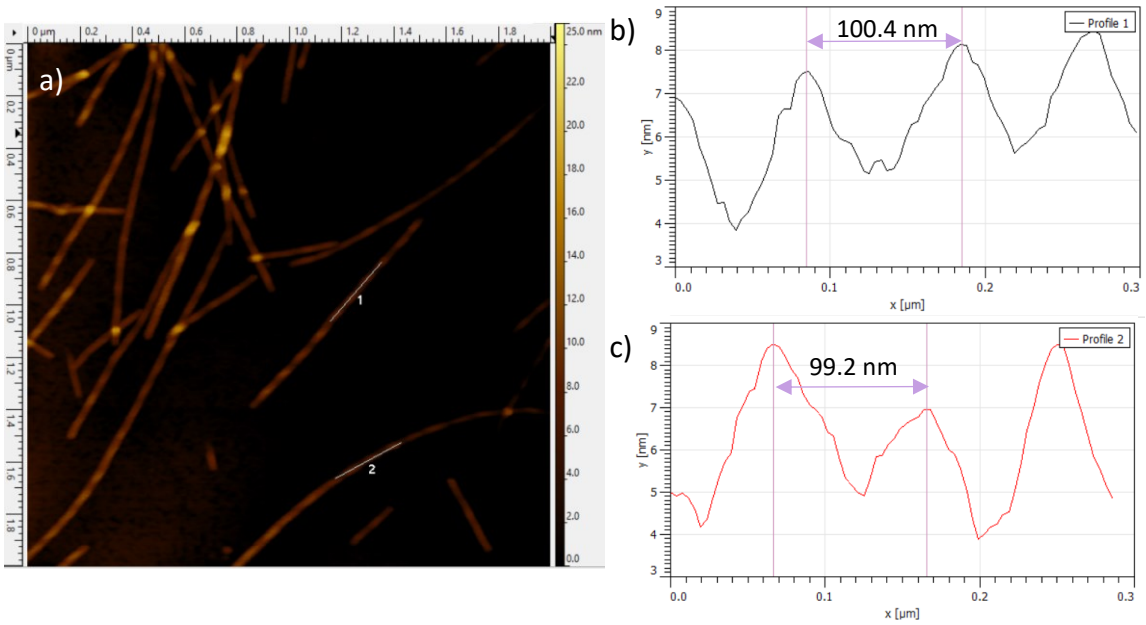

Figure 28. AFM image of H-TTR-NH_2 fibrils with marked distances 1 and 2 (a); profiles of distance 1 (b) and 2 (c). The measured cross-over distance in 1 equals 100.4 nm (b), and in 2 equals 99.2 nm (c) as indicated on the images. The height contrast in (a) is set to 25 nm.

Figure 29. Morphology of H-TTR-NH_2 (a), *D* (b), and *D* + H-TTR-NH_2 (c). Scale bars on the images are set to 200 nm.[187] The images were reprinted with permission.

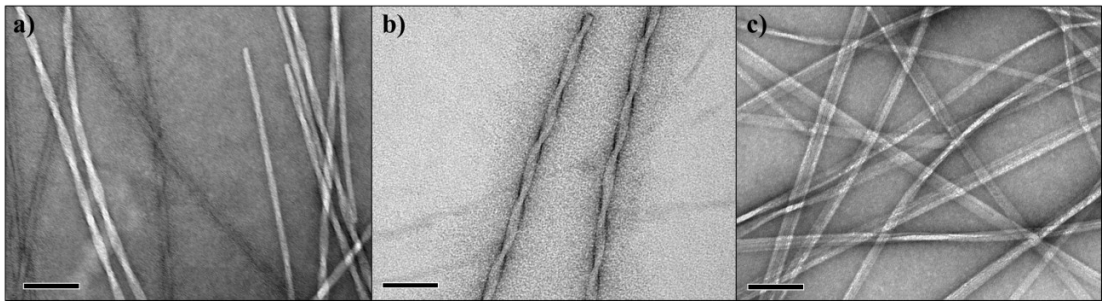

I also investigated the morphology of the samples before incubation which I denote as t_0. The AFM imaging revealed the presence of some aggregates in the case of H-TTR-NH_2 and *D* (**Figure 27a, c**), as opposed to the *D* + H-TTR-NH_2 sample (**Figure 27e**), where some fibrillar structures were already present. These outcomes are in agreement with previous density functional theory computational methods, explaining that the formation of racemic fibrils is energetically preferable over enantiopure ones.[188-189]

As the enantiomeric fibrils differed from the racemic ones in terms of their morphology, I decided to investigate whether the samples also exhibit different optical properties. Firstly, I measured their extinction spectra (**Figure 30**). The maximum absorption peak at 276 nm comes from the tyrosine (Tyr) residues in the TTR(105-115) sequences. After the incubation, I noticed higher extinction intensity in all samples which correlates to the formation of amyloid fibrils scattering the incoming light. Additionally, in the racemic mixture (where the concentration was 2 times lower as compared to the enantiopure samples), the scattering effect was even more pronounced which explains a denser network of fibrils in the sample, as evidenced by morphology imaging (**Figure 27-29**).

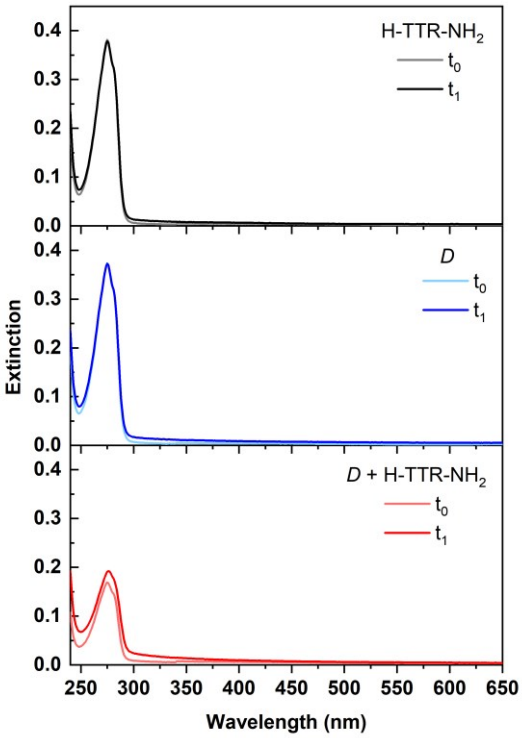

Figure 30. Extinction spectra of the samples at t_0 and t_1: H-TTR-NH_2 (upper panel, grey and black), *D* (middle panel, light blue and blue), and the racemic mixture *D* + H-TTR-NH_2 (bottom panel, light red and red).[187] The pictures were reproduced with permission.

Then, to investigate autofluorescence of the samples, I recorded fluorescence excitation-emission intensity maps (**Figure 31**). They clearly demonstrate that after incubation, upon excitation at 320-400 nm, emission appears with a maximum centred at ~440 nm. In the case of the racemic fibrils, the autofluorescence signal was stronger as compared to the enantiopure ones. Moreover, in racemate, the autofluorescence signal was observed before the incubation period (**Figure 31c**) and its appearance can be explained by the presence of some fibrillar structures, as demonstrated in the AFM image (**Figure 27e**). Additionally, the lower signal intensity before incubation *versus* after incubation (**Figure 31c, d**) confirms that already the fibrillar structures yield an autofluorescence signal which gets enhanced while mature fibrils are formed. This is in agreement with the sigmoid-shaped curve for amyloid fibril formation demonstrating that the highest fluorescence signal emerges from fully developed fibrils.[50]

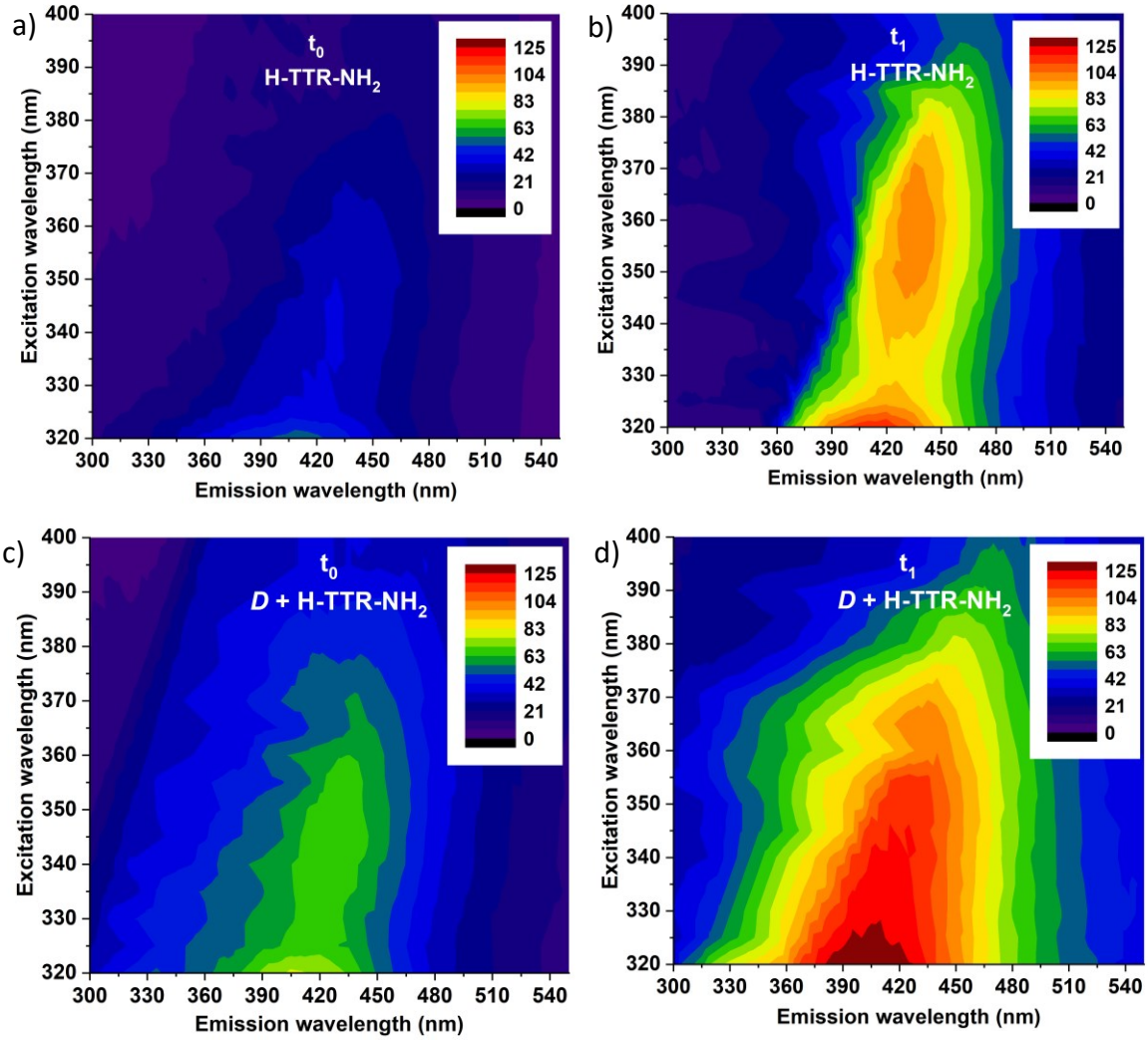

Figure 31. Fluorescence excitation-emission maps in the excitation range 320-400 nm and emission range 300-550 nm recorded for H-TTR-NH_2 (a, b) and the *D* + H-TTR-NH_2 (c, d) at t_0 and t_1.[187] The pictures were adapted with permission.

To evaluate the exact positions of excitation and emission bands, I acquired target spectra at a higher spectral resolution (**Figure 32**). The fluorescence excitation spectra demonstrated a spectral shift between the samples, as the maximum excitation band for the racemic mixture and both enantiopure samples was localized at 350 nm and 365 nm, respectively (**Figure 32a**). The emission spectra also revealed a blue shift for the racemic fibrils as compared to enantiopure ones with autofluorescence maximum position at 431 nm and 436 nm, respectively (**Figure 32b**). The spectral differences in emission and excitation indicate that the local environment of components involved in the autofluorescence phenomenon is different in racemic and enantiopure fibrils.

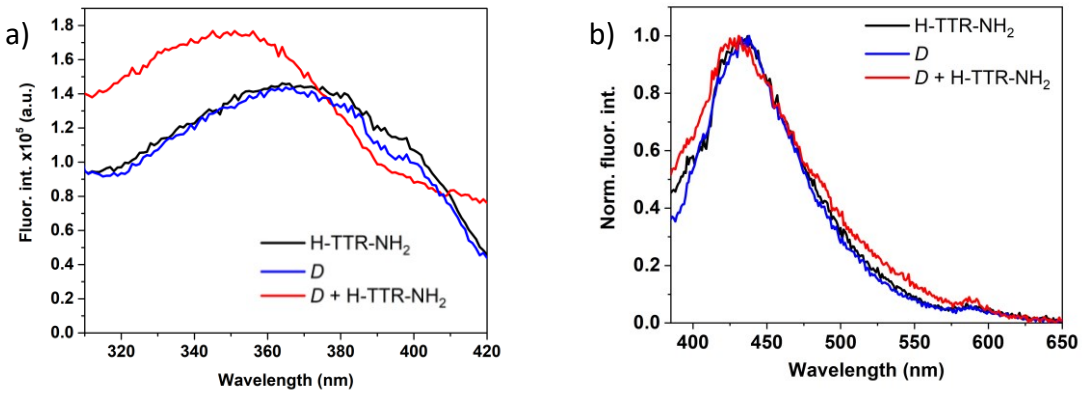

Figure 32. Fluorescence excitation (λ_{em} = 450 nm) (a) and emission spectra (λ_{exc} = 360 nm) (b) acquired for H-TTR-NH$_2$ (black), *D* (blue), and racemic fibrils (red).[187] The images were adapted with permission.

The fluorescence excitation-emission maps (**Figure 33**) demonstrate other optical characteristics of the investigated samples. Namely, upon excitation <330 nm, an emission signal with a maximum localized at ~400 nm occurs. To investigate it more in detail, I collected fluorescence excitation-emission maps in the excitation range 270-320 nm, and emission range within 330-550 nm (**Figure 33**). Besides the fluorescence signal arising from the presence of tyrosine residues (λ_{em}<350 nm), I observed another one, with a maximum λ_{em} at ~405 nm. In the case of the H-TTR-NH$_2$ sample, the maximum λ_{exc} was localized at 292 nm (**Figure 33a, b**). For the racemic sample, the maximum λ_{exc} was at 290 nm, and after incubation, the maximum signal was blue-shifted towards 286 nm (**Figure 33c, d**). Comparing the enantiopure and racemic samples at t_1, the fluorescence signal was of lower intensity for the latter. Interestingly, the signal decreased after the incubation in the racemic mixture, unlike the enantiopure sample.

It has been reported that upon excitation at 315 nm in alkaline environment, or 284 nm in acidic environment, an emission signal within 400-420 nm arises from dityrosine (diTyr) residues.[190-193] Formation of diTyr cross-links is promoted by hydroxyl radicals, oxygen free radicals, or nitrogen dioxide, but also upon UV-irradiation.[193-194] Thus, to verify if in the investigated samples the described signal arises from diTyr cross-links or noncovalent interactions between tyrosine residues, ESI-MS was performed. Since in ESI-MS ion clusters can be present, theoretical simulations have been performed to validate the peaks from experimental MS spectra exactly. The MS spectra revealed the formation of ion clusters (m/z ≈ 2395 and m/z ≈ 1797) which correspond to M2+H$^+$ and M3+2H$^+$ species (**Figure 34**), respectively. Thus, the fluorescence signal (**Figure 33**) does not originate from diTyr cross-links, but probably from noncovalent π-stacking interactions between Tyr residues.

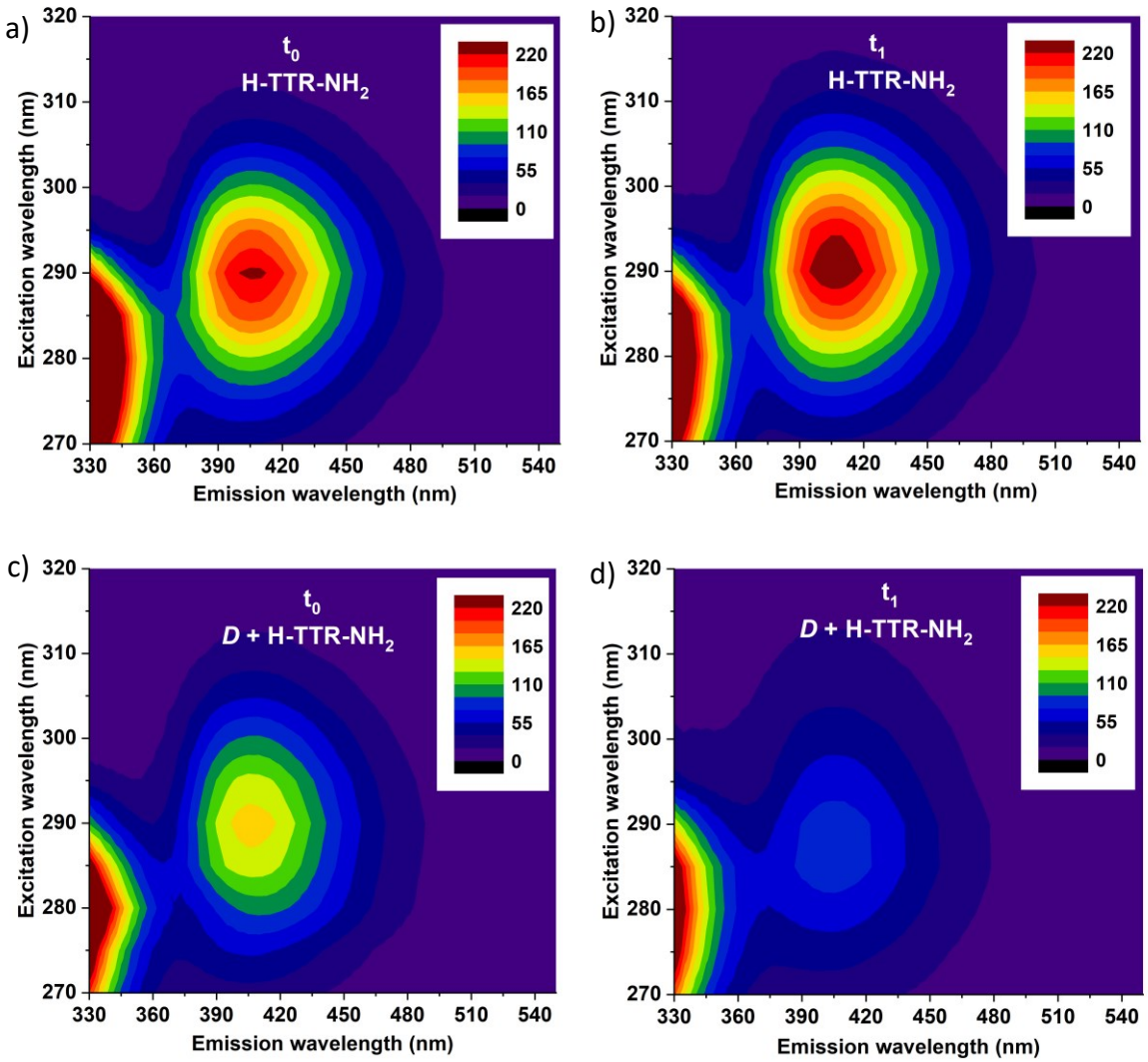

Figure 33. Fluorescence excitation-emission maps in the excitation range 270-320 nm and emission range 330-550 nm recorded for H-TTR-NH_2 (a, b) and *D* + H-TTR-NH_2 (c, d) at t_0 and t_1.[187] The pictures were adapted with permission.

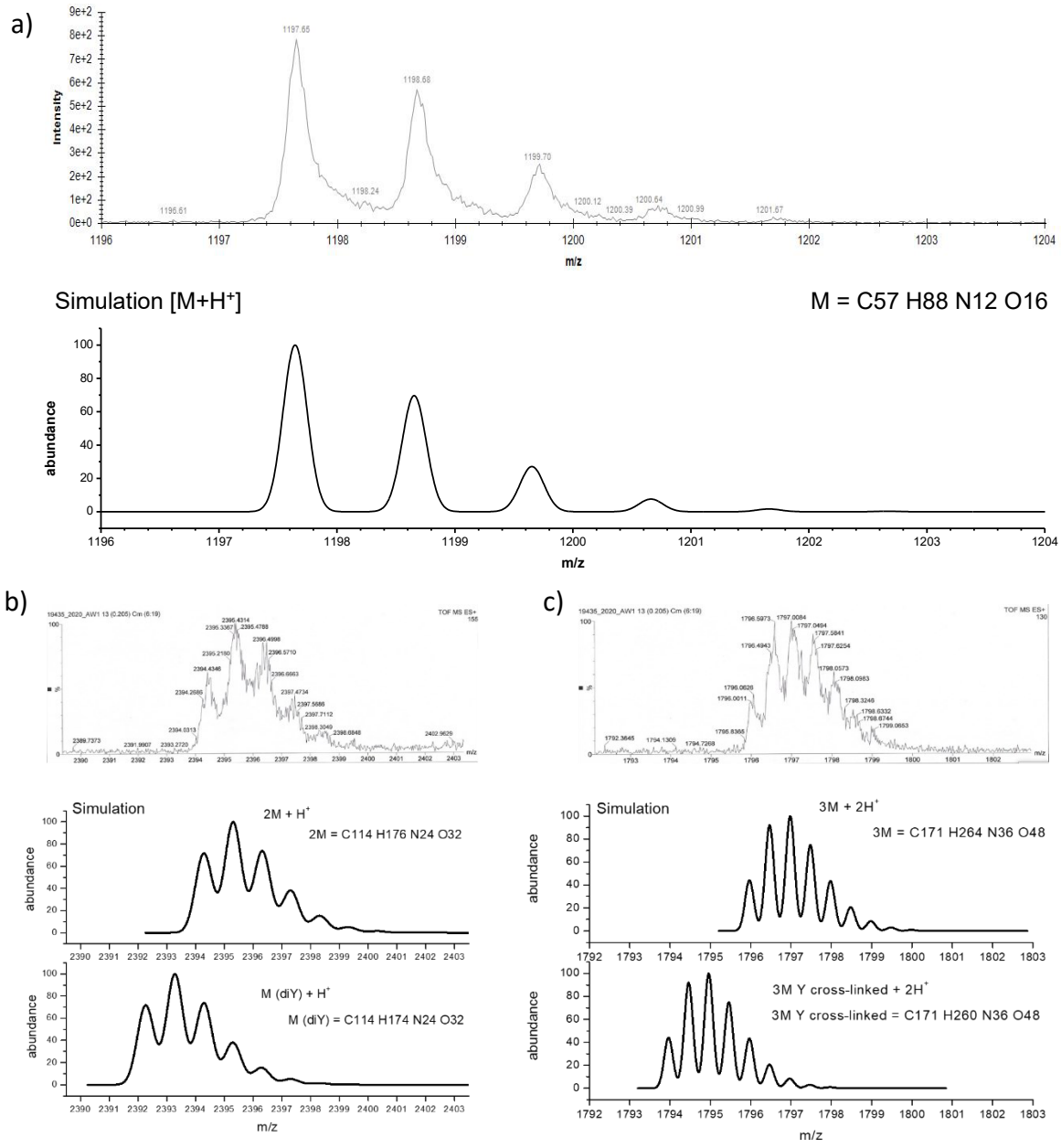

Figure 34. ESI-MS spectra evidencing the absence of covalent Tyr cross-links in H-TTR-NH_2. Experimental MS spectrum for $1H^+$ charge state (upper panel) and its theoretical simulation using IsoPro (v.3) software (lower panel) (a). Experimental MS spectra for ion clusters $2M+H^+$ (b) and $3M+2H^+$ (c) (upper panels) and their corresponding theoretical simulations (middle panels). In addition, theoretical simulations for Tyr cross-links (lower panels) confirming that their masses are lower than the experimental values. The MS spectra were also measured and analysed for the *D* and *D* + H-TTR-NH_2 and the results were similar to those demonstrated in this figure (Figure 34).[187] The pictures were adapted with permission.

Since the enantiopure and racemic samples differed significantly in terms of their morphology, I decided to study their structural properties. Namely, I collected ATR-FTIR spectra of the samples (**Figure 35**). At t_1, in all samples I noticed a clear band indicating the presence of the β-sheet structure (**Figure 35a**). However, in the case of the enantiomeric fibrils, the maximum was centred at ~1629 cm^{-1}, and of the racemic mixture was shifted

towards ~1626 cm^{-1}. The *D* sample had a lower intensity band with a maximum at ~1629 cm^{-1} compared to the H-TTR-NH_2. It indicates a lower number of fibrils in the *D* than in the *L*-sample which is in agreement with the AFM images. The spectral shift between the enantiopure samples and the racemic mixture (~1629 cm^{-1} *versus* ~1626 cm^{-1}) indicates that racemic fibrils possess increased rigidity of β-sheets.[112, 124] The absorption bands centred at ~1670 cm^{-1} may correspond to the α-helical structure, β-turns, or a combination of these structures.[195] Moreover, the absorption peak centred at ~1695 cm^{-1} indicates the presence of an antiparallel β-sheet structure, unlike the enantiopure samples where parallel one predominates.[110, 116] The ATR-FTIR spectra collected for these samples before the incubation indicated antiparallel β-sheet structure in the racemic mixture (**Figure 35b**, the bottom panel) which is in agreement with the observed morphology (**Figure 27e**).

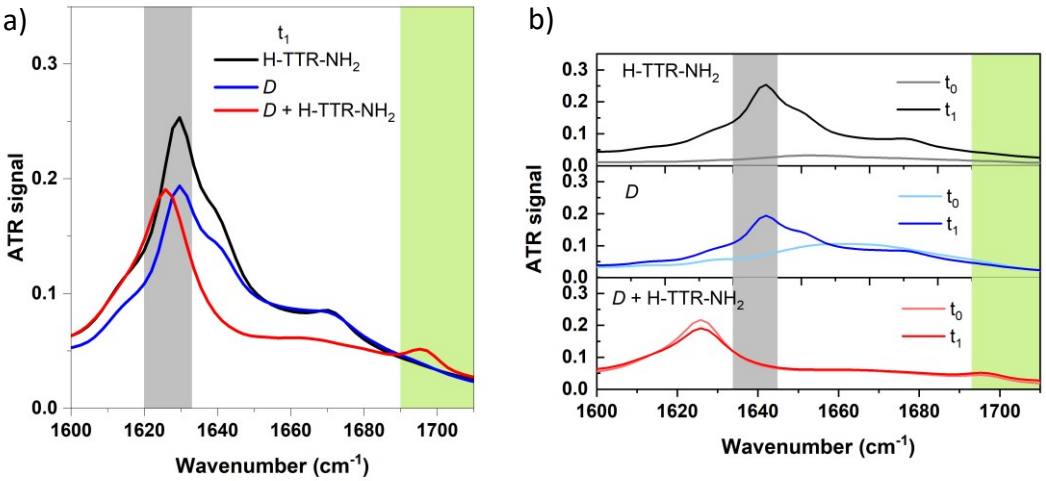

Figure 35. ATR-FTIR spectra collected for H-TTR-NH_2 (black), *D* (blue), and *D* + H-TTR-NH_2 (red) at t_1 (a). Comparison of the ATR-FTIR spectra for each sample at t_0 and t_1: H-TTR-NH_2 (grey and black, top panel), *D* (light blue and blue, middle panel), and *D* + H-TTR-NH_2 (light red and red, bottom panel) (b).[187] The peaks in the grey area represent spectral region characteristic for the β-sheet structure, and the green one - antiparallel β-sheet structure. The images were reproduced with permission.

To better understand the correlation between the observed morphology and the secondary structure, MD simulations were performed (**Figures 36-38**). The atomic resolution structure of parallel *L*-enantiomeric fibrils of 105-115 TTR has been resolved by Jaroniec *et al*.[196] To model the *D*-enantiomeric fibrils, mirror-image structure of the *L*-counterpart was simulated. According to the ATR-FTIR spectra, the racemic fibrils possess antiparallel β-sheet structure (**Figure 35**). Thus, the MD simulations were performed for racemic mixture consisting of alternate *L*- and *D*-strands arranged in an antiparallel orientation. The model structure of *D* + H-TTR-NH_2 fibrils was found to be very stable. Its stability arises from a well-defined hydrogen bond network (**Figure 36c**) and a well-packed hydrophobic core (**Figure 36d**). The high stability is also probably due to edge-to-face π-π

stacking interactions between side chains of (i) Tyr114 (from *L*-strand) and Tyr105 (from *D*-strand) as well as (ii) Tyr105 (from *L*-strand) and Tyr114 (from *D*-strand) (**Figure 37a**). In H-TTR-NH_2 face-to-face interactions of Tyr residue side chains spanning along the fibril axis are present (**Figure 36b, 37a**). However, these interactions are absent in racemic amyloids (**Figure 36d, 37b**) due to the antiparallel arrangement of the β-sheets.

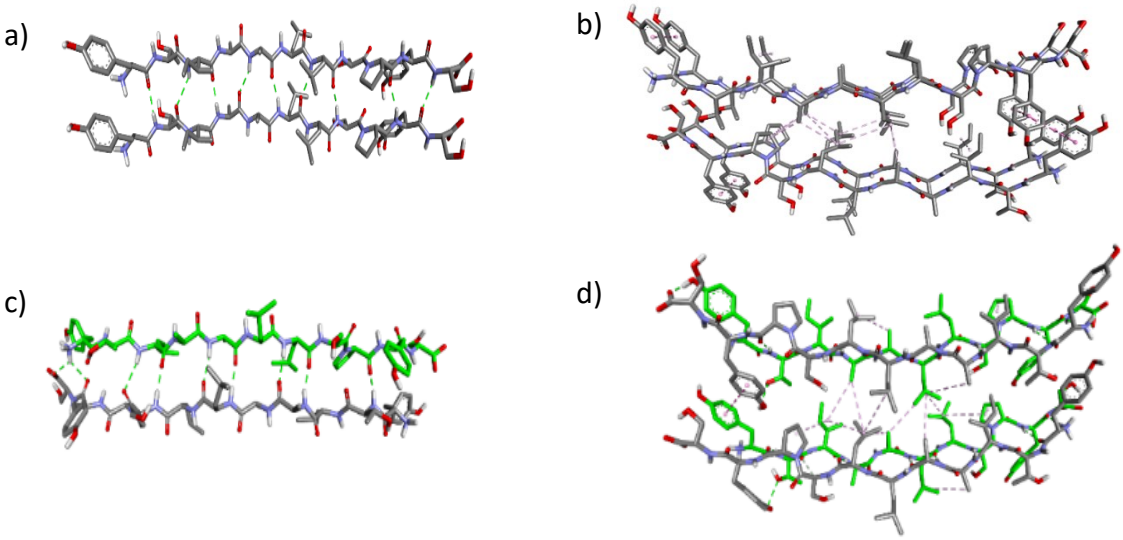

Figure 36. Minimized and equilibrated models of the studied enantiopure and racemic fibrils. A pair of parallel *L*-strands marked in grey with hydrogen bonds highlighted as green dotted lines (a). Four-strand section from the side view and hydrophobic interactions between *L*-strands from two different layers are demonstrated by pink dotted lines (b). A pair of antiparallel *L*- and *D*-strands marked in grey and green, respectively, with hydrogen bonds indicated by green dotted lines (c). Four-strand section from the side view and hydrophobic interactions between strands from two different layers are demonstrated by pink dotted lines (d).[187] The images were adapted with permission.

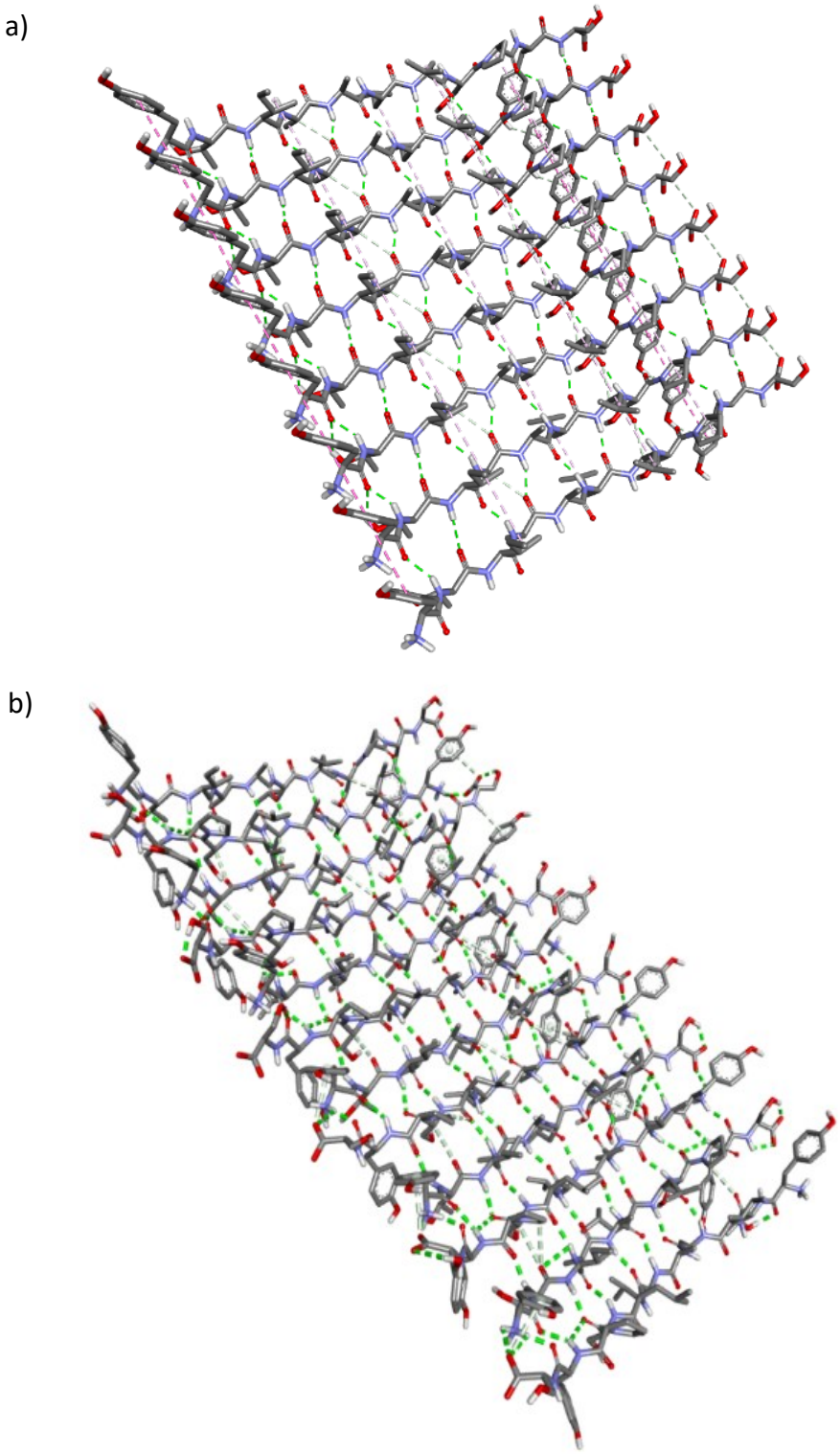

Figure 37. Model structure demonstrating one layer of *L*-strands in parallel orientation in H-TTR-NH_2 (a) and one layer of *L*- and *D*-strands organized in an antiparallel fashion in racemic mixture (b). Green and pink dotted lines indicate hydrogen bonding and hydrophobic interactions, respectively.[187] The images were reprinted with permission.

The MD simulations helped to explain the differences among morphology of the studied samples. The enantiopure samples possess a parallel β-sheet structure where

charge repulsion between the same termini dictates the twisted morphology of the fibrils (**Figure 38a, b**). The flat morphology of racemic fibrils is due to the antiparallel arrangement of the consecutive β-strands where charge repulsion is minimized due to alternate positive and negative charges at the ends of the neighbouring β-strands (**Figure 38c, d**).

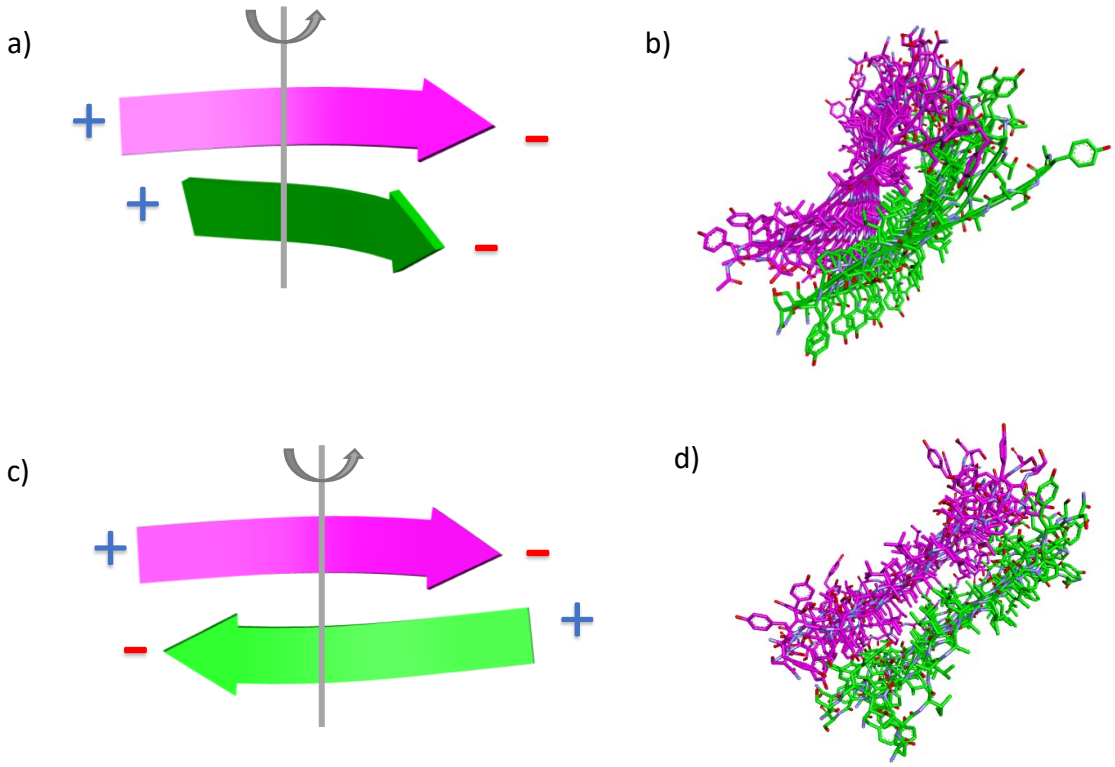

Figure 38. Demonstration of two consecutive β-strands in parallel β-sheet structure in enantiopure amyloids (a). Peptide chains arranged in a parallel orientation form twist (b). Demonstration of two consecutive β-strands in antiparallel β-sheet structure in racemic amyloids (c). The reduced charge repulsion between the neighbouring β-strands favours a flat morphology of the fibrils which is represented by *L*- and *D*-peptide chains oriented in an antiparallel way (d).[197] The images were reprinted with permission.

The excitation-emission maps (**Figure 33**) illustrate fluorescence signal arising from noncovalent interactions between Tyr residues. This signal emerges regardless of the presence of amyloid fibrils, as it appears for peptide aggregates (at t_0 for H-TTR-NH_2), as well as fibrillar structures (at t_1 for H-TTR-NH_2, at t_0 and t_1 for *D* + H-TTR-NH_2). In the case of the *L*-enantiopure sample, this emission band intensity is enhanced after the incubation, contrary to the racemic sample where the signal intensity is decreased at t_1 compared to t_0. This observation can explain the structures simulated by MD. Namely, in the enantiomeric sample, the Tyr residues form a continuous π-π stacking (**Figure 36b, 37a**). However, in the case of the racemic mixture, the interaction is limited only to two Tyr residues (**Figure 36d, 37b**). Thus, the discussed fluorescence signal depends on the organization of the secondary β-sheet structure.

As demonstrated in fluorescence excitation-emission maps (**Figure 31, 33**), both enantiopure and racemic samples yield two emission bands >400 nm of a different origin:

(i) upon excitation at 315-410 nm, emission with a maximum at 430-440 nm occurs and this signal is amyloid-specific.

(ii) when excited at ~290 nm, an emission signal centred at ~405 nm emerges. It arises from π-π stacking interactions between Tyr side chains and is not amyloid-specific.

According to the emission signal mentioned in (i) above → the ATR-FTIR spectra (**Figure 35b**) evidenced that at t_0 in both enantiopure samples the β-sheet structure is absent, indicating the absence of fibrils. This was further verified by the AFM imaging (**Figure 27a, c**). The secondary β-sheet structure and the presence of fibrils at t_1 for these samples were confirmed by the AFM and ATR-FTIR techniques (**Figure 27b, d, 35**). At t_1, the excitation-emission maps (**Figure 33b**) evidenced a clearly visible emission at 430-440 nm for the H-TTR-NH_2 samples. In the case of the *D* + H-TTR-NH_2, the β-sheet structure and some fibrillar assemblies have been identified already at t_0, and mature fibrils at t_1 (**Figure 27e, f, 35**). For the racemic mixture, the fluorescence signal at 430-440 nm was easily detected at t_0 and t_1 (**Figure 33c, d**). These observations are in agreement with theoretical assumptions. Grisanti *et al.*[141] demonstrated that the β-sheet structure is likely to effectively hinder nonradiative relaxation pathways and plays a key role in the photophysics of amyloids. They performed *ab initio* static calculations and nonadiabatic dynamics simulations for model peptides without aromatic amino acids. They demonstrated that the strong stabilization of nπ* states with respect to the deplanarization of amide groups contribute to amyloid autofluorescence. Thus, the different hydrogen bonding networks in enantiopure and racemic samples (validated by ATR-FTIR spectra and MD simulations) seem to be responsible for the observed shift in the positions of autofluorescence spectra (431 nm and 436 nm for racemic and enantiopure amyloids, respectively), and even more distinct shift in the excitation spectra maxima (350 nm and 365 nm for racemic and enantiopure amyloids, respectively). One of the hypotheses assumes that proton transfer between N- and C-termini contributes to autofluorescence of amyloid fibrils.[138] As the investigated peptides possess amide group at their C-terminus, proton transfer between N- and C-termini does not occur in the conditions I studied. Thus, in these systems, I can omit this hypothesis. Nevertheless, I cannot exclude possible short-range excitations close to the charged N-termini.[140] The observed autofluorescence can also originate from the CO-lock mechanism[149] according to which the CO elongation can be hindered by strong local interactions such as hydrogen bonds between CO and NH of the opposite β-strands in amyloid fibrils.

5.5 Conclusions

I performed a detailed analysis of the morphology, secondary structure and autofluorescence properties of 105-115 peptide fragments of TTR. I focused on the *L*-, *D*-enantiomers and the racemic mixture formed by mixing *L*- and *D*-enantiomers in 1/1 molar ratio. The morphology analysis that I performed indicated significant differences between enantiopure samples and the racemic mixture, where helical and tape-like fibrils were present, respectively. The ATR-FTIR spectra that I collected revealed a parallel and antiparallel β-sheet structure in respective enantiopure samples and the racemic mixture. The MD simulations demonstrated that racemic fibrils possess a very stable structure with a well-defined hydrogen bonding network and a well-packed hydrophobic core. Moreover, the racemic fibrils were characterized by a disrupted long-range π–π stacking between Tyr residues of neighbouring peptide chains, unlike the enantiopure fibrils.

Overall, these studies evidence that differences between the enantiopure samples and the racemic mixture in terms of fibril structure and morphology result in distinct optical properties. I confirmed that both pure enantiomeric and racemic fibrils exhibit autofluorescence. However, the latter has blue-shifted excitation and emission bands compared to the enantiopure fibrils. The spectral shift arises potentially from the differences in the secondary β-sheet structure and thus from a distinct organization of hydrogen bonds between the samples. Both enantiopure and racemic samples exhibited fluorescence with a maximum at ~405 nm upon excitation at ~290 nm. This signal arises from noncovalent π–π stacking interactions between Tyr residues and is not restricted to amyloid fibrils. However, its intensity and position depend on the structure of the fibrils which is different in enantiomeric and racemic fibrils. My findings demonstrate that the organization of hydrogen bonds determines the morphology and the secondary structure which further impact the autofluorescence properties. The knowledge gained from these studies may serve as valuable information on the internal structure of amyloid fibrils.

6 Chapter 6. Amyloid engineering – how terminal capping modifies morphology and secondary structure of supramolecular peptide aggregates

The capacity to fibrillate has been regarded as a generic property of polypeptide chains. So far, many peptide models with a specific amino acid sequence have been investigated in terms of their aggregation propensity. However, the influence of peptide N- and C-termini on the aggregation process has been scarcely investigated. Herein, I expand my research on TTR(105-115) functionalized with various functional groups at its termini. Namely, I synthesized TTR(105-115) possessing at the N-terminus α-amino, N-acetyl-α-amino or N,N-dimethyl-α-amino groups, and at the C-terminus either amide or carboxyl groups. I investigated enantiopure samples and quasi-racemic mixtures by mixing in 1/1 molar ratio target enantiomer L with the D one functionalized with H- and -NH_2 groups at its termini. The outcomes indicate that the functions at peptide termini play a decisive role in determining the final morphology of the resulting assemblies. In addition, the formation of fibrils is dictated by a sufficient number of hydrogen bonds that stabilize the β-sheet structure. All quasi-racemic fibrils are characterized by an accelerated fibril formation as compared to the enantiopure samples. In this chapter, I demonstrate how the modifications of peptide ends may be useful in the design of supramolecular aggregates with a predicted morphology.

6.1 Motivation

In the previous chapter, I demonstrated that enantiomers and the racemic mixture of TTR(105-115) display differences in their optical properties, morphology, and secondary structure. The investigated peptides were capped by H- and -NH_2 groups at their N- and C-termini, respectively. Indeed, peptides can be functionalized by other groups as well. Besides the mentioned H- group, another standard capping constitutes *N*-acetyl-α-amino group (Ac-) at the N-terminus. Besides the -NH_2 group, peptides can be functionalized at the C-terminus with a carboxyl group (-OH). The mentioned modifications at peptides' termini play key roles *in vivo*, including protein regulation or signal processing.[198-199] Nevertheless, only several articles deal with the topic of peptides' termini modifications influence on the aggregation process, the ongoing morphology, and the secondary structure of the resulting peptide aggregates. One of these includes the article of Tao *et al*.[200] who studied two variants of Aβ(16-22) peptide possessing at its N- and C-termini: (i) H- and -OH groups, and (ii) Ac- and -NH_2 groups, respectively. The authors noticed different morphology for the two analogues. Namely, the variant possessing H- and -OH

groups led to the formation of long, straight, unbranched nanofibrils, whereas its analogue capped by Ac- and -NH_2 functions to the fibrils in the form of nanotapes. In addition, Andreasen and colleagues[201] performed similar investigations on $hIAPP_{20-29}$. They deduced that the final morphology of amyloid fibrils is related to the number of hydrogen bonds and electrostatic interactions between the terminal groups. Similar observations shared Hou *et al.*[202] who reported that electrostatic interactions between the terminal groups can effectively tune twisted ribbon morphology into flat one. Lee and Na,[203] using computational methods, evidenced that TTR(105-115) capped by (i) Ac- and -NH_2 groups at its termini are characterized by a twisted and ordered fibrillar morphology, whereas (ii) its uncapped variant possesses a twisted fibrillar morphology with disordered terminal regions. The authors evidenced that the end-capping dictates the number of hydrogen bonds and electrostatic interactions, thus stabilizing the TTR(105-115) fibrils. Their results are consistent with the MD simulations reported by Porrini *et al*.[204] for TTR(105-115) oligomers.

Another possible modification of peptides' N-terminus constitutes *N*-α-methylation, which may involve mono-, di-, or trimethylation.[205-206] Hughes and colleagues[207] investigated *N*-methylated derivatives of Aβ(25-35). Among six variants, only one, with *N*-α-methyl-amino group at the N-terminus led to the formation of fibrils similar to those of Aβ(25-35). To date, to the best of my knowledge, peptides capped with *N*,*N*-dimethyl-α-amino (DiMe-) group at the N-terminus have not been investigated in terms of the influence of the DiMe-group on the morphology and the secondary structure of the resulting aggregates.

To better understand the role of peptides' terminal groups on the morphology and the secondary structure of the resulting supramolecular aggregates, I decided to further investigate the TTR(105-115) fragment. I studied peptide fragments termed at the N-terminus with H-, Ac-, or DiMe-groups, and at the C-terminus with: -NH_2 or -OH groups. I extended the studies on quasi-racemic mixtures obtained by mixing in 1/1 molar ratio all synthesized *L*-enantiomers with the *D* one (functionalized with H- and -NH_2 groups). I characterized the morphology of all enantiopure and quasi-racemic mixtures using AFM and the secondary structure using the ATR-FTIR spectroscopy approach. To better understand the correlation between the morphology and the secondary structure, MD simulations were performed.

6.2 Additional information and contributions

Results discussed within this chapter are published in **Grelich-Mucha, M.**; Bachelart, T.; Torbeev, V.; Ożga, K.; Berlicki, Ł.; Olesiak-Bańska, J., *Amyloid engineering – how terminal*

capping modifies morphology and secondary structure of supramolecular peptide aggregates. Biomaterials Science 2024, 12 (6), 1590-1602.

I synthesized the TTR(105-115) peptides functionalized with various groups at their ends. I synthesized the DiMe-variant with the help of Dr. T. Bachelart. I performed the syntheses during my internship supported by the foreign mobility part of the InterDocSchool project implemented under the Polish National Agency for Academic Exchange (NAWA) STER program. MD simulations were performed by Dr. K. Ożga and Prof. Ł. Berlicki (using GROMACS software available at the Wrocław Centre for Networking and Supercomputing (WCSS, Wrocław, Poland). The preliminary ATR-FTIR data were acquired thanks to Dr. Youssef El Khoury and Prof. Petra Hellwig from Université de Strasbourg.

6.3 Materials and methods

Synthesis of peptides. The peptides were synthesized using the Liberty Blue automated microwave peptide synthesizer. The peptides termed at the C-terminus by (i) amide group were prepared using Fmoc-Rink Amide AM resin (100–200 mesh, 0.74 mmol/g, 1% DVB), and by (ii) carboxyl group using a Wang resin preloaded with *L*-serine, namely Fmoc-*L*-Ser(t-Bu)-Wang resin (100–200 mesh, 0.7 mmol/g). To perform acetylation of the N-terminus, after the final deprotection of the Fmoc group, the following procedure was used. The reaction vessel was filled with *N*,*N*-diisopropylethylamine (DIEA) (200 µL), acetic anhydride (200 µL), and DMF (1.4 mL). The procedure was performed 2 times for 6 minutes each. Ninhydrin test was chosen to verify the absence of the α-amino group at the N-terminus. Dimethylation of the N-terminus was performed based on protocols adapted from refs.[208-210] To do so, the purified peptides termed at the N-terminus by α-amino group were dissolved in sodium acetate (0.1 M, pH~4) at a concentration of 1 mg/mL. The mass of the peptide was verified using LC-MS. Then, 37% aq. solution of formaldehyde (1000 eq.) and sodium cyanoborohydride (30 eq., 0.2 M in water) were added to the dissolved peptide (**Figure 39**). After a brief mixing, the mass of the peptide was verified using LC-MS, and the demethylated fractions were purified using a semi-preparative RP-HPLC.

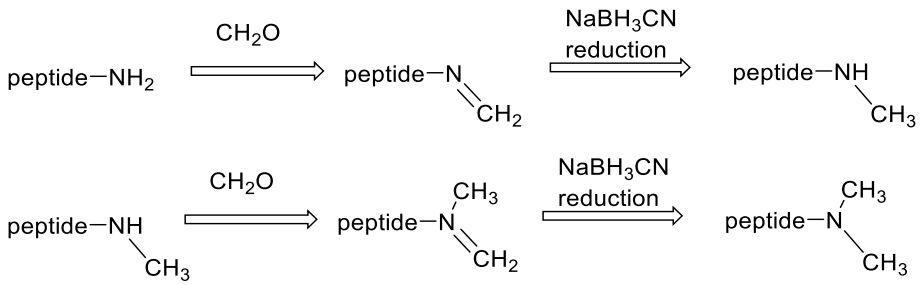

Figure 39. Chemical steps to obtain *N,N*-dimethyl-α-amino group at peptide's N-terminus.[197] The images were reprinted with permission.

Preparation of the samples. To enable dissolution of the peptides in an aqueous solution, they were first dissolved in dimethyl sulfoxide (DMSO). Then, a solution of acetonitrile/HCl at pH 1.5 (1/9, *v/v*) was added. The final content of DMSO was 2% (*v/v*), and the final concentration of the peptides was 1 mM. The quasi-racemic mixtures were prepared by mixing the *D*-enantiopure sample of 105-115 TTR fragment (termed with H- and -NH_2 groups) with each of the synthesized *L*-enantiopure samples in (1/1) molar ratio. The samples were incubated in an Eppendorf Thermomixer C at 37 °C for 3 weeks.

Morphology analysis. The morphology of the samples was analyzed before (t_0) and after incubation (t_1) period. For the AFM imaging, the samples were diluted (or not) to a desired concentration enabling analysis of the morphology. Information on samples' concentration is given in the description of the AFM images included in the following chapter. 30 µL aliquots of each sample was deposited on mica, and after 30 minutes of the adsorption period, the samples were dried.

Spectroscopic studies. For extinction spectra measurements the samples were diluted to a concentration of 166 µM.

Molecular Dynamics Simulations. The stability of the models was examined for 100 ns-long simulations, using GROMACS software and Amber03 force field.

6.4 Results and discussion

I synthesized 105-115 fragments of TTR termed by different functional groups at their N- and C-termini (**Table 4**) *via* SPPS. Namely, at the N-terminus (i) H-, (ii) *N*-acetyl-α-amino (Ac-), or (iii) *N*,*N*-dimethyl-α-amino (DiMe-), whereas at the C-terminus either (i) -NH_2 or (ii) carboxyl (-OH) groups were present. To confirm the composition of the investigated peptides, I recorded ESI-MS (**Figure 40a**). Then, to verify their purity, I recorded analytical RP-HPLC spectra which evidenced high purity of the peptides (>98%) (**Figure 40b**). The ESI-MS spectra revealed not only the presence of $M+H^+$ species, but also of $4M+3H^+$ and $3M+2H^+$ ones (*i.e.* ion clusters). I recorded absorption spectra of the peptides (**Figure 41**) and then, prepared quasi-racemic mixtures by mixing in 1/1 molar ratio of the synthesized *L*-enantiomers with the *D* enantiomer (**Table 4**).

Table 4. 105-115 fragments of TTR termed by the varying functional groups at their N- and C-termini. At the N-terminus, the peptides possess α-amino (H-), *N*-acetyl-α-amino (Ac-) or *N,N*-dimethyl-α-amino (DiMe-) group, and at the C-terminus amide (-NH_2) or carboxyl (-OH) group.[197] The table was adapted with permission.

Name	Composition	Modification at N-terminus	Modification at C-terminus	Amyloid fibrils
Enantiomerically pure peptides				
H-TTR-NH_2	H-*L*-TTR-NH_2	α-amino group	amide group	+
H-TTR-OH	H-*L*-TTR-OH	α-amino group	carboxyl group	+ (slow)
D	H-*D*-TTR-NH_2	α-amino group	amide group	+
Ac-TTR-NH_2	Ac-*L*-TTR-NH_2	*N*-acetyl-α-amino group	amide group	+
Ac-TTR-OH	Ac-*L*-TTR-OH	*N*-acetyl-α-amino group	carboxyl group	+ (slow)
DiMe-TTR-NH_2	DiMe-*L*-TTR-NH_2	*N,N*-dimethyl-α-amino group	amide group	-
DiMe-TTR-OH	DiMe-*L*-TTR-OH	*N,N*-dimethyl-α-amino group	carboxyl group	-
Peptide quasi-racemic mixtures				
***D* + H-TTR-NH_2**	H-*D*-TTR-NH_2 and H-*L*-TTR-NH_2	α-amino group	amide group	+
***D* + H-TTR-OH**	H-*D*-TTR-NH_2 and H-*L*-TTR-OH	α-amino group	amide group and carboxyl group	+
***D* + Ac-TTR-NH_2**	H-*D*-TTR-NH_2 and Ac-*L*-TTR-NH_2	α-amino group and *N*-acetyl-α-amino group	amide group	+
***D* + Ac-TTR-OH**	H-*D*-TTR-NH_2 and Ac-*L*-TTR-OH	α-amino group and *N*-acetyl-α-amino group	amide group and carboxyl group	+
***D* + DiMe-TTR-NH_2**	H-*D*-TTR-NH_2 and DiMe-*L*-TTR-NH_2	α-amino group and *N,N*-dimethyl-α-amino group	amide group	+
***D* + DiMe-TTR-OH**	H-*D*-TTR-NH_2 and DiMe-*L*-TTR-OH	α-amino group and *N,N*-dimethyl-α-amino group	amide group and carboxyl group	+

a)

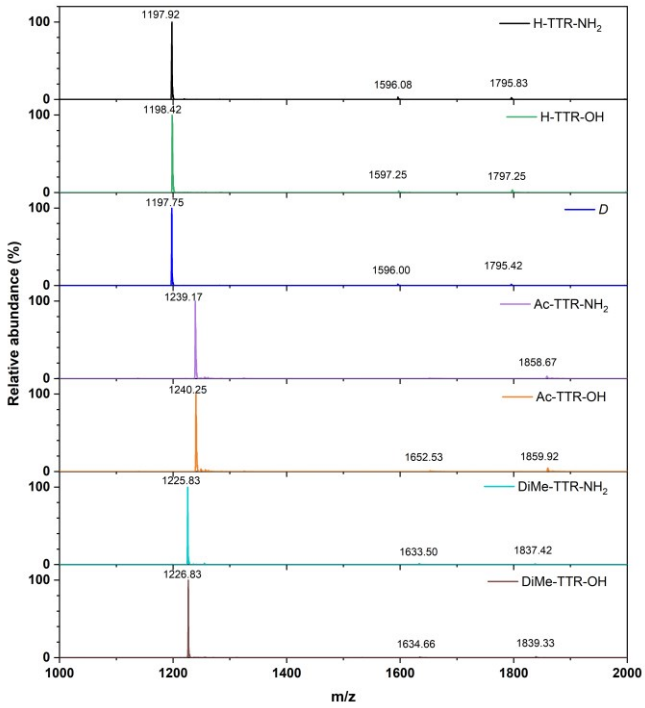

b)

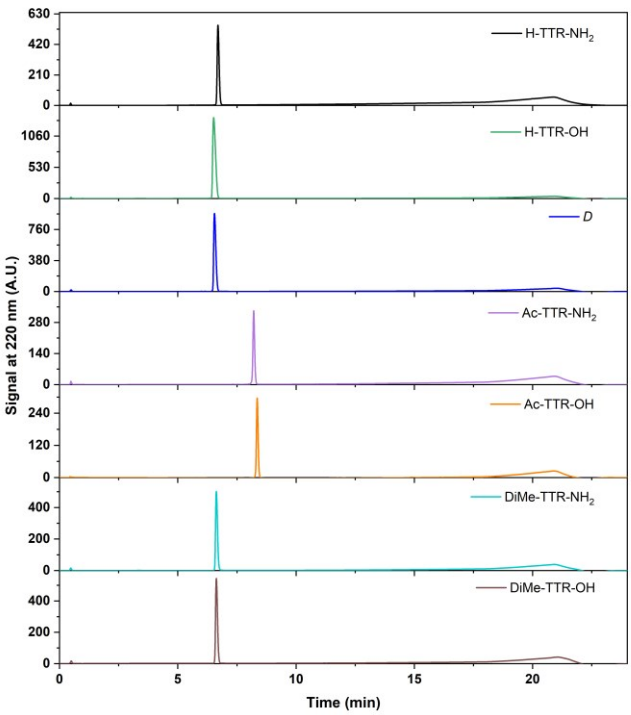

Figure 40. ESI-MS spectra (a) and analytical RP-HPLC traces (b) of H-TTR-NH_2 (black), H-TTR-OH (green), *D* (blue), Ac-TTR-NH_2 (lilac), Ac-TTR-OH (orange), DiMe-TTR-NH_2 (turquoise), and DiMe-TTR-OH (brown) peptides.[197] The images were adapted with permission.

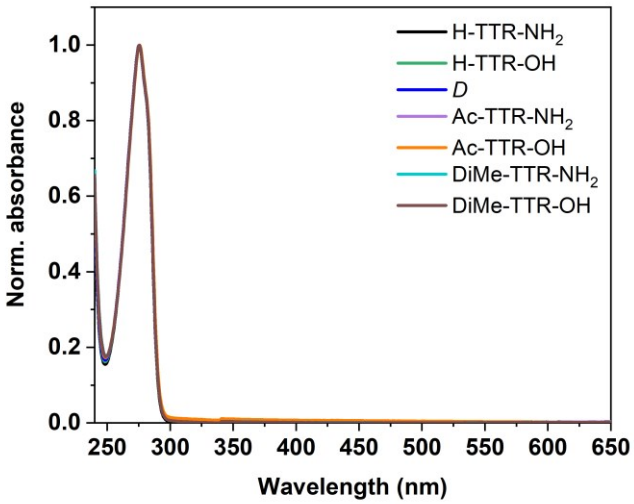

Figure 41. Absorption spectra recorded for H-TTR-NH_2 (black), H-TTR-OH (green), *D* (blue), Ac-TTR-NH_2 (lilac), Ac-TTR-OH (orange), DiMe-TTR-NH_2 (turquoise), and DiMe-TTR-OH (brown) peptides.[197] The image was adapted with permission.

After 3 weeks of incubation, indicated as t_1, I investigated the samples using AFM (**Figure 42**) and noticed differences in their morphology. Namely, the incubation of peptides termed by the **H-group** at the N-terminus resulted in fibrils with **twisted morphology**, regardless of the functional group at the C-terminus (**Figure 42a-c**). Interestingly, these fibrils differed in **handedness which depends on the chirality** of the constituent peptides, as (i) *L*-enantiopure fibrils, H-TTR-NH_2 and H-TTR-OH, are right-handed, and (ii) *D*-enantiopure fibrils are left-handed. These observations are in agreement with the ones described in Chapter 5. Autofluorescence of amyloids determined by enantiomeric composition of peptides. I also performed the morphology analysis (**Table 5**, **Figure 43**) which revealed that the average width, height, and cross-over distance for fibrils obtained from:

(i) H-TTR-NH_2 were equal to 22.1 ± 2.7 nm, 11.7 ± 2.4 nm, and 98.0 ± 6.5 nm;

(ii) H-TTR-OH were equal to 22.2 ± 3.9 nm, 8.5 ± 2.7 nm, and 104.4 ± 11.7 nm;

(iii) *D* were equal to 23.3 ± 2.8 nm, 11.9 ± 2.7 nm, and 96.8 ± 6.9 nm, respectively.

Although the peptides with an α-amino group at the N-terminus possess a twisted morphology, the presence of a carboxyl group at the C-terminus leads to the formation of fibrils that are slightly lower and have a longer cross-over distance as compared to their counterparts with an amide group at the C-terminus (**Table 5**).

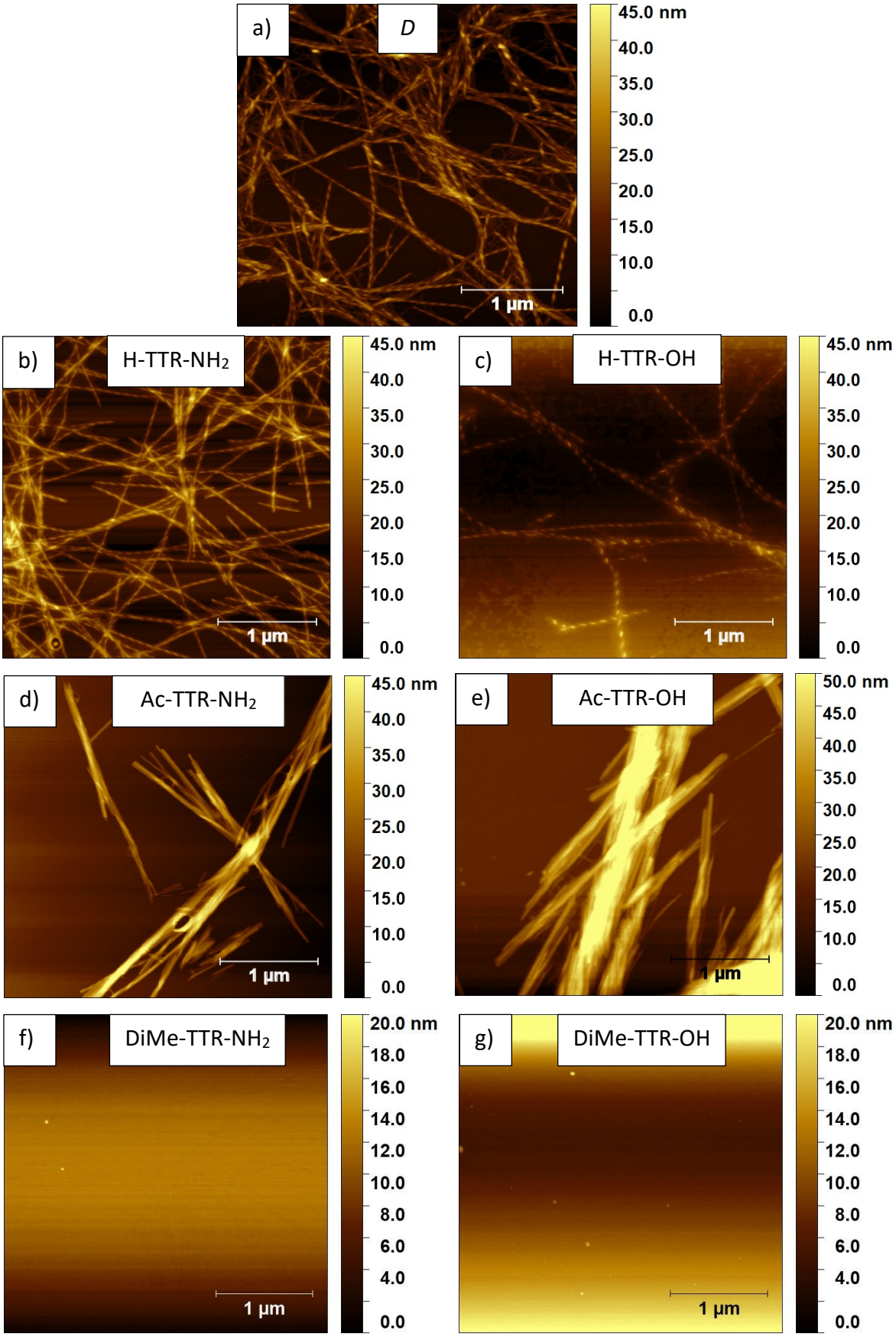

Figure 42. Morphology of peptide aggregates formed at t_1: *D* (a), H-TTR-NH_2 (b), H-TTR-OH (c), Ac-TTR-NH_2 (d), Ac-TTR-OH (e), DiMe-TTR-NH_2 (f), and DiMe-TTR-OH (g). The samples were not diluted for the AFM imaging.[197] The images were adapted with permission.

Table 5. Average width (nm), height (nm), and cross-over distance (nm) of fibrils formed after the incubation of *L*-enantiomers termed by different functional groups at their N- and C-termini, as well as of their quasi-racemic mixtures.[197] The table was adapted with permission.

Sample	Width (nm)	Height (nm)	Cross-over distance (nm)
H-TTR-NH_2	22.1 ± 2.7	11.7 ± 2.4	98.0 ± 6.5
H-TTR-OH	22.2 ± 3.9	8.5 ± 2.7	104.4 ± 11.7
D	23.3 ± 2.8	11.9 ± 2.7	96.8 ± 6.9
DiMe-TTR-NH_2	16.4 ± 2.5	2.5 ± 1.0	-
DiMe-TTR-OH	20.3 ± 8.0	3.6 ± 2.2	-
***D* + H-TTR-NH_2**	103.7 ± 39.8	5.3 ±1.3	-
***D* + H-TTR-OH**	18.0 ± 3.6	6.9 ± 1.7	-
***D* + Ac-TTR-NH_2**	104.6 ± 56.3	5.1 ± 1.3	-
***D* + Ac-TTR-OH**	21.8 ± 3.4	7.4 ± 1.4	-
***D* + DiMe-TTR-NH_2**	63.6 ± 33.5	7.5 ± 2.4	-
***D* + DiMe-TTR-OH**	17.0 ± 3.2	7.3 ± 1.3	-

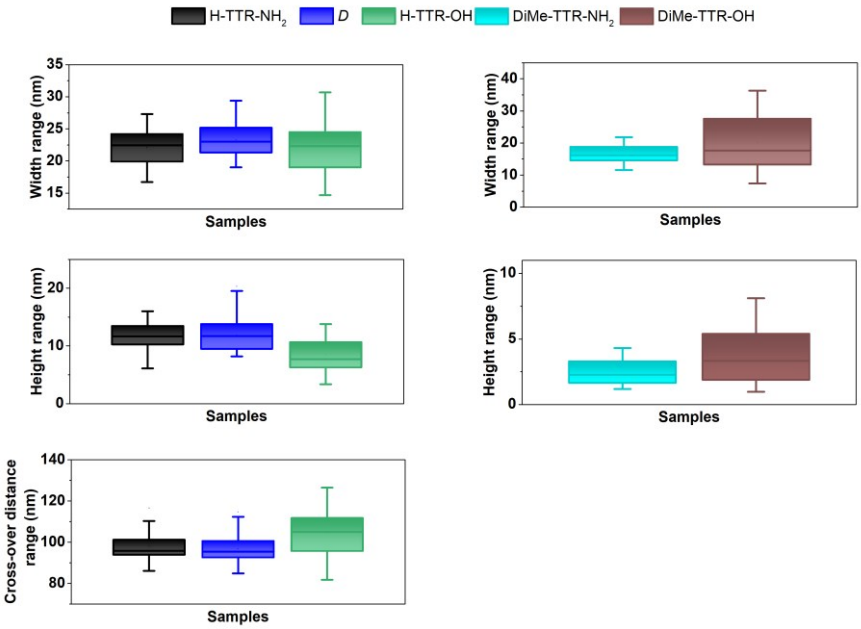

Figure 43. Box charts demonstrating width (nm), height (nm) and cross-over distance ranges (nm) of amyloid fibrils formed after incubation of the enantiopure peptides capped by (a) H-group and of peptide aggregates formed after incubation of (b) DiMe-group at the N-terminus.[197] The images were adapted with permission.

Incubation of peptides that possess **Ac-group** at the N-terminus favours the formation of **elongated fibrils** that stick together (**Figure 42d, e**). Thus, I could not estimate the average width or height of single fibrils. Interestingly, peptides capped by **DiMe-group did not lead to the formation of any amyloid fibrils**. AFM imaging revealed the presence of only **globular peptide aggregates** in these samples (**Figure 42f, g**). I estimated the average width and height of these aggregates which were equal:

(i) 16.4 ± 2.5 nm and 2.5 ± 1.0 nm for DiMe-TTR-NH_2;

(ii) 20.3 ± 8.0 nm and 3.6 ± 2.2 nm for DiMe-TTR-OH, respectively (**Table 5**).

I also studied the morphology of the samples just after their preparation, *i.e.* before incubation, which I defined as t_0. I noticed that at this time point, in the H-TTR-NH_2 (**Figure 44a**) and Ac-TTR-NH_2 (**Figure 44c**) samples some fibrillar structures were present unlike in

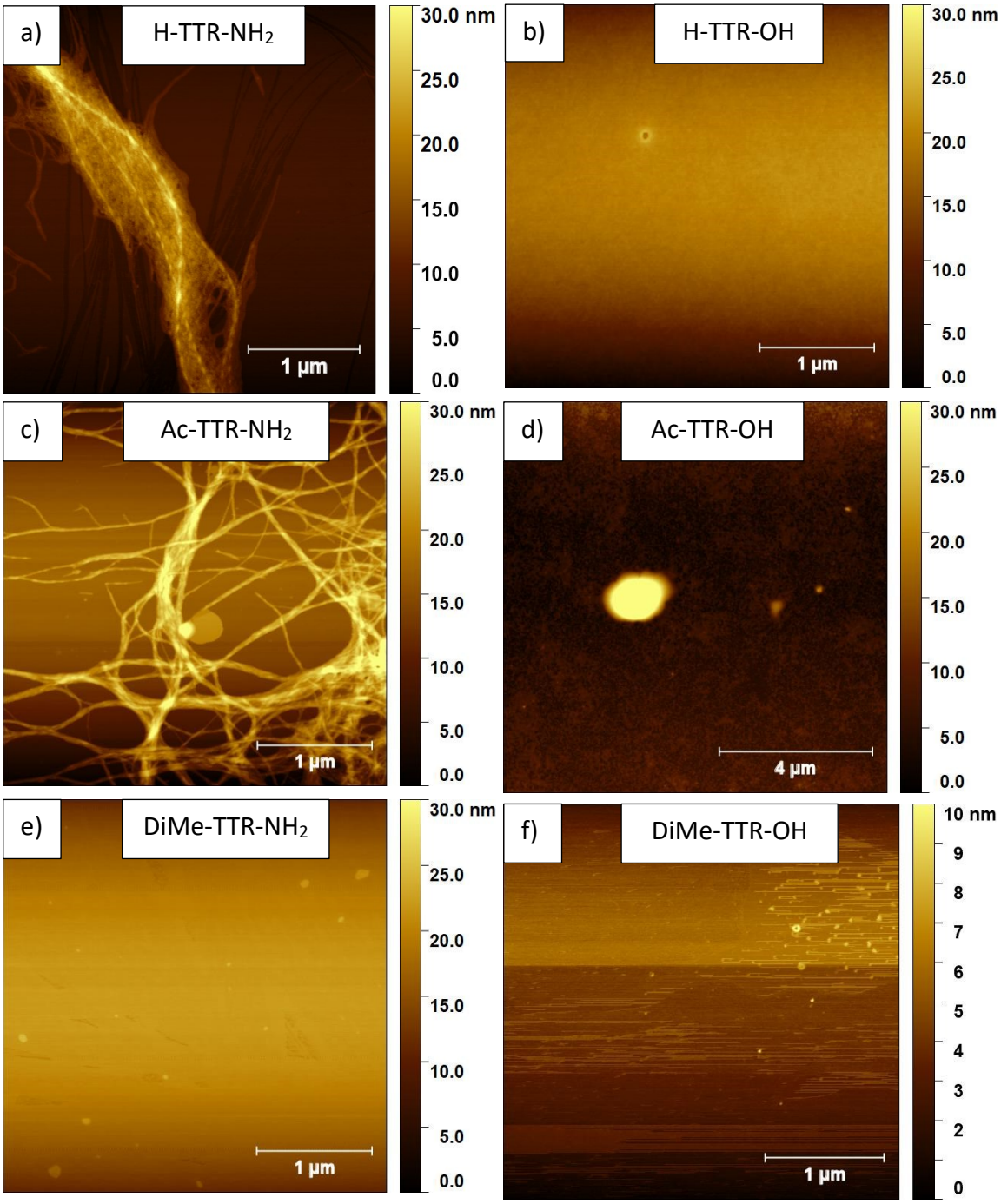

Figure 44. Morphology of peptide structures in enantiopure samples observed at t_0: H-TTR-NH_2 (a), H-TTR-OH (b), Ac-TTR-NH_2 (c), Ac-TTR-OH (d), DiMe-TTR-NH_2 (e), and DiMe-TTR-OH (f). For the AFM imaging the samples were not diluted.[197] The images were reprinted with permission.

their counterpart peptides functionalized with the -OH group at the C-terminus (**Figure 44b, d**). In the DiMe-TTR-NH_2 and DiMe-TTR-OH no fibrils were present at t_0 (**Figure 44e, f**).

Besides the enantiopure samples, I also examined the morphology of the quasi-racemic ones. Interestingly, at t_0 in all quasi-racemic mixtures I observed fibrillar structures (**Figure 45**) contrary to the enantiopure samples (**Figure 44**). The observation is in agreement with the one I discussed in the previous Chapter 5. Autofluorescence of amyloids determined by enantiomeric composition of peptides where I noticed faster fibril formation for *D* + H-TTR-NH_2 contrary to enantiopure *D* and H-TTR-NH_2. The accelerated fibril formation was described by other groups too.[211-213]

When the incubation was over, I examined the morphology of the quasi-racemic mixtures (**Figure 46**). I found amyloid fibrils in all samples, even in the *D* + DiMe-TTR-NH_2 (**Figure 46e**) and *D* + DiMe-TTR-OH (**Figure 46f**). As I illustrated above, in the enantiopure DiMe-TTR-NH_2 and DiMe-TTR-OH samples only globular aggregates were present at t_1 (**Figure 42f, g**). These results are comparable to those reported by Dutta *et al*.[211] who evidenced enhanced fibril formation in a racemic mixture compared to its counterpart enantiomers *L*- and *D*-Aβ(42). The authors confirmed suppression of oligomer formation in the racemic mixture which correlates with the kinetics profile devoid of the lag phase.[211]

Based on the AFM images, I noticed that the quasi-racemic fibrils **significantly differ** in terms of their **width which is correlated with the functional group at their C-terminus** (**Figure 46**). Namely, when the *D* is mixed with *L*-enantiomers possessing an -NH_2 group, the resulting quasi-racemic fibrils are wider than the counterpart ones in which the enantiomer *D* is mixed with the *L* capped by the -OH group (**Table 5, Figure 46, 47**). Additionally, in quasi-racemic mixtures in which *L*-peptides are capped by -NH_2 group, the fibrils possess a relatively large standard deviation of their width (**Table 5**). Accordingly, quasi-racemic fibrils had the following average widths:

(i) 103.7 ± 39.8 nm and 18.0 ± 3.6 nm, *D* + H-TTR-NH_2 and *D* + H-TTR-OH, respectively;
(ii) 104.6 ± 56.3 nm and 21.8 ± 3.4 nm, *D* + Ac-TTR-NH_2 and *D* + Ac-TTR-OH, respectively;
(iii) 63.6 ± 33.5 nm and 17.0 ± 3.2 nm, *D* + DiMe-TTR-NH_2 and *D* + DiMe-TTR-OH, respectively;

To demonstrate the width distribution among fibrils at t_1 for the quasi-racemic mixtures, I included **Figure 47**.

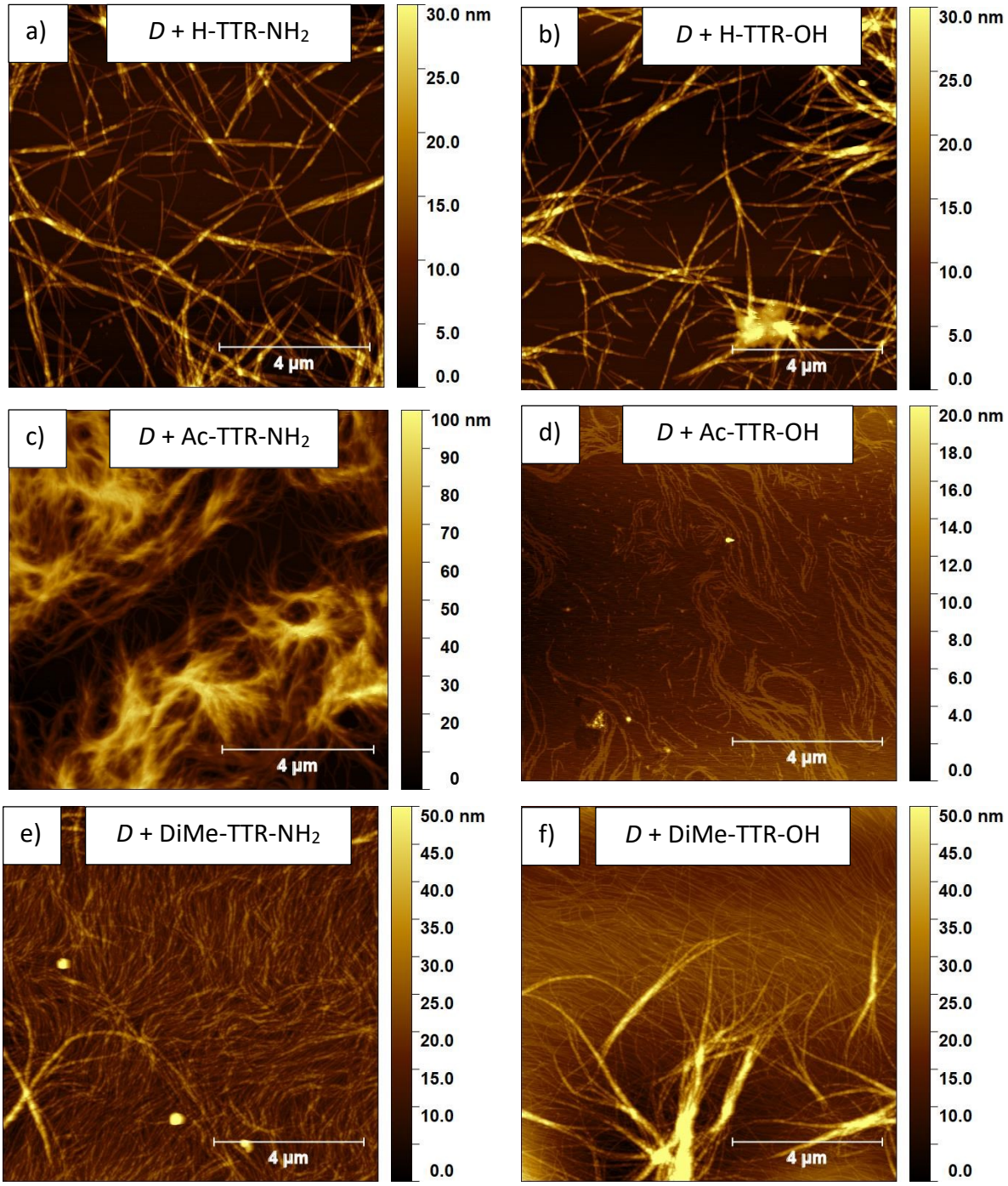

Figure 45. Morphology of fibrillar structures observed in quasi-racemic mixtures at t_0: *D* + H-TTR-NH_2 (a), *D* + H-TTR-OH (b), *D* + Ac-TTR-NH_2 (c), *D* + Ac-TTR-OH (d), *D* + DiMe-TTR-NH_2 (e), and *D* + DiMe-TTR-OH (f). For the AFM imaging the samples (a, b, e, f) were 10 times diluted; and the samples (c, d) were 1000 times diluted.[197] The images were reprinted with permission.

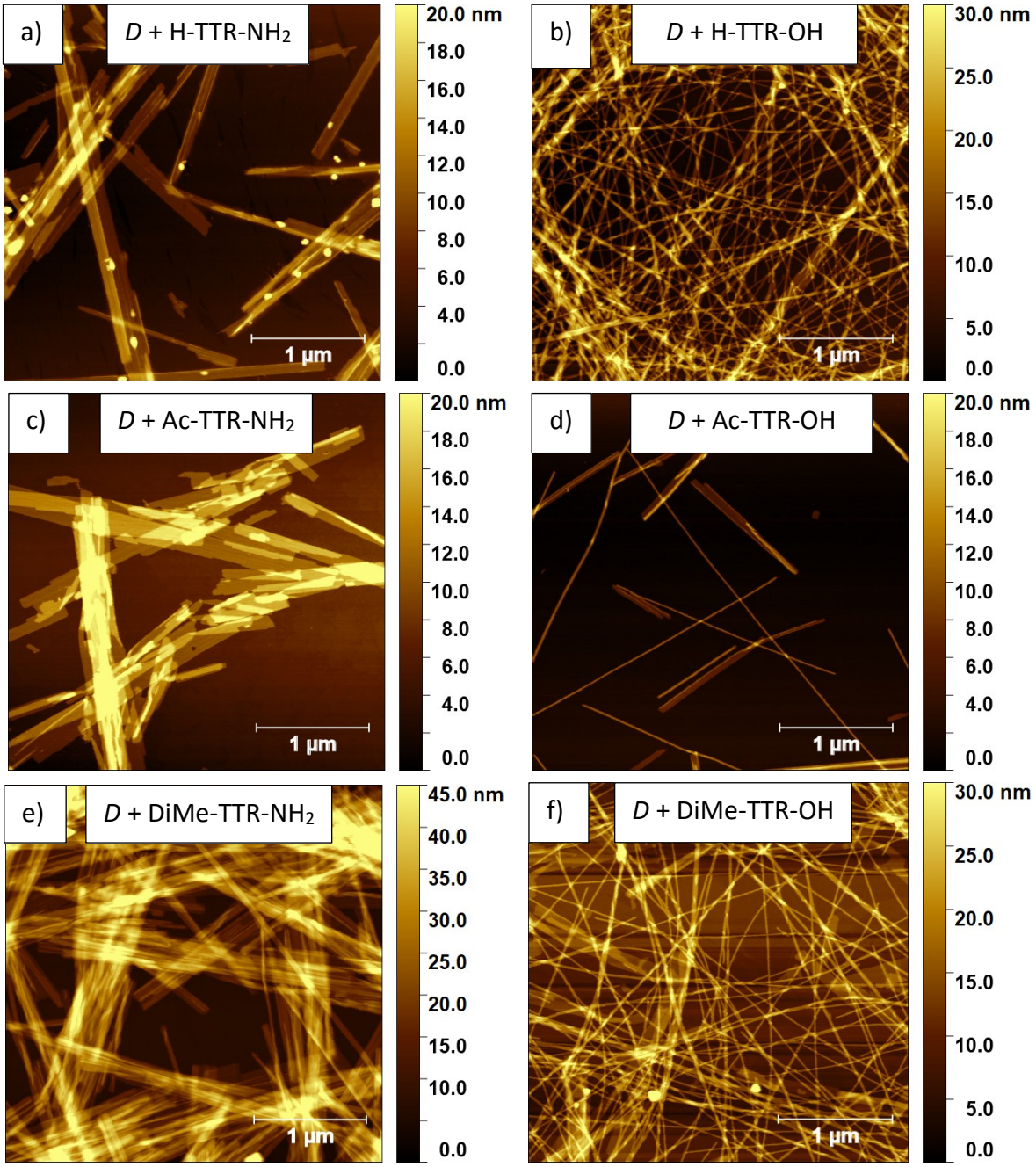

Figure 46. Morphology of fibrils in quasi-racemic mixtures at t_1: *D* + H-TTR-NH_2 (a), *D* + H-TTR-OH (b), *D* + Ac-TTR-NH_2 (c), *D* + Ac-TTR-OH (d), *D* + DiMe-TTR-NH_2 (e), and *D* + DiMe-TTR-OH (f). For the AFM imaging, the samples were diluted 10 times except for *D* + DiMe-TTR-NH_2 (e) which was not diluted.[197] The images were reprinted with permission.

I also analysed the average height values of the quasi-racemic fibrils (**Table 5**) which I estimated to be:

(i) 5.3 ± 1.3 nm and 6.9 ± 1.7 nm for *D* + H-TTR-NH_2 and *D* + H-TTR-OH, respectively;

(ii) 5.1 ± 1.3 nm and 7.4 ± 1.4 nm, for *D* + Ac-TTR-NH_2 and *D* + Ac-TTR-OH, respectively;

(iii) 7.5 ± 2.4 nm and 7.3 ± 1.3 nm for *D* + DiMe-TTR-NH_2 and *D* + DiMe-TTR-OH, respectively.

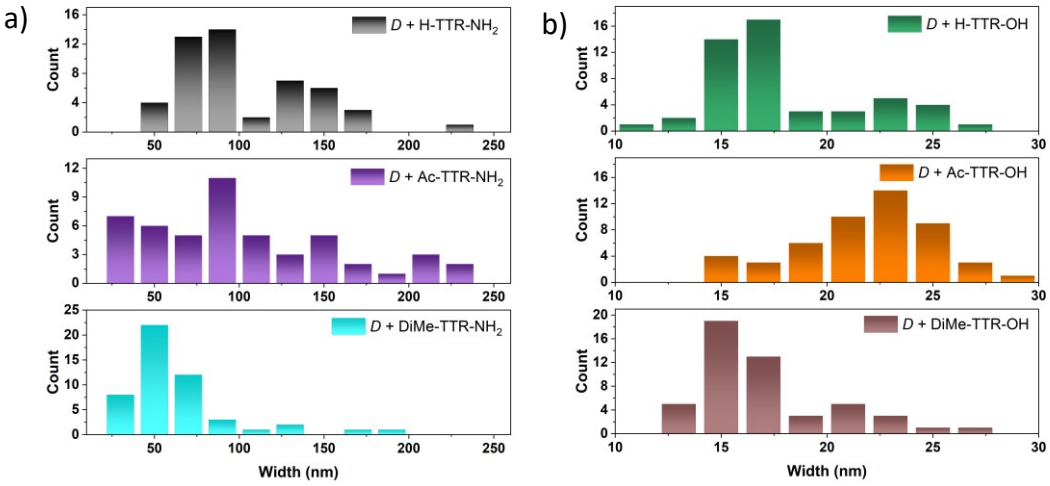

Figure 47. Distribution of the width dimensions among quasi-racemic fibrils obtained upon mixing of the *D* with *L*-enantiomers capped either by -NH_2 (a) or -OH (b) groups at the C-terminus. The dimensions were estimated for the quasi-racemic fibrils at t_1.[197] The images were adapted with permission.

Since the AFM imaging revealed significant differences between the enantiopure fibrils (**Figure 42**) and their counterpart quasi-racemic fibrils (**Figure 46**), I decided to correlate their morphology with their secondary structure. Thus, I recorded ATR-FTIR spectra for all samples at t_1 (**Figure 48**). In the case of the enantiopure samples, I could easily distinguish the characteristic band confirming the secondary β-sheet structure[214-215] for H-TTR-NH_2, *D*, Ac-TTR-NH_2, and Ac-TTR-OH, for which the maximum absorption peak was at ~1630 cm^{-1}, ~1630 cm^{-1}, ~1628 cm^{-1}, and ~1626 cm^{-1}, respectively (**Figure 48a, c**). These results are in agreement with the observed morphology, where amyloid fibrils were present (**Figure 42a, b, d, e**). As in the case of H-TTR-NH_2 and *D* discussed in Chapter 5. Autofluorescence of amyloids determined by enantiomeric composition of peptides, here the signal at ~1670 cm^{-1} also arises and contributes to α-helical structure, β-turns, or a combination of these structures.[195] The maximum absorption peak for DiMe-TTR-NH_2 and DiMe-TTR-OH is at ~1639 cm^{-1} (**Figure 48a, c**), which lies in the spectral location that can be attributed either to the β-sheet structure (1623-1641 cm^{-1}) or to disordered structure (1642-1657 cm^{-1}).[112] However, taking into account the spectral resolution of the measurements being 4 cm^{-1} and the concomitant morphology (**Figure 42f, g**), I establish that the AFT-FTIR signal corresponds to the disordered structure. In the case of enantiopure H-TTR-OH at t_1, the absorption peak is centred at ~1641 cm^{-1} which, similar to the DiMe-samples, could also be attributed to the β-sheet structure or the disordered structure. However, at t_1 in the sample amyloid fibrils were present (**Figure 42c**), which suggests that the peak corresponds to the β-sheet structure. To further evaluate my prediction, I imaged the H-TTR-OH sample after the next 4 weeks of incubation (*i.e.* after the total time of

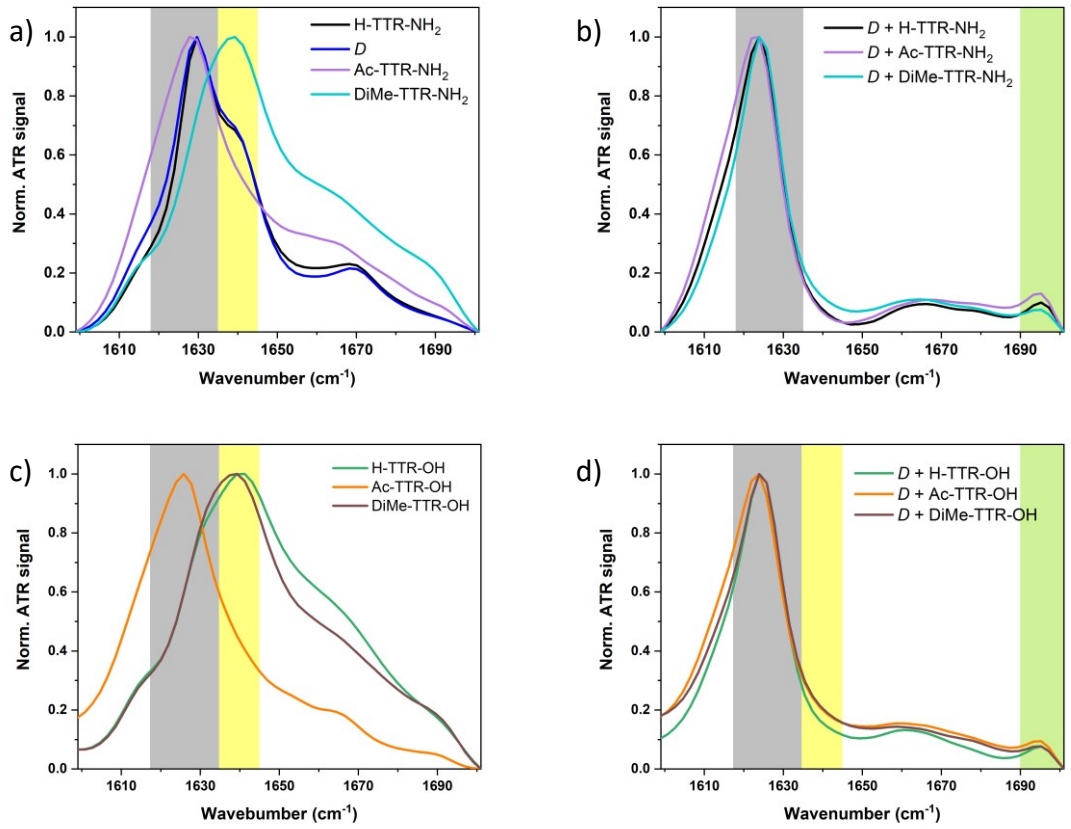

Figure 48. ATR-FTIR spectra of the studied TTR samples at t_1: H-TTR-NH_2, *D*, Ac-TTR-NH_2, DiMe-TTR-NH_2 (a); *D* + H-TTR-NH_2, *D* + Ac-TTR-NH_2, *D* + DiMe-TTR-NH_2 (b); H-TTR-OH, Ac-TTR-OH, DiMe-TTR-OH (c); *D* + H-TTR-OH, *D* + Ac-TTR-OH, *D* + DiMe-TTR-OH (d).[197] The images were adapted with permission.

7 weeks of incubation which I denote as t_2). I noticed an increased number of amyloid fibrils (**Figure 49a**) at t_2 compared to t_1 (**Figure 42c**). I examined and compared the morphology of the H-TTR-OH fibrils at t_1 and t_2 (**Figure 49b**):

(i) The cross-over distance was equal to 104.4 ± 11.7 nm and 102.4 ± 10.8 nm at t_1 and t_2, respectively;

(ii) The average width was equal to 22.2 ± 3.9 nm and 21.5 ± 3.4 nm at t_1 and t_2, respectively;

(iii) The average height was equal to 8.5 ± 2.7 nm and 9.2 ± 1.8 nm at t_1 and t_2, respectively.

These results demonstrate that over time, the dimensions (cross-over distance, width, height) of the H-TTR-OH fibrils do not significantly change, only the number of fibrils increases. To verify if during this time any changes in the secondary structure components occur, I compared the ATR-FTIR spectra for the sample at t_1 and t_2 (**Figure 49c**). They demonstrate an increase in the β-sheet structure content at t_2 compared to t_1 which is in agreement with the observed increased number of amyloid fibrils. However, the most intense IR component at ~1641 cm^{-1} is still present which explains that the fibrils possess

mainly the disordered structure. This observation can be supported by the computational results reported by M. Lee and S. Na[203] who demonstrated that TTR(105-115) fibrils capped by α-amino and carboxyl group exhibit a twisted and disordered conformation. Additionally, it is often found that carboxyl termini in proteins are disordered.[199]

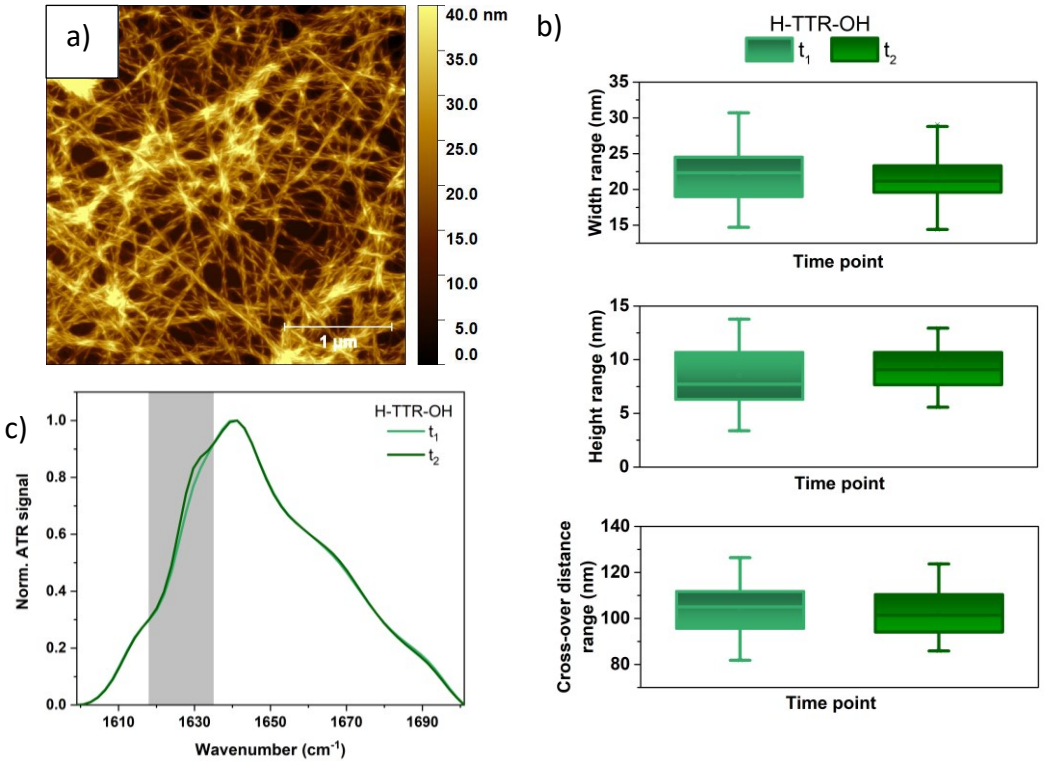

Figure 49. Morphology of enantiopure H-TTR-OH observed after 7 weeks of incubation (a). The scale bar in (a) is set to 1 µm. Box charts presenting width (nm), height (nm) and cross-over distance ranges (nm) calculated for H-TTR-OH fibrils at t_1 (green) and t_2 (dark green) (b). Normalized ATR-FTIR spectra of the H-TTR-OH sample after 3 (t_1) and 7 (t_2) weeks of incubation demonstrating an increase of the content of the β-sheet structure over time.[197] The images were adapted with permission.

Besides the enantiopure samples, I also examined the secondary structure components of the quasi-racemic mixtures (**Figure 48b, d**). The ATR-FTIR spectra unambiguously confirmed the presence of antiparallel β-sheet structure in all of the quasi-racemic samples, as they possess an intense IR signal centred at ~1624 cm^{-1} and a less intense one at ~1695 cm^{-1}.[110, 116] Among the samples, *D* + Ac-TTR-NH_2 has nearly the same signal intensity at 1622 cm^{-1} and 1624 cm^{-1} (**Figure 48b**). All quasi-racemic mixtures possess an absorption band at ~1660 cm^{-1} which corresponds to the presence of α-helical structure, disordered structure, β-turn, or a combination of them.[195, 216]

To understand the ability or disability of proper samples to form amyloid fibrils, MD simulations were performed. The formation of fibrils by H-TTR-NH_2, H-TTR-OH, *D*, Ac-TTR-NH_2, and Ac-TTR-OH (**Figure 42a-e**) can be explained by the molecular models of bilayers showing hydrogen bonds forming when proper capping groups are present (**Figure**

50). Namely, when the H-group is present at the N-terminus (in peptides H-TTR-NH_2, *D*, H-TTR-OH), an interlayer hydrogen bond forms between its hydrogen atom and the hydroxyl group oxygen atom of the serine side chain (**Figure 50a**). The Ac-group (in peptides Ac-TTR-NH_2 and Ac-TTR-OH) forms two hydrogen bonds: the amide oxygen atom may interact (i) with the hydroxyl group hydrogen atom of the serine side chain forming an interlayer hydrogen bond and (ii) within the layer with the amide group hydrogen of the

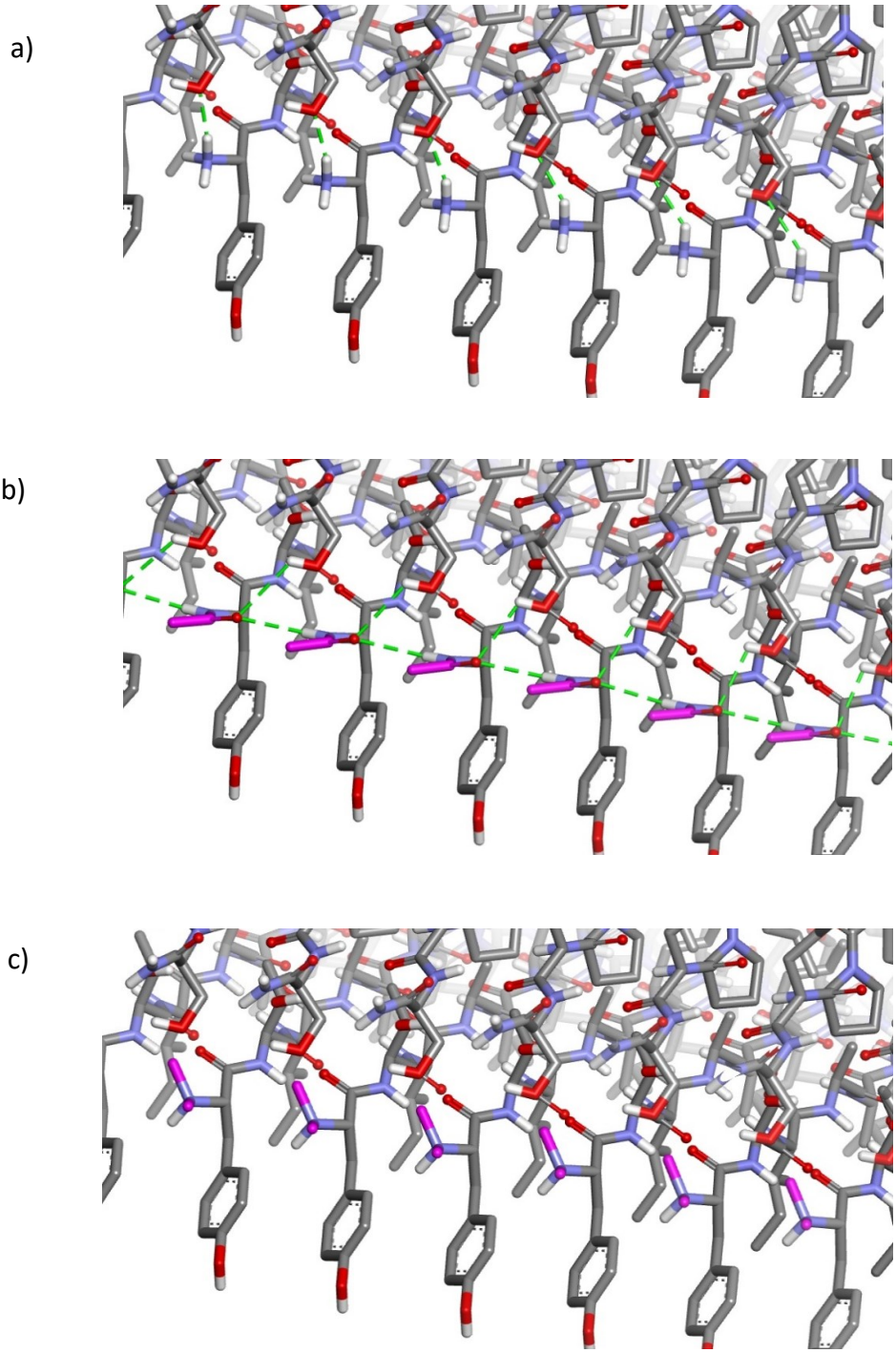

Figure 50. Molecular models of bilayers formed by H-TTR-NH_2 (a), Ac-TTR-NH_2 (b), and DiMe-TTR-NH_2 peptides (c) demonstrating their N-terminal groups. The Ac- (b) and DiMe-groups (c) are represented in magenta; hydrogen bonds are shown as green dotted lines.[197] The images were reprinted with permission.

neighbouring strand (**Figure 50b**). **Figure 50c** explains the disability of the DiMe-peptides in forming amyloid fibrils. Namely, the two methyl groups cause a steric hindrance and to lower it, the DiMe-groups of the neighbouring strands are rotated relative to each other which prevents most of the amine hydrogen atoms from forming a hydrogen bond with a hydroxyl group oxygen atom of the serine side chain (unlike in the peptides possessing a H-group at the N-terminus). In addition, as demonstrated in **Figure 51**, the -NH_2 group present at the C-terminus (in Ac-TTR-NH_2, and not H-TTR-NH_2), provides the formation of a stabilizing intralayer H-bond between the neighbouring strands, which may clarify the formation of longer fibrils.

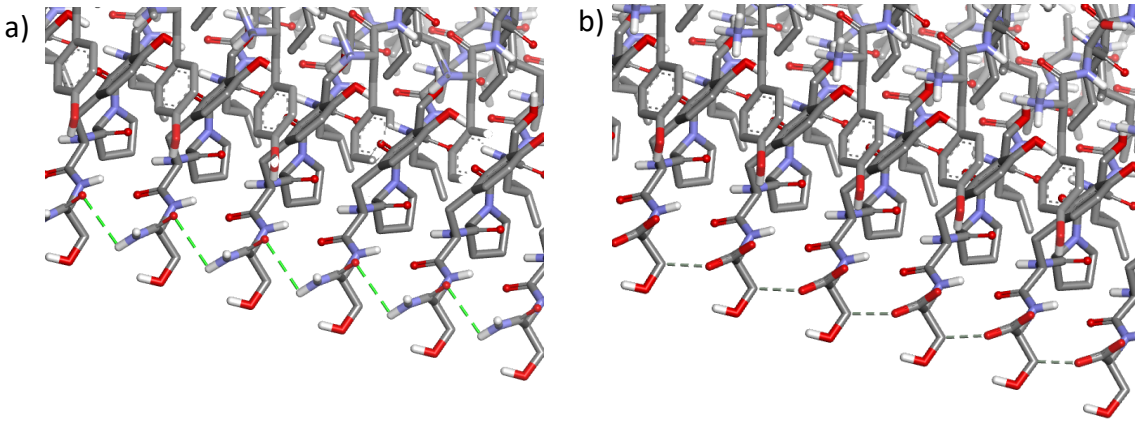

Figure 51. Molecular models of bilayers formed by H-TTR-NH_2 (a) and H-TTR-OH (b) demonstrating their C-termini. The conventional hydrogen bonds are indicated as green dotted lines, whereas the weak carbon-hydrogen bonds as grey dotted lines.[197] The images were reprinted with permission.

As I discussed in Chapter 5. Autofluorescence of amyloids determined by enantiomeric composition of peptides (**Figure 38a, b**), twist of the fibrils formed by the enantiopure samples results from the charge repulsion between the peptide termini, which is also demonstrated in **Figure 52a-c**. In the case of the examined samples, Ac-TTR-NH_2 fibrils (**Figure 52c**) possessing charge-neutralizing capping groups at both termini have the smallest twist. The lack of twist among the quasi-racemic fibrils (**Figure 52d**), results from the antiparallel alignment of the adjacent β-strands which minimizes the charge repulsion. This correlation is in agreement with the one discussed for the racemic mixture (*D* + H-TTR-NH_2) in Chapter 5 (**Figure 38c, d**). The MD simulations indicate that the rippled β-sheet structure is thermodynamically more favourable than the pleated one which is in agreement with the literature data.[179, 217-218]

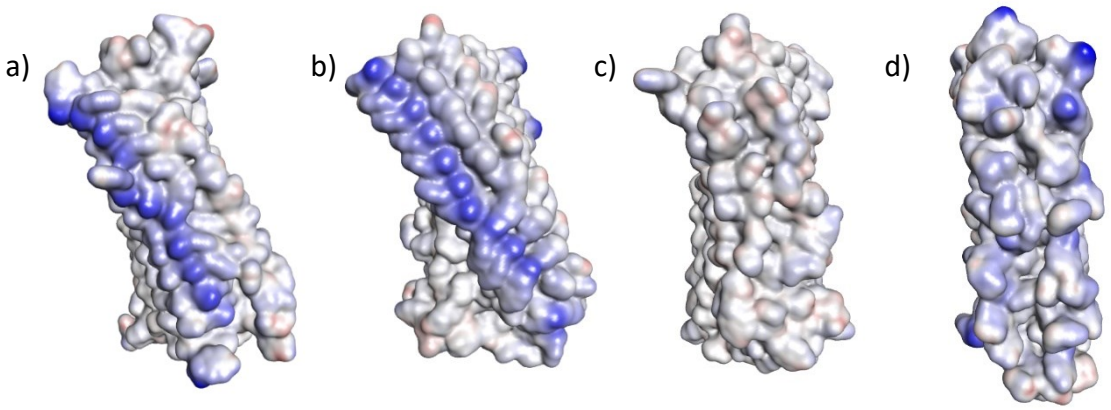

Figure 52. Representation of different twist formation by fibrils on the example of the H-TTR-NH_2 (a), H-TTR-OH (b), Ac-TTR-NH_2 (c), and *D* + H-TTR-OH (d) fibrils. The enantiopure fibrils are characterized by a different twist angle which arises from differences in the charge distribution at their termini arising from the parallel alignment of the β-sheets. The quasi-racemic fibrils lack the twist because the charge repulsion is balanced due to the antiparallel β-sheet structure.[197] The images were adapted with permission.

6.5 Conclusions

This chapter extends the previous one, where I investigated enantiomers and the racemic mixture of TTR(105-115) termed by H- and -NH_2 groups at their termini. Herein, I expand the research on the impact of different functional groups at peptide termini on the morphology and the secondary structure of the resulting supramolecular aggregates of TTR(105-115). I investigated peptides functionalized at their (i) N-terminus by H-, Ac- or DiMe-groups, and at their (ii) C-terminus by -NH_2 and -OH groups. The results indicate that the functional group at the N-terminus plays a key role in determining the morphology of the resulting supramolecular peptide structures. Namely, the H-group at the N-terminus determines the twisted morphology of the resulting fibrils. The Ac-group promotes the formation of elongated fibrils, which stick together, making it difficult to discern individual fibrils. The DiMe-group hampers the formation of amyloid fibrils and promotes the formation of peptide aggregates. The C-terminal group plays a minor role in the morphology but a major role in the kinetics of fibril formation. The studies I performed indicate that the -OH group at the C-terminus causes longer cross-over distances of twisted amyloid fibrils. The ATR-FTIR spectra revealed that in all enantiopure samples where amyloid fibrils were present, peaks corresponding to the parallel β-sheet structure were identified. In the case of H-TTR-OH fibrils, I also confirmed that. Nevertheless, the H-TTR-OH fibrils were mainly composed of a disordered structure, what was confirmed computationally in the literature as well.[203] Among the enantiopure samples, no fibrils were formed in the case of peptides capped with the DiMe-group. This observation is in

agreement with the corresponding ATR-FTIR spectra wherein I confirmed the predominance of a disordered structure. I observed significantly different morphologies in all quasi-racemic mixtures, where some fibrillar structures were formed directly after their preparation. After the incubation period, all quasi-racemic fibrils demonstrated a flat, tape-like morphology. The morphology analysis revealed that the quasi-racemic fibrils are wider when their constituting *L*-enantiomers are capped with the -NH_2 than with the -OH group. In all quasi-racemic fibrils an antiparallel β-sheet structure was identified.

The MD simulations helped to understand the correlation between the observed morphology and the secondary structure in target samples. The lack of fibrils among the DiMe-peptides is because the DiMe-groups hinder the formation of hydrogen bonds at peptides' ends. Additional hydrogen bonds between the capping groups provide the H- and Ac-groups, which explains the formation of fibrils among these samples. The MD simulations indicated that the twist angle among the enantiopure fibrils is linked with the charge repulsion between the adjacent β-strands organized in a parallel orientation.

Overall, the studies presented in this chapter demonstrate that the modulation of peptides' termini determines the final morphology and the secondary structure of the resulting supramolecular peptide aggregates. Such knowledge may be beneficial, *e.g.* in the design of nanostructures with a defined morphology. These nanostructures could further act as scaffolds for nanomaterials/biomaterials. This knowledge may also be helpful in the design of novel biomaterials with the desired morphology and functional properties to be applied in controlled cell growth, biosensors, or biomimetic catalysts.

7 Chapter 7. One- and two-photon excited autofluorescence of lysozyme amyloids

Although the autofluorescence phenomenon of amyloid structures has been mainly investigated in the 1P optical regime, the 2P autofluorescence properties, which raise the potential for in vivo studies, have been scarcely studied. Herein, I investigate the 1P and 2P intrinsic optical properties of hen egg-white lysozyme (HEWL). I examine the HEWL protein in the form of monomers and fibrils at varying concentrations of NaCl. Monomers exhibit autofluorescence, but upon fibrillation, the signal is enhanced. Additionally, the increasing NaCl content contributes to differences in fibrils' morphology and the increase of the secondary β-sheet structure content. This leads to the increase of 1P and 2P autofluorescence signals. What is interesting is that the 2P excited autofluorescence is red-shifted compared to the 1P autofluorescence. An explanation for the different relaxation pathways upon 1P or 2P excitation is provided by the detection of different lifetimes of the 1P and 2P fluorescence decays. In this chapter, I demonstrate that there is a correlation between the changes in optical properties of HEWL assemblies, driven by their morphology and their secondary structure.

7.1 Motivation

In subchapter 3.7 Optical properties – autofluorescence, I explained the possible origins of the autofluorescence phenomenon.[137-138, 140-141, 145, 147-149] Its appearance may also be also related, *e.g.* to aggregation-induced emission since the monomer-to-fibril formation may result in new inter- and intramolecular contacts, contributing to the increased fluorescence signal.[219-221] However, it has been reported that not only amyloid fibrils exhibit autofluorescence but also monomers. Niyangoda *et al*.[222] demonstrated that hen egg-white lysozyme (HEWL) fibrils possess enhanced autofluorescence compared to their monomeric counterparts. The authors claimed that the origin behind the autofluorescence are the carbonyl groups. Additionally, the multiple classical N-H···O=C hydrogen bonds and short contacts such as H-C···O=C, N-H···C=O, N-H···C-H, H-N···N-H, or H-N···O=C stabilizing proteins'/peptides' conformation provide extended electron delocalization, contributing to the visible fluorescence.[220] A concentration- and aggregation-induced emission was reported for bovine serum albumin (583 AAs, molecular weight (MW) ~66 kDa).[220] The concentration- and aggregation-induced fluorescence was also observed for human serum albumin (585 AAs, MW ~66.5 kDa).[223] Accordingly, the authors noticed that the intrinsic fluorescence signal arises in oligomers and increases upon forming fibrils.[223] In 3.8.3 Label-free imaging, I presented some of the research conducted

in terms of the NLO properties of amyloids.[171-174] However, in the literature there is still a deficit of information on this aspect. To the best of my knowledge, multiphoton excited autofluorescence of amyloids has not yet been investigated.

Considering the motifs mentioned above, I decided to investigate the 1P and 2P autofluorescence properties of amyloid fibrils. I have chosen HEWL for the experiments since it is a well-studied amyloidogenic model protein.[224-225] HEWL was incubated at varying NaCl concentrations, which provided fibrils with various morphologies. I characterized the morphology and the secondary structure of the investigated monomers and fibrils using AFM and ATR-FTIR spectroscopy approaches, respectively. Then, the 1P and 2P optical properties of the entities were examined. The obtained results evidence differences between 1P and 2P optical properties of HEWL entities, correlated with the morphology and the secondary structure of the studied assemblies.

7.2 Additional information and contributions

Results discussed within this chapter are published in **Grelich-Mucha, M.**; Lipok, M.; Różycka, M.; Samoć, M.; Olesiak-Bańska, J., *One- and Two-Photon Excited Autofluorescence of Lysozyme Amyloids*. The Journal of Physical Chemistry Letters 2022, 13 (21), 4673-4681.

M. Lipok calculated the $\sigma_{2,eff}$ values at selected wavelengths, measured and analysed 1P and 2P fluorescence decays, calculated FQY, and measured part of the 2P excited emission spectra. Dr. M. Różycka performed the Sedimentation Velocity Analytical Ultracentrifugation experiments and analysis.

7.3 Materials and methods

Preparation of the samples. Hen egg-white lysozyme (HEWL) was purchased from Sigma-Aldrich (L6876). HEWL (20 mg/mL; 1.4 mM) was dissolved in HCl (pH ~1.5) with varying concentrations of NaCl, namely 0 mM, 5 mM, and 50 mM. The samples were incubated in an Eppendorf Mixer C at 85 °C, for 18 h, with agitation set to 1400 rpm.

Morphology analysis. The morphology of the samples was investigated using an AFM. To do so, the samples were diluted to a concentration of 0.01 mg/mL. The droplets of the samples were deposited on mica layers and after 5 minutes of adsorption were rinsed with Milli-Q water and dried.

T-test. The two-sample t-test was calculated by using OriginPro 2016 software. The following assumptions were chosen: equal variance not assumed, the significance level set to 0.05.

Sedimentation Velocity Analytical Ultracentrifugation (SV AUC). The SV AUC experiments were conducted at 20 °C at 50 000 rpm by using a Beckman Coulter ProteomeLab XL-I analytical ultracentrifuge (Beckman Coulter Inc.) equipped with an AN-60Ti rotor and cells with 12 mm path-length charcoal-filled two-channel Epon center pieces. The experiment was carried out for three different concentrations of HEWL, namely 0.2 mg/mL, 2 mg/mL, and 20 mg/mL with varying salt content. For HEWL concentrations 0.2 mg/mL, 2 mg/mL, and 20 mg/mL the absorbance scans were collected at 280 nm, 300 nm, and 307 nm, respectively. The scans were time-corrected[226] and analysed in SEDFIT 16p36 (https://sedfitsedphat.nibib.nih.gov/) using a continuous size distribution c(s) model with a confidence level set on 0.68.[227-228] The partial specific volume, the theoretical molecular weight of HEWL, solution density and dynamic viscosity were estimated using SEDNTERP 3.0.3 (http://www.jphilo.mailway.com/).[229] The hydrodynamic dimensions were calculated using SEDFIT 16p36. The graphs were plotted in GUSSI 1.4.2 software.[230]

Spectroscopic studies. For the spectroscopic studies, the samples were not diluted. The absorption spectra were measured in the range 320−700 nm. Fluorescence excitation and emission spectra were measured at λ_{em} = 460 nm and λ_{exc} = 370 nm, respectively. The 2P excited fluorescence spectra were measured with a 2P microscope setup described before, equipped with a Chameleon Ti:sapphire laser (Coherent Inc.) with ∼100 fs pulses and a repetition rate equal to 80 MHz.[231] 2P excited fluorescence spectra of the samples and the reference were illuminated through a microscope objective (Nikon Plan Fluor, 40x, NA 0.75), and 2P excited fluorescence signals were collected in the epifluorescence mode. The 2P excited fluorescence spectra were measured with a Shamrock 303i spectrometer (Andor) equipped with an iDus camera (Andor).

Power dependence of fluorescence intensity. The measurements were performed to confirm a 2P origin of the autofluorescence signal excited with the fs-laser. The power exponent (*n*) was calculated according to the equation [14].

Two-photon brightness and two-photon absorption cross-section. The $\sigma_{2,\,eff}$ was calculated according to the equation [16]. 2P cross-sections for fluorescein at selected wavelengths were taken from Makarov *et al*.[16]

Fluorescence quantum yield. The FQY measurements were performed using the SC-30 Integrating Sphere Module for FS5 spectrofluorometer (Edinburgh Instruments). For the experiments, λ_{exc} was set to 360 nm.

Fluorescence lifetime measurements and calculations. 1P and 2P excited fluorescence decays were acquired using time-correlated single photon counting (TCSPC) setup (Becker&Hickl GmbH), containing an Acton SpectraPro SP-2300 monochromator (Princeton Instruments) and a high-speed hybrid detector HPM-100-50 (Becker&Hickl GmbH) combined with a DCC-100 card. BDL-375-SMN picosecond laser diode (20 MHz, λ_{exc} = 377 nm) was used as the excitation source. 1P excited fluorescence decays were measured at λ_{em} = 450 nm. To collect 2P excited fluorescence decays, the laser diode was replaced with the Chameleon:sapphire fs laser operating at a 20 MHz repetition rate achieved using a pulse picker (APE pulseSelect). 2P excited fluorescence decays were measured for λ_{exc} = 770 nm, and measured at λ_{em} = 470 nm and λ_{em} = 460 nm, for HEWL fibrils incubated at 0 mM and 50 mM NaCl, respectively. The fluorescence lifetimes were estimated as the average value from three decays for the target set of λ_{exc} and λ_{em}. The collected 1P and 2P fluorescence decays were fitted with triple- or double-exponential decay functions, respectively, using OriginPro software. Then, the average fluorescence lifetimes (τ_{av}) for every decay were calculated using the following equation:

$$\tau_{av} = \frac{\sum_{i=1}^{n} A_i \cdot \tau_i^2}{\sum_{i=1}^{n} A_i \cdot \tau_i} \quad [17]$$

where A_i – the weight of the contribution of the target fitted fluorescence lifetime (τ_i).

Correction of inner filter effect. Due to relatively concentrated samples, the inner filter effect was considered in the calculations. The corrected fluorescence (F_{cor}) intensity values were estimated according to the following equation:[232-233]

$$F_{cor} = F_{obs} \cdot 10^{\frac{A_{exc} + A_{em}}{2}} \quad [18]$$

where F_{cor} and F_{obs} are the corrected and the observed fluorescence intensities, respectively, and A_{exc} and A_{em} are absorbance values at excitation and emission wavelengths, respectively.

Then, the fluorescence enhancement coefficient $F_{enh,\,coeff}$ values were calculated for 1P and 2P processes according to the equation:

$$F_{enh,coeff} = \frac{F_{cor}}{F_{cor,1}} \quad [19]$$

where: $F_{cor,1}$ – corrected fluorescence intensity value calculated for monomers or fibrils incubated without NaCl.

7.4 Results and discussion

To obtain amyloid fibrils of a varying morphology, I incubated HEWL at different concentrations of NaCl: 0 mM, 5 mM, and 50 mM. After the incubation, *i.e.* at t_1, I analyzed the morphology of the samples using AFM (**Figure 53b, d, f**). I noticed that with the increase

of the salt content, the resulting fibrils have increased width (by ~0.7 nm) and height (by ~5.6 nm) dimensions (**Figure 53b, d, f, Table 6, Figure 54**). To further evaluate the differences in mean height and mean width among the possible HEWL samples, I performed a t-test. Although the mean heights do not differ significantly between HEWL fibrils incubated at 0 mM and 50 mM NaCl, the fibrils incubated (i) at 0 mM and 50 mM, (ii) 5mM and 50 mM are statistically different (**Table 7**). The t-test performed to verify

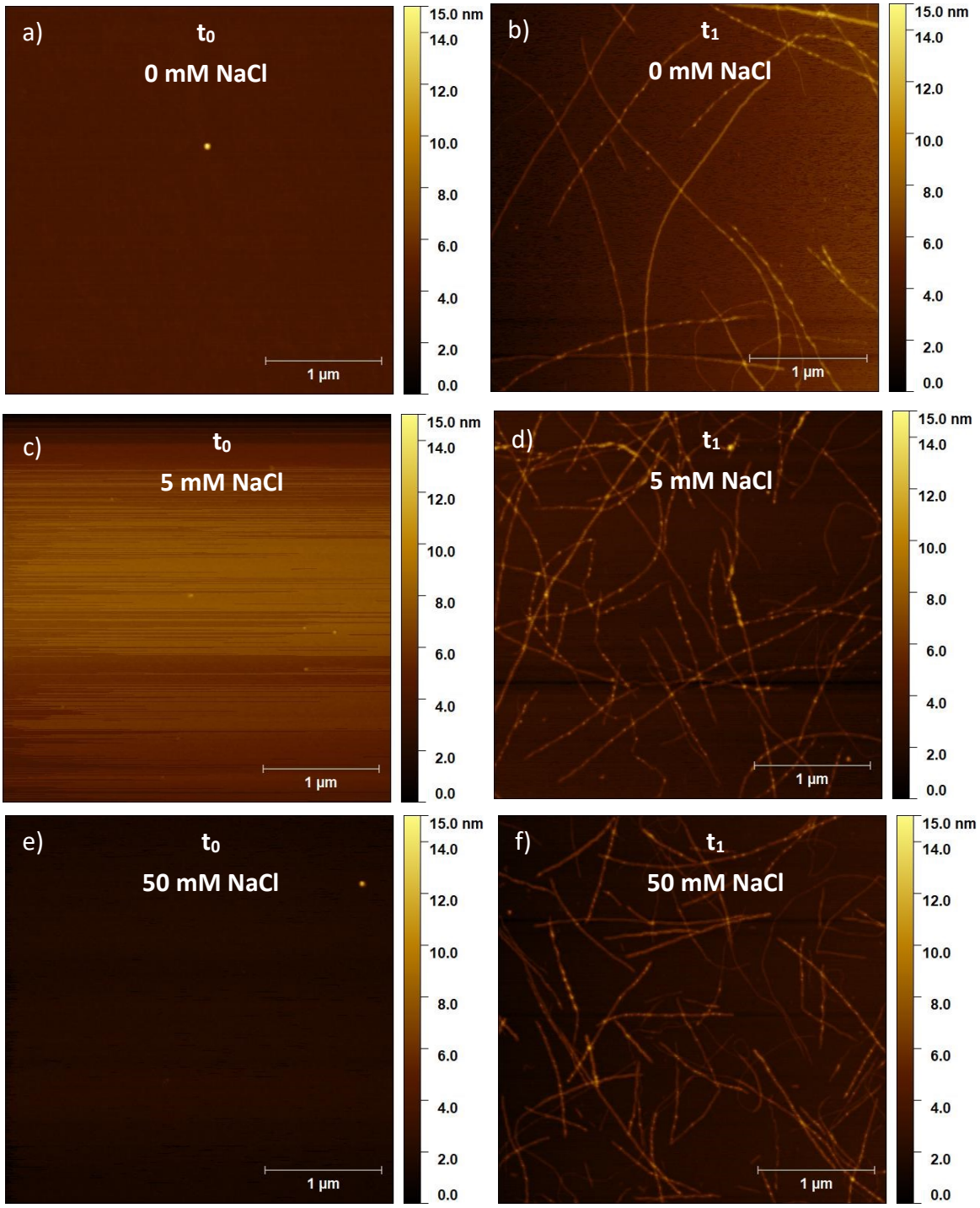

Figure 53. AFM images of HEWL samples at 0 mM (a, b), 5 mM (c, d), and 50 mM NaCl (e, f) before and after incubation, respectively.[234] The images were reproduced with permission.

differences in the mean width indicated significant differences between fibrils incubated at (i) 0 mM and 5 mM NaCl, (ii) 0 mM and 50 mM NaCl; however the differences between 5 mM and 50 mM NaCl were not significant. The t-tests evidence that the increase of NaCl concentration impacts the width and height dimensions of the resulting fibrils.

Table 6. Mean height (nm) and width (nm) of HEWL amyloid fibrils incubated at 0 mM, 5 mM, and 50 mM NaCl.[234] The table was adapted with permission.

Sample	Height (nm)	Width (nm)
0 mM NaCl	2.0 ± 0.7	18.1 ± 5.1
5 mM NaCl	2.2 ± 0.6	22.3 ± 4.4
50 mM NaCl	2.7 ± 1.1	23.7 ± 4.0

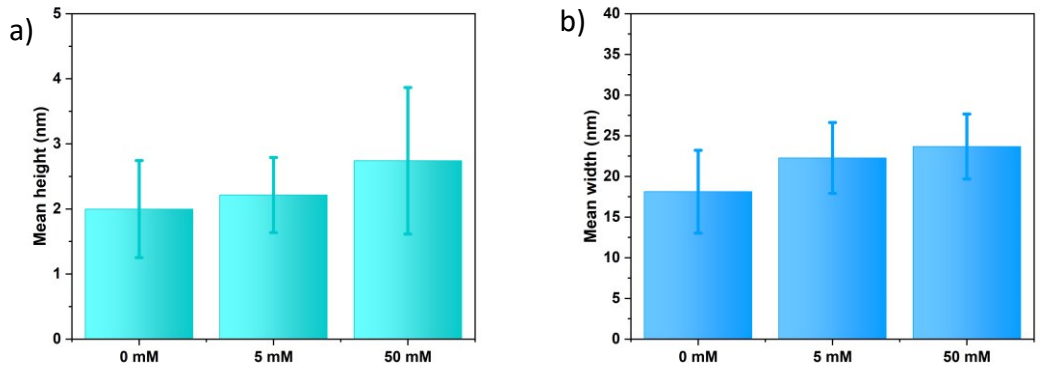

Figure 54. Mean height (nm) (a) and mean width (nm) (b) of HEWL fibrils incubated at the varying concentrations of NaCl: 0 mM, 5 mM, and 50 mM.[234] The images were adapted with permission.

Table 7. T-test statistics performed for the height among the possible groups of HEWL fibrils including the samples incubated at (i) 0 mM and 5 mM NaCl, (ii) 0 mM and 50 mM NaCl, (iii) 5 mM and 50 mM NaCl.[234] The table was adapted with permission.

Group of samples	t Statistic	Prob>|t|
0 mM NaCl 5 mM NaCl	1.62048	0.10854
0 mM NaCl 50 mM NaCl	3.88849	1.99442E-4
5 mM NaCl 50 mM NaCl	2.94118	0.00438

The ionic strength also influenced other morphological parameters. In the absence of any salt, the resulting fibrils were long and flexible (**Figure 53b**). With the increase of the ionic strength, the fibrils became shorter (**Figure 53d, f**). As the isoelectric point of HEWL is

~10.7,[235] at the experimental conditions (pH ~1.5) the protein is positively charged and repulsive Coulombic interactions predominate between HEWL molecules. In addition, the increased ionic strength causes screening of electrostatic repulsion.[236-237] Thus, the effective repulsive forces become reduced. Indeed, the AFM images demonstrate that with the increase of NaCl content, fibrils tended to stick together (**Figure 53b, d, f**).

I also examined the morphology of the samples before the incubation, *i.e.* at t_0. I observed that at t_0 all samples possess a similar morphology. I noticed small aggregates present with a size ranging from ~25 nm to ~100 nm (**Figure 53a, c, e**). To evaluate if at t_0 HEWL monomers are present in the samples, sedimentation velocity analytical ultracentrifugation (SV AUC) analysis was acquired. According to the HEWL amino acid sequence and the information provided by the producer, the theoretical molecular weight (MW_{theor}) of HEWL was established to be 14.30 kDa. The SV AUC analysis revealed that at t_0 monomers predominate in all samples (**Table 8, Figure 55**). We noticed that with the increase of HEWL concentration, the frictional ratio (f/f_0) values increase (**Table 8**). This data suggests that the increasing HEWL concentration causes its conformational changes but preserves its monomeric state.

Table 8. Parameters established from the SV AUC experiments, namely s – sedimentation coefficient (S), $s_{20,w}$ (S) - sedimentation coefficient corrected for water at 20°C, f/f_0 - frictional ratio, R_s (nm) – Stokes radius, MW_{app} (kDa) - apparent molecular weight, MW_{theor} - theoretical molecular weight (kDa), RMSD - root mean square deviation.[234] The table was adapted with permission.

c (mg/mL)	NaCl (mM)	s (S)	$s_{20,w}$ (S)	f/f_0	R_S (nm)	MW_{app} (kDa)	% of signal	RMSD
0.2	0	1.826	1.828	1.241	1.98	14.39	99.79	0.00690
	5	1.816	1.823	1.251	2.00	14.50	99.85	0.00746
	50	1.782	1.803	1.252	1.99	14.28	99.92	0.00691
2.0	0	1.739	1.741	1.306	2.09	14.45	99.63	0.00879
	5	1.750	1.757	1.301	2.09	14.56	99.52	0.00764
	50	1.721	1.743	1.313	2.11	14.59	99.50	0.00857
20.0	0	1.209	1.214	1.859	2.96	14.28	95.50	0.01279
		4.320	4.336		5.60	96.44	3.463	
	5	1.209	1.213	1.869	2.99	14.39	96.46	0.01322
		4.435	4.452		5.72	101.13	2.383	
	50	1.395	1.412	1.600	2.55	14.31	98.91	0.01199
						MW_{theor} (kDa)		
						14.30		

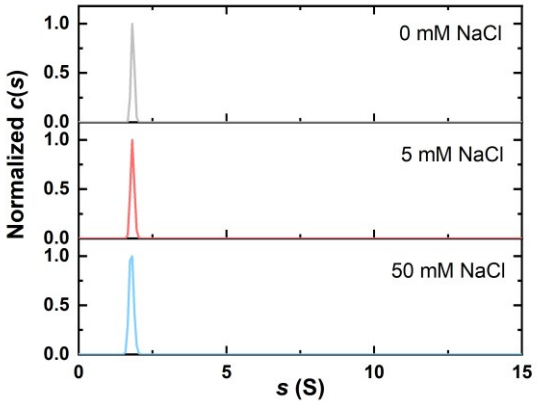

Figure 55. Normalized sedimentation coefficient distributions c(s) of the HEWL samples at 0.2 mg/mL at varying concentrations of NaCl, namely 0 mM (top panel), 5 mM (middle panel), and 50 mM (bottom panel).[234] The image was adapted with permission.

To gain information on the secondary structure of the investigated samples, I recorded their ATR-FTIR spectra (**Figure 56**). I noticed that all HEWL fibrils are characterized by the presence of the secondary β-sheet structure with the maximum absorption band localized at ~1629 cm^{-1}, ~1625 cm^{-1}, and ~1625 cm^{-1} in the case of fibrils incubated at 0 mM, 5 mM, and 50 mM NaCl, respectively (**Figure 56b**). Additionally, the normalized ATR-FTIR spectra evidence that with the increase of salt content among the HEWL fibrils, the β-sheet structure content is increasing, which is demonstrated by a white arrow in **Figure 56b**. The ATR-FTIR spectra demonstrate that the HEWL fibrils possess a relatively high content of α-helical structure. The corresponding absorption bands possess maximum positions at ~1649 cm^{-1}, ~1651 cm^{-1}, and ~1649 cm^{-1},[112] in the case of fibrils incubated at 0 mM, 5 mM, and 50 mM NaCl, respectively (**Figure 56b**). I also recorded ATR-FTIR spectra of the samples at t_0 and the spectra reveal the predominance of the α-helical structure which is consistent with data reported by Foley and colleagues.[238] The corresponding maximum absorption

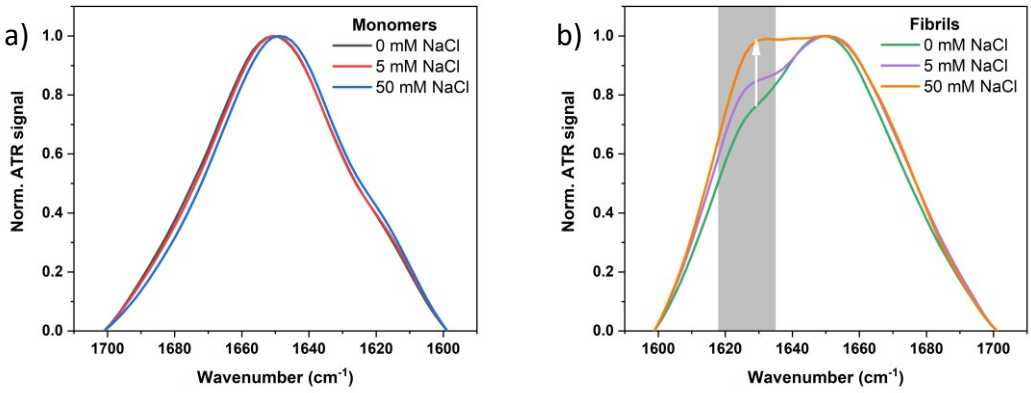

Figure 56. ATR-FTIR spectra of HEWL monomers (a) and fibrils (b) at the varying NaCl concentrations: HEWL monomers at 0 mM NaCl (black), 5 mM NaCl (red), and 50 mM NaCl (blue); HEWL fibrils at 0 mM NaCl (green), 5 mM NaCl (lilac), and 50 mM NaCl (orange).[234] The images were adapted with permission.

bands are positioned at ~1651 cm^{-1}, ~1651 cm^{-1}, and ~1649 cm^{-1}, for the HEWL samples containing 0 mM, 5 mM, and 50 mM NaCl, respectively (**Figure 56a**).

Having analyzed the morphology and the secondary structure of target HEWL entities, I decided to investigate their optical properties, starting in the 1P optical regime. The absorption spectra of HEWL samples were characterized by an increase in the absorbance in the 320-410 nm range and a broad tail extending towards longer wavelengths (**Figure 57a**). These absorption spectra are consistent with the ones reported by Ansari and colleagues.[239] They suggested that such absorption spectra originate from charge-transfer transitions and can be utilized to track protein aggregation. The observed protein charge-transfer spectra (ProCharTS) arise from interactions between charged residues including, *e.g.* $-NH_3^+$ in lysine or $-COO^-$ in glutamic acid.[134, 239] The significant increase in absorption-tail intensity can also be explained by considering the morphology (**Figure 53b, d, f**) and the corresponding ATR-FTIR spectra (**Figure 56b**). Namely, the ATR-FTIR spectra indicate that with the increase of salt content, the β-sheet content is increasing (**Figure 56b**). It suggests that the number of amyloid fibrils is increasing as well, which may explain the enhancing scattering in the spectra (**Figure 57a**) of HEWL fibrils while the concentration of NaCl is increasing. I measured excitation spectra at λ_{em} = 460 nm for HEWL monomers and fibrils (**Figure 57b**). HEWL fibrils had maximum positions at 373 nm, 376 nm, and 374 nm when incubated at 0 mM, 5 mM, and 50 mM NaCl, respectively. The measured signal was enhanced for fibrils compared to monomers. Moreover, the excitation spectra show that the excitation band responsible for HEWL fibrils autofluorescence (λ~370 nm) has a significantly higher intensity than the one associated with aromatic amino acids (λ~310 nm). To compare, in HEWL monomers the mentioned excitation bands have a similar intensity (**Figure 57b**). I also recorded emission spectra (λ_{exc} = 370 nm). I noticed that amyloid fibrils have a maximum emission peak at 451 nm, 450 nm, and 450 nm (**Figure 57c**), when incubated at 0 mM, 5 mM, and 50 mM NaCl, respectively, and that the intensity of the fluorescence signal is increasing with the increase of salt content. In the case of the monomeric state, all HEWL samples emitted with a maximum intensity peaked at 450 nm (**Figure 57c**). To examine the contribution of light scattering, I compared the normalized emission spectra of the HEWL fibrils at 2 mg/mL (*i.e.* 10-fold dilution) and the ones at 20 mg/mL, incubated at 5 mM NaCl (**Figure 57d**). The emission spectra for the HEWL fibrils overlapped regardless of HEWL concentration (**Figure 57d**). In addition, both emission and excitation spectra demonstrate that upon HEWL aggregation, the measured signal intensity increases ~5 times (**Figure 57b, c**). Further, FQY measurements were performed which revealed that HEWL fibrils are characterized by a higher FQY value than their counterpart monomers. Namely,

(i) at 0 mM NaCl, the FQY for HEWL monomers and fibrils was equal to 1.23% and 4.88%, respectively;

(ii) at 50 mM NaCl, the FQY for HEWL monomers and fibrils increased to 2.63% and 5.31%, respectively.

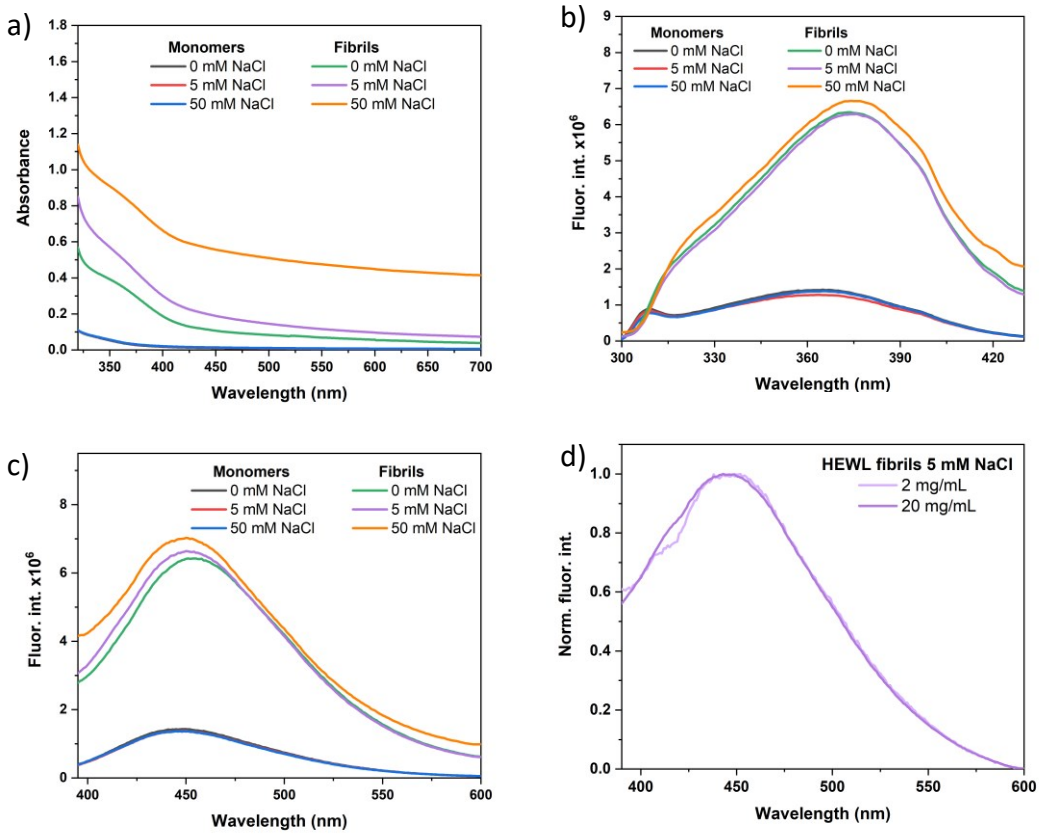

Figure 57. One-photon optical properties of HEWL monomers and fibrils at the varying NaCl concentration. Absorption spectra (a), fluorescence excitation spectra recorded at λ_{em} = 460 nm (b), fluorescence emission spectra recorded at λ_{exc} = 370 nm (c). HEWL monomers at 0 mM NaCl (black), 5 mM NaCl (red), and 50 mM NaCl (blue); HEWL fibrils at 0 mM NaCl (green), 5 mM NaCl (lilac), and 50 mM NaCl (orange). Emission spectra (λ_{exc} = 370 nm) recorded for HEWL fibrils at 2 mg/mL (light lilac) and 20 mg/mL (lilac) at 5 mM NaCl (d).[234] The images were adapted with permission.

As I mentioned in 3.8.3 Label-free imaging, there is insufficient information regarding the multi-photon (*i.e.* 2P, 3P, etc.) excited autofluorescence spectra of amyloid structures. Thus, I decided to measure multiphoton excited autofluorescence spectra of HEWL monomers and fibrils using an fs-laser excitation from 730 nm to 950 nm. The samples demonstrated the highest fluorescence intensity upon two-photon excitation at 750 nm (**Figure 58a**). Both monomers and fibrils emitted fluorescence with the same maximum position. However, monomers exhibited significantly weaker fluorescence signals than the corresponding fibrils, and the emission intensity was independent of NaCl content. In the case of fibrils, the resulting fluorescence signal was increasing with the increase of salt content. Thus, the most intense signal was recorded for amyloid fibrils incubated at 50 mM NaCl (**Figure 58a**). According to the equation [14], the exponent *n* was determined: we confirmed that the measured autofluorescence signal for both HEWL

amyloid fibrils and monomers was of 2P origin. The calculations were performed at λ_{exc} = 750 nm, leading to the following results:

(i) for fibrils incubated at 0 mM and 50 mM NaCl, the *n* was equal to 1.8 and 2.2, respectively.

(ii) for monomers at 0 mM and 50 mM NaCl, the *n* had lower values and it was equal to 1.7 and 1.6, respectively.

Nevertheless, the 2P autofluorescence spectra (**Figure 58a**) reveal that fibrils exhibit enhanced fluorescence signals compared to monomeric HEWL. Thus, the fibrillation process increases the probability of 2PA. To quantify the 2PA of HEWL monomers and fibrils, the $\sigma_{2,eff}$ was calculated (see equation [16]). At 750 nm the $\sigma_{2,eff}$ were equal to 0.15 GM and 0.18 GM for HEWL fibrils incubated at 0 mM and 50 mM NaCl, respectively and 0.08 GM for both HEWL monomers at 0 mM and 50 mM NaCl (**Figure 58b**). By taking into account 1P FQY value, $\sigma_{2,s}$ was calculated (see equation [15]) to be ~3 GM in the maximum (per one HEWL molecule), being in the same order of magnitude as some other fluorescent dyes, including Coumarin 153, Perylene, or Lucifer Yellow.[240] However, the calculated values of $\sigma_{2,eff}$ and $\sigma_{2,s}$ should be carefully interpreted when compared to other fluorescent probes. The reason behind is the fact that calculating the $\sigma_{2,s}$ and $\sigma_{2,eff}$, it is assumed that the FQY is the same in the 1P and 2P processes. As I will demonstrate herein, the studied HEWL amyloids have different relaxation pathways upon 1P and 2P excitation.

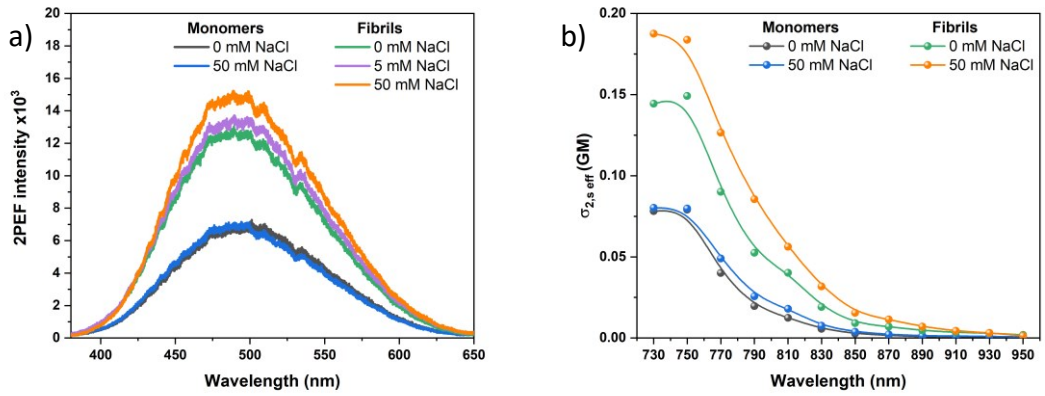

Figure 58. Two-photon excited emission spectra obtained upon excitation at 750 nm (a) and effective two-photon absorption cross-sections (b) for HEWL monomers and fibrils at varying NaCl content. HEWL monomers at 0 mM NaCl (black), and 50 mM NaCl (blue); HEWL fibrils at 0 mM NaCl (green), 5 mM NaCl (lilac), and 50 mM NaCl (orange).[234] The images were adapted with permission.

The presented 2PA properties agree with the results reported by Pinotsi *et al.*[138] who demonstrated that the 2PA process for amyloid fibrils occurs in the range of 750-950 nm. In contrast, as I explained in 3.8.3 Label-free imaging, Hanczyc *et al.*[173] evidenced that amyloid fibrils exhibit 2PA in the 525-600 nm range and 3PA in the 700-750 nm range, using the Z-scan technique.[173] The following differences between our results and those obtained

by Hanczyc *et al*.[173] cannot be straightforwardly compared, as two different methodologies were applied. The discrepancies may arise from the fact that:

(i) the appearance of multiphoton absorption is related to the laser pulse width and its intensity. The Z-scan measurements were performed at high-intensity femtosecond pulses with a repetition rate of 1 kHz.[173] However, the 2PEF measurements discussed here were performed with femtosecond pulses (with a repetition rate of 80 MHz and lower intensity compared to the Z-scan).

(ii) the Z-scan technique measures transmittance variations of the laser beam propagated through the investigated samples. This technique is not selective for 2PA as it may also show *inter alia* other non-linear absorption phenomena (*e.g.* excited-state absorption) and non-linear scattering. Contrary, in the case of fluorescent systems, the 2PEF signal recorded *via* the fluorescence-based assay corresponds directly to the preceding 2PA.

When I compared the 1P and 2P excited fluorescence spectra of HEWL fibrils (at a concentration of 20 mg/mL), I noticed a significant spectral shift between them. Namely, upon 2P excitation, the resulting emission signal had a maximum position at ~488 nm (~2.54 eV), whereas the emission band was blue-shifted towards 451 nm (2.75 eV) upon 1P excitation (**Figure 59a, Table 9**). Thus, the resulting 1P and 2P fluorescence emission processes occur from different electronic levels, and the energy difference equals ~0.21 eV (**Table 9**). In contrast, for 1P and 2P fluorescence excitation spectra, the corresponding maxima were localized at 373 nm (3.33 eV) and ~750 nm (~1.65 eV), respectively. This indicates that 1P excitation requires nearly two times higher energy than the 2P excitation process. Thus, when the 1P excitation spectrum is plotted at doubled wavelength compared to the 2P excitation spectrum, both excitation spectra overlap as expected (**Figure 59a, Table 9**). Then, we wanted to evaluate the spectral difference in fluorescence emission upon 1P and 2P excitation. We evidenced that the spectral shift does not arise from the equipment artifacts, as the 1P and 2P fluorescence emission spectra of fluorescein (a reference dye) overlapped. To examine the possible contribution of the relatively high concentration of HEWL samples on the relaxation pathway (by charge or energy transfer processes), the 2P fluorescence emission spectra were compared for the original samples (20 mg/mL) to the diluted ones (2 mg/mL). Indeed, **Figure 59b** demonstrates that the normalized fluorescence emission spectra overlap. Then, to identify the possible explanation for the different 1P and 2P fluorescence emission profiles, 1P and 2P excited fluorescence decays were measured. In this experiment, significant differences between

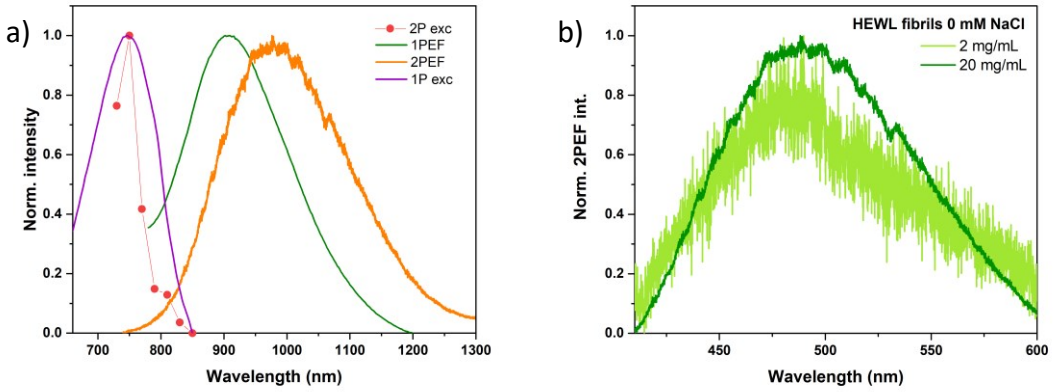

Figure 59. 1P and 2P optical properties of HEWL fibrils incubated at 0 mM NaCl. Normalized 1P fluorescence excitation spectrum (1P exc, violet line) recorded for λ_{em} = 460 nm, normalized 2P fluorescence excitation spectrum (2P exc, red line with red circles) recorded for λ_{em} = 550 nm, normalized 1P fluorescence emission spectrum (1PEF, green line) recorded for λ_{exc} = 370 nm, and normalized 2P fluorescence emission spectrum (2PEF, orange line) recorded for λ_{exc} =750 nm. 1PEF, 2PEF, and 1P exc spectra were plotted at a doubled wavelength with respect to 2P exc spectrum (a). Normalized 2P fluorescence emission spectra of HEWL fibrils incubated at 0 mM NaCl (b); the sample was diluted to 2 mg/mL (light green) or was not diluted and the concentration was equal 20 mg/mL (green). Each of the spectra were normalized separately.[234] The images were adapted (a) or reproduced (b) with permission.

1P and 2P processes were noticed. Namely, the most suitable fitting models for 1P and 2P fluorescence decays were a triple- and a double-exponential functions, respectively (**Figure 60**). Moreover, the 1P process is characterized by a longer τ_{av} than the 2P process in the case of HEWL fibrils incubated at 0 mM, as well as 50 mM NaCl (**Figure 60a, b, Table 10**). The 1P and 2P fluorescence dynamics possess distinct sensitivities to the varying aqueous environment. Namely, the 1P τ_{av} slightly increases while the ionic strength increases: at 0 mM NaCl the 1P τ_{av} was 2.87 ns, whereas at 50 mM NaCl, it reached a value of 2.99 ns (**Table 10**). By contrast, in the case of 2P excited fluorescence decay, the 2P τ_{av} increased ~1.8 times when comparing fibrils incubated at 0 mM NaCl *versus* at 50 mM NaCl (from 1.16 ns to 2.08 ns) (**Table 10**). The significant increase in the 2P τ_{av} may result from the rise of the second lifetime-component (τ_2) value from 1.3 ns (0 mM NaCl) to 2.5 ns (50 mM NaCl) (**Figure 60b**). The differences in the chosen fitting model, the determined τ_{av} values, and their sensitivity to the ionic composition of the aqueous medium support the hypothesis about different relaxation pathways upon 1P and 2P excitations (**Figure 59a**).

Table 9. Peak positions for the 1P and 2P fluorescence emission and excitation spectra for HEWL fibrils incubated at 0 mM NaCl; the corresponding energy is given.[234] The table was adapted with permission.

Fluorescence process		Peak position (nm)	Energy (eV)
Emission	1P	451	2.75
	2P	488	2.54
Excitation	1P	373	3.33
	2P	750	1.65

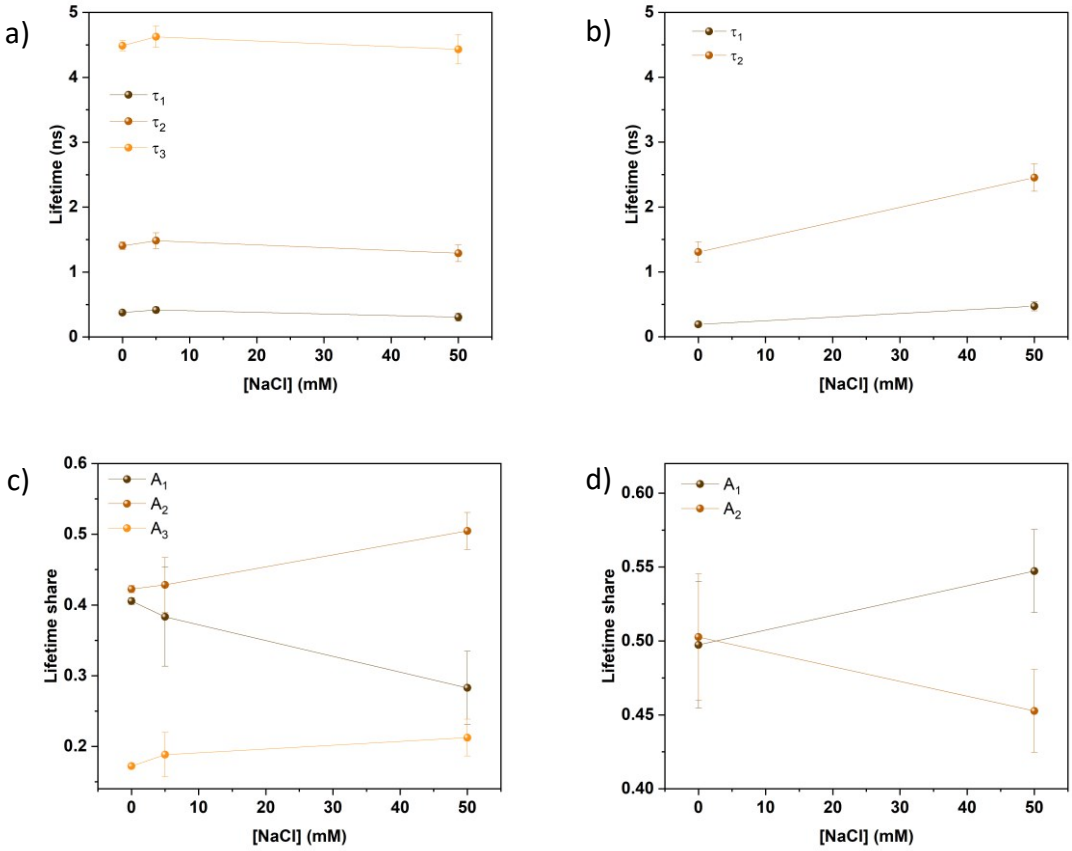

Figure 60. 1P and 2P excited fluorescence lifetimes (a and b, respectively) estimated after fitting the corresponding fluorescence decays along with their share (c and d, respectively). Calculations were performed for HEWL fibrils incubated at 0 mM, 5 mM, and 50 mM NaCl.[234] The images were adapted with permission.

Table 10. The average 1P and 2P fluorescence lifetimes (τ_{av}) of HEWL fibrils incubated at 0 mM and 50 mM NaCl.[234] The table was adapted with permission.

NaCl concentration (mM)	τ_{av} (ns)	
	1P	2P
0	2.87	1.16
50	2.99	2.08

To examine whether the different relaxation pathways (dependent on the excitation mechanism) are also characteristic for other amyloid fibril systems, 1P and 2P fluorescence emission spectra were measured for bovine insulin fibrils (**Figure 61**). The 2P fluorescence emission spectrum of bovine insulin fibrils demonstrated a significant red-shift compared to the 1P fluorescence spectrum, with an even higher energy difference

than in the case of HEWL fibrils (~0.35 eV *versus* ~0.21 eV). Therefore, the various relaxation pathways upon 1P and 2P excitation appear to be a characteristic feature of amyloid fibrils.

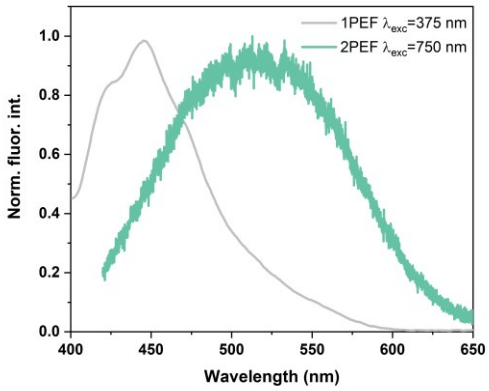

Figure 61. Normalized 1P and 2P fluorescence emission spectra of bovine insulin fibrils, recorded at λ_{exc} = 375 nm (grey) and λ_{exc} = 750 nm (cyan), respectively.[234] The images were adapted with permission.

Figure 57c demonstrates that HEWL monomers provide a relatively weak autofluorescence signal. Its appearance may result from CT transitions in their absorption spectra,[148] as HEWL, among the total number of 129 AAs in its structure, contains 27 amino acid residues with electrically charged side chains (~21% of the total number of AAs).[148, 239] The fluorescence emission intensity increases as the concentration of HEWL monomers increases (**Figure 62a**). In addition, the autofluorescence signal in both 1P and 2P excitation regimes is enhanced upon fibrillation (**Figure 57c, 58a**). In the case of HEWL fibrils, the signal intensity scales with the NaCl content (**Figure 57c, 58a**). Thus, the autofluorescence enhancement may be linked with the change of the secondary structure, as HEWL monomers possess mainly α-helical structure, whereas in fibrils, the peak indicating the presence of the β-sheet structure arises (**Figure 56**) and increases while the ionic strength of the surrounding medium increases. The enhanced autofluorescence signal may arise from the stated hypotheses, including the proton/charge transfer process, the large number of nπ* states, short hydrogen bonds, or the CO-lock mechanism. Due to the complexity of the studied system, the exact mechanism behind the autofluorescence cannot be specified.

The concentration of HEWL samples for 1P fluorescence experiments was relatively high. Thus, to compensate for the inner filter effect, the measured fluorescence intensity values were corrected for their absorption at excitation and emission wavelengths according to equation [18]. Then, the fluorescence enhancement coefficients ($F_{enh,\ coeff}$) for HEWL fibrils and monomers as a function of NaCl concentration (0 mM, 5 mM, and 50 mM) were calculated according to equation [19] (**Figure 62b**). The results demonstrate a rise of $F_{enh,\ coeff}$ values for fibrils for both 1P and 2P processes at the increasing NaCl content. In

the case of HEWL fibrils incubated at 5 mM NaCl, the $1PEF_{cor}$ and $2PEF_{cor}$ are enhanced by a factor of 1.3 and 1.2, respectively. When fibrils are incubated at 50 mM NaCl, the $1PEF_{cor}$ and $2PEF_{cor}$ are enhanced by a factor of 3.2 and 2.9, respectively. Contrarily to fibrils, HEWL monomers exhibit nearly no fluorescence enhancement ($F_{enh,\ coeff}$ ~1.0) (**Figure 62b**). As I presented above, the SV AUC analysis revealed that at t_0, at the relatively high HEWL concentration (1.4 mM; 20 mg/mL), monomers predominate (**Table 8, Figure 55**). In addition, the ATR-FTIR spectra indicated that HEWL monomers are predominated by the α-helical structure, whereas in fibrils the β-sheet content increases with the increase of the ionic strength of the surrounding medium (**Figure 56**). Therefore, the observed enhancement in fibrils' fluorescence emission in both 1P and 2P excitation regimes as the function of NaCl concentration suggests a key role of the β-sheet structure in the autofluorescence mechanism.

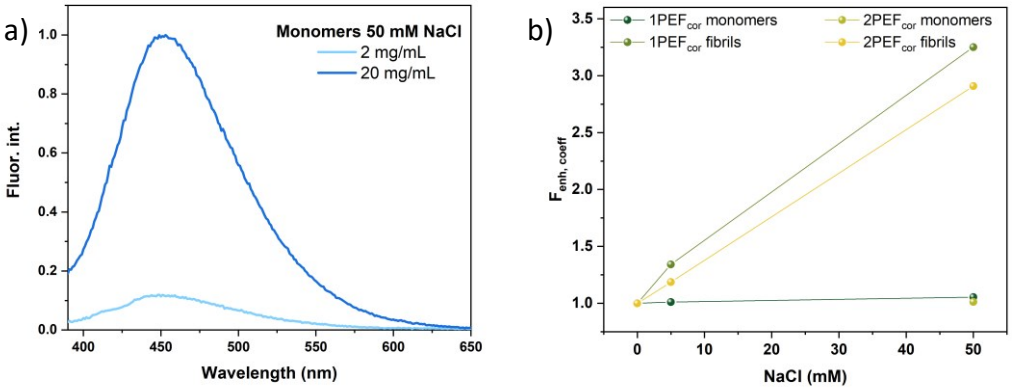

Figure 62. 1P fluorescence emission spectra recorded at λ_{exc} = 370 nm for HEWL monomers at concentrations 2 mg/mL (light blue) and 20 mg/mL (blue) in 50 mM NaCl (a). The spectra (a) were obtained by dividing by the maximum fluorescence emission intensity for the sample at 20 mg/mL. Fluorescence enhancement coefficient ($F_{enh,\ coeff}$) of HEWL monomers and fibrils in the function of NaCl concentration for 1P and 2P emission processes (b). $1PEF_{cor}$ and $2P_{cor}$ are corrected fluorescence values obtained upon λ_{exc} = 370 nm and λ_{exc} = 750 nm, respectively.[234] The images were adapted with permission.

7.5 Conclusions

In this chapter, the 1P and 2P autofluorescence properties of HEWL monomers and fibrils were investigated in aqueous media with ionic strengths regulated by the NaCl concentration. I noticed that the varying salt concentration ensured the formation of fibrils of various morphology and β-sheet content. The spectroscopic results demonstrate that HEWL monomers and fibrils exhibit 1P and 2P excited autofluorescence. However, HEWL fibrils are characterized by enhanced autofluorescence signal and higher FQY as compared to HEWL monomers. To quantify the multiphoton excitation efficiencies for fibrils and

monomers, $\sigma_{2,eff}$ were determined. The $\sigma_{2,eff}$ values increase upon fibrillation, which evidences that fibrils are characterized by a higher probability of 2PA to occur than their corresponding monomers. In addition, the results indicate that the 1P and 2P autofluorescence intensity of HEWL fibrils also rises with the increase of ionic strength. The increase in the NaCl concentration induces morphology changes among the incubated fibrils and enhancement in the contribution of the secondary β-sheet structure. Thus, it is evident that the β-sheet structure plays a pivotal role in the autofluorescence phenomenon. The present dense hydrogen bond network may be involved in the possible proton/charge transfer, providing a large number of nπ* states, short hydrogen bonds, or contribute to the CO-lock mechanism.

I noticed that HEWL fibrils, in the 1PA and 2PA processes, undergo the transition to the same excited state. However, the resulting emission occurs from levels of different energy, as the 2P fluorescence emission spectrum is red-shifted, as compared to the 1P process. The explanation for the differences in the relaxation pathways upon 1P or 2P excitation was found in the fluorescence dynamics (*via* fluorescence lifetimes). Namely, upon 1P excitation the resulting τ_{av} is longer than upon 2P excitation. To evidence that the red-shifted emission upon 2P excitation is characteristic not only for HEWL fibrils, the 1P and 2P fluorescence emission spectra were also studied for bovine insulin fibrils. Indeed, the same tendency was observed. It suggests that the different relaxation pathways, dependent on the excitation mechanism, are common characteristics of amyloid fibrils.

The obtained results indicate that the differences in autofluorescence intensity can serve to distinguish between monomers and fibrils, and even between different morphologies of amyloids. The data discussed in this chapter bring a great deal of information regarding the 2P autofluorescence properties of proteins' monomers and fibrils. To the best of my knowledge, for the first time, a red-shifted 2P autofluorescence (as compared to 1P analogue) was demonstrated and explained. The presented outcomes hold a promise for the potential label-free *in vivo* detection of amyloid deposits.

8 Chapter 8. Summary, perspectives, and challenges

The present Doctoral Dissertation covers the main research conducted throughout the author's doctoral studies. To summarize this work, in this chapter, the stated hypotheses are discussed and verified with the research outcomes. Then, the potential perspectives and challenges are put forward.

- **Hypothesis 1:** The morphology and the secondary structure affect the autofluorescence properties of amyloid fibrils.

Verification of hypothesis 1:

This hypothesis was validated by investigating amyloid structures of two different origins (*i.e.* synthesized TTR(105-115) fragments and HEWL) in two separate research themes, presented in Chapters 5 and 7.

Firstly, in Chapter 5, I focused on TTR(105-115) peptide fragments: enantiopure H-TTR-NH_2 (*L*-form) and *D* (*D*-form), and their racemic mixture *D* + H-TTR-NH_2. I noticed significant differences between the samples in terms of their morphology. Incubation of enantiopure peptides led to the formation of helical fibrils, whereas the racemic mixture – to flat, tape-like fibrils. I investigated the optical properties of enantiopure and racemic samples. The recorded fluorescence emission spectra indicated that upon excitation at λ_{exc} = 360 nm, both enantiopure samples emit an autofluorescence signal with a maximum at 436 nm. At the same excitation wavelength, the maximum autofluorescence signal for the racemic mixture was blue-shifted towards 431 nm. The ATR-FTIR spectra indicated that the enantiopure samples and the racemic mixture vary in terms of the arrangement of the secondary β-sheet structure. In both enantiopure fibrils a parallel β-sheet structure prevailed, whereas in the racemic fibrils, an antiparallel one. The outcomes were further supported by the MD simulations. Accordingly, the helical morphology of enantiopure fibrils stems from the repulsive interactions between the same terminal groups. In racemic fibrils, the repulsions are minimized due to an antiparallel alignment of the consecutive β-strands. These outcomes demonstrate that differences in the morphology of amyloid fibrils and alignment of the β-sheets impact the **autofluorescence signal position**. Thus, they **positively validate hypothesis 1**.

Secondly, I investigated HEWL monomers and fibrils, and the research is covered in Chapter 7. HEWL incubation at varying ionic strength led to the formation of amyloid fibrils with different morphologies. The AFM imaging and the t-test statistics revealed that the varying ionic strength affects the morphology parameters (*i.e.* width and height dimensions) of the resulting fibrils. The ATR-FTIR spectra demonstrated that with the increase of NaCl concentration, the resulting fibrils possess a higher content of the

secondary β-sheet structure. However, HEWL monomers regardless of salt concentration (i) display morphology with a size ranging from ~25 nm to ~100 nm, (ii) are predominated by α-helical structure. Upon excitation at 370 nm, monomers and fibrils emitted an autofluorescence signal with a maximum at ~450 nm. In the case of fibrils, the signal was enhanced compared to monomers, and its intensity increased with the increase of NaCl content. The calculated FQY values indicated that HEWL fibrils possess higher FQY than their monomeric counterparts, evidencing that the fibrillation process provides more efficient autofluorescence. The recorded 2P excited emission spectra for HEWL monomers and fibrils revealed that upon λ_{exc} = 750 nm, the species emit an autofluorescence signal with a maximum at ~488 nm. As in 1P autofluorescence, (i) fibrils demonstrated enhanced emission signal compared to monomers, (ii) the signal intensity increased with the increase of salt content in the incubated fibrils. The presented outcomes **support hypothesis 1.** They demonstrate that the variations in the morphology dimensions (height, width) and the increase in the β-sheet structure content affect the **autofluorescence intensity**. In addition, the results evidence that monomers also emit autofluorescence signal, but the signal is weaker compared to fibrils.

- **Hypothesis 2:** The morphology and secondary structure of supramolecular aggregates can be controlled by the terminal groups of the constituting peptide units.

Verification of hypothesis 2:

I studied TTR(105-115) peptide functionalized (i) at the N-terminus with: H-, Ac- or DiMe- groups, and (ii) at the C-terminus with: -NH_2 or -OH groups. AFM imaging revealed that in enantiopure samples functionalized with H- at the N-terminus (H-TTR-NH_2, H-TTR-OH, and *D* enantiomer), helical fibrils predominated. They had a similar mean width (~22-23 nm). The H-TTR-NH_2 and *D* fibrils had a similar mean height equal to 11.7 ± 2.4 nm and 11.9 ± 2.7 m, respectively. However, the H-TTR-OH fibrils had a lower mean height, equal to 8.5 ± 2.7 nm. Moreover, the H-TTR-NH_2 and *D* fibrils had a similar cross-over distance equal to 98.0 ± 6.5 nm and 96.8 ± 6.9 nm, respectively, while the H-TTR-OH fibrils had a longer cross-over distance equal to 104.4 ± 11.7 nm. Peptides functionalized with Ac- at their N-terminus (Ac-TTR-NH_2 and Ac-TTR-OH) yielded very long fibrils whose dimensions were difficult to estimate because the structures were rather stuck together. In enantiopure DiMe-samples (DiMe-TTR-NH_2 and DiMe-TTR-OH) no fibrils were formed and I observed only peptide aggregates. Interestingly, in all quasi-racemic mixtures (obtained by mixing in 1/1 molar ratio enantiomer *D* with each of the functionalized *L*-enantiomers), fibrils with a flat morphology were formed and the C-terminal group played a key role in impacting the width dimension of the fibrils. Wider fibrils were observed in quasi-racemic

mixtures in which the *L*-enantiomers possessed -NH_2 at the C-terminus compared to their counterparts functionalized with -OH group. For example, the fibrils in the *D* + H-TTR-NH_2 sample had a mean width of 103.7 ± 39.8 nm, whereas in *D* + H-TTR-OH of only 18.0 ± 3.6 nm. The recorded ATR-FTIR spectra indicated that in enantiopure DiMe-samples a disordered structure predominated, which is consistent with the presence of peptide aggregates. In the remaining *L*-enantiopure samples, a parallel β-sheet structure prevailed, and in all quasi-racemic mixtures - an antiparallel one. The MD simulations helped to correlate the morphology and the secondary structure of the investigated samples. First of all, they indicated that a sufficient number of hydrogen bonds is required for amyloid fibrils formation. The steric hindrance provided by the DiMe-groups causes them to be rotated relative to each other. Thus, hydrogen bond formation is hindered. This effect is minimized in the quasi-racemic mixtures with DiMe-peptides and therefore the fibrils were formed there. The MD simulations clarified the twist or the lack of twist in amyloid fibrils. Indeed, the electrostatic interactions determine the twist of amyloid fibrils. The stronger the repulsions between peptide termini, the more pronounced the twist (*i.e.* reflected in shorter cross-over distance). The lack of twist in quasi-racemic fibrils was dictated by minimized repulsive interactions between peptides' terminal groups provided by the antiparallel β-sheet structure. These findings further **corroborate hypothesis 2** and demonstrate how modifications of peptide terminal groups affect the morphology and the secondary structure of the resulting assemblies.

- **Hypothesis 3:** The autofluorescence of amyloids can appear upon a multi-photon excitation process.

Verification of hypothesis 3:

To validate this hypothesis, I studied the optical properties of HEWL monomers and fibrils upon a femtosecond laser-beam irradiation in the NIR region; the results are discussed in Chapter 7. Upon excitation at 750 nm, the emerging fluorescence signal had the highest intensity for all samples, and the maxima were located at ~488 nm. To examine the multiphoton nature of the corresponding excitation process, the power exponent *n* was determined. The *n* values were found to be 1.8 and 2.2 for fibrils incubated at 0 mM and 50 mM NaCl, respectively. These results evidenced the 2P origin of the autofluorescence – they **support** the stated **hypothesis 3**. In addition, the *n* values for monomers at 0 mM and 50 mM NaCl were estimated to be 1.7 and 1.6, respectively, revealing a significant contribution of 1P in the 2P process in the NIR excitation of monomers. These results confirm the above outcomes and reflect that the fibrillation process and the increase of the β-sheet structure content increase the probability of a 2PA process.

- **Hypothesis 4:** The mechanism behind the one- and multi-photon excited fluorescence emission is different for these two processes.

Verification of hypothesis 4:

To validate this hypothesis, I focused on the results obtained for HEWL fibrils incubated at 0 mM NaCl. I confirmed that upon excitation at 750 nm, the resulting signal is of 2P origin. When comparing 1P and 2P excitation spectra, the results suggested that the 2P excitation is possible at nearly double the wavelength (half of the energy) of the 1P process. However, there was a spectral shift between the 1P and 2P autofluorescence. The 2P autofluorescence was red-shifted compared to the 1P autofluorescence. It indicated that the emission in 1P and 2P processes occurs from electronic states of different energy. Indeed, the calculated energy difference was ~0.21 eV. The different relaxation pathways upon 1P and 2P excitation were further confirmed by different τ_{av} values. Additionally, the 1P and 2P fluorescence decays were best fitted by a triple-exponential and double-exponential function, respectively. For the 1P process, the τ_{av} was calculated to be 2.87 ns, whereas for the 2P process, it was 1.16 ns. These outcomes **confirm hypothesis 4**.

The research outcomes presented in this Doctoral Dissertation have positively validated the stated hypotheses. In addition, the results give some perspectives and raise further challenges:

(i) I have proven that enantiopure and racemic fibrils from TTR(105-115) peptide differ in morphology and secondary structure, and these variations affect the position of autofluorescence. I also demonstrated that different capping groups at TTR(105-115) termini dictate the morphology and the secondary structure of the resulting peptide assemblies. Thus, it would be interesting to investigate how the different terminal groups affect the autofluorescence properties. Such knowledge would be beneficial to better understand and potentially clarify the autofluorescence phenomenon.

(ii) I demonstrated how different functional groups at peptides' termini impact the morphology and secondary structure of the resulting assemblies. It would be appreciated to examine which of these assemblies are the best choice for developing novel biomaterials. To do so, target analogues should be investigated in terms of their biocompatibility, mechanical properties, degradability, or bioactivity. Examination of these features could verify their usage in the intended application, *e.g.* drug delivery systems, tissue scaffolds, or implants.

(iii) I confirmed that amyloids can be excited in a 2P regime which opens a possibility for their non-invasive *in vivo* detection, without the use of any extrinsic labels. This holds a promise for the development of diagnostic methods and treatment of amyloid-related diseases.

Scientific achievements and activities

Publications discussed in this dissertation

I. In **II. MAIN RESEARCH CONDUCTED** (main author):

1. **Grelich-Mucha, M.**; Garcia, A. M.; Torbeev, V.; Ożga, K.; Berlicki, Ł.; Olesiak-Bańska, J., *Autofluorescence of Amyloids Determined by Enantiomeric Composition of Peptides*. The Journal of Physical Chemistry B **2021**, 125 (21), 5502-5510.
2. **Grelich-Mucha, M.**; Bachelart, T.; Torbeev, V.; Ożga, K.; Berlicki, Ł.; Olesiak-Bańska, J*., Amyloid engineering – how terminal capping modifies morphology and secondary structure of supramolecular peptide aggregates*. Biomaterials Science **2024**, 12 (6), 1590-1602.
3. **Grelich-Mucha, M.**; Lipok, M.; Różycka, M.; Samoć, M.; Olesiak-Bańska, J., *One- and Two-Photon Excited Autofluorescence of Lysozyme Amyloids*. The Journal of Physical Chemistry Letters **2022**, 13 (21), 4673-4681.

II. In **I. INTRODUCTION** (co-author):

4. Hajda, A.; **Grelich-Mucha, M.**; Rybczyński, P.; Ośmiałowski, B.; Zaleśny, R.; Olesiak-Bańska, J., *BF2-Functionalized Benzothiazole Amyloid Markers: Effect of Donor Substituents on One- and Two-Photon Properties*. ACS Applied Bio Materials **2023**, 6 (12), 5676-5684.
5. Obstarczyk, P.; Lipok, M.; **Grelich-Mucha, M.**; Samoć, M.; Olesiak-Bańska, J., *Two-Photon Excited Polarization-Dependent Autofluorescence of Amyloids as a Label-Free Method of Fibril Organization Imaging*. The Journal of Physical Chemistry Letters **2021**, 12 (5), 1432-1437.

Publications not discussed in this dissertation

6. Kalitnik, A.; **Grelich-Mucha, M.**; Olesiak-Bańska, J., *Chitosan oligosaccharides inhibit the fibrillation of insulin and disassemble its preformed fibrils*. International Journal of Biological Macromolecules **2024**, 254, 127857.
7. Szarszoń, K.; Mikołajczyk, A.; **Grelich-Mucha, M.**; Wieczorek, R.; Matera-Witkiewicz, A.; Olesiak-Bańska, J.; Rowińska-Żyrek, M.; Wątły, J., *Bioinorganic chemistry of shepherin II complexes helps to fight Candida albicans?* Journal of Inorganic Biochemistry **2024**, 253, 112476.
8. Wątły, J.; Szarszoń, K.; Mikołajczyk, A.; **Grelich-Mucha, M.**; Matera-Witkiewicz, A.; Olesiak-Bańska, J.; Rowińska-Żyrek, M., *Zn(II) Induces Fibril Formation and Antifungal Activity in Shepherin I, An Antimicrobial Peptide from Capsella bursa-pastoris*. Inorganic Chemistry **2023**, 62 (48), 19786-19794.

Manuscripts – publications in preparation

1. Hajda, A.; **Grelich-Mucha, M.**; Obstarczyk, P.; Olesiak-Bańska, J.; *Targeting amyloids with labels and label-free two-photon fluorescence microscopy*, review article.
2. **Grelich-Mucha, M.**; Garcia, A. M.; Torbeev, V; Olesiak-Bańska, J.; *H-bonding network disruption affects morphology, structure and autofluorescence of the resulting peptide aggregates*, manuscript in preparation.

Post-conference materials

1. **Grelich M.**, Grzesik A., Olesiak-Bańska J., *Optical and structural properties of amyloids obtained from bovine insulin*, Optoelectronics and Microsystems Packaging: proceedings of 2018 International Students and Young Scientists Workshop: 22-24 November 2018, Dresden, Germany /eds. Sergiusz Patela, Wojciech Kijaszek, Dariusz Przybylski, Wrocław: Wydawnictwo GMORK, **2019**, 25-30.

Peer-reviewed scientific monographs

1. Benkowska-Biernacka D. A., **Grelich-Mucha M.**, Hajda A., Pniakowska A., *PANIC Summer School 2022: PhoBiA Annual Nanophotonics International Conference*, 30 May - 3 June 2022, Wrocław, Poland. Wrocław: Oficyna Wydawnicza Politechniki Wrocławskiej, **2022**, 1-87.
2. Benkowska-Biernacka D. A., **Grelich-Mucha M.**, Hajda A., Pniakowska A., *1st HighLIGHTing Science Meeting & PANIC 2021 PhoBiA Annual Nanophotonics International Conference*, 26-28 May 2021: Book of Abstracts. Wrocław: Oficyna Wydawnicza Politechniki Wrocławskiej, **2021**, 1-101.

Grants

1. National Science Centre (NCN) OPUS (2021/43/B/ST5/00753) - *New two-photon absorbers with dipolar and quadrupolar architecture: from synthesis to applications*, scholarship holder – doctoral student, 09.2022-07.2024 (break 02.2023-02.2024); amount awarded: 2 234 400,00 PLN, project leader: Prof. Borys Ośmiałowski (Nicolaus Copernicus University, Toruń, Poland).
2. PHC Polonium, joint research projects between Poland and France, National Agency for Academic Exchange (NAWA)/Poland; Ambassade de France en Pologne - Service de Coopération et d'Action Culturelle, Ministère de l'Europe et des Affaires Étrangères, Ministère de l'Enseignement supérieur, de la Recherchen et de l'Innovation/France ; (BPN/BFR/2021/1/00018) - *Peptide-functionalized gold nanoparticles "PeGoNa"*, scholarship holder - doctoral

student, 01-12.2022; amount awarded: 15 100,00 PLN, project leaders: Prof. Joanna Olesiak-Bańska, Prof. Vladimir Torbeev.

3. InterDocSchool Project, NAWA STER program, foreign mobility of Wrocław University of Science and Technology (Politechnika Wrocławska) doctoral students; three-month internship at Prof. Torbeev's group (Université de Strasbourg, France), 10-12.2021 - project leader, amount awarded: 38 000 PLN.
4. Wrocławskie Centrum Akademickie (WCA), Fundusz Aktywności Studenckiej (FAST), *Tajniki mikroskopii – warsztaty dla uczniów wrocławskich szkół* (Secrets of microscopy - workshops for students of Wrocław schools), 07-12.2021 - co-author of grant proposal, amount awarded: 4 851,32 PLN, project leaders: Prof. Katarzyna Matczyszyn, Dr. Krzysztof Nadolski.
5. Foundation for Polish Science (FNP) First Team, *Nonlinear Optics, Nanoparticles and Amyloids (NONA) – application of nonlinear optics and gold nanoparticles to study amyloid formation*, 02.2020-12.2021 - junior specialist, then specialist; 09.2018-09.2019 – scholarship holder, master student; amount awarded: 1 744 780,00 PLN, project leader: Prof. Joanna Olesiak-Bańska.

Internships

1. 02-16.10.2022 - Université de Strasbourg, Strasbourg, France, title: *Peptide-functionalized gold nanoparticles "PeGoNa"*, within the joint PHC Polonium project (see grant number 2 above), supervisor: Prof. Vladimir Torbeev.
2. 01.10-18.12.2021 - Université de Strasbourg, Strasbourg, France, topic: Synthesis and initial investigations of amyloidogenic peptides functionalized with different groups at their N- and C-termini, within the InterDocSchool project (see grant number 3 above), supervisor: Prof. Vladimir Torbeev.
3. 22.10-22.12.2019 - Université de Strasbourg, Strasbourg, France, topic: synthesis of amyloidogenic peptides, within the Erasmus 2014-2020 program, supervisor: Prof. Vladimir Torbeev.
4. 06.07-30.09.2018 - Université de Strasbourg, Strasbourg, France, topic: synthesis of amyloidogenic peptides, within the Erasmus 2014-2020 program, supervisor: Prof. Vladimir Torbeev.
5. 01.08-30.09.2016 - Université de Rennes 1, Rennes, France, topic: synthesis of isocyanurates' derivates, within the Erasmus 2014-2020 program, supervisor: Prof. Frédéric Paul.
6. 06.07-30.09.2015 – start-up company SIOD GmbH, Technische Universität Chemnitz, Germany (currently INURU, Berlin, Germany), topic: preparation and investigations of organic light-emitting diodes (OLEDs), within the project Bionanomaterials-BioNaM: a new interdisciplinary field of Postgraduate PhD

studies and an internship programme for undergraduate and postgraduate Master programme and PhD students, supervisors: Patrick Barkowski, Marcin Ratajczak.

Awards and scholarships

1. 2023, 2022 - An honorable distinction in the contest "Studencki Program Stypendialny" for achievements in the field of interdisciplinary research. The honor was awarded by the Jan Mozrzymas scholarship committee; the contest was organized by the WCA.
2. Academic year 2022/2023 – doctoral student scholarship for scientific achievements in the former academic year (2021/2022) at Wroclaw University of Science and Technology (WUST) Doctoral School.
3. 2022 – a special award of WUST's Rector for significant scientific achievements in the academic year 2021/2022.
4. 2022 - travel grant obtained for participating in The Leuven Protein Aggregation Meeting (21-23.09.2022).
5. 2022, 2021 – Primus program: award for publishing an article with the highest score in the lists of the Ministry of Science and Higher Education, WUST.
6. Academic year 2021/2022 – beneficiary of a scholarship for the best WUST doctoral students implementing PhD in international cooperation; the scholarship was financed by the InterDocSchool project implemented under the NAWA STER program.
7. 2021 – award of the dean of the Faculty of Chemistry, WUST, for scientific achievements.
8. 2021-2022 – organizing commitee of a scientific exhibition organized within Microscopic Art Non-Limited International Annual Contest MANIAC co-financed from the "Social Responsibility of Science" program of the Minister of Science and Higher Education in Poland.
9. 2017-2022 - organizing committee of PhoBiA Annual Nanophotonics International Conference „PANIC".
10. 2017-2018 – a scholarship holder for selected students in the Molecular Nano- and Biophotonics for telecommunications and biotechnologies (MONABIPHOT) graduate program, funded by Université Paris-Saclay (France).

Conferences

1. 11.06.2024 – WrocChem 2024, Wrocław, Poland, *Wpływ grup końcowych peptydów na morfologię oraz strukturę drugorzędową powstających agregatów*

supramolekularnych – **M. Grelich-Mucha**, T. Bachelart, V. Torbeev, K. Ożga, Ł. Berlicki, J. Olesiak-Bańska, oral presentation.

2. 21-23.09.2022 **-** The Leuven Protein Aggregation Meeting, Leuven, Belgium, *The role of terminal capping on self-assembly of peptide aggregates* – **M. Grelich-Mucha**, T. Bachelart, V. Torbeev, K. Ożga, Ł. Berlicki, J. Olesiak-Bańska, poster presentation.
3. 30.05-03.06.2022 **-** PANIC Summer School 2022 : PhoBiA Annual Nanophotonics International Conference, Wrocław, Poland, *Autofluorescence properties of lysozyme amyloids* **– M. Grelich-Mucha**, M. Lipok, M. Różycka, M. Samoć, J. Olesiak-Bańska, oral presentation.
4. 03-07.07.2021 **-** The 45th FEBS Congress, remote conference, *Autofluorescence of amyloid fibrils determined by variations in β-sheet organization* **- M. Grelich-Mucha**, A.M. Garcia, V. Torbeev, K. Ożga, Ł. Berlicki, J. Olesiak-Bańska, poster presentation.
5. 24-25.06.2021 **-** Chemistry & Biotechnology International Conference ChemBiotIC, remote conference, *Transthyretin (105-115) peptide – a correlation between the structure and optical properties of enantiomers and the racemate* - **M. Grelich-Mucha**, A. M. Garcia, V. Torbeev, K. Ożga, Ł. Berlicki, J. Olesiak-Bańska, oral presentation.
6. 09-11.06.2021 **-** NanoTech Poland 2021, remote conference, *Label-free detection of amyloid fibrils reveals the importance of H-bonding network in their structure* - **M. Grelich-Mucha**, A. Garcia, V. Torbeev, J. Olesiak-Bańska, poster presentation.
7. 26.05.2021 **-** PhoBiA Annual Nanophotonics International Conference PANIC 2021, remote conference, *The importance of H-bonding network for amyloid fibrils autofluorescence* – **M. Grelich-Mucha**, A. M. Garcia, V. Torbeev, K. Ożga, Ł. Berlicki, J. Olesiak-Bańska, oral presentation.
8. 09-11.11.2020 **-** Single-Molecule Sensors and NanoSystems International Conference, remote conference, *Label-free detection of amyloid fibrils based on their intrinsic fluorescence properties* **- M. Grelich-Mucha**, J. Olesiak-Bańska, oral presentation.
9. 12-14.10.2020 **-** PhoBiA Annual Nanophotonics International Conference PANIC 2020, remote conference, *Structural and optical properties of fibrils obtained from enantiomers and racemate of transthyretin (105-115) peptide* – **M. Grelich-Mucha**, A. M. Garcia Fernandez, V. Torbeev, K. Ożga, Ł. Berlicki, J. Olesiak-Bańska, oral presentation.
10. 15-17.05.2019 **-** PhoBiA Annual Nanophotonics International Conference PANIC 2019, Wrocław, Poland, *Insight into the optical properties and morphology of*

amyloid fibrils – **M. Grelich**, V. Bauer, E. Naudin, V. Torbeev, J. Olesiak-Bańska, oral presentation.

11. 11-15.03.2019 - Sixth International Conference on Multifunctional, Hybrid and Nanomaterials, Sitges, Spain, *Characteristics of fibrils obtained from β-amyloid peptides: Aβ(1-40), Aβ(1-42) and Aβ(33-42)* - **M. Grelich**, V. Bauer, E. Naudin, V. Torbeev, J. Olesiak-Bańska, poster presentation.
12. 01-02.03.2019 - 3rd Wroclaw Scientific Meetings, Wrocław, Poland, *Kinetics of bovine insulin fibrillation* **– M. Grelich**, J. Olesiak-Bańska, poster presentation.
13. 24-26.04.2017 - PhoBiA Annual Nanophotonics International Conference PANIC 2017, Wrocław, Poland, *Characteristics of spherulites and fibrils obtained from β-lactoglobulin and hen egg white lysozyme* - **M. Grelich**, M. Rząsa, K. Brach, J. Olesiak-Bańska, K. Matczyszyn, M. Samoć, poster presentation.

References

1. Stucky, G. D.; Marder, S. R.; Sohn, J. E., Linear and Nonlinear Polarizability. **1991,** *455*, 2-30.
2. Klausen, M.; Blanchard-Desce, M., Two-photon uncaging of bioactive compounds: Starter guide to an efficient IR light switch. *Journal of Photochemistry and Photobiology C: Photochemistry Reviews* **2021,** *48*, 100423.
3. Medishetty, R.; Zaręba, J. K.; Mayer, D.; Samoć, M.; Fischer, R. A., Nonlinear optical properties, upconversion and lasing in metal–organic frameworks. *Chemical Society Reviews* **2017,** *46* (16), 4976-5004.
4. Lakowicz, J. R., *Principles of fluorescence spectroscopy*. 3rd ed.; Springer: New York, 2006; p 1-10.
5. Valeur, B., *Molecular fluorescence : principles and applications*. Wiley-VCH: Weinheim ; New York, 2002; p 3-48.
6. Berezin, M. Y.; Achilefu, S., Fluorescence Lifetime Measurements and Biological Imaging. *Chemical Reviews* **2010,** *110* (5), 2641-2684.
7. Diaspro, A.; Chirico, G.; Collini, M., Two-photon fluorescence excitation and related techniques in biological microscopy. *Quarterly Reviews of Biophysics* **2006,** *38* (2), 97-166.
8. Nonlinear optical microscopy. In *Femtosecond Biophotonics: Core Technology and Applications*, Gu, M.; Bird, D.; Day, D.; Fu, L.; Morrish, D., Eds. Cambridge University Press: Cambridge, 2010; pp 9-34.
9. Kaiser, W.; Garrett, C. G. B., Two-Photon Excitation in CaF2:Eu2+. *Physical Review Letters* **1961,** *7* (6), 229-231.
10. He, G. S.; Tan, L.-S.; Zheng, Q.; Prasad, P. N., Multiphoton Absorbing Materials: Molecular Designs, Characterizations, and Applications. *Chemical Reviews* **2008,** *108* (4), 1245-1330.
11. Rumi, M.; Perry, J. W., Two-photon absorption: an overview of measurements and principles. *Advances in Optics and Photonics* **2010,** *2* (4), 451.
12. Kauert, M.; Stoller, P. C.; Frenz, M.; Rička, J., Absolute measurement of molecular two-photon absorption cross-sections using a fluorescence saturation technique. *Opt. Express* **2006,** *14* (18), 8434-8447.
13. Oulianov, D. A.; Tomov, I. V.; Dvornikov, A. S.; Rentzepis, P. M., Observations on the measurement of two-photon absorption cross-section. *Optics Communications* **2001,** *191* (3-6), 235-243.
14. Xu, C.; Webb, W. W., Measurement of two-photon excitation cross sections of molecular fluorophores with data from 690 to 1050 nm. *Journal of the Optical Society of America B* **1996,** *13* (3), 481-491.
15. Olesiak-Banska, J.; Waszkielewicz, M.; Obstarczyk, P.; Samoc, M., Two-photon absorption and photoluminescence of colloidal gold nanoparticles and nanoclusters. *Chemical Society Reviews* **2019,** *48* (15), 4087-4117.
16. Makarov, N. S.; Drobizhev, M.; Rebane, A., Two-photon absorption standards in the 550-1600 nm excitation wavelength range. *Opt. Express* **2008,** *16* (6), 4029-4047.
17. Makarov, N. S.; Campo, J.; Hales, J. M.; Perry, J. W., Rapid, broadband two-photon-excited fluorescence spectroscopy and its application to red-emitting secondary reference compounds. *Opt. Mater. Express* **2011,** *1* (4), 551-563.

18. Drobizhev, M.; Makarov, N. S.; Tillo, S. E.; Hughes, T. E.; Rebane, A., Two-photon absorption properties of fluorescent proteins. *Nature Methods* **2011,** *8* (5), 393-399.
19. Drobizhev, M.; Tillo, S.; Makarov, N. S.; Hughes, T. E.; Rebane, A., Absolute Two-Photon Absorption Spectra and Two-Photon Brightness of Orange and Red Fluorescent Proteins. *The Journal of Physical Chemistry B* **2009,** *113* (4), 855-859.
20. Hajda, A.; Grelich-Mucha, M.; Rybczyński, P.; Ośmiałowski, B.; Zaleśny, R.; Olesiak-Bańska, J., BF2-Functionalized Benzothiazole Amyloid Markers: Effect of Donor Substituents on One- and Two-Photon Properties. *ACS Applied Bio Materials* **2023,** *6* (12), 5676-5684.
21. Mäde, V.; Els-Heindl, S.; Beck-Sickinger, A. G., Automated solid-phase peptide synthesis to obtain therapeutic peptides. *Beilstein Journal of Organic Chemistry* **2014,** *10*, 1197-1212.
22. Kessel, A.; Ben-Tal, N., *Introduction to proteins : structure, function, and motion*. Second edition. ed.; CRC Press, Taylor & Francis Group: Boca Raton, 2018; p 1-32.
23. Diao, L.; Meibohm, B., Pharmacokinetics and Pharmacokinetic–Pharmacodynamic Correlations of Therapeutic Peptides. *Clinical Pharmacokinetics* **2013,** *52* (10), 855-868.
24. Ouellette, R. J.; Rawn, J. D., Amino Acids, Peptides, and Proteins. **2018**, 929-971.
25. Fasman, G. D., *Practical handbook of biochemistry and molecular biology*. CRC Press: Boca Raton, Fla., 1989; p 3-59.
26. Petsko, G. A.; Ringe, D., *Protein structure and function*. New Science Press; Sinauer Associates; Blackwell Pub.: London Sunderland, MA Oxford, 2004; p 1-10.
27. Brändén, C.-I.; Tooze, J., *Introduction to protein structure*. 2nd ed.; Garland Pub.: New York, 1999; p 1-32.
28. Valeur, E.; Bradley, M., Amide bond formation: beyond the myth of coupling reagents. *Chem. Soc. Rev.* **2009,** *38* (2), 606-631.
29. Ben-Shem, A.; Garreau de Loubresse, N.; Melnikov, S.; Jenner, L.; Yusupova, G.; Yusupov, M., The Structure of the Eukaryotic Ribosome at 3.0 Å Resolution. *Science* **2011,** *334* (6062), 1524-1529.
30. Fischer, E.; Fourneau, E., Ueber einige Derivate des Glykocolls. *Berichte der deutschen chemischen Gesellschaft* **2006,** *34* (2), 2868-2877.
31. Nilsson, B. L.; Soellner, M. B.; Raines, R. T., Chemical Synthesis of Proteins. *Annual Review of Biophysics and Biomolecular Structure* **2005,** *34* (1), 91-118.
32. Goodman, M.; Cai, W.; Smith, N. D., The bold legacy of Emil Fischer. *Journal of Peptide Science* **2003,** *9* (9), 594-603.
33. Wieland, T.; Bodanszky, M., Syntheses of Peptides. The First Epoch. **1991**, 23-43.
34. https://www.nobelprize.org/prizes/chemistry/1902/summary/.
35. Vigneaud, V. d.; Ressler, C.; Swan, C. J. M.; Roberts, C. W.; Katsoyannis, P. G.; Gordon, S., The Synthesis of an Octapeptide Amide with the Hormonal Activity of Oxytocin. *Journal of the American Chemical Society* **2002,** *75* (19), 4879-4880.
36. https://www.nobelprize.org/prizes/chemistry/1955/summary/.
37. Bruckdorfer, T.; Marder, O.; Albericio, F., From Production of Peptides in Milligram Amounts for Research to Multi-Tons Quantities for Drugs of the Future. *Current Pharmaceutical Biotechnology* **2004,** *5* (1), 29-43.
38. Zompra, A. A.; Galanis, A. S.; Werbitzky, O.; Albericio, F., Manufacturing peptides as active pharmaceutical ingredients. *Future Medicinal Chemistry* **2009,** *1* (2), 361-377.
39. https://www.nobelprize.org/prizes/chemistry/1984/summary/.

40. Coin, I.; Beyermann, M.; Bienert, M., Solid-phase peptide synthesis: from standard procedures to the synthesis of difficult sequences. *Nature Protocols* **2007,** *2* (12), 3247-3256.
41. Muttenthaler, M.; Albericio, F.; Dawson, P. E., Methods, setup and safe handling for anhydrous hydrogen fluoride cleavage in Boc solid-phase peptide synthesis. *Nature Protocols* **2015,** *10* (7), 1067-1083.
42. Pedersen, S. L.; Tofteng, A. P.; Malik, L.; Jensen, K. J., Microwave heating in solid-phase peptide synthesis. *Chem. Soc. Rev.* **2012,** *41* (5), 1826-1844.
43. Vanier, G. S., Microwave-Assisted Solid-Phase Peptide Synthesis Based on the Fmoc Protecting Group Strategy (CEM). **2013,** *1047*, 235-249.
44. Whitford, D., *Proteins : structure and function*. J. Wiley & Sons: Hoboken, NJ, 2005; p 1-58.
45. https://www.ncbi.nlm.nih.gov/books/NBK470235/.
46. Crichton, R. R., Structural and Molecular Biology for Chemists. **2008**, 43-76.
47. https://www.ncbi.nlm.nih.gov/books/NBK470269/.
48. Ouellette, R. J.; Rawn, J. D., Amino Acids, Peptides, and Proteins. **2015**, 371-396.
49. Cordeiro, Y.; Macedo, B.; Silva, J. L.; Gomes, M. P. B., Pathological implications of nucleic acid interactions with proteins associated with neurodegenerative diseases. *Biophysical Reviews* **2014,** *6* (1), 97-110.
50. Adamcik, J.; Mezzenga, R., Amyloid Polymorphism in the Protein Folding and Aggregation Energy Landscape. *Angewandte Chemie International Edition* **2018,** *57* (28), 8370-8382.
51. Dill, K. A., Dominant forces in protein folding. *Biochemistry* **1990,** *29* (31), 7133-7155.
52. Bicout, D. J.; Szabo, A., Entropic barriers, transition states, funnels, and exponential protein folding kinetics: A simple model. *Protein Science* **2008,** *9* (3), 452-465.
53. Jahn, T. R.; Radford, S. E., Folding versus aggregation: Polypeptide conformations on competing pathways. *Archives of Biochemistry and Biophysics* **2008,** *469* (1), 100-117.
54. Iadanza, M. G.; Jackson, M. P.; Hewitt, E. W.; Ranson, N. A.; Radford, S. E., A new era for understanding amyloid structures and disease. *Nature Reviews Molecular Cell Biology* **2018,** *19* (12), 755-773.
55. Kyle, R. A., Amyloidosis: a convoluted story. *British Journal of Haematology* **2001,** *114* (3), 529-538.
56. Sipe, J. D.; Cohen, A. S., Review: History of the Amyloid Fibril. *Journal of Structural Biology* **2000,** *130* (2-3), 88-98.
57. Cohen, A. S.; Calkins, E., Electron Microscopic Observations on a Fibrous Component in Amyloid of Diverse Origins. *Nature* **1959,** *183* (4669), 1202-1203.
58. Eanes, E. D.; Glenner, G. G., X-Ray Diffraction Studies on Amyloid Filaments. *Journal of Histochemistry & Cytochemistry* **1968,** *16* (11), 673-677.
59. Bonar, L.; Cohen, A. S.; Skinner, M. M., Characterization of the Amyloid Fibril as a Cross- Protein. *Experimental Biology and Medicine* **1969,** *131* (4), 1373-1375.
60. Sunde, M.; Serpell, L. C.; Bartlam, M.; Fraser, P. E.; Pepys, M. B.; Blake, C. C. F., Common core structure of amyloid fibrils by synchrotron X-ray diffraction 1 1Edited by F. E. Cohen. *Journal of Molecular Biology* **1997,** *273* (3), 729-739.
61. Greenwald, J.; Riek, R., Biology of Amyloid: Structure, Function, and Regulation. *Structure* **2010,** *18* (10), 1244-1260.

62. Maji, S. K.; Wang, L.; Greenwald, J.; Riek, R., Structure–activity relationship of amyloid fibrils. *FEBS Letters* **2009,** *583* (16), 2610-2617.
63. Tycko, R., Solid-State NMR Studies of Amyloid Fibril Structure. *Annual Review of Physical Chemistry* **2011,** *62* (1), 279-299.
64. Antzutkin, O. N.; Leapman, R. D.; Balbach, J. J.; Tycko, R., Supramolecular Structural Constraints on Alzheimer's β-Amyloid Fibrils from Electron Microscopy and Solid-State Nuclear Magnetic Resonance. *Biochemistry* **2002,** *41* (51), 15436-15450.
65. Lövestam, S.; Scheres, S. H. W., High-throughput cryo-EM structure determination of amyloids. *Faraday Discussions* **2022,** *240*, 243-260.
66. Fitzpatrick, A. W. P.; Falcon, B.; He, S.; Murzin, A. G.; Murshudov, G.; Garringer, H. J.; Crowther, R. A.; Ghetti, B.; Goedert, M.; Scheres, S. H. W., Cryo-EM structures of tau filaments from Alzheimer's disease. *Nature* **2017,** *547* (7662), 185-190.
67. Gremer, L.; Schölzel, D.; Schenk, C.; Reinartz, E.; Labahn, J.; Ravelli, R. B. G.; Tusche, M.; Lopez-Iglesias, C.; Hoyer, W.; Heise, H.; Willbold, D.; Schröder, G. F., Fibril structure of amyloid-β(1–42) by cryo–electron microscopy. *Science* **2017,** *358* (6359), 116-119.
68. Wang, L.; Hall, C. E.; Uchikawa, E.; Chen, D.; Choi, E.; Zhang, X.; Bai, X.-c., Structural basis of insulin fibrillation. *Science Advances* **2023,** *9* (37), eadi1057.
69. Serpell, L. C.; Sunde, M.; Benson, M. D.; Tennent, G. A.; Pepys, M. B.; Fraser, P. E., The protofilament substructure of amyloid fibrils11Edited by F. E. Cohen. *Journal of Molecular Biology* **2000,** *300* (5), 1033-1039.
70. Chiti, F.; Dobson, C. M., Protein Misfolding, Functional Amyloid, and Human Disease. *Annual Review of Biochemistry* **2006,** *75* (1), 333-366.
71. Close, W.; Neumann, M.; Schmidt, A.; Hora, M.; Annamalai, K.; Schmidt, M.; Reif, B.; Schmidt, V.; Grigorieff, N.; Fändrich, M., Physical basis of amyloid fibril polymorphism. *Nature Communications* **2018,** *9* (1), 699.
72. Yakupova, Elmira I.; Bobyleva, Liya G.; Vikhlyantsev, Ivan M.; Bobylev, Alexander G., Congo Red and amyloids: history and relationship. *Bioscience Reports* **2019,** *39* (1).
73. Del Pozo-Yauner, L.; Becerril, B.; Ochoa-Leyva, A.; Rodríguez-Ambriz, S. L.; Carrión, J. I. P.; Zavala-Padilla, G.; Sánchez-López, R.; Velasco, D. A. F., The Structural Determinants of the Immunoglobulin Light Chain Amyloid Aggregation. **2015**, 1-28.
74. Eisenberg, D.; Jucker, M., The Amyloid State of Proteins in Human Diseases. *Cell* **2012,** *148* (6), 1188-1203.
75. Perrett, S.; Serpell, L., Amyloid structure. *Essays in Biochemistry* **2014,** *56*, 1-10.
76. Chiti, F.; Dobson, C. M., Protein Misfolding, Amyloid Formation, and Human Disease: A Summary of Progress Over the Last Decade. *Annual Review of Biochemistry* **2017,** *86* (1), 27-68.
77. Ostermeier, L.; de Oliveira, G. A. P.; Dzwolak, W.; Silva, J. L.; Winter, R., Exploring the polymorphism, conformational dynamics and function of amyloidogenic peptides and proteins by temperature and pressure modulation. *Biophysical Chemistry* **2021,** *268*, 106506.
78. Jiménez, J. L.; Nettleton, E. J.; Bouchard, M.; Robinson, C. V.; Dobson, C. M.; Saibil, H. R., The protofilament structure of insulin amyloid fibrils. *Proceedings of the National Academy of Sciences* **2002,** *99* (14), 9196-9201.
79. Arosio, P.; Knowles, T. P. J.; Linse, S., On the lag phase in amyloid fibril formation. *Physical Chemistry Chemical Physics* **2015,** *17* (12), 7606-7618.

80. Krebs, M. R. H.; MacPhee, C. E.; Miller, A. F.; Dunlop, I. E.; Dobson, C. M.; Donald, A. M., The formation of spherulites by amyloid fibrils of bovine insulin. *Proceedings of the National Academy of Sciences* **2004,** *101* (40), 14420-14424.
81. Smith, M. I.; Foderà, V.; Sharp, J. S.; Roberts, C. J.; Donald, A. M., Factors affecting the formation of insulin amyloid spherulites. *Colloids and Surfaces B: Biointerfaces* **2012,** *89*, 216-222.
82. Vetri, V.; Foderà, V., The route to protein aggregate superstructures: Particulates and amyloid-like spherulites. *FEBS Letters* **2015,** *589* (19PartA), 2448-2463.
83. Picken, Maria M., The Pathology of Amyloidosis in Classification: A Review. *Acta Haematologica* **2020,** *143* (4), 322-334.
84. Sawaya, M. R.; Hughes, M. P.; Rodriguez, J. A.; Riek, R.; Eisenberg, D. S., The expanding amyloid family: Structure, stability, function, and pathogenesis. *Cell* **2021,** *184* (19), 4857-4873.
85. Naiki, H.; Sekijima, Y.; Ueda, M.; Ohashi, K.; Hoshii, Y.; Shimoda, M.; Ando, Y., Human amyloidosis, still intractable but becoming curable: The essential role of pathological diagnosis in the selection of type-specific therapeutics. *Pathology International* **2020,** *70* (4), 191-198.
86. Fowler, D. M.; Koulov, A. V.; Balch, W. E.; Kelly, J. W., Functional amyloid – from bacteria to humans. *Trends in Biochemical Sciences* **2007,** *32* (5), 217-224.
87. Chapman, M. R.; Robinson, L. S.; Pinkner, J. S.; Roth, R.; Heuser, J.; Hammar, M.; Normark, S.; Hultgren, S. J., Role of Escherichia coli Curli Operons in Directing Amyloid Fiber Formation. *Science* **2002,** *295* (5556), 851-855.
88. Otzen, D.; Riek, R., Functional Amyloids. *Cold Spring Harbor Perspectives in Biology* **2019,** *11* (12), a033860.
89. Yan, Z.; Yin, M.; Chen, J.; Li, X., Assembly and substrate recognition of curli biogenesis system. *Nature Communications* **2020,** *11* (1) 241.
90. Bokhove, M.; Claessen, D.; de Jong, W.; Dijkhuizen, L.; Boekema, E. J.; Oostergetel, G. T., Chaplins of Streptomyces coelicolor self-assemble into two distinct functional amyloids. *Journal of Structural Biology* **2013,** *184* (2), 301-309.
91. Watt, B.; van Niel, G.; Fowler, D. M.; Hurbain, I.; Luk, K. C.; Stayrook, S. E.; Lemmon, M. A.; Raposo, G.; Shorter, J.; Kelly, J. W.; Marks, M. S., N-terminal Domains Elicit Formation of Functional Pmel17 Amyloid Fibrils. *Journal of Biological Chemistry* **2009,** *284* (51), 35543-35555.
92. Kelly, J. W.; Balch, W. E., Amyloid as a natural product. *The Journal of Cell Biology* **2003,** *161* (3), 461-462.
93. Knowles, T. P. J.; Buehler, M. J., Nanomechanics of functional and pathological amyloid materials. *Nature Nanotechnology* **2011,** *6* (8), 469-479.
94. Shammas, Sarah L.; Knowles, Tuomas P. J.; Baldwin, Andrew J.; MacPhee, Cait E.; Welland, Mark E.; Dobson, Christopher M.; Devlin, Glyn L., Perturbation of the Stability of Amyloid Fibrils through Alteration of Electrostatic Interactions. *Biophysical Journal* **2011,** *100* (11), 2783-2791.
95. Meersman, F.; Dobson, C. M., Probing the pressure–temperature stability of amyloid fibrils provides new insights into their molecular properties. *Biochimica et Biophysica Acta (BBA) - Proteins and Proteomics* **2006,** *1764* (3), 452-460.
96. Aubrey, L. D.; Blakeman, B. J. F.; Lutter, L.; Serpell, C. J.; Tuite, M. F.; Serpell, L. C.; Xue, W.-F., Quantification of amyloid fibril polymorphism by nano-morphometry reveals the individuality of filament assembly. *Communications Chemistry* **2020,** *3* (1) 125.

97. Lutter, L.; Serpell, C. J.; Tuite, M. F.; Xue, W.-F., The molecular lifecycle of amyloid – Mechanism of assembly, mesoscopic organisation, polymorphism, suprastructures, and biological consequences. *Biochimica et Biophysica Acta (BBA) - Proteins and Proteomics* **2019,** *1867* (11), 140257.
98. White, H. E.; Hodgkinson, J. L.; Jahn, T. R.; Cohen-Krausz, S.; Gosal, W. S.; Müller, S.; Orlova, E. V.; Radford, S. E.; Saibil, H. R., Globular Tetramers of β2-Microglobulin Assemble into Elaborate Amyloid Fibrils. *Journal of Molecular Biology* **2009,** *389* (1), 48-57.
99. Fändrich, M.; Meinhardt, J.; Grigorieff, N., Structural polymorphism of Alzheimer Aβ and other amyloid fibrils. *Prion* **2014,** *3* (2), 89-93.
100. Fändrich, M.; Nyström, S.; Nilsson, K. P. R.; Böckmann, A.; LeVine, H.; Hammarström, P., Amyloid fibril polymorphism: a challenge for molecular imaging and therapy. *Journal of Internal Medicine* **2018,** *283* (3), 218-237.
101. Adamcik, J.; Mezzenga, R., Proteins Fibrils from a Polymer Physics Perspective. *Macromolecules* **2011,** *45* (3), 1137-1150.
102. Usov, I.; Adamcik, J.; Mezzenga, R., Polymorphism Complexity and Handedness Inversion in Serum Albumin Amyloid Fibrils. *ACS Nano* **2013,** *7* (12), 10465-10474.
103. Ke, P. C.; Zhou, R.; Serpell, L. C.; Riek, R.; Knowles, T. P. J.; Lashuel, H. A.; Gazit, E.; Hamley, I. W.; Davis, T. P.; Fändrich, M.; Otzen, D. E.; Chapman, M. R.; Dobson, C. M.; Eisenberg, D. S.; Mezzenga, R., Half a century of amyloids: past, present and future. *Chemical Society Reviews* **2020,** *49* (15), 5473-5509.
104. Reynolds, N. P.; Adamcik, J.; Berryman, J. T.; Handschin, S.; Zanjani, A. A. H.; Li, W.; Liu, K.; Zhang, A.; Mezzenga, R., Competition between crystal and fibril formation in molecular mutations of amyloidogenic peptides. *Nature Communications* **2017,** *8* (1).
105. Zielinski, M.; Röder, C.; Schröder, G. F., Challenges in sample preparation and structure determination of amyloids by cryo-EM. *Journal of Biological Chemistry* **2021,** *297* (2), 100938.
106. Bolisetty, S.; Adamcik, J.; Mezzenga, R., Snapshots of fibrillation and aggregation kinetics in multistranded amyloid β-lactoglobulin fibrils. *Soft Matter* **2011,** *7* (2), 493-499.
107. Zhang, S.; Andreasen, M.; Nielsen, J. T.; Liu, L.; Nielsen, E. H.; Song, J.; Ji, G.; Sun, F.; Skrydstrup, T.; Besenbacher, F.; Nielsen, N. C.; Otzen, D. E.; Dong, M., Coexistence of ribbon and helical fibrils originating from hIAPP 20–29 revealed by quantitative nanomechanical atomic force microscopy. *Proceedings of the National Academy of Sciences* **2013,** *110* (8), 2798-2803.
108. Lu, K.; Jacob, J.; Thiyagarajan, P.; Conticello, V. P.; Lynn, D. G., Exploiting Amyloid Fibril Lamination for Nanotube Self-Assembly. *Journal of the American Chemical Society* **2003,** *125* (21), 6391-6393.
109. Morris, K. L.; Zibaee, S.; Chen, L.; Goedert, M.; Sikorski, P.; Serpell, L. C., The Structure of Cross-β Tapes and Tubes Formed by an Octapeptide, αSβ1. *Angewandte Chemie International Edition* **2013,** *52* (8), 2279-2283.
110. Sarroukh, R.; Goormaghtigh, E.; Ruysschaert, J.-M.; Raussens, V., ATR-FTIR: A "rejuvenated" tool to investigate amyloid proteins. *Biochimica et Biophysica Acta (BBA) - Biomembranes* **2013,** *1828* (10), 2328-2338.
111. Kafle, B.; Böcker, U.; Wubshet, S. G.; Dankel, K.; Måge, I.; O`Farrell, M.; Afseth, N. K., Fourier-transform infrared spectroscopy for characterization of liquid protein solutions: A comparison of two sampling techniques. *Vibrational Spectroscopy* **2023,** *124*, 103490.
112. Barth, A., Infrared spectroscopy of proteins. *Biochimica et Biophysica Acta (BBA) - Bioenergetics* **2007,** *1767* (9), 1073-1101.

113. Oh, K. I.; Fiorin, G.; Gai, F., How Sensitive is the Amide I Vibration of the Polypeptide Backbone to Electric Fields? *ChemPhysChem* **2015,** *16* (17), 3595-3598.
114. Kong, J.; Yu, S., Fourier Transform Infrared Spectroscopic Analysis of Protein Secondary Structures. *Acta Biochimica et Biophysica Sinica* **2007,** *39* (8), 549-559.
115. Surewicz, W. K.; Mantsch, H. H., New insight into protein secondary structure from resolution-enhanced infrared spectra. *Biochimica et Biophysica Acta (BBA) - Protein Structure and Molecular Enzymology* **1988,** *952*, 115-130.
116. Barth, A.; Zscherp, C., What vibrations tell about proteins. *Quarterly Reviews of Biophysics* **2003,** *35* (4), 369-430.
117. Rodger, A., Far UV Protein Circular Dichroism. **2013**, 726-730.
118. Micsonai, A.; Wien, F.; Kernya, L.; Lee, Y.-H.; Goto, Y.; Réfrégiers, M.; Kardos, J., Accurate secondary structure prediction and fold recognition for circular dichroism spectroscopy. *Proceedings of the National Academy of Sciences* **2015,** *112* (24), E3095-E3103.
119. Micsonai, A.; Wien, F.; Bulyáki, É.; Kun, J.; Moussong, É.; Lee, Y.-H.; Goto, Y.; Réfrégiers, M.; Kardos, J., BeStSel: a web server for accurate protein secondary structure prediction and fold recognition from the circular dichroism spectra. *Nucleic Acids Research* **2018,** *46* (W1), W315-W322.
120. Greenfield, N. J., Using circular dichroism spectra to estimate protein secondary structure. *Nature Protocols* **2007,** *1* (6), 2876-2890.
121. Woollett, B.; Whitmore, L.; Janes, R. W.; Wallace, B. A., ValiDichro: a website for validating and quality control of protein circular dichroism spectra. *Nucleic Acids Research* **2013,** *41* (W1), W417-W421.
122. Roach, C. A.; Simpson, J. V.; JiJi, R. D., Evolution of quantitative methods in protein secondary structure determination via deep-ultraviolet resonance Raman spectroscopy. *The Analyst* **2012,** *137* (3), 555-562.
123. Huang, C. Y.; Balakrishnan, G.; Spiro, T. G., Protein secondary structure from deep-UV resonance Raman spectroscopy. *Journal of Raman Spectroscopy* **2006,** *37* (1-3), 277-282.
124. Moran, S. D.; Zanni, M. T., How to Get Insight into Amyloid Structure and Formation from Infrared Spectroscopy. *The Journal of Physical Chemistry Letters* **2014,** *5* (11), 1984-1993.
125. Micsonai, A.; Bulyáki, É.; Kardos, J., BeStSel: From Secondary Structure Analysis to Protein Fold Prediction by Circular Dichroism Spectroscopy. **2021,** *2199*, 175-189.
126. Miles, A. J.; Wallace, B. A., Circular dichroism spectroscopy of membrane proteins. *Chemical Society Reviews* **2016,** *45* (18), 4859-4872.
127. Ren, H.; Jiang, J.; Mukamel, S., Deep UV Resonance Raman Spectroscopy of β-Sheet Amyloid Fibrils: A QM/MM Simulation. *The Journal of Physical Chemistry B* **2011,** *115* (47), 13955-13962.
128. Adamcik, J.; Mezzenga, R., Study of amyloid fibrils via atomic force microscopy. *Current Opinion in Colloid & Interface Science* **2012,** *17* (6), 369-376.
129. Bednarikova, Z.; Gazova, Z.; Valle, F.; Bystrenova, E., Atomic force microscopy as an imaging tool to study the bio/nonbio complexes. *Journal of Microscopy* **2020,** *280* (3), 241-251.
130. Rizvi, A.; Mulvey, J. T.; Carpenter, B. P.; Talosig, R.; Patterson, J. P., A Close Look at Molecular Self-Assembly with the Transmission Electron Microscope. *Chemical Reviews* **2021,** *121* (22), 14232-14280.

131. Wang, Z. L.; Lee, J. L., Electron Microscopy Techniques for Imaging and Analysis of Nanoparticles. **2008**, 395-443.
132. Franken, L. E.; Grünewald, K.; Boekema, E. J.; Stuart, M. C. A., A Technical Introduction to Transmission Electron Microscopy for Soft-Matter: Imaging, Possibilities, Choices, and Technical Developments. *Small* **2020,** *16* (14), 1906198.
133. Wang, M.; Wang, J.; Zhou, P.; Deng, J.; Zhao, Y.; Sun, Y.; Yang, W.; Wang, D.; Li, Z.; Hu, X.; King, S. M.; Rogers, S. E.; Cox, H.; Waigh, T. A.; Yang, J.; Lu, J. R.; Xu, H., Nanoribbons self-assembled from short peptides demonstrate the formation of polar zippers between β-sheets. *Nature Communications* **2018,** *9* (1), 5118.
134. Prasad, S.; Mandal, I.; Singh, S.; Paul, A.; Mandal, B.; Venkatramani, R.; Swaminathan, R., Near UV-Visible electronic absorption originating from charged amino acids in a monomeric protein. *Chemical Science* **2017,** *8* (8), 5416-5433.
135. Wetlaufer, D. B., Ultraviolet spectra Of Proteins and Amino Acids. In *Advances in Protein Chemistry*, Anfinsen, C. B.; Bailey, K.; Anson, M. L.; Edsall, J. T., Eds. Academic Press: 1963; Vol. 17, pp 303-390.
136. Eftink, M. R., The use of fluorescence methods to monitor unfolding transitions in proteins. *Biophysical Journal* **1994,** *66* (2), 482-501.
137. Morzan, U. N.; Díaz Mirón, G.; Grisanti, L.; González Lebrero, M. C.; Kaminski Schierle, G. S.; Hassanali, A., Non-Aromatic Fluorescence in Biological Matter: The Exception or the Rule? *The Journal of Physical Chemistry B* **2022,** *126* (38), 7203-7211.
138. Pinotsi, D.; Grisanti, L.; Mahou, P.; Gebauer, R.; Kaminski, C. F.; Hassanali, A.; Kaminski Schierle, G. S., Proton Transfer and Structure-Specific Fluorescence in Hydrogen Bond-Rich Protein Structures. *Journal of the American Chemical Society* **2016,** *138* (9), 3046-3057.
139. Sirangelo, I.; Borriello, M.; Irace, G.; Iannuzzi, C., Intrinsic blue-green fluorescence in amyloyd fibrils. *AIMS Biophysics* **2018,** *5* (2), 155-165.
140. Jong, K. H.; Azar, Y. T.; Grisanti, L.; Stephens, A. D.; Jones, S. T. E.; Credgington, D.; Kaminski Schierle, G. S.; Hassanali, A., Low energy optical excitations as an indicator of structural changes initiated at the termini of amyloid proteins. *Physical Chemistry Chemical Physics* **2019,** *21* (43), 23931-23942.
141. Grisanti, L.; Sapunar, M.; Hassanali, A.; Došlić, N., Toward Understanding Optical Properties of Amyloids: A Reaction Path and Nonadiabatic Dynamics Study. *Journal of the American Chemical Society* **2020,** *142* (42), 18042-18049.
142. Lapshina, N.; Shishkin, I. I.; Nandi, R.; Noskov, R. E.; Barhom, H.; Joseph, S.; Apter, B.; Ellenbogen, T.; Natan, A.; Ginzburg, P.; Amdursky, N.; Rosenman, G., Bioinspired Amyloid Nanodots with Visible Fluorescence. *Advanced Optical Materials* **2018,** *7* (5), 1801400.
143. Apter, B.; Lapshina, N.; Lapsker, I.; Handelman, A.; Accardo, A.; Diaferia, C.; Morelli, G.; Rosenman, G., Fold-Sensitive Visible Fluorescence in β-Sheet Peptide Structures. *Advanced Optical Materials* **2021,** *9* (23), 2002247.
144. Arnon, Z. A.; Kreiser, T.; Yakimov, B.; Brown, N.; Aizen, R.; Shaham-Niv, S.; Makam, P.; Qaisrani, M. N.; Poli, E.; Ruggiero, A.; Slutsky, I.; Hassanali, A.; Shirshin, E.; Levy, D.; Gazit, E., On-off transition and ultrafast decay of amino acid luminescence driven by modulation of supramolecular packing. *iScience* **2021,** *24* (7), 102695.
145. Joseph, S. K.; Kuritz, N.; Yahel, E.; Lapshina, N.; Rosenman, G.; Natan, A., Proton-Transfer-Induced Fluorescence in Self-Assembled Short Peptides. *The Journal of Physical Chemistry A* **2019,** *123* (9), 1758-1765.

146. Zhou, S.; Wang, L., Unraveling the structural and chemical features of biological short hydrogen bonds. *Chemical Science* **2019,** *10* (33), 7734-7745.
147. Stephens, A. D.; Qaisrani, M. N.; Ruggiero, M. T.; Díaz Mirón, G.; Morzan, U. N.; González Lebrero, M. C.; Jones, S. T. E.; Poli, E.; Bond, A. D.; Woodhams, P. J.; Kleist, E. M.; Grisanti, L.; Gebauer, R.; Zeitler, J. A.; Credgington, D.; Hassanali, A.; Kaminski Schierle, G. S., Short hydrogen bonds enhance nonaromatic protein-related fluorescence. *Proceedings of the National Academy of Sciences* **2021,** *118* (21), e2020389118.
148. Kumar, A.; Ahari, D.; Priyadarshi, A.; Ziauddin Ansari, M.; Swaminathan, R., Weak Intrinsic Luminescence in Monomeric Proteins Arising from Charge Recombination. *The Journal of Physical Chemistry B* **2020,** *124* (14), 2731-2746.
149. Mirón, G. D.; Semelak, J. A.; Grisanti, L.; Rodriguez, A.; Conti, I.; Stella, M.; Velusamy, J.; Seriani, N.; Došlić, N.; Rivalta, I.; Garavelli, M.; Estrin, D. A.; Kaminski Schierle, G. S.; González Lebrero, M. C.; Hassanali, A.; Morzan, U. N., The carbonyl-lock mechanism underlying non-aromatic fluorescence in biological matter. *Nature Communications* **2023,** *14* (1), 7325.
150. Chopade, P.; Chopade, N.; Zhao, Z.; Mitragotri, S.; Liao, R.; Chandran Suja, V., Alzheimer's and Parkinson's disease therapies in the clinic. *Bioengineering & Translational Medicine* **2022,** *8* (1), e10367.
151. Stsiapura, V. I.; Maskevich, A. A.; Kuzmitsky, V. A.; Turoverov, K. K.; Kuznetsova, I. M., Computational Study of Thioflavin T Torsional Relaxation in the Excited State. *The Journal of Physical Chemistry A* **2007,** *111* (22), 4829-4835.
152. Qin, Z.; Sun, Y.; Jia, B.; Wang, D.; Ma, Y.; Ma, G., Kinetic Mechanism of Thioflavin T Binding onto the Amyloid Fibril of Hen Egg White Lysozyme. *Langmuir* **2017,** *33* (22), 5398-5405.
153. Groenning, M., Binding mode of Thioflavin T and other molecular probes in the context of amyloid fibrils—current status. *Journal of Chemical Biology* **2009,** *3* (1), 1-18.
154. Krebs, M. R. H.; Bromley, E. H. C.; Donald, A. M., The binding of thioflavin-T to amyloid fibrils: localisation and implications. *Journal of Structural Biology* **2005,** *149* (1), 30-37.
155. Biancalana, M.; Koide, S., Molecular mechanism of Thioflavin-T binding to amyloid fibrils. *Biochimica et Biophysica Acta (BBA) - Proteins and Proteomics* **2010,** *1804* (7), 1405-1412.
156. Wu, C.; Scott, J.; Shea, J.-E., Binding of Congo Red to Amyloid Protofibrils of the Alzheimer Aβ9–40 Peptide Probed by Molecular Dynamics Simulations. *Biophysical Journal* **2012,** *103* (3), 550-557.
157. Klunk, W. E.; Pettegrew, J. W.; Abraham, D. J., Quantitative evaluation of congo red binding to amyloid-like proteins with a beta-pleated sheet conformation. *The journal of histochemistry and cytochemistry : official journal of the Histochemistry Society* **1989,** *37* (8), 1273-81.
158. Carter, D. B.; Chou, K. C., A Model for Structure-Dependent Binding of Congo Red to Alzheimer β-Amyloid Fibrils. *Neurobiology of Aging* **1998,** *19* (1), 37-40.
159. Turnell, W. G.; Finch, J. T., Binding of the dye congo red to the amyloid protein pig insulin reveals a novel homology amongst amyloid-forming peptide sequences. *Journal of Molecular Biology* **1992,** *227* (4), 1205-1223.
160. Hemmer, E.; Benayas, A.; Légaré, F.; Vetrone, F., Exploiting the biological windows: current perspectives on fluorescent bioprobes emitting above 1000 nm. *Nanoscale Horizons* **2016,** *1* (3), 168-184.

161. Hemmer, E.; Venkatachalam, N.; Hyodo, H.; Hattori, A.; Ebina, Y.; Kishimoto, H.; Soga, K., Upconverting and NIR emitting rare earth based nanostructures for NIR-bioimaging. *Nanoscale* **2013,** *5* (23), 11339-11361.
162. Gao, D.; Hu, D.; Liu, X.; Zhang, X.; Yuan, Z.; Sheng, Z.; Zheng, H., Recent Advances in Conjugated Polymer Nanoparticles for NIR-II Imaging and Therapy. *ACS Applied Polymer Materials* **2020,** *2* (10), 4241-4257.
163. Tong, H.; Lou, K.; Wang, W., Near-infrared fluorescent probes for imaging of amyloid plaques in Alzheimer's disease. *Acta Pharmaceutica Sinica B* **2015,** *5* (1), 25-33.
164. Nesterov, E. E.; Skoch, J.; Hyman, B. T.; Klunk, W. E.; Bacskai, B. J.; Swager, T. M., In Vivo Optical Imaging of Amyloid Aggregates in Brain: Design of Fluorescent Markers. *Angewandte Chemie International Edition* **2005,** *44* (34), 5452-5456.
165. Ran, C.; Xu, X.; Raymond, S. B.; Ferrara, B. J.; Neal, K.; Bacskai, B. J.; Medarova, Z.; Moore, A., Design, Synthesis, and Testing of Difluoroboron-Derivatized Curcumins as Near-Infrared Probes for in Vivo Detection of Amyloid-β Deposits. *Journal of the American Chemical Society* **2009,** *131* (42), 15257-15261.
166. Peng, C.; Wang, X.; Li, Y.; Li, H.-W.; Wong, M. S., Versatile fluorescent probes for near-infrared imaging of amyloid-β species in Alzheimer's disease mouse model. *Journal of Materials Chemistry B* **2019,** *7* (12), 1986-1995.
167. Hintersteiner, M.; Enz, A.; Frey, P.; Jaton, A.-L.; Kinzy, W.; Kneuer, R.; Neumann, U.; Rudin, M.; Staufenbiel, M.; Stoeckli, M.; Wiederhold, K.-H.; Gremlich, H.-U., In vivo detection of amyloid-β deposits by near-infrared imaging using an oxazine-derivative probe. *Nature Biotechnology* **2005,** *23* (5), 577-583.
168. Wu, J.; Shao, C.; Ye, X.; Di, X.; Li, D.; Zhao, H.; Zhang, B.; Chen, G.; Liu, H.-K.; Qian, Y., In Vivo Brain Imaging of Amyloid-β Aggregates in Alzheimer's Disease with a Near-Infrared Fluorescent Probe. *ACS Sensors* **2021,** *6* (3), 863-870.
169. Bajad, N. G.; Kumar, A.; Singh, S. K., Recent Advances in the Development of Near-Infrared Fluorescent Probes for the in Vivo Brain Imaging of Amyloid-β Species in Alzheimer's Disease. *ACS Chemical Neuroscience* **2023,** *14* (17), 2955-2967.
170. Chen, Y.; Yuan, C.; Xie, T.; Li, Y.; Dai, B.; Zhou, K.; Liang, Y.; Dai, J.; Tan, H.; Cui, M., N,O-Benzamide difluoroboron complexes as near-infrared probes for the detection of β-amyloid and tau fibrils. *Chemical Communications* **2020,** *56* (53), 7269-7272.
171. Kwan, A. C.; Duff, K.; Gouras, G. K.; Webb, W. W., Optical visualization of Alzheimer's pathology via multiphoton-excited intrinsic fluorescence and second harmonic generation. *Opt. Express* **2009,** *17* (5), 3679-3689.
172. Johansson, P. K.; Koelsch, P., Label-free imaging of amyloids using their intrinsic linear and nonlinear optical properties. *Biomedical Optics Express* **2017,** *8* (2), 743-756.
173. Hanczyc, P.; Samoc, M.; Norden, B., Multiphoton absorption in amyloid protein fibres. *Nature Photonics* **2013,** *7* (12), 969-972.
174. Obstarczyk, P.; Lipok, M.; Grelich-Mucha, M.; Samoć, M.; Olesiak-Bańska, J., Two-Photon Excited Polarization-Dependent Autofluorescence of Amyloids as a Label-Free Method of Fibril Organization Imaging. *The Journal of Physical Chemistry Letters* **2021,** *12* (5), 1432-1437.
175. Pansieri, J.; Josserand, V.; Lee, S.-J.; Rongier, A.; Imbert, D.; Sallanon, M. M.; Kövari, E.; Dane, T. G.; Vendrely, C.; Chaix-Pluchery, O.; Guidetti, M.; Vollaire, J.; Fertin, A.; Usson, Y.; Rannou, P.; Coll, J.-L.; Marquette, C.; Forge, V., Ultraviolet–visible–near-infrared optical properties of amyloid fibrils shed light on amyloidogenesis. *Nature Photonics* **2019,** *13* (7), 473-479.

176. Tian, Y.; Viles, J. H., pH Dependence of Amyloid-β Fibril Assembly Kinetics: Unravelling the Microscopic Molecular Processes. *Angewandte Chemie International Edition* **2022,** *61* (48), e202210675.
177. Pauling, L.; Corey, R. B., Configurations of Polypeptide Chains With Favored Orientations Around Single Bonds. *Proceedings of the National Academy of Sciences* **1951,** *37* (11), 729-740.
178. Pauling, L.; Corey, R. B., Two Rippled-Sheet Configurations of Polypeptide Chains, and a Note about the Pleated Sheets. *Proceedings of the National Academy of Sciences* **1953,** *39* (4), 253-256.
179. Raskatov, J. A.; Schneider, J. P.; Nilsson, B. L., Defining the Landscape of the Pauling-Corey Rippled Sheet: An Orphaned Motif Finding New Homes. *Accounts of Chemical Research* **2021,** *54* (10), 2488-2501.
180. Dutta, S.; Foley, A. R.; Warner, C. J. A.; Zhang, X.; Rolandi, M.; Abrams, B.; Raskatov, J. A., Suppression of Oligomer Formation and Formation of Non-Toxic Fibrils upon Addition of Mirror-Image Aβ42 to the Natural l-Enantiomer. *Angewandte Chemie International Edition* **2017,** *56* (38), 11506-11510.
181. Swanekamp, R. J.; DiMaio, J. T. M.; Bowerman, C. J.; Nilsson, B. L., Coassembly of Enantiomeric Amphipathic Peptides into Amyloid-Inspired Rippled β-Sheet Fibrils. *Journal of the American Chemical Society* **2012,** *134* (12), 5556-5559.
182. Nagy-Smith, K.; Beltramo, P. J.; Moore, E.; Tycko, R.; Furst, E. M.; Schneider, J. P., Molecular, Local, and Network-Level Basis for the Enhanced Stiffness of Hydrogel Networks Formed from Coassembled Racemic Peptides: Predictions from Pauling and Corey. *ACS Central Science* **2017,** *3* (6), 586-597.
183. Nagy, K. J.; Giano, M. C.; Jin, A.; Pochan, D. J.; Schneider, J. P., Enhanced Mechanical Rigidity of Hydrogels Formed from Enantiomeric Peptide Assemblies. *Journal of the American Chemical Society* **2011,** *133* (38), 14975-14977.
184. Manolis, A. S.; Manolis, A. A.; Manolis, T. A.; Melita, H., Cardiac amyloidosis: An underdiagnosed/underappreciated disease. *European Journal of Internal Medicine* **2019,** *67*, 1-13.
185. Jaroniec, C. P.; MacPhee, C. E.; Astrof, N. S.; Dobson, C. M.; Griffin, R. G., Molecular conformation of a peptide fragment of transthyretin in an amyloid fibril. *Proceedings of the National Academy of Sciences* **2002,** *99* (26), 16748-16753.
186. Fitzpatrick, A. W. P.; Debelouchina, G. T.; Bayro, M. J.; Clare, D. K.; Caporini, M. A.; Bajaj, V. S.; Jaroniec, C. P.; Wang, L.; Ladizhansky, V.; Müller, S. A.; MacPhee, C. E.; Waudby, C. A.; Mott, H. R.; De Simone, A.; Knowles, T. P. J.; Saibil, H. R.; Vendruscolo, M.; Orlova, E. V.; Griffin, R. G.; Dobson, C. M., Atomic structure and hierarchical assembly of a cross-β amyloid fibril. *Proceedings of the National Academy of Sciences* **2013,** *110* (14), 5468-5473.
187. Grelich-Mucha, M.; Garcia, A. M.; Torbeev, V.; Ożga, K.; Berlicki, Ł.; Olesiak-Bańska, J., Autofluorescence of Amyloids Determined by Enantiomeric Composition of Peptides. *The Journal of Physical Chemistry B* **2021,** *125* (21), 5502-5510.
188. Raskatov, J. A., A DFT study of structure and stability of pleated and rippled cross-β sheets with hydrophobic sidechains. *Biopolymers* **2020,** *112* (1).
189. Raskatov, J. A., Conformational Selection as the Driving Force of Amyloid β Chiral Inactivation. *ChemBioChem* **2020,** *21* (20), 2945-2949.
190. Lee, J.; Ju, M.; Cho, O. H.; Kim, Y.; Nam, K. T., Tyrosine-Rich Peptides as a Platform for Assembly and Material Synthesis. *Advanced Science* **2018,** *6* (4), 1801255.

191. Malencik, D. A.; Sprouse, J. F.; Swanson, C. A.; Anderson, S. R., Dityrosine: Preparation, Isolation, and Analysis. *Analytical Biochemistry* **1996,** *242* (2), 202-213.
192. Malencik, D. A.; Anderson, S. R., Dityrosine as a product of oxidative stress and fluorescent probe. *Amino Acids* **2003,** *25* (3-4), 233-247.
193. Subramanyam, R.; Correia, M.; Neves-Petersen, M. T.; Jeppesen, P. B.; Gregersen, S.; Petersen, S. B., UV-Light Exposure of Insulin: Pharmaceutical Implications upon Covalent Insulin Dityrosine Dimerization and Disulphide Bond Photolysis. *PLoS ONE* **2012,** *7* (12), e50733.
194. Mukherjee, S.; Kapp, E. A.; Lothian, A.; Roberts, A. M.; Vasil'ev, Y. V.; Boughton, B. A.; Barnham, K. J.; Kok, W. M.; Hutton, C. A.; Masters, C. L.; Bush, A. I.; Beckman, J. S.; Dey, S. G.; Roberts, B. R., Characterization and Identification of Dityrosine Cross-Linked Peptides Using Tandem Mass Spectrometry. *Analytical Chemistry* **2017,** *89* (11), 6136-6145.
195. Miller, L. M.; Bourassa, M. W.; Smith, R. J., FTIR spectroscopic imaging of protein aggregation in living cells. *Biochimica et Biophysica Acta (BBA) - Biomembranes* **2013,** *1828* (10), 2339-2346.
196. Jaroniec, C. P.; MacPhee, C. E.; Bajaj, V. S.; McMahon, M. T.; Dobson, C. M.; Griffin, R. G., High-resolution molecular structure of a peptide in an amyloid fibril determined by magic angle spinning NMR spectroscopy. *Proceedings of the National Academy of Sciences* **2004,** *101* (3), 711-716.
197. Grelich-Mucha, M.; Bachelart, T.; Torbeev, V.; Ożga, K.; Berlicki, Ł.; Olesiak-Bańska, J., Amyloid engineering – how terminal capping modifies morphology and secondary structure of supramolecular peptide aggregates. *Biomaterials Science* **2024,** *12* (6), 1590-1602.
198. Varland, S.; Osberg, C.; Arnesen, T., N-terminal modifications of cellular proteins: The enzymes involved, their substrate specificities and biological effects. *Proteomics* **2015,** *15* (14), 2385-2401.
199. Sharma, S.; Schiller, M. R., The carboxy-terminus, a key regulator of protein function. *Critical Reviews in Biochemistry and Molecular Biology* **2019,** *54* (2), 85-102.
200. Tao, K.; Wang, J.; Zhou, P.; Wang, C.; Xu, H.; Zhao, X.; Lu, J. R., Self-Assembly of Short Aβ(16−22) Peptides: Effect of Terminal Capping and the Role of Electrostatic Interaction. *Langmuir* **2011,** *27* (6), 2723-2730.
201. Andreasen, M.; Skeby, K. K.; Zhang, S.; Nielsen, E. H.; Klausen, L. H.; Frahm, H.; Christiansen, G.; Skrydstrup, T.; Dong, M.; Schiøtt, B.; Otzen, D., The Importance of Being Capped: Terminal Capping of an Amyloidogenic Peptide Affects Fibrillation Propensity and Fibril Morphology. *Biochemistry* **2014,** *53* (44), 6968-6980.
202. Hu, Y.; Lin, R.; Zhang, P.; Fern, J.; Cheetham, A. G.; Patel, K.; Schulman, R.; Kan, C.; Cui, H., Electrostatic-Driven Lamination and Untwisting of β-Sheet Assemblies. *ACS Nano* **2015,** *10* (1), 880-888.
203. Lee, M.; Na, S., End Capping Alters the Structural Characteristics and Mechanical Properties of Transthyretin (105-115) Amyloid Protofibrils. *ChemPhysChem* **2016,** *17* (3), 425-432.
204. Porrini, M.; Zachariae, U.; Barran, P. E.; MacPhee, C. E., Effect of Protonation State on the Stability of Amyloid Oligomers Assembled from TTR(105–115). *The Journal of Physical Chemistry Letters* **2013,** *4* (8), 1233-1238.
205. Stock, A.; Clarke, S.; Clarke, C.; Stock, J., N-terminal methylation of proteins: Structure, function and specificity. *FEBS Letters* **1987,** *220* (1), 8-14.

206. Diaz, K.; Meng, Y.; Huang, R., Past, present, and perspectives of protein N-terminal methylation. *Current Opinion in Chemical Biology* **2021,** *63*, 115-122.
207. Hughes, E.; Burke, R. M.; Doig, A. J., Inhibition of Toxicity in the β-Amyloid Peptide Fragment β-(25–35) Using N-Methylated Derivatives. *Journal of Biological Chemistry* **2000,** *275* (33), 25109-25115.
208. Cho, K. C.; Kang, J. W.; Choi, Y.; Kim, T. W.; Kim, K. P., Effects of peptide acetylation and dimethylation on electrospray ionization efficiency. *Journal of Mass Spectrometry* **2016,** *51* (2), 105-110.
209. Jentoft, N.; Dearborn, D. G., Labeling of proteins by reductive methylation using sodium cyanoborohydride. *Journal of Biological Chemistry* **1979,** *254* (11), 4359-4365.
210. Dasgupta, S.; Castro, L. M.; Tashima, A. K.; Fricker, L., Quantitative Peptidomics Using Reductive Methylation of Amines. **2018,** *1719*, 161-174.
211. Dutta, S.; Foley, A. R.; Warner, C. J. A.; Zhang, X.; Rolandi, M.; Abrams, B.; Raskatov, J. A., Suppression of Oligomer Formation and Formation of Non-Toxic Fibrils upon Addition of Mirror-Image Aβ42 to the Natural L-Enantiomer. *Angewandte Chemie International Edition* **2017,** *56* (38), 11506-11510.
212. Dutta, S.; Foley, A. R.; Kuhn, A. J.; Abrams, B.; Lee, H. W.; Raskatov, J. A., New insights into differential aggregation of enantiomerically pure and racemic Aβ40 systems. *Peptide Science* **2019,** *111* (6), e24139.
213. Garcia, A. M.; Giorgiutti, C.; El Khoury, Y.; Bauer, V.; Spiegelhalter, C.; Leize-Wagner, E.; Hellwig, P.; Potier, N.; Torbeev, V., Aggregation and Amyloidogenicity of the Nuclear Coactivator Binding Domain of CREB-Binding Protein. *Chemistry – A European Journal* **2020,** *26* (44), 9889-9899.
214. Glassford, S. E.; Byrne, B.; Kazarian, S. G., Recent applications of ATR FTIR spectroscopy and imaging to proteins. *Biochimica et Biophysica Acta (BBA) - Proteins and Proteomics* **2013,** *1834* (12), 2849-2858.
215. Surewicz, W. K.; Mantsch, H. H.; Chapman, D., Determination of protein secondary structure by Fourier transform infrared spectroscopy: A critical assessment. *Biochemistry* **2002,** *32* (2), 389-394.
216. Conway, K. A.; Harper, J. D.; Lansbury, P. T., Fibrils Formed in Vitro from α-Synuclein and Two Mutant Forms Linked to Parkinson's Disease are Typical Amyloid. *Biochemistry* **2000,** *39* (10), 2552-2563.
217. Raskatov, J. A.; Foley, A. R.; Louis, J. M.; Yau, W.-M.; Tycko, R., Constraints on the Structure of Fibrils Formed by a Racemic Mixture of Amyloid-β Peptides from Solid-State NMR, Electron Microscopy, and Theory. *Journal of the American Chemical Society* **2021,** *143* (33), 13299-13313.
218. Raskatov, J. A., Chiral Inactivation: An Old Phenomenon with a New Twist. *Chemistry - A European Journal* **2017,** *23* (67), 16920-16923.
219. Zhao, Z.; Zhang, H.; Lam, J. W. Y.; Tang, B. Z., Aggregation-Induced Emission: New Vistas at the Aggregate Level. *Angewandte Chemie International Edition* **2020,** *59* (25), 9888-9907.
220. Wang, Q.; Dou, X.; Chen, X.; Zhao, Z.; Wang, S.; Wang, Y.; Sui, K.; Tan, Y.; Gong, Y.; Zhang, Y.; Yuan, W. Z., Reevaluating Protein Photoluminescence: Remarkable Visible Luminescence upon Concentration and Insight into the Emission Mechanism. *Angewandte Chemie International Edition* **2019,** *58* (36), 12667-12673.

221. Tang, S.; Yang, T.; Zhao, Z.; Zhu, T.; Zhang, Q.; Hou, W.; Yuan, W. Z., Nonconventional luminophores: characteristics, advancements and perspectives. *Chemical Society Reviews* **2021,** *50* (22), 12616-12655.
222. Khodarahmi, R.; Niyangoda, C.; Miti, T.; Breydo, L.; Uversky, V.; Muschol, M., Carbonyl-based blue autofluorescence of proteins and amino acids. *Plos One* **2017,** *12* (5), e0176983.
223. Bhattacharya, A.; Bhowmik, S.; Singh, A. K.; Kodgire, P.; Das, A. K.; Mukherjee, T. K., Direct Evidence of Intrinsic Blue Fluorescence from Oligomeric Interfaces of Human Serum Albumin. *Langmuir* **2017,** *33* (40), 10606-10615.
224. Hill, S. E.; Robinson, J.; Matthews, G.; Muschol, M., Amyloid Protofibrils of Lysozyme Nucleate and Grow Via Oligomer Fusion. *Biophysical Journal* **2009,** *96* (9), 3781-3790.
225. Tokunaga, Y.; Sakakibara, Y.; Kamada, Y.; Watanabe, K.-i.; Sugimoto, Y., Analysis of Core Region from Egg White Lysozyme Forming Amyloid Fibrils. *International Journal of Biological Sciences* **2013,** *9* (2), 219-227.
226. Zhao, H.; Ghirlando, R.; Piszczek, G.; Curth, U.; Brautigam, C. A.; Schuck, P., Recorded scan times can limit the accuracy of sedimentation coefficients in analytical ultracentrifugation. *Analytical Biochemistry* **2013,** *437* (1), 104-108.
227. Schuck, P., Sedimentation Analysis of Noninteracting and Self-Associating Solutes Using Numerical Solutions to the Lamm Equation. *Biophysical Journal* **1998,** *75* (3), 1503-1512.
228. Schuck, P., Size-Distribution Analysis of Macromolecules by Sedimentation Velocity Ultracentrifugation and Lamm Equation Modeling. *Biophysical Journal* **2000,** *78* (3), 1606-1619.
229. Harding, S. E.; Rowe, A. J.; Horton, J. C., *Analytical ultracentrifugation in biochemistry and polymer science*. Royal Society of Chemistry: Cambridge England, 1992; p xiii, 629 p.
230. Brautigam, C. A., Calculations and Publication-Quality Illustrations for Analytical Ultracentrifugation Data. **2015,** *562*, 109-133.
231. Grande, V.; Shen, C.-A.; Deiana, M.; Dudek, M.; Olesiak-Banska, J.; Matczyszyn, K.; Würthner, F., Selective parallel G-quadruplex recognition by a NIR-to-NIR two-photon squaraine. *Chemical Science* **2018,** *9* (44), 8375-8381.
232. Kubista, M.; Sjöback, R.; Eriksson, S.; Albinsson, B., Experimental correction for the inner-filter effect in fluorescence spectra. *The Analyst* **1994,** *119* (3), 417-419.
233. Jesus, C. S. H.; Soares, H. T.; Piedade, A. P.; Cortes, L.; Serpa, C., Using amyloid autofluorescence as a biomarker for lysozyme aggregation inhibition. *The Analyst* **2021,** *146* (7), 2383-2391.
234. Grelich-Mucha, M.; Lipok, M.; Różycka, M.; Samoć, M.; Olesiak-Bańska, J., One- and Two-Photon Excited Autofluorescence of Lysozyme Amyloids. *The Journal of Physical Chemistry Letters* **2022,** *13* (21), 4673-4681.
235. Abeyrathne, E. D. N. S.; Lee, H. Y.; Ahn, D. U., Sequential separation of lysozyme, ovomucin, ovotransferrin, and ovalbumin from egg white. *Poultry Science* **2014,** *93* (4), 1001-1009.
236. Topping, T. B.; Gloss, L. M., The impact of solubility and electrostatics on fibril formation by the H3 and H4 histones. *Protein Science* **2011,** *20* (12), 2060-2073.
237. Babenko, V.; Surmacz-Chwedoruk, W.; Dzwolak, W., On the Function and Fate of Chloride Ions in Amyloidogenic Self-Assembly of Insulin in an Acidic Environment: Salt-Induced Condensation of Fibrils. *Langmuir* **2015,** *31* (7), 2180-2186.

238. Foley, J.; Hill, S. E.; Miti, T.; Mulaj, M.; Ciesla, M.; Robeel, R.; Persichilli, C.; Raynes, R.; Westerheide, S.; Muschol, M., Structural fingerprints and their evolution during oligomeric vs. oligomer-free amyloid fibril growth. *The Journal of Chemical Physics* **2013,** *139* (12), 121901.
239. Ansari, M. Z.; Kumar, A.; Ahari, D.; Priyadarshi, A.; Lolla, P.; Bhandari, R.; Swaminathan, R., Protein charge transfer absorption spectra: an intrinsic probe to monitor structural and oligomeric transitions in proteins. *Faraday Discussions* **2018,** *207*, 91-113.
240. de Reguardati, S.; Pahapill, J.; Mikhailov, A.; Stepanenko, Y.; Rebane, A., High-accuracy reference standards for two-photon absorption in the 680–1050 nm wavelength range. *Opt. Express* **2016,** *24* (8), 9053-9066.

Publishing statements

Herein, I included information that target figures/tables contained within this Doctoral Thesis constitute own source or were prepared by the author of the Thesis. Moreover, I present which figures/tables were reproduced, reprinted, or adapted and indicate the permissions.

In I. Introduction:

Figure 1-6: the graphs were prepared by the author of this dissertation.

Figure 7: the graphs (a-d) were adapted with permission from Brändén, C.-I.; Tooze, J., Introduction to protein structure. 2nd ed.; Garland Pub.: New York, 1999; p 1-32. Order license ID: 1599325-1.

Figure 8: the graph was adapted from Jahn, T. R.; Radford, S. E., Folding versus aggregation: Polypeptide conformations on competing pathways. Archives of Biochemistry and Biophysics 2008, 469 (1), 100-117 (available on https://www.sciencedirect.com/science/article/pii/S0003986107002731?via%3Dihub) with permission from Elsevier. The license: CC BY 3.0.

Figure 9: the graph was prepared by the author of this dissertation.

Figure 10: the graphs a-c were adapted from Fitzpatrick, A. W. P.; Falcon, B.; He, S.; Murzin, A. G.; Murshudov, G.; Garringer, H. J.; Crowther, R. A.; Ghetti, B.; Goedert, M.; Scheres, S. H. W., Cryo-EM structures of tau filaments from Alzheimer's disease. Nature 2017, 547 (7662), 185-190 (available on https://www.nature.com/articles/nature23002) with permission from Nature upon author's request. The license number: 6011321341222.

Figure 11: the graphs were adapted from Perrett, S.; Serpell, L., Amyloid structure. Essays in Biochemistry 2014, 56, 1-10 (available on https://portlandpress.com/essaysbiochem/article-abstract/doi/10.1042/bse0560001/78373/Amyloid-structure?redirectedFrom=fulltext) with permission from Portland Press.

Figure 12: the graph was reprinted from Adamcik, J.; Mezzenga, R., Amyloid Polymorphism in the Protein Folding and Aggregation Energy Landscape. Angewandte Chemie International Edition 2018, 57 (28), 8370-8382 (available on https://onlinelibrary.wiley.com/doi/abs/10.1002/anie.201713416) with permission from John Wiley and Sons upon author's request. The license number: 6011330150780.

Figure 13: the graphs (a, b) were adapted from Krebs, M. R. H.; MacPhee, C. E.; Miller, A. F.; Dunlop, I. E.; Dobson, C. M.; Donald, A. M., The formation of spherulites by amyloid fibrils of bovine insulin. Proceedings of the National Academy of Sciences 2004, 101 (40), 14420-14424 (available on https://www.pnas.org/doi/10.1073/pnas.0405933101) with permission. Copyright (2004) National Academy of Sciences.

Figure 14: the graphs (a, b, c) were adapted from Knowles, T. P. J.; Buehler, M. J., Nanomechanics of functional and pathological amyloid materials. Nature Nanotechnology 2011, 6 (8), 469-479 (available on https://www.nature.com/articles/nnano.2011.102) with permission from Springer Nature upon author's request. The license number: 6011330448780.

Figure 15: the graph (a) was adapted from Zielinski, M.; Röder, C.; Schröder, G. F., Challenges in sample preparation and structure determination of amyloids by cryo-EM. Journal of Biological Chemistry 2021, 297 (2), 100938 (available on https://www.jbc.org/article/S0021-9258(21)00738-9/fulltext) with permission from Elsevier. The license: Creative Commons CC-BY. The graph (b) was adapted with permission from Adamcik, J.; Mezzenga, R., Amyloid Polymorphism in the Protein Folding and Aggregation Energy Landscape. Angewandte Chemie International Edition 2018, 57 (28), 8370-8382 (available on: https://onlinelibrary.wiley.com/doi/epdf/10.1002/anie.201713416) with permission from John Wiley and Sons upon author's request. The license number: 6011330743439.

Figure 16: the graph (a) was prepared by the author of this dissertation. The graph (b) was adapted from Moran, S. D.; Zanni, M. T., How to Get Insight into Amyloid Structure and Formation from Infrared Spectroscopy. The Journal of Physical Chemistry Letters 2014, 5 (11), 1984-1993 (available on: https://pubs.acs.org/doi/10.1021/jz500794d) with permission. Copyright © 2014 American Chemical Society. The graphs (c, d) were adapted from Micsonai, A.; Bulyáki, É.; Kardos, J., BeStSel: From Secondary Structure Analysis to Protein Fold Prediction by Circular Dichroism Spectroscopy. 2021, 2199, 175-189 (available on: https://link.springer.com/protocol/10.1007/978-1-0716-0892-0_11#citeas) with permission from Spinger Nature under the terms of the Creative Commons Attribution 4.0 International License (http://creativecommons.org/licenses/by/4.0/).

Figure 17: the graph (a) was adapted from Adamcik, J.; Mezzenga, R., Study of amyloid fibrils via atomic force microscopy. Current Opinion in Colloid & Interface Science 2012, 17 (6), 369-376 (available on: https://www.sciencedirect.com/science/article/abs/pii/S1359029412000957) with permission from Elsevier upon author's request. The licence number: 6011330993593. The graph (b) was reprinted with permission from Rizvi, A.; Mulvey, J. T.; Carpenter, B. P.; Talosig, R.; Patterson, J. P., A Close Look at Molecular Self-Assembly with the Transmission Electron Microscope. Chemical Reviews 2021, 121 (22), 14232-14280 (available on https://pubs.acs.org/doi/10.1021/acs.chemrev.1c00189). Copyright © 2021 American Chemical Society. The graphs (c, d) were adapted from Wang, M.; Wang, J.; Zhou, P.; Deng, J.; Zhao, Y.; Sun, Y.; Yang, W.; Wang, D.; Li, Z.; Hu, X.; King, S. M.; Rogers, S. E.; Cox, H.; Waigh, T. A.; Yang, J.; Lu, J. R.; Xu, H., Nanoribbons self-assembled from short peptides demonstrate the formation of polar zippers between β-sheets. Nature Communications 2018, 9 (1), 5118 (available on: https://www.nature.com/articles/s41467-018-07583-2#citeas) with permission from Nature Springer under the terms of Creative Commons Attribution 4.0 International License (http://creativecommons.org/licenses/by/4.0/).

Figure 18: the graph (a) was prepared by the author of this dissertation. The graph (b) was adapted from Wetlaufer, D. B., Ultraviolet spectra Of Proteins and Amino Acids. 1963, 17, 303-390 (available on: https://www.sciencedirect.com/science/article/abs/pii/S006532330860056X?via%3Dihub) with permission from Elsevier. License number: 6011331380295.

Figure 19: the graphs (a, b, c) were adapted with permission from Pinotsi, D.; Grisanti, L.; Mahou, P.; Gebauer, R.; Kaminski, C. F.; Hassanali, A.; Kaminski Schierle, G. S., Proton Transfer and Structure-Specific Fluorescence in Hydrogen Bond-Rich Protein Structures. Journal of the American Chemical Society 2016, 138 (9), 3046-3057 (available on https://pubs.acs.org/doi/10.1021/jacs.5b11012). Copyright © 2016 American Chemical Society.

Figure 20: the graphs (a-d) were adapted from Mirón, G. D.; Semelak, J. A.; Grisanti, L.; Rodriguez, A.; Conti, I.; Stella, M.; Velusamy, J.; Seriani, N.; Došlić, N.; Rivalta, I.; Garavelli, M.; Estrin, D. A.; Kaminski Schierle, G. S.; González Lebrero, M. C.; Hassanali, A.; Morzan, U. N., The carbonyl-lock mechanism underlying non-aromatic fluorescence in biological matter. Nature Communications 2023, 14 (1), 7325 (available on: https://www.nature.com/articles/s41467-023-42874-3#rightslink) with permission from Springer Nature under the terms of the Creative Commons Attribution 4.0 International License (http://creativecommons.org/licenses/by/4.0/).

Figure 21: the graph (a) was prepared by the author of this dissertation. The graph (b) was adapted from Biancalana, M.; Koide, S., Molecular mechanism of Thioflavin-T binding to amyloid fibrils. Biochimica et Biophysica Acta (BBA) - Proteins and Proteomics 2010, 1804 (7), 1405-1412 (available on: https://www.sciencedirect.com/science/article/pii/S1570963910000993?via%3Dihub) with permission from Elsevier upon author's request. License number: 6012020009498.

Figure 22: the graphs (a, b) were adapted from Carter, D. B.; Chou, K. C., A Model for Structure-Dependent Binding of Congo Red to Alzheimer β-Amyloid Fibrils. Neurobiology of Aging 1998, 19 (1), 37-40 (available on: https://www.sciencedirect.com/science/article/abs/pii/S0197458097001644) with permission from Elsevier upon author's request. License number: 6012020161572.

Figure 23: the graph (a) was adapted from Hemmer, E.; Benayas, A.; Légaré, F.; Vetrone, F., Exploiting the biological windows: current perspectives on fluorescent bioprobes emitting above 1000 nm. Nanoscale Horizons 2016, 1 (3), 168-184 (available on:

https://pubs.rsc.org/en/content/articlelanding/2016/nh/c5nh00073d) with permission from Royal Society of Chemistry upon author's request. Order License ID: 1601203-1. The graph (b) was adapted with permission from Gao, D.; Hu, D.; Liu, X.; Zhang, X.; Yuan, Z.; Sheng, Z.; Zheng, H., Recent Advances in Conjugated Polymer Nanoparticles for NIR-II Imaging and Therapy. ACS Applied Polymer Materials 2020, 2 (10), 4241-4257 (available on: https://pubs.acs.org/doi/10.1021/acsapm.0c00679). Copyright © 2020 American Chemical Society.

Figure 24: the graphs (a, b, c) were prepared by the author of this dissertation. The graph (d) was adapted with permission from Hajda, A.; Grelich-Mucha, M.; Rybczyński, P.; Ośmiałowski, B.; Zaleśny, R.; Olesiak-Bańska, J., BF2-Functionalized Benzothiazole Amyloid Markers: Effect of Donor Substituents on One- and Two-Photon Properties. ACS Applied Bio Materials 2023, 6 (12), 5676-5684 (available on: https://pubs.acs.org/doi/10.1021/acsabm.3c00815). The publication is licensed under CC-BY 4.0. Copyright © 2023 The Authors. Published by American Chemical Society.

Figure 25: the graphs (a-e) were adapted from Johansson, P. K.; Koelsch, P., Label-free imaging of amyloids using their intrinsic linear and nonlinear optical properties. Biomedical Optics Express 2017, 8 (2), 743-756 (available on: https://opg.optica.org/boe/fulltext.cfm?uri=boe-8-2-743&id=357274#articleBody) with permission. © Johansson and Koelsch [2017] Optical Society of America. The graph (f) was adapted from Obstarczyk, P.; Lipok, M.; Grelich-Mucha, M.; Samoć, M.; Olesiak-Bańska, J., Two-Photon Excited Polarization-Dependent Autofluorescence of Amyloids as a Label-Free Method of Fibril Organization Imaging. The Journal of Physical Chemistry Letters 2021, 12 (5), 1432-1437 (available on: https://pubs.acs.org/doi/10.1021/acs.jpclett.0c03511) with permission. The publication is licensed under CC-BY. Copyright © 2021 The Authors. Published by American Chemical Society. The graph (g) was adapted from Pansieri, J.; Josserand, V.; Lee, S.-J.; Rongier, A.; Imbert, D.; Sallanon, M. M.; Kövari, E.; Dane, T. G.; Vendrely, C.; Chaix-Pluchery, O.; Guidetti, M.; Vollaire, J.; Fertin, A.; Usson, Y.; Rannou, P.; Coll, J.-L.; Marquette, C.; Forge, V., Ultraviolet–visible–near-infrared optical properties of amyloid fibrils shed light on amyloidogenesis. Nature Photonics 2019, 13 (7), 473-479 (available on: https://www.nature.com/articles/s41566-019-0422-6) with permission from Springer Nature. License number: 6012021425419.

Figure 26: graphs (a-c) are own source of the author of this dissertation.

In II. MAIN RESEARCH CONDUCTED:

(a) In Chapter 5. Autofluorescence of amyloids determined by enantiomeric composition of peptides are included figures and tables that constitute own source of the author of this dissertation, or that were reproduced, reprinted or adapted with permission from Grelich-Mucha, M.; Garcia, A. M.; Torbeev, V.; Ożga, K.; Berlicki, Ł.; Olesiak-Bańska, J., Autofluorescence of Amyloids Determined by Enantiomeric Composition of Peptides. The Journal of Physical Chemistry B 2021, 125 (21), 5502-5510 (available on: https://pubs.acs.org/doi/epdf/10.1021/acs.jpcb.1c00808?ref=article_openPDF). The publication is licensed under CC-BY 4.0. Copyright © 2021 The Authors. Published by American Chemical Society. Under these conditions, the following figures were reproduced: **Figure 27** graphs (b, d, f), **Figure 30**, **Figure 35** graphs (a, b); own source includes: **Figure 28** graphs (a-c); reprinted: **Figure 29** graphs (a-c); adapted: **Figure 31** graphs (a-d), **Figure 32** graphs (a, b), **Figure 33** graphs (a-d), **Figure 34** graphs (a-c), **Figure 36** (a-d), **Figure 37** graphs (a, b). **Figure 38** graphs (a-d) were adapted with permission from Grelich-Mucha, M.; Bachelart, T.; Torbeev, V.; Ożga, K.; Berlicki, Ł.; Olesiak-Bańska, J., Amyloid engineering – how terminal capping modifies morphology and secondary structure of supramolecular peptide aggregates. Biomaterials Science 2024, 12 (6), 1590-1602 (available on: https://pubs.rsc.org/en/content/articlelanding/2024/bm/d3bm01641b) from Royal Society of Chemistry. The article is licensed under a Creative Commons Attribution-NonCommercial 3.0 Unported Licence.

(b) In Chapter 6. Amyloid engineering – how terminal capping modifies morphology and secondary structure of supramolecular peptide aggregates figures that constitute own source of the author of this dissertation, or that were reproduced, reprinted or adapted with permission from Grelich-Mucha, M.; Bachelart, T.; Torbeev, V.; Ożga, K.; Berlicki, Ł.; Olesiak-Bańska, J., Amyloid engineering

– how terminal capping modifies morphology and secondary structure of supramolecular peptide aggregates. Biomaterials Science 2024, 12 (6), 1590-1602 (available on: https://pubs.rsc.org/en/content/articlelanding/2024/bm/d3bm01641b) from the Royal Society of Chemistry. The article is licensed under a Creative Commons Attribution-NonCommercial 3.0 Unported Licence. Under these conditions, the following figures/tables were reprinted: **Figure 39**, **Figure 44** graphs (a-f), **Figure 45** graphs (a-f), **Figure 46** graphs (a-f), **Figure 50** graphs (a-c); adapted: **Table 4**, **Figure 40** graphs (a, b), **Figure 41**, **Figure 42** graphs (a-g), **Table 5**, **Figure 43**, **Figure 47** graphs (a, b), **Figure 48** graphs (a-d), **Figure 49** graphs (a-c), **Figure 51** (a, b), **Figure 52** graphs (a-d).

(c) In Chapter 7. One- and two-photon excited autofluorescence of lysozyme amyloids are included figures and tables that were reproduced or adapted with permission from Grelich-Mucha, M.; Lipok, M.; Różycka, M.; Samoć, M.; Olesiak-Bańska, J., One- and Two-Photon Excited Autofluorescence of Lysozyme Amyloids. The Journal of Physical Chemistry Letters 2022, 13 (21), 4673-4681 (available on: https://pubs.rsc.org/en/content/articlelanding/2024/bm/d3bm01641b). The publication is licensed under CC-BY 4.0. Copyright © 2022 The Authors. Published by American Chemical Society. Under these conditions, the following figures were reproduced: **Figure 53** graphs (a-f), **59** graph (b); adapted: **Table 6**, **Figure 54** graphs (a, b), **Table 7**, **Table 8**, **Figure 55**, **Figure 56** graphs (a, b), **Figure 57** graphs (a-d), **Figure 58** graphs (a, b), **Figure 59** graph (a), **Table 9**, **Figure 60** graphs (a-d), **Table 10**, **Figure 61**, **Figure 62** graphs (a-b).